Isomer Decay Spectroscopy of $N \leq 126$ Neutron-Rich Nuclei

Steven John Steer

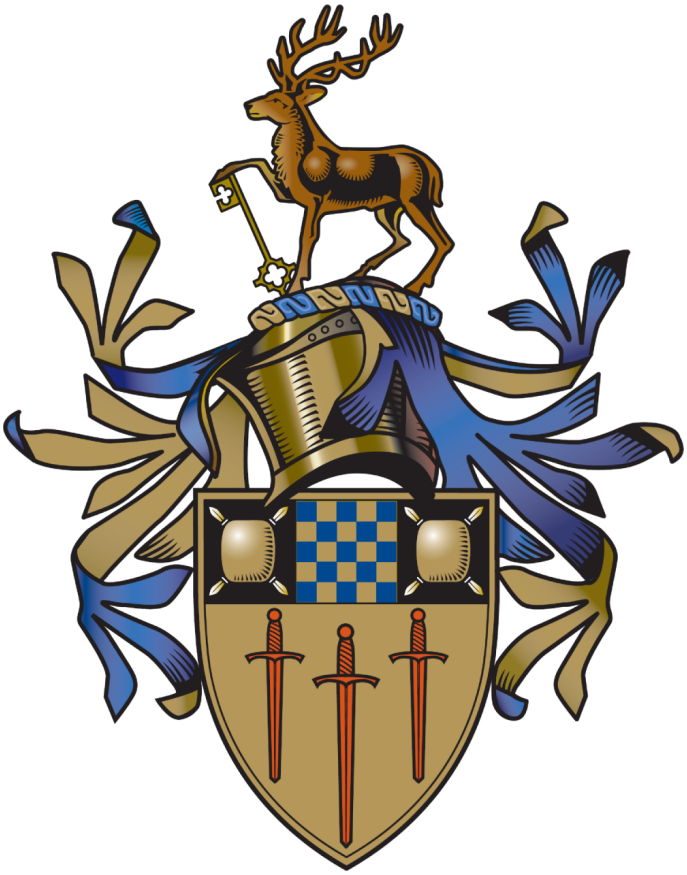

Submitted for the degree of Doctor of Philosophy

Department of Physics,
Faculty of Engineerings and Physical Sciences,
University of Surrey.

October 2008

Abstract

Relativistic projectile fragmentation at 1 GeV per nucleon with doubly-magic $^{208}_{82}Pb_{126}$ on a 2.5 g/cm^2 thick $^{9}_{4}Be_{5}$ target has been performed at GSI. Ions in the secondary beam ranging $107 \leq N \leq 127$ and $69 \leq Z \leq 81$ were selected with the fragment separator, while identifying them simultaneously on an event-by-event basis through time-of-flight, magnetic rigidity, energy loss and position measurements. The selected ions were brought to a halt in an $\sim$ 8 mm plastic stopper, positioned at the centre of the RISING γ-ray spectrometer array. Photon emissions from metastable excited states of the stopped particles were observed for half-lives $\sim$ 10 ns $\rightarrow$ 1 ms. Analysis of this investigation has made the first experimental measurement on two $N = 126$ nuclear species: $^{204}_{78}$Pt and $^{203}_{77}$Ir. These are the lightest $N = 126$ nuclides measured to date. Also presented is the first information on excited states in another $N = 126$ nuclide, $^{205}_{79}$Au. The findings have been interpreted in terms of the independent single-particle spherical shell model. In part, the model fails to reproduce the experimental findings, corrections to the parametrisation of the model are suggested. From the measured $N < 126$ nuclei: 6 nuclear species have had states measured for the first time ($^{199-201}_{77}$Ir, $^{197,198}_{76}$Os, $^{191}_{74}$W); another 7 have had excited states observed for the first time ($^{204,202}_{79}$Au, $^{203}_{78}$Pt, $^{202}_{77}$Ir, $^{199}_{76}$Os, $^{196}_{75}$Re, $^{189}_{73}$Ta); 7 isomers are reported for the first time ($^{204,205}_{80}$Hg, $^{201}_{79}$Au, $^{197,199}_{78}$Pt, $^{195}_{77}$Ir, $^{193}_{76}$Os); and repeat measurements on 17 previously reported isomers have been performed ($^{203-206}_{80}$Hg, $^{203}_{79}$Au, $^{198,200-202}_{78}$Pt, $^{198}_{77}$Ir, $^{195}_{76}$Os, $^{191-194}_{75}$Re, $^{190}_{76}$W, $^{188}_{73}$Ta). From these 47 observed isomers, isomeric ratio information has been measured in 34 cases.

Acknowledgements

The physics department at Surrey has been a delightful place to study for my doctorate, the trips to Germany for RISING experiments have come to feel more like visits to old friends than going to work. There are literally dozens of people - family, friends and colleagues - to whom I owe thanks and gratitude. Here I mention in name only the very few, whose assistance I could never have completed my PhD without.

First and foremost, I would like to thank Zsolt Podolyák, he has guided me through all of my work, he has always made time for me, his understanding of the subject area, and his appreciation of what is and isn't important when carrying out research is excellent. My second supervisor, Paddy Regan, has persuaded me to go to GSI on many occasions, and I must admit that although I 'kicked and screamed' at the time, in hindsight the experiences have been invaluable. He has been ready with advice whenever necessary and also kept a hand firmly on the physics too. I consider myself very lucky to have been supervised by Zsolt and Paddy, their complimentry talents as scientists and teachers has placed me in a highly privileged position for my studies.

Stephane Pietri was instrumental in ensuring that the data examined in this thesis is of an extremely high quality and Adam Garnsworthy provided me with an excellent platform from which I have been able to analyse that data. Without their assistance, I am certain most of the findings in this thesis would not exist, thank you both.

Finally, thank you Warren. Without your enthusiasm for teaching I would never have wanted or had the grades to go to Manchester for my undergraduate degree, let alone make it this far.

"...he has a particular interest in atomic and nuclear physics."

A-level school report, King Edwards VI School, Lichfield

Warren Dransfield-Scott (2000)

Contents

List of Figures

List of Tables

Chapter 1

Motivations and Aims

1.1 Motivations: Nuclear Structure

One of the major goals of nuclear physics is the development of accurate theoretical predictions of the structure of nuclei. Shell closures provide excellent testing grounds for the behaviour of individual nucleons [1]. Microscopic predictions succeed due to the high purity of the wavefunctions in low-lying excited states. Additionally sudden increases in particle separation energies occur at closed shells, reducing the level density. These circumstances allow for realistic modelling in terms of single particles (holes) orbiting in mean fields. Experimentation is necessary in attaining information with which one may then test the shell model predictions and make corrections where the model fails.

1.2 Motivations: Projectile Fragmentation

The projectile fragmentation technique provides opportunities to observe nuclei far from stability [2], however the reaction is not deeply understood. Tests of the capabilities of fragmentation have been performed to establish population ratios of nucleon configurations in nuclei, and also to determine how much spin can be imparted on the outgoing fragments [3–5]. From this information the technique's potential may be fully harnessed in future experimentation, opening avenues for wider nuclear research interests.

1.3 Broader Motivations: the *r*-process and Shell Quenching

There is astrophysical interest in studying the nucleus $^{195}_{69}\mathrm{Tm}_{125}$ and lighter $N = 125$ isotones as they are predicted to be of particular importance during the r-process [6]. With modern technology these nuclei are experimentally out of reach (figure 1.1 shows how far $^{195}_{69}\mathrm{Tm}_{125}$ lies from current measurements). This work extends physical knowledge at the neutron-rich end of the $N = 126$ isotone. Although it offers no pertenant insight regarding the r-process, it does act as a technological stepping stone towards experimentally observing $^{195}_{69}\mathrm{Tm}_{125}$ and other nuclei of astrophysical interest. Similarly this experiment also takes steps towards anticipated shell quenching effects far from stability, again current technology forbids the examination of the nuclei of most interest, but the current work builds a foundation for future studies.

1.4 Specific Aims of the Project

This work is to expand experimental information regarding neutron-rich $N = 126$ nuclei. Through the nuclear fragmentation reaction, 4-proton cold knockout of accelerated ^{208}Pb particles were to manufacture $^{204}\mathrm{Pt}_{126}$. The extent of experimental evidence on nuclei in the vicinity of ^{208}Pb prior to March 2006 (i.e. before the experiment) are noted in figure 1.1. Spectroscopic information is presented as cited by the NNDC evaluated and unevaluated databases [7]. Each star indicates a previously reported isomer whose half-life is between 10 ns $\rightarrow$ 1 ms, it is expected that these isomers would be detectable in the experiment described in the current work. No spectroscopic information has previously been reported regarding ^{204}Pt. The ^{204}Pt nuclei populated in this experiment, once selected and identified, were to be observed by the RISING spectrometer. Expected metastable excitations in this nuclide were to give insight into single-particle behaviour. The experiment is capable of populating and ascertaining information on other nuclei in parallel to ^{204}Pt. Isomers in these nuclei offer similar nuclear structure information. The experiment is also able to define isomeric ratios, allowing tests of theoretical calculations of fragmentation population capabilities. Regarding isomeric ratios, here the key measurement is on ^{206}Hg, as from a theoretical perspective it involves a relatively simple 2-proton cold knockout reaction.

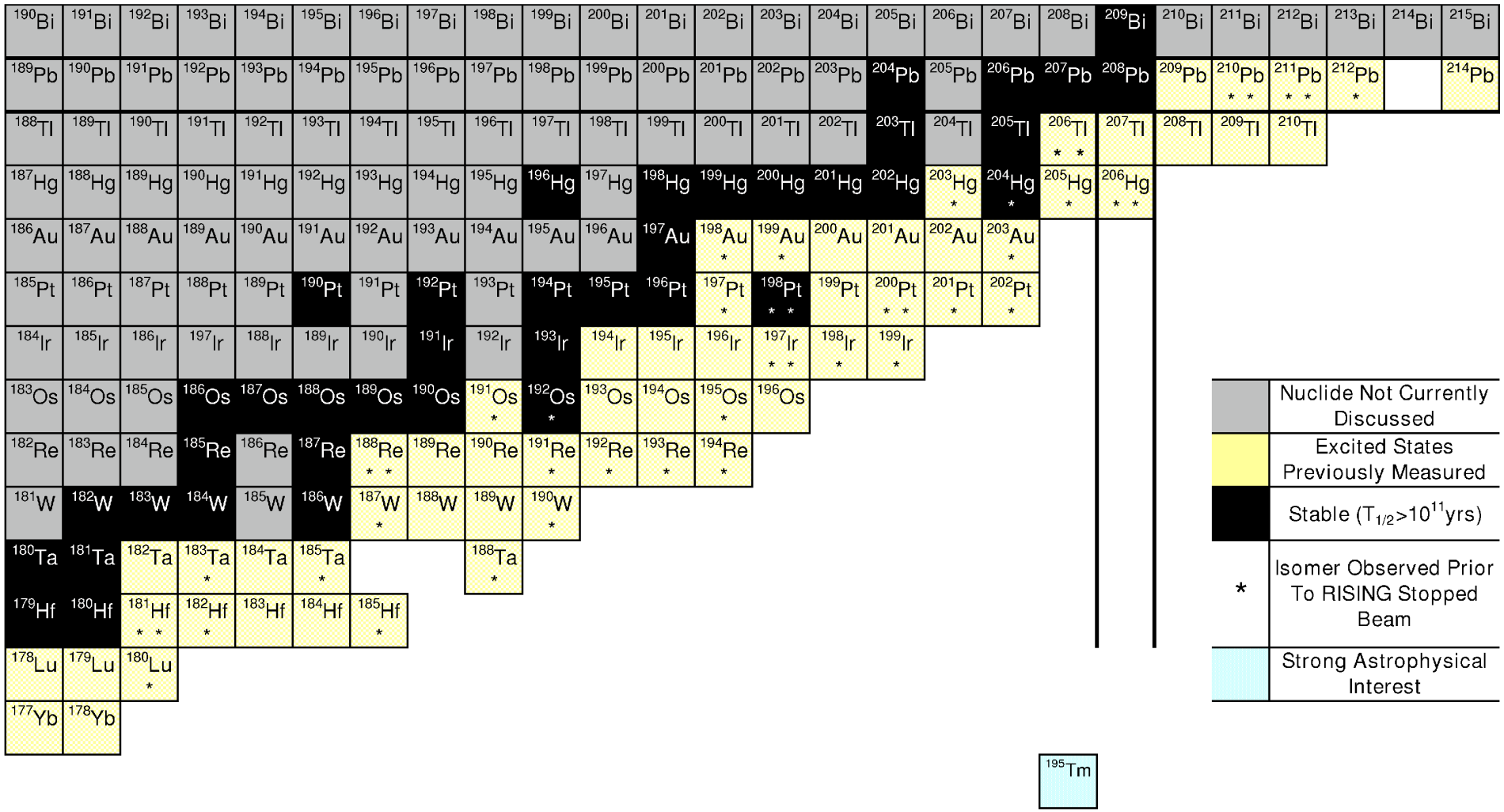

Figure 1.1: Section of the nuclear chart indicating in which nuclides excited states have been measured prior to March 2006. Of the stable nuclei, only ^{192}Os, ^{198}Pt and ^{204}Hg have their previously measured isomers indicated presently.

Chapter 2

Nuclear Theory

The independent-particle, spherical shell model approach to describe the structure of nuclei is the method best applied when considering heavy mass nuclei where only few valence nucleons are free to change their quantum state. When greater numbers of nucleons are involved in excitations, a microscopic description of nuclear behaviour breaks down. This is due to the complexities caused by the vast number of relevant interactions. The spherical nature of the modelling technique also breaks down in instances of permanent, static deformation to the nucleus. Shape changes in the nuclear body introduce an angular dependence to wavefunctions.

The work presented in this thesis focuses on nuclei approaching the doubly magic system ^{208}Pb, observing structural excitations of up to a few MeV above the ground state. In these cases only the surface particles or holes exhibit degrees of freedom, allowing them, and them only, to be used when defining the structure of excitations. Additionally, the close proximity to ^{208}Pb of the nuclei studied in the present work makes a spherical approximation of nuclear shape valid. It should be noted that the independent particle model is designed to apply to nuclei with only a single particle (hole) added to the closed core [8]. For the nuclei examined in this work, the furthest from ^{208}Pb suffer an unworkable break down in the spherical and single-particle approximation. Modelling of these nuclei needs additional or different considerations to account for their structure. The interpretation of this group of nuclei goes beyond the scope of this thesis. The independent single-particle spherical shell model is used to interpret the present findings. Before it can be explained and then applied, some foundations about nuclei are discussed.

2.1 Observations of Nuclei Without a Model

Some simple observations regarding nuclei explain why an independent-particle spherical shell model is valid. The separation energy for nucleons can be as much as $\sim$ 10 MeV and the average kinetic energy of a nucleon can be expected to be $\sim$ 25 MeV [9]. Their mass-energies are $\approx$ 940 MeV/c^2 and the lightest virtual exchange particles, π mesons, have mass-energy $\approx$ 137 MeV/c^2 [9]. There is thus a substantial difference between particle mass-energies and the energy required to induce state-changing effects in a nucleus. This energy difference validates an approximation that nuclei are a collection of individual particles.

Observations have shown very clear interference patterns during scattering experiments on nuclei [9]. The interference proves that at the very least, mean free paths of nucleons are comparable to the nuclear radius; in most cases they are greater. These observations enable a modelling assumption of independent particle motion within the nuclear matter.

All of the nucleons in the nucleus contribute to the resultant mean field in which they individually move. This mean field will be placed aside for the time being, it is addressed in section 2.2. Nucleon kinetic energy in the nucleus is such that $(v/c)^2 \sim 1/10$, allowing relativistic considerations to be neglected [10].

Characterisations of the nucleus' individual particles can be made in terms of state symmetries. One example of this is nucleon symmetry, where each nucleon is deemed to be in a 'proton' or 'neutron' state. Treating protons and neutrons as states of the same particle is validated by isobaric symmetry, which is a special case of isospin symmetry. Isospin symmetry states that neutrons and protons are indistinguishable to the strong nuclear force. Isobaric symmetry categorises isospin symmetric nuclei into groups by their atomic mass [11].

Low energy *pp* and *np* scattering by Breit and Wigner [12] provided the first experimental evidence for isospin symmetry. In both types of scattering a near identical cross section is observed for the ^{1}S channel after normalising for the Coulomb force. The ^{1}S channel refers to cases of anti-parallel intrinsic spin alignment of the nucleon pair. The result implies charge independence of the strong nuclear force and hence introduces this concept of nucleon symmetry. In the experiment cases of parallel alignment of spins were observed only in the *np* case, not the *pp*. This is due to Pauli exclusion [13], which

forbids indistinguishable fermions with an identical set of quantum numbers to exist in the same quantum state at the same time. In the instance of Breit and Wigner's scattering experiment Pauli's principle forbids intrinsic spin alignment in *pp* scattering. This exclusion principle has a profound influence on nuclear composition, requiring all fermions to be anti-symmetrised.

2.1.1 Wave Functions

When treating a system as a collection of non-interacting single particles in quantised motion, the resulting wave can be expressed as a linear product of single particle states. Here the term 'motion' does not mean, as in the classical sense, that particles move smoothly through space, but instead particles are annihilated at one locality while being simultaneously created in another. The quantum concept of locality is not only a spatial coordinate, it can extend to a full set of quantum numbers. By using a Slater determinant one is able to write out all the combinations of particle configurations;

$$< x_1 x_2 \cdots x_A | v_1 v_2 \cdots v_A >= \frac{1}{\sqrt{A!}} \begin{vmatrix} \varphi_{v_1}(x_1) & \varphi_{v_2}(x_1) & \cdots & \varphi_{v_A}(x_1) \\ \varphi_{v_1}(x_2) & \varphi_{v_1}(x_2) & \cdots & \varphi_{v_A}(x_2) \\ \vdots & \vdots & & \vdots \\ \varphi_{v_1}(x_A) & \varphi_{v_1}(x_A) & \cdots & \varphi_{v_A}(x_A) \end{vmatrix}, \qquad (2.1)$$

here φ_{v_i} are the wavefunctions for each orbit, where v_i are a complete set of labels for the one-particle orbits and x_j is the coordinates of the particle, including the spin and isospin variables. The total number of different orbits (combinations of the quantum numbers) is $A!$. This Slater determinant is the basis for many-particle system calculations. Further details of this representation of nuclei can be found in reference [9] and the mathematics of handling quantum mechanical state equations are comprehensively explained in reference [14].

It has been established that any given nucleon is non-interacting over the nuclear radius. All the wave function representations of nucleon orbits, v_i, then are also non-interacting. The wave functions are thus orthogonal to one another. By the isospin considerations it is also established that they are anti-symmetric. Mathematically speaking: observed, orthogonal, anti-symmetrised wave functions never co-exist. This is consistent with Pauli's exclusion principle. When a nucleus is in its lowest energy

state the nucleons fill the available orbitals, v_i, always taking the lowest available energy eigenvalue. Up to $2j+1$ nucleons can occupy each orbital as their fermionic nature has been shown to forbid otherwise. The lowest possible energy state of the nucleus is hence greater than zero. This lowest possible energy is named the Fermi energy.

These insights invite modelling systems by ordering the different quantum states based on their binding energy in a mean field and then filling these states with a defined number of particles. This method of modelling can be extended beyond the ground state of a nucleus, defining how nuclei configure when excited.

2.2 The Independent-Particle Spherical Shell Model

As so far described in this thesis, the nucleon wavefunctions do not interact with their environment. The strong force which binds the nucleons together was earlier likened to a mean field due to the mean free path of nucleons being long compared to the nuclear size. This mean field potential is now represented by $V(r)$. The time-dependent Schrödinger equation to describe particles in a mean field potential thus takes the form [14];

$$i\hbar\frac{\partial}{\partial t}\Psi(\mathbf{r},t) = \left(-\frac{\hbar^2}{2m}\triangle + V(r)\right)\Psi(\mathbf{r},t), \tag{2.2}$$

Ψ is the particle's wave function with respect to t and $\mathbf{r}$; m is the particle mass, as the system is non-relativistic this is the rest mass, m_0, and $\triangle$ is the Laplacian operator. For the nuclei described in this thesis, the angular dependence of the Schrödinger equation (equation 2.2) can be dealt with analytically as the model is assuming the nucleus to be spherical. To solve the Schrödinger equation one must determine the potential of the mean field.

2.2.1 The Woods-Saxon Potential

Evidence for single-particle shell closures in the nuclear mean field is observed at $N, Z = 2,\ 8,\ 20,\ 28,\ 50,\ 82,\ 126$ [15, 16]. There are various pieces of experimental evidence proving this including: proton and neutron separation energy discontinuities; α-particle emission energies for different isotopes of an element; neutron-capture cross sections and sudden changes in the nuclear charge radius [17]. A mean field potential

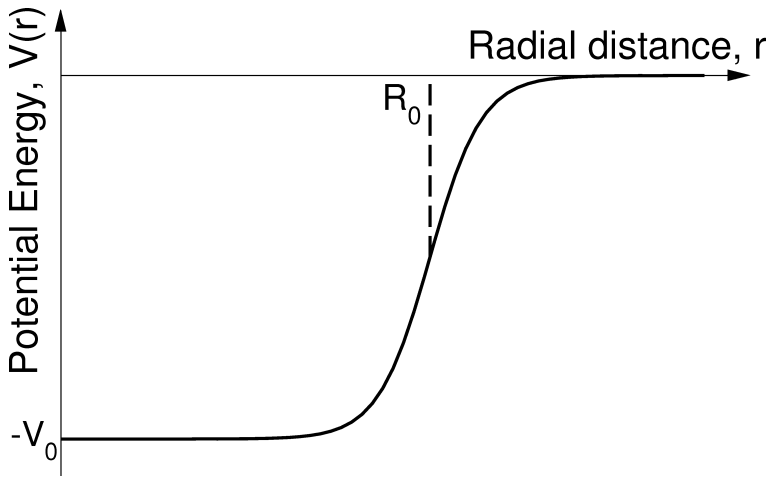

Figure 2.1: Schematic of the Woods-Saxon potential.

needs to be able to reproduce these shells. A Woods-Saxon [18] style potential with an additional spin-orbit term successfully does this while also being analytically solvable. The potential is defined [10];

$$V^{W.S}(r) = -V_0 \left[1 + exp\left(\frac{r - R_0}{a} \right) \right]^{-1}, \tag{2.3}$$

where r is radial distance from the centre of the potential, a determines the diffuseness of the nuclear surface ($a \simeq 0.5$ fm), V_0 is the depth of the potential ($V_0 \simeq 50$ MeV) and R_0 is a measure of nuclear size;

$$R_0 = r_0 A^{1/3}, \tag{2.4}$$

here $r_0 \sim 1.2$ fm and A is the number of nucleons in the system. The Woods-Saxon potential is schematically represented in figure 2.1.

The additional spin-orbit term is defined by;

$$V_{l\cdot\mathbf{s}} = -V_{ls} \frac{d\left(\dfrac{V^{W.S.}(r)}{V_0} \right)}{dr} \mathbf{l} \cdot \mathbf{s}. \tag{2.5}$$

The spin-orbit contribution is primarily a surface effect [8]; the surface being where the nucleon density and hence the Woods-Saxon potential, $V^{W.S.}(r)$, reduces. In equation 2.5 $V_{l\cdot\mathbf{s}}$ is the spin-orbit potential where V_{ls} is a strength constant and the quantum numbers l and s are the orbital angular momentum and intrinsic spin, respectively.

Note that the l-s coupling relationship implies that there will be a larger contribution to the potential from the spin-orbit term for higher angular momentum states than lower. This additional spin-orbit term breaks the degeneracy of states in an orbital of given n (the principle quantum number) and l. The resulting mean field is thus defined by:

$$V(\mathbf{r}) = V^{W.S.}(r) + V_{l\cdot\mathbf{s}} \tag{2.6}$$

2.3 Energy Levels

To define the energy levels the Woods-Saxon potential is modified with an additional spin-orbit term (equation 2.6) and applied to the Schrödinger equation (equation 2.2) for all combinations of the set of quantum numbers; n, the principal quantum number; l, orbital angular momentum and j, total angular momentum where $j = l + s$ (the orbital angular momentum plus the intrinsic spin component). The resulting eigenvalue energies order the orbitals (each degenerate with $2j + 1$ states) recreating the physically observed shell structure of nuclei for both the proton and neutron states of nucleons. This level scheme is shown in figure 2.2 with standard labelling. It should be noted that the precise single-particle ordering and separation of these energies changes depending on the nuclear mass, A, and also on Coulomb effects [8]. These slight differences do not affect the observed shell gaps when considering non-exotic, spherical nuclei.

2.3.1 Residual Interactions by a δ-function

There are multiple particles in each named orbit on figure 2.2. These levels are degenerate under the model explained thus far. There is however a breaking in this degeneracy which can be explained with a residual interaction. A δ-function [8] is an appropriate way to model its effects on the particles within the (under explanations so far) degenerate orbitals, as it is highly localised. This residual interaction is easiest explained by exemplifying a case of only two particles in a given orbital.

Two particles with different projections on the symmetry axis (in this spherical case the symmetry axis is arbitrary) of their angular momentum, m, but with an

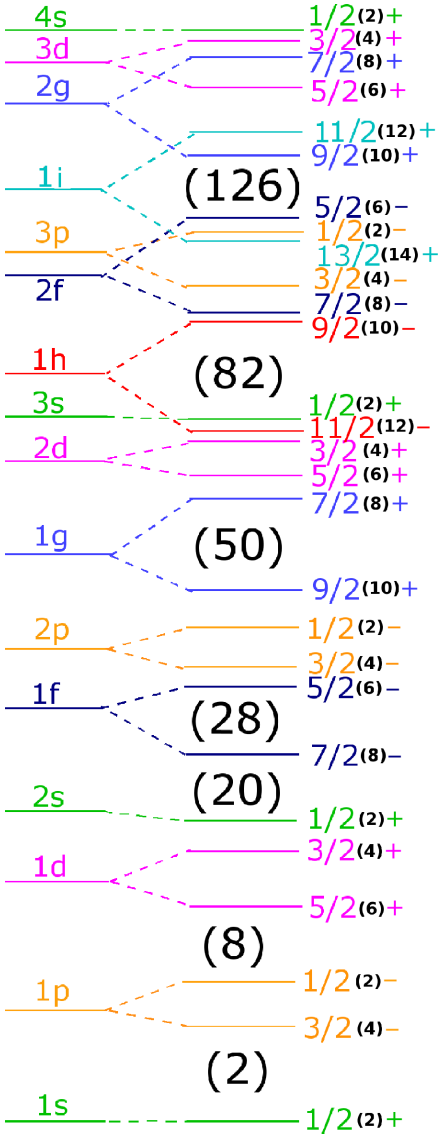

Figure 2.2: Nucleon level ordering in an independent-particle spherical nucleus with a Woods-Saxon style mean field potential and an additional spin-orbit term. The number of particles in each orbital are noted in black on the right-hand side of the diagram. This scheme is a modified picture from reference [19].

otherwise identical set of quantum numbers, spatially overlap to a greater than normal degree. The mean field potential explained thus far does not account for the increased strength of the strong nuclear force these two nucleons feel between each other. The magnitude of this increased strength is dependent on the specific spatial overlap of each individual m-state with the other projections of the angular momentum in the concerned orbit.

Figure 2.3 pictorially shows the degree of overlap between two such pairs of nu-

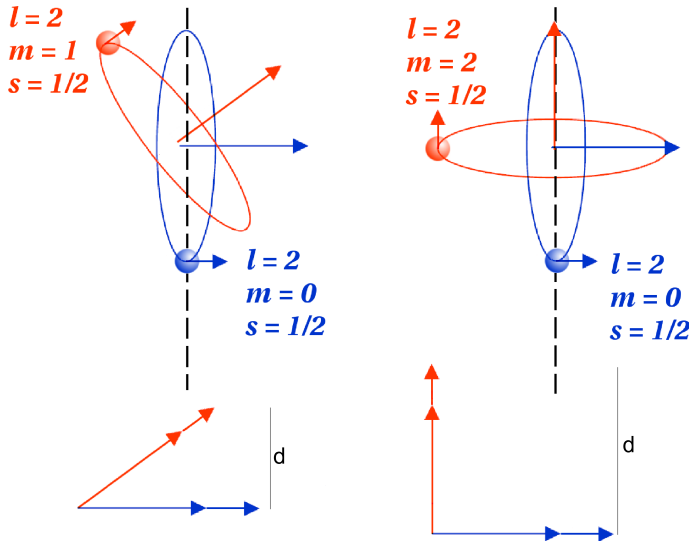

Figure 2.3: A pictorial example of how orbital wave function overlap differs between pairs of substates. These two pairs of substates are taken from a $d_{5/2}$ orbital. The dashed black line is the symmetry axis. Notice that the difference in angular momentum projected onto the symmetry axis of the nucleons in the left pair is smaller than for the right. This wave function orientation difference is indicated by d.

cleons (the examples are taken from a $d_{5/2}$ orbit). Assuming the two nucleons are indistinguishable and from identical orbits, the formula governing the residual interaction potential, $V_{12}(\delta)$, is given as;

$$V_{12}(\delta) = -\frac{-V_0}{r_1 r_2}\delta(\mathbf{r}_1 - \mathbf{r}_2). \tag{2.7}$$

In this equation subscripts 1 and 2 identify the two nucleons, each with a spatial position, $\mathbf{r}$; δ represents the Kronecker δ-function and V_0 is the maximum depth of the potential felt between the two particles. By applying this potential to the Schrödinger equation (equation 2.2) the relative energy splitting of different angular momentum states is determined. The magnitude of the potential and thus the relative splitting of states in the interaction is dependent only on the angular separation of the wave functions. However the magnitude of the resulting energy splitting is increased in amplitude by having larger values of n and l for the two similar orbits [8]. It is stressed once more that all of this is true when the two particles are indistinguishable and reside in identical orbits. Figure 2.4 characterises the effects of the residual interaction.

2.4 Even-Even Nuclei Near $Z = 82$, $N = 126$

One of the principal aims of the current work is to establish the near yrast spectrum for $^{204}Pt_{126}$. This nuclide is 4-proton-holes from doubly magic ^{208}Pb. Similar such studies have already been made in the other three cases of 2 particle (hole) pair deviations from ^{208}Pb. In addition all four of the single pair deviations have also been studied. Low-lying yrast states in these nuclei are displayed in figure 2.5 [20–31]. At low energy excitations in these nuclei one expects the breaking of a single pair of nucleons, the broken pair then defines the resultant spin, I, and parity, π, of the nucleus.

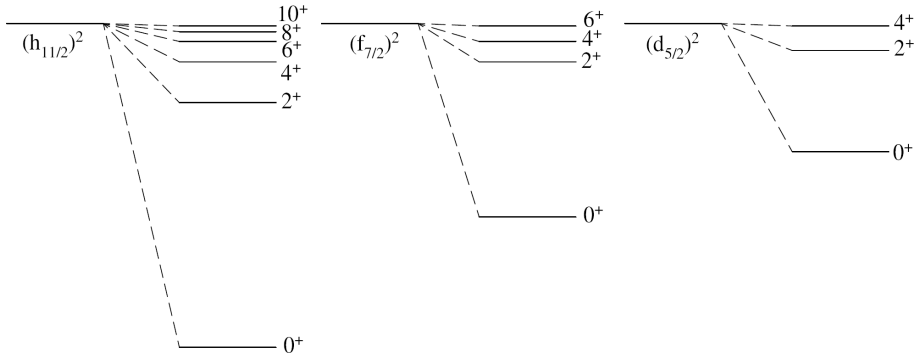

Figure 2.4: Examples of the δ-residual interaction breaking degeneracy in an orbital for a pair of like-nucleons in a single j-shell. The effects of this *relative* splitting increase for greater angular momenta. This figure is modified from reference [32].

In the neutron-hole cases of ^{206}Pb and ^{204}Pb, low-lying states with spins of greater than $I = 4$ require the occupation of the $1i_{13/2}$ neutron orbital. For excitations up to $I = 8$ holes can occupy the $2f_{7/2}$ and $1h_{9/2}$ orbitals also, but contributions from these orbits must come from deeper into the $N = 126$ shell. The presence of a large angular momentum intruder orbital introduces some negative parity states to the low-lying yrast levels .

The cases for neutron or proton pairs added to the ^{208}Pb core (^{210}Pb, ^{212}Pb, ^{210}Po and ^{212}Rn) are considered together as they express similar behaviour. For additional protons pairs the $2f_{7/2}$ and $1h_{9/2}$ orbitals are each of $\pi = -$ parity, offering a maximum spin alignment of I=8; for additional neutrons the $\pi = +$ orbitals ($1i_{11/2}$ and $2g_{9/2}$) align to a maximum I=10. In all four cases these orbitals form the yrast structure of the nucleus until multiple pair-breaking becomes energetically available, together with the possible onset of collective behaviour.

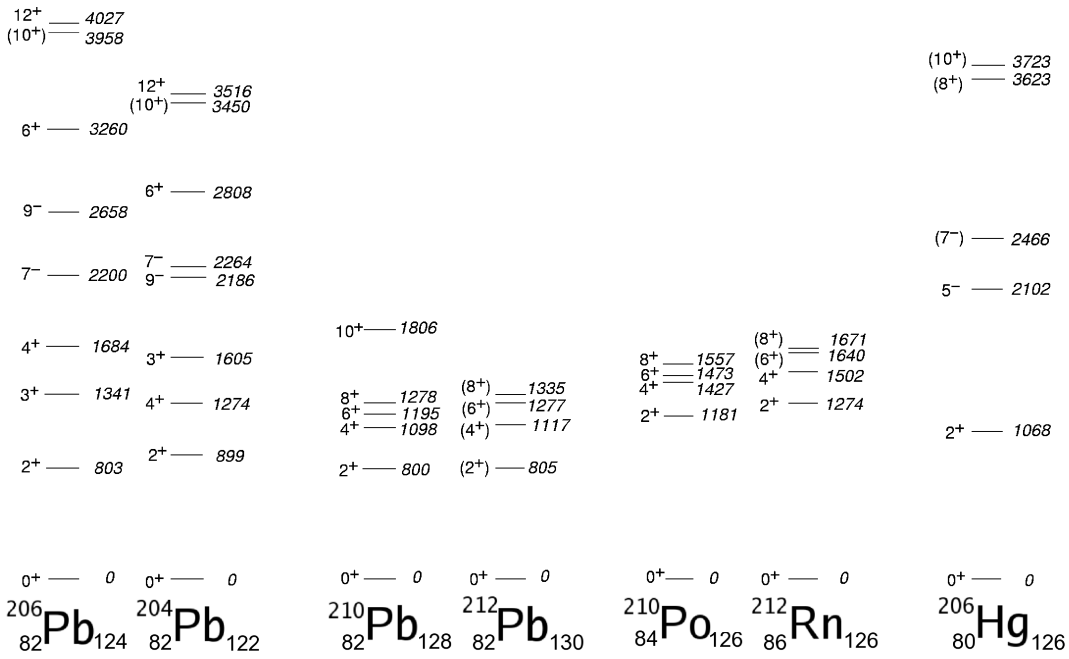

Figure 2.5: Low-lying yrast states for even-even Z=82, N=126 doubly magic nuclei with an additional 2 or 4 particles (holes) added. The data are taken from references [20–31].

The final case, a proton-hole pair in ^{206}Hg, bares some resemblance to neutron-holes in ^{208}Pb. The $1h_{11/2}$ opposite parity intruder orbital is the only available high-angular momentum orbital at low excitation energy. As with the neutron-holes the result is a switch in parity for some excitations and a reliance on having both proton-holes of the broken pair reside in the $1h_{11/2}$ orbital if spin is to be greater than > 6. The next closest high-spin orbitals reside above the $Z = 82$ shell gap and thus would require energies of ~ 4 MeV to be reached.

The independent spherical shell model succeeds in reproducing experimentally observed single-particle states in these nuclei. From their systematics it suggests then that in the case of removing a second proton-hole pair from ^{208}Pb, forming ^{204}Pt one can expect levels similar to ^{206}Hg to be observed.

2.5 Neutron-Holes in the $N = 82$ Shell Closure

A comparison can be drawn between the proton-holes in the 82 particle shell closure and neutron-holes in the same shell. Neutron-rich isotopes of $_{50}$Sn offer this opportunity. Some deviations in the observed behaviour are expected due to reduced

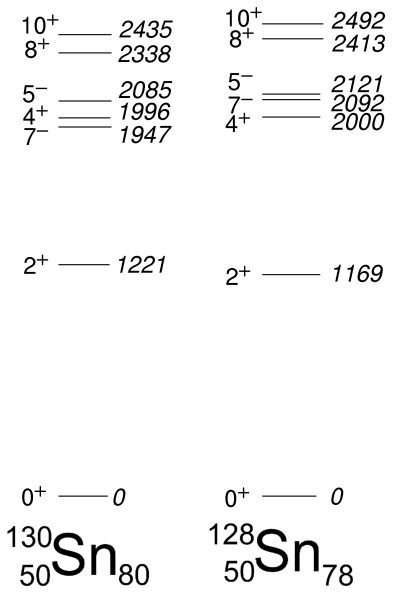

Figure 2.6: Tin isotopes with one and two neutron-hole pairs in $N = 82$. The data are taken from reference [33].

coulomb effects in the Sn nuclei and also due to the lower mass of the nucleus compared to the nuclides near ^{208}Pb. The yrast excitations in the one and two-pair neutron-hole nuclei, ^{130}Sn and ^{128}Sn, are shown in figure 2.6 [33].

The yrast states of ^{130}Sn and ^{128}Sn show similar structure to ^{206}Hg (see figure 2.5). The yrast 4^+ state in the Sn nuclei is important, in that unlike in the ^{206}Hg, case this state is lower in energy than the yrast 5^- state.

2.6 Electromagnetic Decay

The decay of one nuclear state to another is a statistical process with an exponential form through time ($e^{-\lambda t}$). The value of the decay constant, λ, is understood through transition rates. When a decay takes place energy is released through one of a selection of mechanisms. Two mechanisms are of relevance to the current work: decays by γ-ray emission and decays by internal conversion.

2.6.1 Gamma Decay

When γ-ray emission decay takes place the increased binding of the nucleus is balanced by the energy of the emitted γ-ray, E_γ, and by momentum conservation such that [17];

$$\Delta E = E_i - E_f = E_\gamma + \frac{E_\gamma^2}{2M_0c^2}, \tag{2.8}$$

here E_i and E_f are the initial and final energies, respectively and M_0 is the rest mass of the nucleus. The correction for momentum conservation is a small factor, considerably smaller than the resolving power of the detectors. The term is neglected henceforth, thus $\Delta E = E_\gamma$. Additionally to carrying away energy, γ-rays carry orbital angular momentum from the nucleus, such that;

$$|I_i - I_f| \leq L \leq I_i + I_f. \tag{2.9}$$

where the parity of the multipole is then defined;

$$\begin{aligned} \Delta\pi(EL) &= (-1)^L, \\ \Delta\pi(ML) &= (-1)^{L+1}, \end{aligned} \tag{2.10}$$

for electric (E) and magnetic (M) transitions respectively. One should note that in addition to orbital angular momentum, γ rays possess an intrinsic spin of $S = \pm 1$. This intrinsic spin forbids γ decay by a single γ ray for cases of $L = 0$; it has to take place by alternative means. These means are internal conversion (see section 2.6.2), internal pair formation (creation of an e^-e^+ pair), double γ-ray emission (for example $E1 - E1$) or higher order processes [34].

2.6.2 Internal Conversion

Electron orbit wave functions overlap to varying degrees with the wave function of the nucleus. Due to this cross-over there is a finite probability that nucleons will interact with the orbiting electrons, the probability is proportional to the square modulus of the overlap. When such interactions take place the excitation energy, ΔE, is emitted through internal conversion, which is a competing process with γ-ray decay. For internal conversion to occur ΔE ($= E_\gamma$) must overcome the binding energy, B_j, of the electron, i.e. E_j must be positive where;

$$E_j = E_\gamma - B_j; \quad j = K, L_I, L_{II}, ..., M_V, ... \tag{2.11}$$

In equation 2.11 atomic orbitals are labelled because the binding energy for each electron shell differs (it is also perturbed by specific orbital occupation in a given shell).

Only electrons from orbitals with a positive E_j can internally convert. This implies the creation of scenarios where only the less strongly bound electrons can be involved in the electromagnetic decay process. The internal conversion energy imparted to the electron ejects it from the atom with kinetic energy E_j. This leaves a vacancy into which higher lying electrons de-excite. From this a characteristic X-ray (or competing Auger electron emission), or a series of X-rays, is/are emitted from the atom analogously to nuclear γ-ray de-excitation. Binding energy differences between the involved electron orbits determine the X-ray energy. This energy is nuclear charge (Z) dependent, hence X-ray energies are characteristic for each element. An alternative to X-ray emission following internal conversion is Auger electron emission. Here the kinetic energy, E_j, from an electron de-excitation is passed to a third (outer) electron. This is then ejected from the atom, taking the energy with it. Less probable higher order processes may also occur [34], however the X-ray intensity reduction due to Auger electrons is already below the sensitivity of the current experiment.

2.6.3 Internal Conversion of Highly Stripped Ions

When nuclei are highly stripped of electrons, there are changes to the internal conversion decay branch of excited states that warrant discussion here. In the current work, nuclei are highly stripped in-flight. Considering first fully stripped ions, there are no electrons that may internally convert, completely forbidding decays through this mechanism. Things become more complex for H-like and He-like ions (those with one and two electrons, respectively). For these, limited internal conversion can take place. In this work this conversion is always assumed to be α_K internal conversion, on the understanding that the electron(s) attached to the nucleus is/are in the lowest lying ($1s$) orbital, i.e. the K-shell. K-shell internal conversion is well understood for neutral atoms, but not for near fully stripped ions. There is very limited scientific knowledge regarding changes to internal conversion coefficients for near fully ionised nuclei. It is likely that there are perturbations to the understood neutral atom α_K internal conversion coefficient when electrons of other shells are removed from the nucleus.

There have been some previous studies into this matter, including a study of the $I^\pi = 3/2^+$ 14.4 keV isomer in ^{57}Fe for H- and He-like charge states [35]; this study

identifies a dependency on the total spin, F, of the atom. Scientists working with the GSI storage ring have reported results from investigations on highly stripped ions concerning isomer and bound-electron decay/capture rates [36–38]. The rate for both internal conversion and electron-capture decay is proportional to the square modulus of the overlap of the atomic electron and nuclear wavefunctions. This indicates that each process will be similarly affected by the degree of stripping of the nucleus. Among other findings, the GSI storage ring studies of electron-capture in ^{140}Pr have measured the electron capture rate to counter intuitively increase for stripped ions when compared to neutral atoms [38]. The change in the rate is less than a factor of 2, as with the ^{57}Fe case [35].

There is not enough robust information available that may be quantitatively applied to the current study to fully account for internal conversion rate changes in-flight. This recognised issue is not incorporated into the measurement of isomeric ratios for non-fully stripped ions in this thesis (see section 6). Although it is important to be aware of this issue, it is not anticipated to have a pivotal (or likely even measureable) influence on the present results. The α_K values for neutral atoms have been used for in-flight internal conversion coefficients for the isomeric ratio determinations in section 6 involving H- and He-like ions.

2.6.4 Transition Rates

The decay rate through nuclear states by γ-ray decay is derived in terms of transition probabilities. Estimates of the half-lives of these states (Weißkopf estimates) are made by making the assumption that the decay involves the changing of state of only a single nucleon situated in a spherical basis. The transition probability calculations are made through the theory of electromagnetic radiative power from multipoles applied to a quantised system, (i.e. the nucleus). The mathematical derivations are not detailed here (see reference [10] for an example of them). Combining the result of these derivations with the Weißkopf single-particle assumptions gives rise to equations 2.12 and 2.13 [17], these provide an insight to the variables that define decay rates of states.

$$\lambda(EL) \cong \frac{8\pi(L+1)}{L[(2L+1)!!]^2}\frac{e^2}{4\pi\epsilon_0\hbar c}\left(\frac{E}{\hbar c}\right)^{2L+1}\left(\frac{3}{L+3}\right)^2 cR^{2L} \qquad (2.12)$$

$$\lambda(ML) \cong \frac{8\pi(L+1)}{L[(2L+1)!!]^2}\left(\mu_p - \frac{1}{L+1}\right)^2\left(\frac{\hbar}{m_p c}\right)^2\left(\frac{e^2}{4\pi\epsilon_0\hbar c}\right) \times \left(\frac{E}{\hbar c}\right)^{2L+1}\left(\frac{3}{L+2}\right)^2 cR^{2L-2} \tag{2.13}$$

In these equations the decay rate is defined λ, the radius is R, where it is assumed that $R = r_0 A^{1/3}$. Thus there are three variables that govern decay rate in this simple picture; A, the atomic mass number; E, the energy difference between the initial and final states, and L, the angular momentum difference between those states.

Although the assumptions made by Weißkopf are simple and specifically only for protons in a spherical basis, they are found to predict surprisingly similar decay rates to experimental results for "pure" single-particle-like transitions. This is particularly true near closed shells, where the nucleus is spherical to first order; also only a few nucleons are significantly involved with the excited states, validating the single-particle aspect of Weißkopf's estimate. For collective transitions, one is able to show that excitations are highly collective in nature by their large decay probability compared to the Weißkopf single-particle estimate.

When considering likely multipolarity transitions one obtains the equations given in table 2.1. It is clear that for a given nuclear mass and transition energy the lower multipolarities are the dominate decay route. Note that, in general, the electric transitions are faster than the magnetic for a given L.

To quantify to what degree a decay is single-particle in nature, Weißkopf estimates are compared with experimental measurements giving values termed $B(\lambda L)$. These are reduced matrix elements and are assigned the unit "Weißkopf units" (W.u.). As the Weißkopf estimate assumes a decay takes place through the change in orbit of one nucleon alone, equation 2.14 will take a value of 1 if the decay involves a single nucleon (in a spherical basis). In practice transitions range from many orders of magnitude less than 1 to many orders of magnitude larger.

$$B(\lambda L) = \frac{T_{1/2}^{Weiß}}{T_{1/2}^{\gamma}} \tag{2.14}$$

In equation 2.14, $T_{1/2}^{Weiß}$ is the Weißkopf predicted half-life and $T_{1/2}^{\gamma}$ is the partial half-life of the experimental measurement. The partial experimental half-life (and not the actual

Table 2.1: Estimates for transition rates of differing electric and magnetic multipolarity transitions [17]. Energy, E, is in MeV, A is atomic mass number.

L	$\lambda(EL)$ (s^{-1})	$T_{1/2}^{Weiß}(EL)$ (s)
1	$1 \times 10^{14} A^{2/3} E^3$	$6.76 \times 10^{-15} A^{-2/3} E^{-3}$
2	$7.3 \times 10^{7} A^{4/3} E^5$	$9.52 \times 10^{-9} A^{-4/3} E^{-5}$
3	$34 A^2 E^7$	$2.04 \times 10^{-2} A^{-2} E^{-7}$
4	$1.1 \times 10^{-5} A^{8/3} E^9$	$6.5 \times 10^{4} A^{-8/3} E^{-9}$
5	$2.4 \times 10^{-12} A^{10/3} E^{11}$	$2.89 \times 10^{11} A^{-10/3} E^{-11}$
	$\lambda(ML)$ (s^{-1})	$T_{1/2}^{Weiß}(ML)$ (s)
1	$5.6 \times 10^{13} E^3$	$2.2 \times 10^{-14} E^{-3}$
2	$3.5 \times 10^{7} A^{2/3} E^5$	$3.1 \times 10^{-8} A^{-2/3} E^{-5}$
3	$16 A^{4/3} E^7$	$6.66 \times -2 A^{-4/3} E^{-7}$
4	$4.5 \times 10^{-6} A^2 E^9$	$2.12 \times 10^{5} A^{-2} E^{-9}$
5	$7.4 \times 10^{-13} A^{8/3} E^{11}$	$9.37 \times 10^{11} A^{-8/3} E^{-11}$

one) is used because Weißkopf estimates neglect decays through internal conversion and do not consider competing parallel decay branches. The partial half-life normalises for these additional factors and is calculated as;

$$T_{1/2}^{\gamma} = T_{1/2}^{exp} \sum_{i=1}^{n} \frac{(1+\alpha_i)}{(BR)_i}, \tag{2.15}$$

where, $T_{1/2}^{exp}$ is the experimentally measured half-life, n is the number of possible decay multipolarities, α_i is the total internal conversion of each branch and finally $(BR)_i$ is the branching ratio of that i^{th} decay route.

2.7 Isomeric States

Using the Walker and Dracoulis [39] definition, isomers are considered to be nuclear excited states longer-lived than $\sim 10^{-9}$ s, there is no upper limit on their half-life. For the purposes of this thesis isomers are deemed to have half-lives ≥ 1 ns. From a physics point of view this value of 1 ns is arbitrary.

Different, independent physical artifacts can be responsible for the existence of metastable states. These are generally grouped into three categories: spin-trap, K- and shape isomers [39]. Spin-trap isomers are of primary interest in this work.

2.7.1 Spin-Trap Isomers

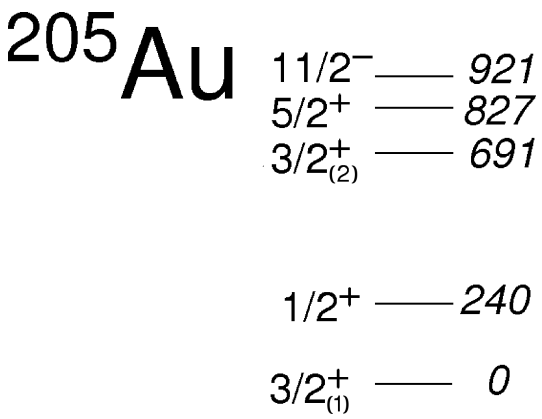

Figure 2.7: Calculation of the low-lying excited states in $N = 126$, $Z = 79$ ^{205}Au. This calculation was performed by M. Górska [40], details regarding the calculation are given in section 6.5.

Spin-trap isomers are features of medium to heavy nuclei near closed shells. These nuclei have a low level density over a wide energy range in the lower part of their decay scheme. This allows one to individually examine each level of excitation considering their transition rates. As stated in section 2.6.4, Weißkopf estimates are successful at reproducing transition rates of near single-particle decays in such nuclei.

Figure 2.7 uses a shell model calculation (see section 6.5 for details of the model [40]) to identify expected level energies in ^{205}Au for all low-lying states up to the first $11/2^-$ excitation. By applying Weißkopf estimates and using calculated internal conversion coefficients [41] the expected half-life for decay from each of these levels to all of the other low-lying levels can be estimated to within approximately an order of magnitude. This is done in table 2.2. Transitions from the $1/2^+$, $3/2^+_{(2)}$ and $5/2^+$ states have half-lives of the order $\sim 10^{-13}$ s. Transitions from the $11/2^-$ state however have half-lives $10^{11} \rightarrow 10^{18}$ orders of magnitude longer. The predictions give the shortest-lived decay branch as the $E3_{(94\ \mathrm{keV})}$ transition, with $T_{1/2} = 4.0 \times 10^{-2}$ s. Therefore, should this $11/2^+$ state be populated the nucleus would be expected to remain in the excited state for an extended time compared to the other nearby states.

Table 2.2: Weißkopf single-particle unit half-lives of decays from predicted low-lying states in ^{205}Au. Note that only the dominant multipole transition between any two states has been considered, that $T_{1/2}$ is calculated assuming 1 W.u. and is inclusive of any internal conversion branch.

Transition			λL	**Energy (keV)**	α_{Total}	$T_{1/2}$ **(seconds)**
$1/2^+$	$\rightarrow$	$3/2^+_{(1)}$	$M1$	240	0.64	9.7×10^{-13}
$3/2^+_{(2)}$	$\rightarrow$	$1/2^+$	$M1$	451	0.12	2.1×10^{-13}
	$\rightarrow$	$3/2^+_{(1)}$	$M1^a$	691	0.72	1.1×10^{-12}
$5/2^+$	$\rightarrow$	$3/2^+_{(2)}$	$M1$	136	3.17	2.1×10^{-12}
	$\rightarrow$	$1/2^+$	$E2$	587	0.018	1.11×10^{-10}
	$\rightarrow$	$3/2^+_{(1)}$	$M1$	827	0.024	3.8×10^{-14}
$11/2^-$	$\rightarrow$	$5/2^+$	$E3$	94	185.0	4.0×10^{-2}
	$\rightarrow$	$3/2^+_{(2)}$	$M4$	230	57.3	4.8×10^{4}
	$\rightarrow$	$1/2^+$	$E5$	681	0.25^b	3.1×10^{5}
	$\rightarrow$	$3/2^+_{(1)}$	$M4$	921	0.17	9.1

[a] *May also decay by a partial E0 branch; the 2^{nd} order multipole is quoted.*
[b] *Considers only K- and L-shell electrons taken from reference [42].*

The equations 2.12 and 2.13 highlight a strong dependence of electromagnetic decay rate on the change in angular momentum between two states. In this case of ^{205}Au the $11/2^-$ state arises from the single proton-hole occupation of the $h_{11/2}$ intruder orbital. By its intruder character, the $h_{11/2}$ ($l = 5$) orbital is considerably higher in angular momentum than its neighbouring single-particle hole states, which arise from $s_{1/2}$, $d_{3/2}$, $d_{5/2}$ and $g_{7/2}$ orbitals. It is understandable then that a transition from the initial state (dominated by the $h_{11/2}$ orbital) to another state requires the depopulating γ-ray to carry away a large amount of orbital angular momentum. This is an inhibited process, thus the isomer arises due to the high spin, single-particle nature of the decaying state. Hence the name spin-trap isomer.

2.7.2 Seniority

Before examining the importance of spin-trap isomers, the quantum number "seniority", ν, needs to be defined. Simplifying from the mathematical interpretation of reference [43], seniority is most easily understood as the number of unpaired nucleons, which describe the wavefunction of a given state (i.e. the number of nucleons that do not couple to $J = 0$). Therefore in the shell model the dominant contributing wavefunction of an even-even nucleus in its ground state has seniority $\nu = 0$, for odd-even nuclei $\nu = 1$.

Examining the low-lying yrast structure of nuclei, that being pivotal to the current work, excited states are populated by the breaking of a single pair of nucleons. For even-even nuclei, the dominant seniority of these low-lying excited states then is $\nu = 2$. Transitions between these states are $\Delta\nu = 0$ and transitions from these states to the ground state change by $\Delta\nu = 2$. Trends of $B(E2 : J \rightarrow J - 2)$ values across a number of nuclei show interesting facets when drawn together with seniority.

The value of $B(E2)$ for a "good" seniority nucleus in the shell model for a single-j shell is directly related to [44];

$$\begin{array}{ll} 1 - 2f & \Delta\nu = 0, \\ \sqrt{f(1-f)} & \Delta\nu = 2. \end{array} \tag{2.16}$$

where f is the occupation of an orbital with n vacancies for a given j and is defined as:

$$f = \frac{n}{(2j+1)}. \tag{2.17}$$

By plotting the variation of $B(E2)$ values with respect to f for $\Delta\nu = 0, 2$ one observes two strikingly different trends. This is shown in figure 2.8 (left). The $B(E2)$ values of seniority conserving and non-conserving transitions follow opposing parabolas to one another as the single-j orbit population changes. In both collective and seniority nuclei, the $B(E2)$ of the first excited states express similar parabola. For higher-lying transitions the $B(E2)$ parabola is inverted for seniority nuclei, but not for collective [44] (see figure 2.8 (right) for the evolution of collective $B(E2)$ values).

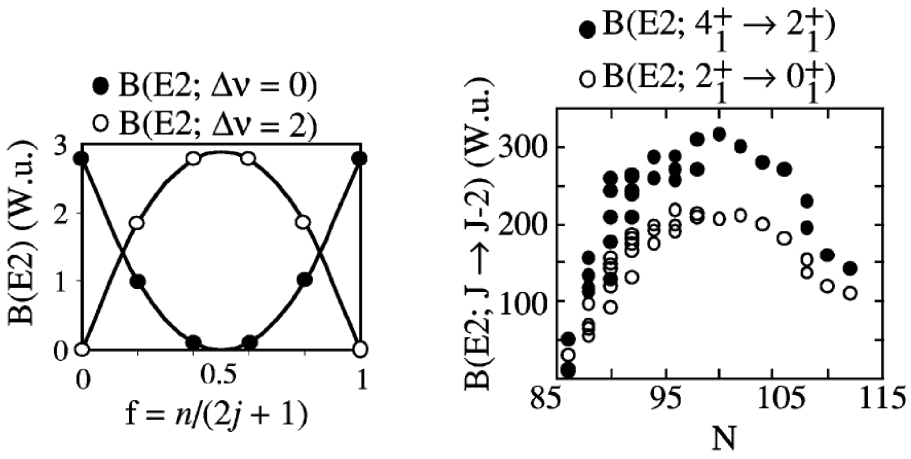

Figure 2.8: **Left:** $B(E2)$ values as orbital occupancy changes in a single-j shell for conserving and non-conserving seniority transitions in a single-particle model. **Right:** Experimental yrast $B(E2)$ values for $62 \leq Z \leq 74$ (i.e. nuclei that express collective behaviour), some known low-lying intruder orbital states have been omitted for clarity. These figures are taken from [44].

2.7.3 Seniority and Spin-Trap Isomers

Seniority is considered to be a reasonably good quantum number for low-spin states in nuclei near shell closures; spin-trap isomers also occur near shell closures. Commonly these spin-trap isomer states decay through seniority conserving transitions ($\Delta\nu = 0$). By measuring the half-life of these isomers in even-even nuclei one is able to extract $B(E2)$ information for $\Delta\nu = 0$ decays (i.e. $J \rightarrow J-2$ where $J-2 \neq 0$). This is of particular importance for exotic nuclei, where low population cross sections make half-life measurements of non-isomeric states very challenging. By investigating trends in $B(E2)$ values of exotic nuclei above the first excited state, indication is given as to the presence of shell closures far from stability. This is done by searching for switches between up and down sloping gradients of $B(E2)$ parabola [44].

2.8 Relativistic Fragmentation

For the experimental results discussed in this thesis, relativistic fragmentation was used as the reaction mechanism for populating the nuclei. Fragmentation can be understood through an abrasion-ablation approach [45]. This separates the reaction into two distinct phases. In the first of these phases, abrasion, the projectile collides

with the target nucleus (in this case ^{9}Be). The beam has a highly relativistic velocity [46] (in the work presented in this thesis the beam was ^{208}Pb with β=0.8579). When approximating the range of the strong nuclear force to the nucleon radius ($\sim$ 1.2 fm), this makes the interaction time window $\sim 10^{-23}$ s between any two nucleons. Calculating from the orbital energy of the nucleons (see section 2.1), this results in the relative motion of particles being only $\sim$ 0.1 fm during the interaction time. This enables the abrasion phase of the fragmentation reaction to treat the nucleons as being static. All of the energy transfer in the reaction then is localised between the static wavefunction overlap of the nucleons in each nucleus. Those nucleons which are observed to be outside of this "abrasion zone" are unaware of the reaction taking place; their wavefunctions and velocities are undisturbed [45].

Specific orbitals are depopulated when nucleons are suddenly removed from the nucleus. In cases where these nucleons are from the surface the daughter nucleus is often populated in excited states, which will then γ-ray decay to cool down. In the context of this thesis, the decay of some fraction of the daughter nuclei will involve the population of isomeric states, which may then be measured. For nucleons ejected from further below the Fermi surface particle-decay branches dominate over γ-ray emission. The evaporation of further particles following the initial abrasion is understood as the second phase of the fragmentation reaction, ablation. When the ablation period is over ($\sim 10^{-23} - 10^{-16}$ s depending on energies and the stability of the pre-fragment) the final fragment is likely to exist in an excited state, again isomers may be populated and measured if they are present. Both nuclei from ablated and non-ablated fragments will be discussed in this work.

Chapter 3

Experimental Technique: Preparing the Nuclei of Interest

3.1 Principal Requirements of the Experiment

There are specific requirements which an experiment aimed at examining ^{204}Pt must meet. These requirements are not arbitrary, due to the interdependency of the factors involved. First and foremost, there must be a mechanism in place capable of populating ^{204}Pt nuclei; the degree of this population is however dependent on numerous factors. Secondly, and critically, it must also be possible to make spectroscopic measurements of the ^{204}Pt nuclei after production.

For the work performed projectile fragmentation has been used as the population mechanism. The use of the fragmentation technique brings further experimental requirements. During the fragmentation of primary beam particles, broad swathes of nuclear species are synthesised. Accurate spectroscopic measurements of single species among these nuclei requires an association between the nucleus emitting the radiation and the corresponding observed γ ray. Hence another experimental requirement is the unambiguous identification of secondary beam nuclei on an event-by-event basis.

Any practical solution for particle identification requires a finite time to perform the task, this finite time is much greater than the scale for de-excitation of uninhibited nuclear excited states ($\sim 10^{-15}$ – 10^{-12} s). Upon synthesis of exotic nuclei detecting the prompt γ rays is unfortunately not an option; spectroscopic measurements made about the production target are blinded by radiation from the much greater popula-

tion of nuclei that are "uninteresting" to the current experiment. One way to make a spectroscopic measurement of low production cross-section nuclei is to measure γ rays emitted after a particle selection process, when the more intensely populated nuclei have been removed from the detection area; this selection can be performed simultaneously with particle identification, which then selects nuclides from those implanted in the detection area. A combination of this selection and identification allows for very clean spectroscopic measurements. However as measurement must follow the selection process, which takes $\sim$ 300 ns, it is experimentally limited to studying only delayed photon emissions, i.e. isomeric states. As only isomers are to be studied, a further experimental requirement is made. The produced, selected and identified nuclei need to be stopped, so that their isomeric states decay in view of the γ ray spectrometer.

Returning to the original issue of the population quantity required to perform the experiment, it is defined by accounting for: (1) losses during particle selection and identification and losses in stopping the nuclei; (2) γ-ray detection efficiency and (3) a reasonable reduction of statistical uncertainty. The precise method of how these requirements were met for the presented findings is detailed throughout this chapter and the one following.

3.2 The Primary Beam

The staff of the GSI laboratory are responsible for delivering the primary beam to the experimental hall. The delivery of this beam is a two step process, the initial acceleration of the particles is done through the use of GSI's UNIversal Liner ACcelerator (UNILAC), following this the particles are subsequently injected into the SchwerIonen Synchrotron 18 (SIS-18) for full acceleration.

3.2.1 UNILAC

The UNILAC accelerator (pictured in figure 3.1) initiates particle acceleration with either PIG or MUCIS/MEVVA ion sources (PIG – PennInG ion source; MUCIS – MUltiCusp Ion Source; MEVVA – MEtal Vapour Vacuum Arc) [48]. Following beam transport particles are accelerated through a 36 MHz Radio Frequency Quadrupole (RFQ) accelerator. Now with an energy of 1.4 MeV/u the particles undergo a degree

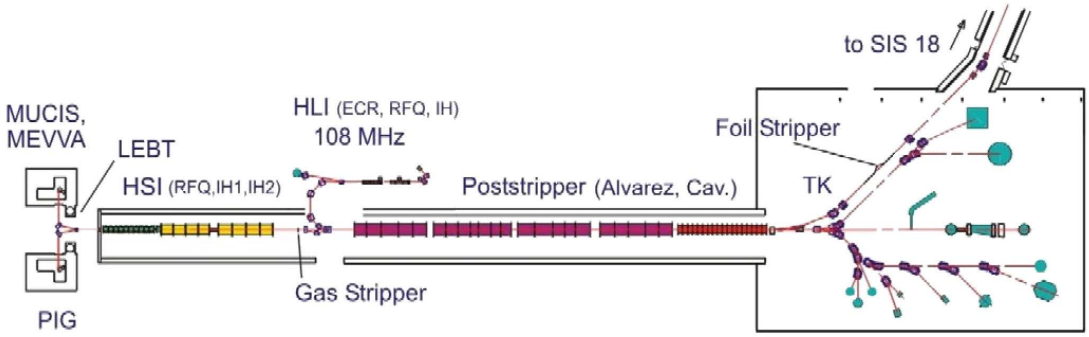

Figure 3.1: Schematic of the GSI UNILAC showing key stages of beam development until injection into the SIS-18. This picture is taken from reference [47].

of electron stripping through jets of nitrogen gas before being accelerated for a second time at 108 MHz in an ALVAREZ Cavity style linear accelerator [49]. With an energy of $\sim$ 11.4 MeV/u the nuclei are now injected into the SIS-18 synchrotron.

3.2.2 SIS-18

To help achieve high energy acceleration in the SIS-18 the UNILAC injected beam is passed through carbon foils to further strip the beam nuclei. The GSI synchrotron (pictured in figure 3.2) has a radius of 34.5 m and can achieve a maximum bending power of 18 Tm from its 24 dipole magnets. There are two RF cavities providing beam acceleration at 16 kV. For the described experiment, the SIS-18 outputted a beam of $^{208}Pb^{+67}$ at 1 GeV/u. This was the primary beam and was passed to the experimental hall.

3.3 Fragmenting the Primary Beam

When exiting the SIS-18 the ^{208}Pb beam particles interact with matter reducing the beam energy to 999.1 MeV/u, this energy loss is calculated by simulation using the ATIMA code [51]. At 999.1 MeV/u the primary beam impinges on the fragmentation target. For this experiment a target of 2.526 g/cm^2 ^{9}Be was used. Of the targets available at the GSI laboratory, this one best optimises the production of the nuclei of interest by a single- or multi-step fragmentation process, whilst limiting losses of those nuclei through subsequent fragmentation reactions prior to exiting the target.

The beam nuclei leaving the target are passed through a thin Nb foil. For high

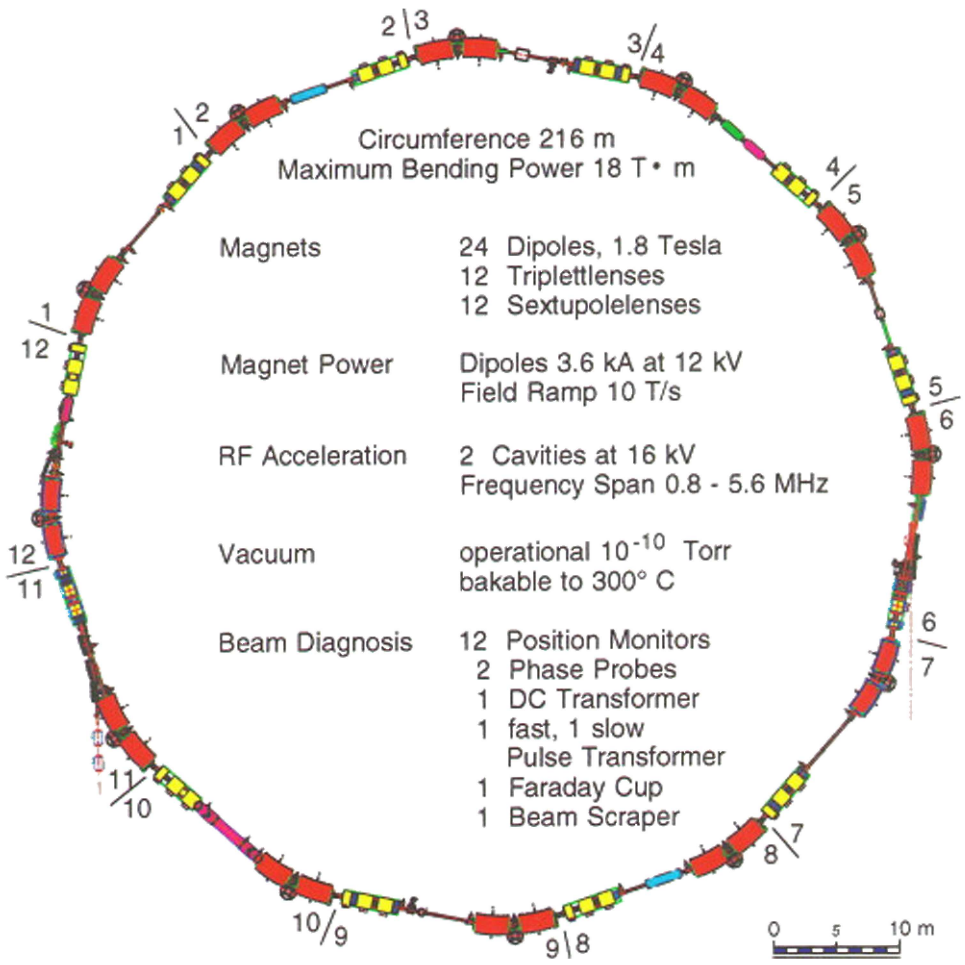

Figure 3.2: Schematic of the GSI SIS-18, this is the final stage of beam development, outputted is a $^{208}Pb^{+67}$ at 1 GeV/u. This picture is taken from reference [50].

energies, such as those in this experiment, beryllium although a good fragmentation target, it is not an ideal electron stripping material. Medium masses make the optimum strippers, as heavy nuclei interfere with the beam optics to too great of a degree. The electrons are removed from the nucleus due to Z-dependent atomic interactions: radiative electron capture, kinematic capture and ionisation [52,53]. Now as the fragmented nuclei leave the Nb stripping foil they are near all fully ionised (see section 5.1.5 for a detailed review of this stripping).

The removal of electrons provides two key advantages when performing the experiment. The main reason for ionising the secondary beam is for the benefit of particle identification and selection. The particle separation process is highly dependent on q. An additional effect of electron stripping is the inhibition of internal conversion decay paths in-flight. The time that passes for particles from fragmentation to measurement

is $\sim$ 300 ns. By prohibitting internal conversion, isomeric half-lives are extended for highly stripped ions when compared to $q \ll Z$ ions, allowing for measurement of isomers which would have otherwise decayed in-flight. The shortest half-life measured currently with the FRS using the isomer spectroscopy technique is $T_{1/2} = 10.3(24)$ ns in ^{200}Pt [54].

3.4 Components of the Fragment Separator

When the nuclei of interest have been produced they need to be selected and identified. The selection is performed by the FRS [55] while simultaneously the information needed for nuclide identification is recorded for subsequent off-line software analysis. There are several devices involved in the selection and identification process, they are detailed in the following subsections. A simplified overview of the FRS structure is first given in figure 3.3.

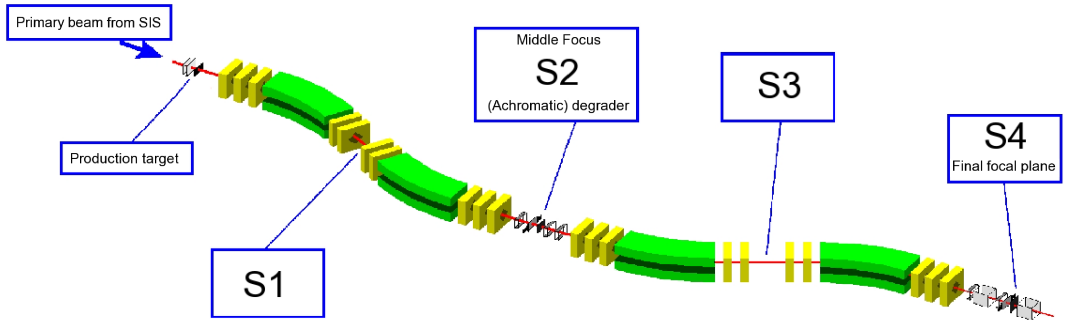

Figure 3.3: Sketch of the FRS. Highlighted in green are the dipole magnets, the quadrupole magnets are yellow. Localities along the separator are labelled by S1, S2, S3 and S4; the number index increases after each dipole magnet. The total beam path of the FRS is $\sim$ 70 m. This diagram was modified from reference [56].

3.4.1 Dipole Magnets

Dipole magnets are used for their ability to bend charged particles through circular arcs. To make charged particle selection, the secondary beam products are passed through four dipole magnets. These magnets have fixed radii but the magnetic field which is applied to them may be varied as required, with field strengths up to 1.6 T. The magnets are set up such that particle dispersion is across the horizontal plane, this

is often referred to as the x-dimension. The maximum acceptance width for particles is ± 100 mm about the x-plane centre. By virtue of this spatial limit, the arc traversed by any particle must trace a path which falls within the 200 mm width. All other particles fall out of the beam line and are thus removed from experimental consideration. This arc of travel is defined in terms of the magnetic rigidity of a particle, $B\rho$, where B is the magnetic field strength and ρ is the radius of curvature. This magnetic rigidity is governed by particle mass, the electric charge and its velocity, such that;

$$B\rho = \beta\gamma uc \, . \, \frac{A}{qe} \tag{3.1}$$

where β is velocity divided by the speed of light, γ is the relativistic Lorentz contraction, u is the atomic mass unit, c is the speed of light, A is the atomic mass number, q is the charge of the ion and e is the unit of electrical charge.

3.4.2 Quadrupole Magnets

Quadrupole magnets are positioned throughout the FRS. They characteristically focus nuclei in one Cartesian plane while defocussing in another [57]. Groups of three quadrupole magnets are placed either end of the dipole magnets. The magnetic field strengths combined with the geometric separation of these magnets is such that an optimum optical focus of the beam is attained. They correct dispersions due to in-beam matter interactions prior to the dipole magnet and variances in dipole magnet bending effects after the particles traverse the dipole magnets. Note should be made of sextupole magnets which are also placed before and after the dipole magnets, these make 2^{nd} order corrections to the beam focus.

3.4.3 Slits

Pairs of thick copper blocks, serving as slits, are placed in the beam line. They are thick enough to stop any nuclear fragment incident on them, allowing only particles between the two blocks to continue along the FRS. The copper blocks are adjustable across the x-plane of the beam and can be used asymmetrically. They are used to remove unwanted nuclei from the secondary beam by effectively reducing the 200 mm maximum width of the beam.

3.4.4 Multiwire Proportional Counters

There are several two-stage MultiWire Proportional Counters (MWPC) [58] available for use along the beam pathway. They are used to measure particle position in the x- and y-planes. Some are used only for calibration and others to give recorded measurements during experimental readings. Inside a MWPC is a mixed gas (P-10) of CO_2, Ar and a small amount of alcohol. An example of the operation of a two-stage MWPC is depicted in figure 3.4. The pre-gap in the schematic (the additional 2^{nd} stage of the two-stage MWPC) is for use only with light ions ($Z < 6$) and so is not used in this experiment; effectively making the MWPC chambers single-stage.

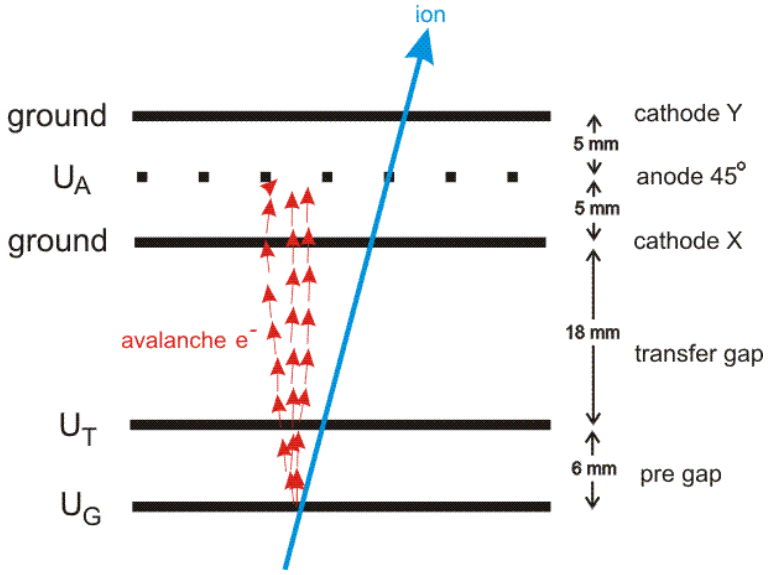

Figure 3.4: Schematic example of a two-stage MWPC. This figure was modified from reference [59].

Incident particles ionise electrons from atoms of the chamber gas. An electric field ($\sim$ 2 kV) applied to the chamber induces an electronic drift towards one of the anodes, U_A. An electronic avalanche occurs with increasing significance as the electrons approach the anode, achieving a gain of $\sim 10^3$ [58]. The anode is orientated by a 45° offset from the cathodes. When a cascade occurs on the anode, it induces a positive signal on the horizontal and vertical cathode wires closest to where the cascade hits the anode. The difference in magnitude of charge collected at either end of the cathodes (i.e. left and right or up and down) measures the position of the incident particle along that plane, such that:

$$x = f_{0_x}(Q_{l_x} - Q_{r_x}) + f_{1_x}, \qquad y = f_{0_y}(Q_{u_y} - Q_{d_y}) + f_{1_y}. \tag{3.2}$$

Equation 3.2 gives the particle position calculation where x is the horizontal position; y is the vertical position; f_{0_x}, f_{1_x}, f_{0_y} and f_{1_y} are constants where f_0 depends on the response curve of the electronics and f_1 is the offset between the left and right signals; and Q_{l_x}, Q_{r_x}, Q_{u_y} and Q_{d_y} are the charge collections of the cathodes. The MWPCs are capable of resolving position with 0.5 mm precision.

3.4.5 Scintillation Detectors

Charged particles are also detected using scintillation detectors, which measure particle position, rate of energy loss and time of detection. The specific scintillators from this experiment are the organic plastic Bicron BC420 model [60]. This model of Bicron scintillator has low self-absorption and maintains a fast timing response (decay constant of 1.5 ns) for large sheet areas [61], such as the 200 × 80 mm typical beam area of the current work. The scintillation detectors resolve particle position with a $FWHM = 4$ mm and in time with a $FWHM = 40$ ps [60].

When a beam particle is incident on a scintillation detector, electrons are excited, they consequently de-excite emitting visible light. The refractive index of the scintillator material (refractive index = 1.58) serves to raise the probability of total internal reflection for the photons striking the edge of the detector; hence the photons are trapped inside the scintillator. Eventually they strike the photo-sensitive plate (the photocathode), which connects to a PhotoMultiplier (PM) tube. Inside the PM tube a resulting ionised electron is directed towards a dynode by an electric field. It accelerates towards this dynode and upon colliding with it it interacts with the matter, ionising more electrons. At a higher potential difference these electrons are again accelerated towards another dynode for a larger scale repeat reaction. After repeating this process several times the electronic signal is now amplified for digital processing after it strikes the anode and is outputted from the device. Total charge collections give ΔE and the fast timing nature of the detector makes it suitable for accurate timing measurements.

3.4.6 Degraders

There are two degraders used in the current work. The degraders are made from aluminium and are shaped differently. The homogeneous degrader is the simpler case; it is homogeneous with respect to the beam direction of travel and its purpose is to reduce the energy of secondary beam particles. Aluminium is used principally for technical reasons as it is easily machined and a non-toxic material.

The other degrader (sometimes termed the wedge) is designed to separate the different beam particle species. This degrader is angular (wedge shaped) and is pivoted at its centre. The angle results in a varying aluminium thickness across the horizontal plane of the beam line. Thus particles passing through the degrader at different positions pass through different thicknesses of material (See figure 3.5 (left)). In this experiment the degrader was set at an angle which operated in what is termed "achromatic" mode. This mode characterises momentum of all the beam particles. By having defined momenta after traversing the degrader, the nuclei can be mass-charge (A/q) separated across the horizontal plane, improving the particle selection and identification.

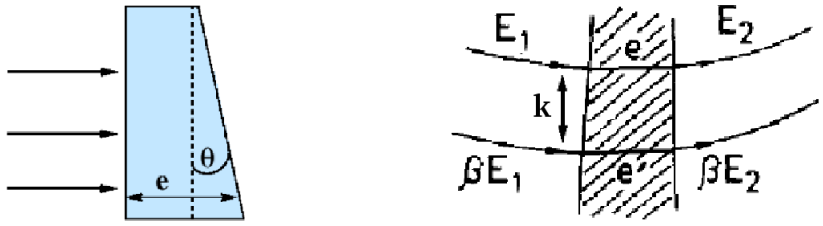

Figure 3.5: Sketches of particles passing through the achromatic degrader. **Left** exemplifies an exaggerated variation in degrader thickness. The sketch is modified from reference [62]. **Right** shows the separation of two particles to visually complement the details of equation 3.3. This sketch is modified from reference [63].

The optimum achromatic angle is calculated by considering the momentum dispersion from the first pair of dipole magnets, Dis_1. Looking nuclide-by-nuclide after production there is a linear momentum spread for the particles. This linear momentum spread manifests itself as a positional distribution after passing through the first dipole magnet pair. If these nuclei now pass through a variable thickness degrader their relative momentum properties are changed. The angle which optimises achromaticity is one which does not alter relative momenta, but instead maintains the same energy

ratio between nuclei upon departure from the degrader as when entering it. Hence:

$$\begin{aligned} E_i - e\left(\frac{dE}{dx}\right)_{E_i} &= E_f, \\ \beta E_i - e'\left(\frac{dE}{dx}\right)_{\beta E_i} &= \beta E_f, \end{aligned} \tag{3.3}$$

where E_i and E_f are the initial and final energies of a particle of any given trajectory, dx is an infinitesimal step through the depth of the degrader, e and e' are the thicknesses of aluminium traversed for two different particle pathways and β is the ratio of ingoing energy difference between the two routes. β is given by;

$$\beta = (k + (1/100)Dis_1)^2, \tag{3.4}$$

where k is the horizontal separation of the two trajectories at the degrader (quoted in cm). The situation is depicted in figure 3.5 (right). The aromaticity of all particles depends only on the magnetic dispersion, Dis_1 (quoted in metres), within an accuracy of 10^{-3} [63]. All nuclear species in the secondary beam will be achromatically separated.

3.4.7 Multi-Sampling Ionisation Chambers

Energy loss rates are measured during the experiment. As previously mentioned, the scintillation detectors give this information but for higher resolution values MUlti-Sampling Ionisation Chambers (MUSIC) are used, specifically the MUSIC80 model. After passing a Mylar foil entrance window, these chambers (pictured in figure 3.6) contain tetrafluoromethane gas (CF_4) over a length of 420 mm along the beam direction of travel, where the effective measuring range is 400 mm. The gas is used at 1 atmosphere (atm), operates at room temperature ($\sim$ 293 K) and its purity is maintained by a pumping system.

Inside the chamber there are 8 anodes, which are evenly spaced over the length of the chamber they each take a measurement of the energy deposited by incident particles over a localised region. The response of each anode is normalised and then an average value for the energy loss of particles is used for experimental measurements. As with the MWPCs the measurement is made by detecting electron-ion pairs following ionisation. The gas traversed by beam particles in the MUSIC chambers are of such

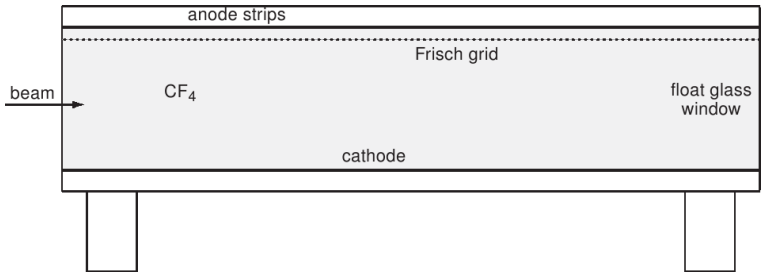

Figure 3.6: Schematic of a MUSIC detector. This figure is taken from reference [64].

density and effective length that they cover many electron pick ups and losses by the nucleus. Hence the anode-averaged signal from the MUSIC detector is a measure of the effective nuclear charge, q_{eff}, not the ingoing charge state, q, or (directly) the Z of the element. The charge response on the anodes of a MUSIC detector is near linear over a very wide range of nuclear charges and energies [65]. The velocity of the measured particle (and hence the time available for interactions in the chamber) affects the energy it deposits. A velocity correction is made to normalise this response based on calibrated particle velocity measurements of known nuclei, usually the primary beam.

The charge response is position dependent over the area of the MUSIC detector tangential to beam direction. A normalisation of this response is made with a Frisch grid. The Frisch grid acts like a gate, which is "closed" once the desired signal has been received at the anodes. When it is in use this stops back-scattered positive ions from interfering with the response [66]. Untended, back-scattering reduces the charge response for beam particles; the effects are more pronounced the closer the secondary beam particle passes to the cathode. The Frisch grid is not perfect, back-scattering is still a measureable affect across the horizontal plane of the MUSIC detector. The calibrated MUSIC signal needs a position-dependent correction made to it. This is done by sweeping unambiguously identified ions (normally the primary beam) across the MUSIC chamber and then normalising the response for different positions.

The MUSIC chambers are subject to further shifts in their charge response to beam particles. Changes in the gas pressure and temperature perturb the response. Pressure and temperature changes occur due to the varying ambient atmospheric conditions of the experimental hall; i.e. the MUSIC signals differ subject to the weather conditions during the experiment. This effect can be dealt with by making time-dependent normalisation corrections to the calibration parameters.

3.5 The FRS System

The operations of individual components of the FRS have now been defined. With an understanding of how they work in mind, the selection and separation of the fragmented nuclei can be explained. So far in this document it has been described that the primary beam at 999.1 MeV/u has fragmented on a ^{9}Be target, resulting in the synthesis of a broad swathe of secondary beam nuclei, these will now be manipulated in preparation for γ-ray spectroscopy.

The fragments are passed through the first dipole magnet, coupled with its quadrupole and sextupole focussing magnets. In future, for simplicity, groups of these magnets will be referred to as D_i, where i is the FRS location index named in figure 3.3. Therefore, this is the D_1 magnet. The momentum distribution and magnetic rigidity properties of the beam particles spreads them across the x-plane. The S1 slits which follow the D_1 magnet now restrict which of the nuclei are accepted by the slit positioning, the precise postion of the slits differs for each experiment. This process is visualised in figure 3.7.

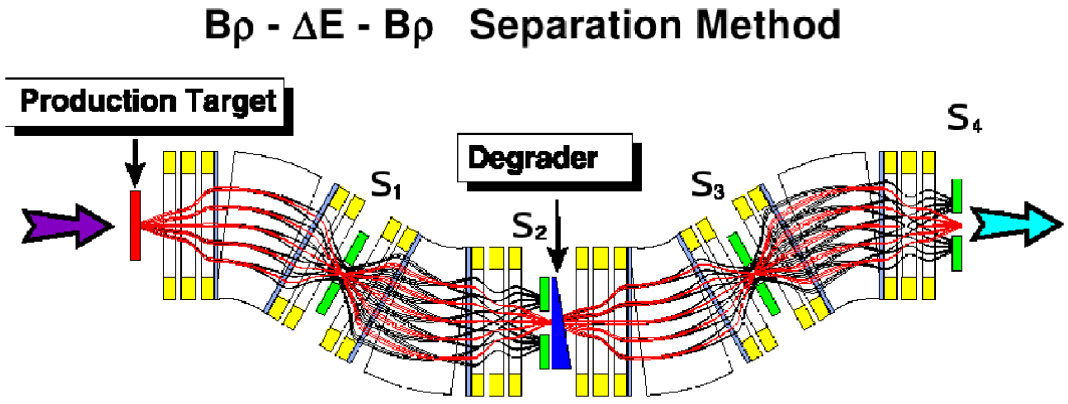

Figure 3.7: Diagram of nuclide selection through the FRS showing an example of using beam optics to select the synthesised nuclei. This diagram is modified from reference [67].

After this first selection of nuclei, the fragments are brought back into focus at the intermediate focal position by the D_2 magnet. Upon exiting this second dipole magnet there is a second slit available for selecting nuclei by choosing the beam acceptance width. The first beam line detector is a scintillation detector (Sci21). Timing information is recorded here, which will be discussed later. Positional information, which tracks the flight path of each particle in the secondary beam, is written to the data

stream. It was earlier stated that MWPCs resolve particle position with higher precision than scintillation detectors. MWPCs are not used here due to two reasons; firstly they are very quickly damaged and inefficient at working with the beam intensities at S2; secondly they also introduce inhomogeneities into the beam. The inhomogeneities arise from the wire structure in the MWPC; approximately 10 % of beam particles strike the cathode wires, which degrades the beam optics [59]. There are actually two MWPCs in use at this stage along the FRS, but only prior to the final experimental set up. These are named MW21 and MW22, and are placed before and after Sci21 to callibrate it. They are removed once the experiment proper begins.

Following Sci21, the beam passes through the S2 achromatic degrader (the wedge). The outgoing beam nuclides are taken through a Nb foil to maintain electron stripping and then on to the next pair of magnets, D_3 and D_4, with another slit placed between the two. Until now the beam has been kept in vacuum, it now passes the FRS exit window (90 mg/cm^2 of Ti) and henceforth travels in air.

As the magnets have all been traversed there are less concerns over beam optics after D_4 and the beam intensity at this stage is relatively low ($\sim 10^3$ Hz). It is now beneficial and possible to use MWPC detectors for position measurements. The particles next pass through one of these, MW41. There are two MUSIC detectors placed after MW41, these are MUSIC41 and MUSIC42. These two chambers are separated by a Nb stripper foil. Upon entering the MUSIC gas, particles have already changed charge state from the state they were in whilst traversing magnets D_3 and D_4. This is a result of interacting with the FRS exit window, air, components of MW41 and the MUSIC chamber entrance window.

The next beam line detector to be encountered is Sci41, which provides the master trigger for *all* data recording in the current work. This scintillation detector, as Sci21, measures both position and time. The timing signals between the two scintillators (Sci21 and Sci41) provides a Time of Flight (ToF) measurement, i.e. a measure of the particle ToF over the latter half of the FRS. Both of these scintillators have PM tubes placed on their left and right side. The difference in the arrival time of the Sci21 (left) signal is taken against Sci41 (left), and right is taken against right. This measurement is made with a Time-to-Amplitude Converter (TAC) [68]. The Sci21 signal is temporally delayed by approximately 200-300 ns and the Sci41 signal is then used as the "start" trigger. The lower beam intensity at Sci41 ensures start signals

are not triggered on undesirable particles, thus reducing the electronic dead time. The pulse amplitude output from accepted TAC signals is proportional to the difference in arrival time of the start and stop signals. The pulse is then passed to an Analog-to-Digital Converter [68] for recording in the data stream.

The x-position of where the particle strikes the scintillators perturbs the recorded signal as a result of charge travel time across the scintillator itself. By taking an average between the left-left and right-right ToF measurements, this charge collection time is eliminated. Thus;

$$ToF_{21-41} = \frac{(ToF_{l-l}.f_{0_{l-l}} + f_{1_{l-l}}) + (ToF_{r-r}.f_{0_{r-r}} + f_{1_{r-r}})}{2} = T_{41} - T_{21}, \qquad (3.5)$$

where ToF_{21-41} is the actual particle TOF, T_{41} and T_{21} are the absolute times when the particle passes the scintillators, $f_{0_{l-l}}$ and $f_{0_{r-r}}$ are the calibration gradients of the TACs and $f_{1_{l-l}}$ and $f_{1_{r-r}}$ are constants, which normalise the scales of the TACs and also account for the deliberate time delay for signals from Sci21.

Although equation 3.5 is the standard method for calculating the ToF in the FRS, this was not possible in the current experiment. There were technical issues encountered with the response of the right PM tube in Sci21. This inhibited accurate TOF measurements, although position information was less strongly affected and still acceptable. Using only the left-left ToF signal and factoring in charge travel time across the scintillator the problem is avoided. Thus in the results presented in this thesis, the ToF_{21-41} was determined using;

$$ToF_{21-41} = (ToF_{l-l}.f_{0_{l-l}} + f_{1_{l-l}}) - 2\frac{\Delta x_{S2}}{c_{Sci}} \,.\, x_{Sci21} + 2\frac{\Delta x_{Sci41}}{c_{Sci}} \,.\, x_{Sci41} = T_{41} - T_{21}, \quad (3.6)$$

here c_{Sci} is the effective speed of light in the scintillation material and x_{Sci21} and x_{Sci41} are the positions of the particle at the two measured locations. The factors of 2 arise from the positional scale being calibrated to zero at the midpoint of the detector.

The next detector is a second MWPC, MW42, where another position measurement is made. The distance between MW41 and MW42 is known. From the position measurements in both of these the $\Delta x_{(MW_{41} \rightarrow MW_{42})}$ of each particle relative to the overall beam direction can be extracted. Knowing the angle the particle is travelling at and its x-position at any of Sci41, MW41 or MW42 makes it possible to extrapolate

the particle position at any stage along the S4 location of the FRS. This enables the implementation of the position calibration correction to the MUSIC detector charge collection measurements, and also optimises the position resolution by monitoring particle positions at the beam focal point, x_{S4}. Optimum resolution in this is achieved by applying the correction to MW42 ($x_{MW_{42}}$), this is because it is higher in resolution than Sci41 and because it is the closest of the three detectors to the beam focus (thus reducing the propagation of error in the correction). The focal position calculation is shown as an example of one of these corrections;

$$x_{S4} = x_{MW_{41}} + \Delta x_{(MW_{41} \rightarrow MW_{42})} \cdot \frac{DIST_{(MW_{41} \rightarrow focus)}}{DIST_{(MW_{41} \rightarrow MW_{42})}}, \tag{3.7}$$

where $DIST_{(MW_{41} \rightarrow focus)}$ and $DIST_{(MW_{41} \rightarrow MW_{42})}$ are the physical separation distances of the named locations.

Next the final slits for removing particles from the secondary beam are placed, this is done as late as possible in the beam line to improve selection, as the optimum beam focus is not reached until inside the RISING γ-ray array (see section 4). The particles are next slowed using a homogeneous Aluminium (S4) degrader. Reactions take place inside this degrader. It is in essence, and unavoidably, another target for the beam particles to fragment in. To quantify and account for these losses, energy measurements are made from another scintillation detector (Sci42) placed after the degrader (see section 5.1.3 for details of this).

After Sci42 the particles still have significant kinetic energy (approximately $\leq$ 100 MeV/u) and so enter the stopper which is inside the RISING germanium detector array, where they are intended to implant. One final scintillation detector for particle identification, Sci43, is placed after the stopper (the stopper is detailed in section 4.2). Its purpose is to identify, through energy measurements, any ions which were not stopped inside the RISING array. A schematic of all of the detectors located at the S4 position is shown in figure 3.8.

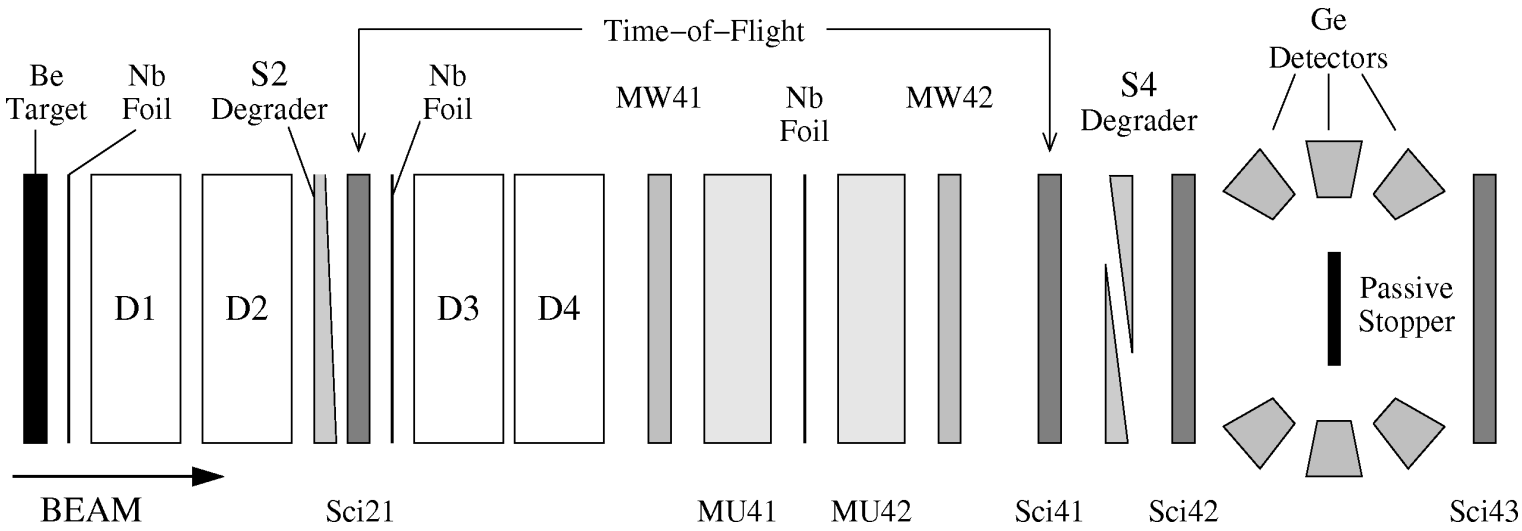

Figure 3.8: Schematic of the S4 detector arrangement as used in the currently discussed experiment. This diagram is taken from reference [69].

Chapter 4

Experimental Technique: RISING

4.1 The RISING "Stopped Beam" Collaboration

RISING, or Rare ISotope INvestigations at GSI [70], is an international collaboration of nuclear physicists. These scientists originate from over two dozen countries; in the current experiment they total 17 nationalities from 19 institutions in 11 different countries. RISING has performed a series of experimental campaigns [70]. In each campaign the selective power of the FRS has been used to measure exotic nuclei far from stability all over the nuclear chart. This thesis concerns the first stage of the RISING "Stopped Beam" campaign (see figures 4.1 and 4.2 for photographs of the array in its Stopped Beam configuration). As the name suggests, and as has been mentioned already, the beam is brought to a halt in the middle of the array in this experiment.

4.2 The Stopper

In this first phase of the Stopped Beam campaign a passive stopper was used for experiments. In more recent experiments the passive stopper has been replaced with Double Sided Silicon Strip Detectors (DSSSD). By using a DSSSD the stopper is then termed "active", in that it itself is now a detector, it measures charged particle decay events [72]. The work presented in this thesis uses exclusively the passive stopper. Its purpose is to stop the beam-like fragments, for spectroscopic measurement of γ rays from isomeric states.

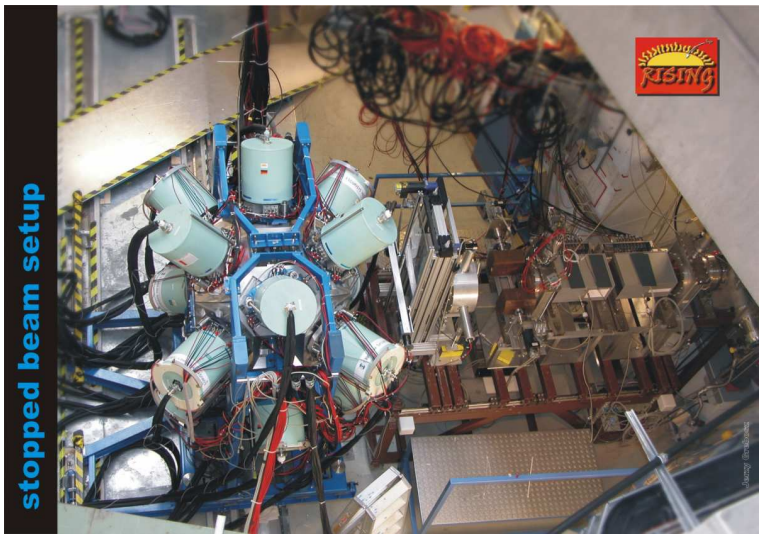

Figure 4.1: From right to left are the detectors of the S4 position followed by the RISING array. This picture is taken from reference [71].

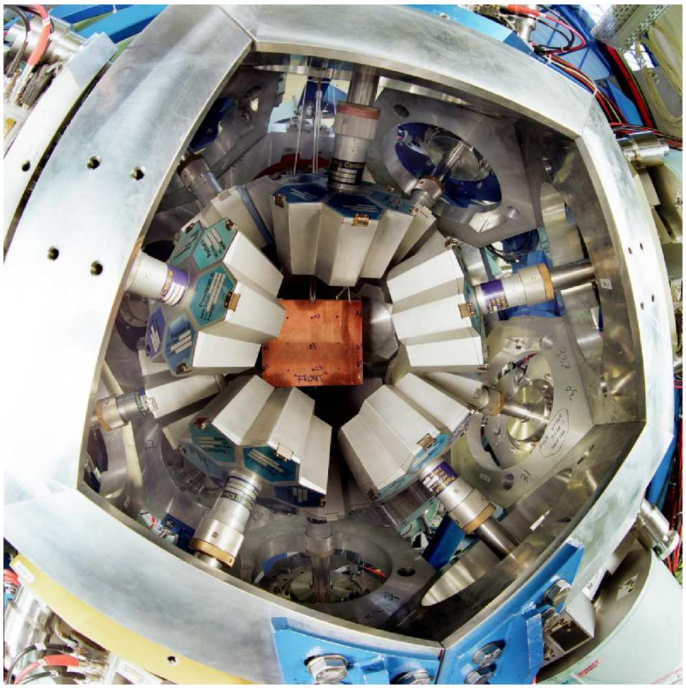

Figure 4.2: A "fish eye" view inside the RISING array. Central is a Copper stopper. For the experimental data presented in this thesis, a perspex stopper was used. This picture is taken from reference [71]

There are factors affecting the material used for stopping particles, which need to be accounted for. An appropriate thickness for the passive stopper must be chosen. The FRS was used in its achromatic style, offering high resolution in particle identification after selection. By virtue of making the beam achromatic in nature there is a broad spread in energy for beam nuclei (energies range $\sim 10 \rightarrow 100$ MeV/u when exiting exiting Sci42). This implies a broad stopping distance; the stopper needs to be thick enough to stop all of the secondary beam fragments. However, the thicker the stopper the more it photoabsorbs, reducing the photopeak efficiency for γ-ray detection in the RISING array. The stopper therefore needs to be thick enough to stop the fragments of interest but no thicker, so as to avoid needless efficiency losses. Plastic stoppers, 7 and 9 mm deep, were appropriate for the requirements of the current work and were used in the experiment. This required thickness was ascertained through simulations of the experiment using the program MOCADI [73]. Perspex is a good choice of material technically, economically and physically. The low Z elements it contains reduce the amount of detectable Bremsstrahlung radiation emitted during implantation. Upon stopping, nuclei fully recombine with electrons, neutralising the atom.

One can now draw together in more detail the function of the S4 homogeneous degrader. In their approach to the degrader, the nuclei have an energy ~ 400 MeV/u. It is clear that there is a benefit in removing most of this energy before entering the RISING array. Without the degrader a very thick stopper would be needed, considerably reducing γ-ray detection efficiency. More importantly this method would also magnify another experimental consideration, the prompt flash (see section 4.3 for details). Furthermore it would forbid experimentally identifying particles lost through nuclear reactions when decelerating nuclei as there would be no facility for using scintillation detector Sci42.

4.3 Physical Considerations when Stopping Nuclei

There are two physics issues which must be accounted for when stopping the secondary beam fragments. The less critical of the two is the need to understand what reaction losses occur after Sci42. These are losses to reactions both in air and also in the plastic stopper. At this stage there is no further particle identification unless the particle reaches Sci43. If they react, change their nuclear species and also stop, then

the recorded data will mis-associate the spectroscopic information with the nuclear species responsible for its emission. It is a limit of the experimental setup that these reactions cannot be measured. The γ rays detected here will increase the background levels of the spectroscopic readings. The losses can be, and have been, theoretically quantified however with LISE++ simulations [46,74]. For the nuclei in this experiment ~ 7.5 % react and stop after Sci42 but before Sci43. As this is an unmeasured value, the percentage is applied to isomeric ratio data only as a contributing uncertainty.

The second and greater issue when implanting nuclei in the stopper results from bremsstrahlung. Decelerating nuclei ionise atoms in the matter they traverse. The resulting free electrons, now with kinetic energy of their own, also decelerate by interacting with matter. Energy is radiated from the electrons through bremsstrahlung. The result is termed a "prompt flash" and it is emitted each time a particle is implanted in the stopper. During the time in which the flash is emitted, photons associated with isomeric-decay cannot easily be distinguished.

Each γ-ray detector in the array can process only up to one γ ray per event [75]. If the flash is high in intensity then all of the detectors are effectively blinded before the isomer-related γ rays are emitted for detection. An example of the effect of the prompt flash is shown in figure 4.3. The high intensity of the prompt flash also exemplifies low energy walk, which is discussed in section 4.6.

During an "interesting" event the situation is such that a desired nucleus has been selected, identified, implanted, has caused the release of prompt flash radiation and has emitted γ rays when its metastable state decays. Random background radiation is also present in this system from ambient radioactive materials in the experimental area, these include ^{40}K and the ^{238}U and ^{232}Th natural decay chains. All of these γ rays are detected by the High Purity Ge Detectors (HPGe) of the RISING array.

4.4 High-Purity Ge Detectors

The RISING array is composed of 15 cluster High-Purity Ge (HPGe) detectors [76]. A cluster detector houses 7 individual, closely packed Ge crystals, which independently detect γ rays, this is a total of 105 crystals. During the experiment reported in this thesis, ≥ 100 of these crystals were operational at any given time.

If a γ ray interacts with the (semi-conducting) Ge crystal either photo-electric

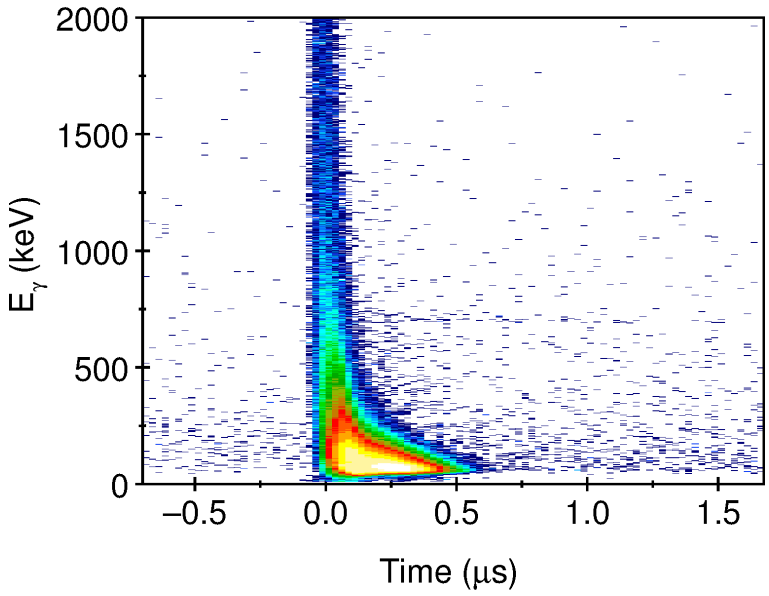

Figure 4.3: Example of the prompt flash due to particle implantation. The time scale (which uses the DGF devices) is normalised to the time of implantation. Note that at lower energies the flash appears broader, this is solely an artifact of the Ge walk effect, see text.

absorption, Compton scattering, pair production or one of several less probable processes occurs [68]. In explaining the functions of Ge crystals it is for now assumed that all the energy of the initial γ-ray is absorbed; i.e. only photoabsorbtion is considered. The result of this absorption is electron excitations, whose number are proportional to the energy of the incident γ ray. At this point it is appropriate to introduce the concept of "holes". These are electron vacancies in the valence band of the germanium lattice and can be thought of as effective positive charges. When one of these excited electrons is promoted to the conduction band, as with γ-ray absorption, an electron-hole pair is thought to be "created" in the system. This pair goes on to induce the creation of many more secondary pairs.

At room temperature, thermal energies are great enough to excite semi-conductor electrons inside their lattice ($E_{room}(rms) \sim 0.03$ eV). Note that this is not necessarily the excitation of an electron within levels of a single atom (the electrons are still strongly bound), but the movement of electrons to a more excited location in the lattice as a whole. This causes large contributions to electronic noise. By reducing the temperature of the semi-conductor the number of these thermal excitations also reduce. When in use, Ge crystals are thus kept at low temperatures using liquid nitrogen (77 K) and

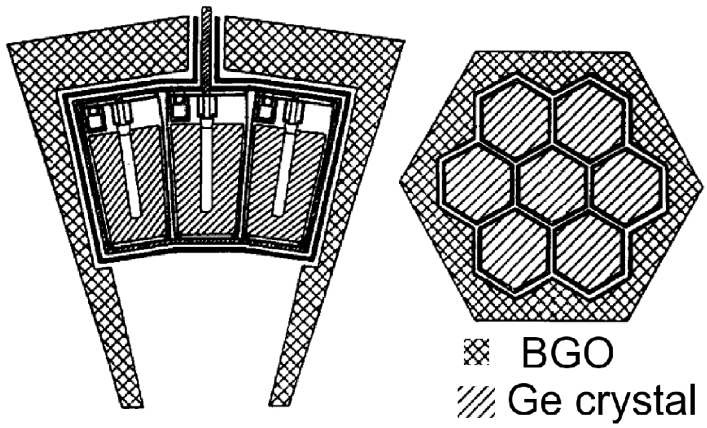

Figure 4.4: Detecting head of a cluster detector, the pictured BGO shielding was removed for RISING. This schematic is taken from reference [78].

thermal conduction through a copper cold finger. The cluster detectors used in the current work form a single detecting unit with one dewar and one cold finger between them. The detecting head thus differs from a single crystal Ge detector, the cluster head is pictured in figure 4.4. For the Ge detectors in this experiment each crystal has a 70 mm diameter and a length of 78 mm [77].

The energy required to produce an electron-hole pair in high voltage reverse biased Ge is $\sim$ 3 eV. After correcting for the Fano factor [68], incident γ rays of $\sim$ 100 $\rightarrow$ 1000 keV produce many hundreds, even thousands of electron-hole pairs. Measuring the signal of a large number of pairs gives only small statistical variances in charge collection and hence Ge detectors offer high energy resolution ($FWHM \sim 1.5$ keV).

4.5 Compton Scattering and Pair Production

Previously it was assumed that all of the energy of the γ ray was absorbed in a single photo-electric interaction. This is not usually the case. In instances of Compton scattering or pair production it is not uncommon for only partial absorption of the initial γ-ray energy to take place. In Compton scattering the scattered γ ray is not always detected by the crystal. The scattered photon has energy given by:

$$E_{\gamma}^{'} = \frac{E_{\gamma}}{1 + (E_{\gamma}/m_0c^2)(1 - cos\theta)} \tag{4.1}$$

where E_{γ} and $E_{\gamma}^{'}$ are the incoming and outgoing (i.e. Compton scattered) γ-ray en-

ergies, respectively, m_0 is the electron rest mass, c is the speed of light and θ is the scattering angle.

Following pair production, a thermalised positron may annihilate with an electron in the material, emitting two 511 keV γ-rays. One or both of these secondary γ-rays may not be detected by the crystal. In these events what are termed "single" and "double" escape peaks are seen in energy spectra, they are characteristically lower in energy than the initial E_γ by m_0c^2 or $2m_0c^2$ respectively. Pair production becomes the dominant interaction at γ-ray energies of 5-10 MeV but was a negligible factor in the current work.

4.6 HPGe Timing Resolution and the Walk Effect

There are two decisive factors in resolving γ-ray (or X-ray) decay times [68]. Firstly the drift velocity of the charge carriers in the crystal is $\sim$ 10^5 m/s, which is ~ 100 ns/cm of Ge crystal. Remembering the dimensions of the detector crystal from section 4.4, this can result in the collection time being anything up to ~ 0.5 μs. The second important factor is the locality at which charge carriers are created. At the fringes of the active volume for detection, the collection times for electrons and holes are appreciably different, resulting in only one of the two particle types dominating the pulse rise time. There are a number of other issues affecting charge collection, including instances of secondary γ-ray absorptions in the crystal, localised lattice structure effects which trap charge, non-saturated drift velocities and the involvement of the non-activated region of the crystal [68, 79]. Without explicitly detailing these effects, the timing resolution of large crystal Ge detectors used in the current work is good enough for resolving the time difference between implant and isomer decay, but they cannot resolve the detection order of cascades of "promptly" emitted γ rays.

The low-energy walk effect is another factor that has a strong influence on the gathering of timing information. When a low-energy γ ray deposits its energy the ionised electron creates further electron-hole pairs over a localised area. The region over which electron energy is deposited for higher energy γ rays is considerably larger. Additionally, lower energy γ rays have higher cross sections for absorption and so tend to deposit their energy near the crystal surface, where charge drift takes longest. For these two reasons the time resolution for low energy γ rays is broader when compared

to instances of high energy absorption. This effect is visualised in figure 4.3 by the prompt flash effect. In reality photons from the prompt flash physically occur over the same time interval for all energies, however it is recorded by the Ge detector to have a different characteristic time width depending on the γ-ray energy. This is an artifact of the discussed time walk effect and is the case at any point in time, not just during the flash.

4.7 Electronic Processing of γ-ray Signals

Energy and timing information is recorded from the HPGe. For energy recordings XIA Digital Gamma Finder (DGF) modules are used [80], these devices handle all of the signal processing tasks that analog electronics classically deal with post-preamplification. The DGF modules are also used to process the time of arrival of signals. There are in total three timing circuits in the experiment, the DGF modules are only one of these, the other two use Time to Digital Converters (TDC) and analog electronics.

Each timing circuit differs from the other; the DGFs offer 25 ns time resolution with a measuring range of up to 400 μs. There is a so called "Long Range" (LR) circuit with 0.7629 ns resolution with a 100 μs range and finally a Short Range (SR) circuit with 0.293 ns resolution per channel operating for an effective range of 850 ns. For the LR and SR circuits a single electrical signal is passed from the Ge detector through a Timing Filter Amplifier (TFA) and a Constant Fraction Discriminator (CFD). The signal pathway is then split as it is passed to a different TDC for each circuit.

The SR and LR circuits did not operate in an ideal fashion. Their efficiency was energy dependent; as the γ ray energy reduced so too did the efficiency with the TDCs. This is in addition to the normal efficiency dependence of γ-ray detection using Ge-crystals and is understood as being due to electronic pile up [81]. The RISING array achieves an efficiency of 15 % at 661 keV with the DGFs [82]. Figure 4.5 shows the efficiency of the array.

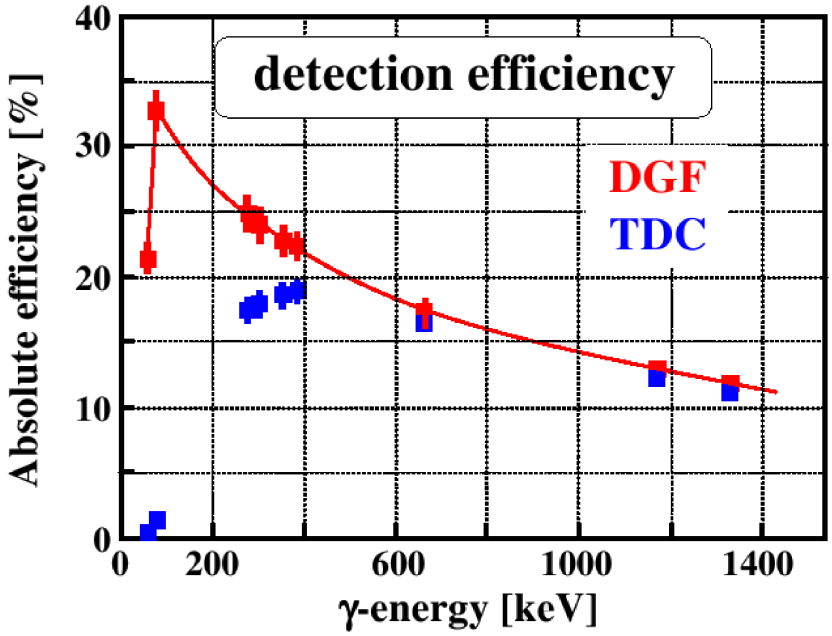

Figure 4.5: Absolute efficiency of the RISING array for DGF and TDC electronic pathways. This efficiency was measured using the following sources: ^{133}Ba, ^{152}Eu, ^{137}Cs and ^{109}Cd. This plot is taken from reference [83].

4.8 Experimentally Measuring Isomeric Ratios

The isomeric ratio is defined as the number of times a nucleus is populated in a particular isomeric state after prompt decays have decayed divided by the number of times that nucleus is populated in total [3, 4]. When measuring this ratio one must consider several affecting factors: detection efficiency of γ rays; internal conversion decays; in-flight decay of isomers; reactions post-particle identification and branching ratios. The isomeric ratio is thus defined by [3]:

$$R = \frac{Y}{N_{imp} F G}, \tag{4.2}$$

where R is the isomeric ratio, Y is the number of times a nucleus was measured to decay from an isomeric state, N_{imp} is the number of implanted ions, F is a correction for in-flight decay losses and G is a factor correcting for the finite detection window of γ-rays. The total isomeric yield, Y, is measured as such:

$$Y = \frac{N_\gamma (1 + \alpha_{tot})}{\epsilon_{eff} b_\gamma}, \tag{4.3}$$

N_γ is the number of detected γ-rays depopulating a state, α_{tot} is the total internal conversion for the transition, ϵ_{eff} is the Ge-detector efficiency for that energy and b_γ is the branching ratio between decay paths.

The factors F and G are measured as follows:

$$F = exp\left[-\left(\lambda^{q_1}\frac{TOF_1}{\gamma_1} + \lambda^{q_2}\frac{TOF_2}{\gamma_2}\right)\right], \tag{4.4}$$

$$G = exp(-\lambda t_i) - exp(-\lambda t_f). \tag{4.5}$$

Here λ^{q_1} and λ^{q_2} are the radioactive decay constants for the isomer in charge states q_1 and q_2, λ is the decay constant of the neutralised nucleus, TOF_1 and γ_1 the time of flight and relativistic Lorentz correction experienced by the nucleus in the first half of the FRS, respectively, and similarly TOF_2 and γ_2 are for the second half, finally t_i and t_f are the initial and final times of γ-ray measurement, where the scale is normalised such that $t = 0$ is considered to be the time of implantation.

The charge dependency of the radioactive decay constant is as follows:

$$\lambda^j = \lambda \sum_i \frac{b_{\gamma i}}{1 + \alpha^i_{tot}(j)}, \tag{4.6}$$

where j refers to the number of electrons bound to the nucleus in flight and $\alpha^i_{tot}(j)$ denotes the total internal conversion coefficient for all i decay paths where α_{tot} is affected by the number of electrons, j, in the system.

When measuring an isomeric ratio, uncertainties arise from a number of the factors in equations 4.2 to 4.6. For isomers with half-lives up to $\sim$ 200 ns, a large contributing error is identifying $t = 0$, the time of implantation. This uncertainty is considered to be 8 ns (this is the measured $\sigma(t)$ for the Ge detectors when using the SR times at γ-ray energies $>$ 400 keV). For these relatively short-lived isomers this uncertainty affects strongly the measured degree of de-population prior to γ ray measurement. For cases of low γ-ray statistics this creates knock-on errors due to branching ratios and half-life errors, these are large factors in such instances. When the statistics are higher and the isomer is long-lived enough to reduce the importance of the time of implantation error, the largest contributing uncertainty is from the unmeasured number of reactions upon particle implantation ($\sim$ 7.5%).

Chapter 5

Particle Identification

5.1 Method of Particle Identification

Nine different settings of the FRS (see section 5.2) were recorded. Each of these settings pass through the same off-line processing with regards to identifying nuclei and removing false events from the data. An overview of this processing is now demonstrated. To save back-referencing when understanding the data selections described presently, the S4 detectors are shown again, this is done in figure 5.1.

Following calibration the first step in the analysis is to ensure event-by-event that beam-line detectors have operated correctly. For nuclei where a detector fails, events are considered "bad" and are rejected. Tests are performed on the multiwires (MW41 and MW42) and also on the midfocal plane scintillation detector (Sci21).

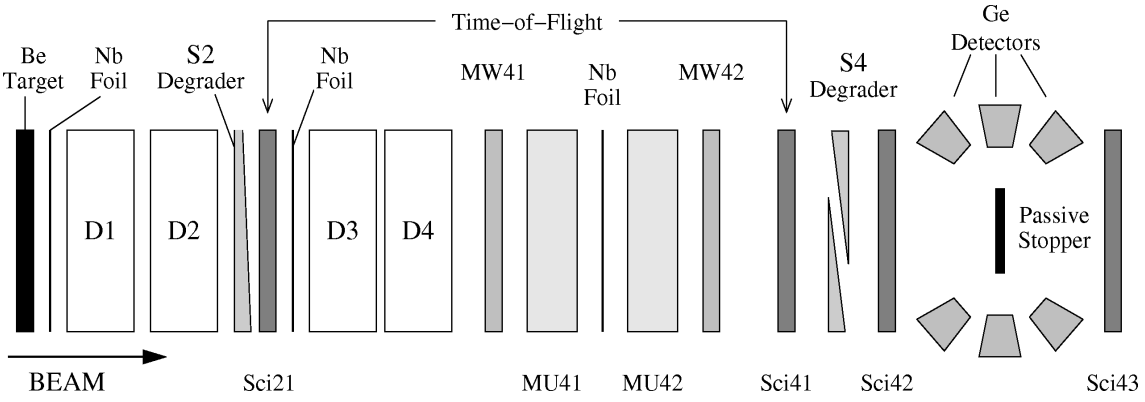

Figure 5.1: Schematic of the S4 detector arrangement as used in the currently discussed experiment. This diagram is taken from reference [69].

5.1.1 Removing "Bad" Multiwire Events

The energy deposited in a multiwire detector by desirable particles is well defined, even across the different Z values expected to be transmitted. Any other events observed by the multiwire detectors deposit a very different energy. Predominantly these other events are charge collection interference from multiple fires of the detector or they occur due to light ions. This is demonstrated with MW41 in figure 5.2. In this figure the "good" data is bound by red lines and software "cuts" are made at these channels in the off-line analysis. Once these "good" events are selected in both multiwires the operation of scintillation detector Sci21 is checked.

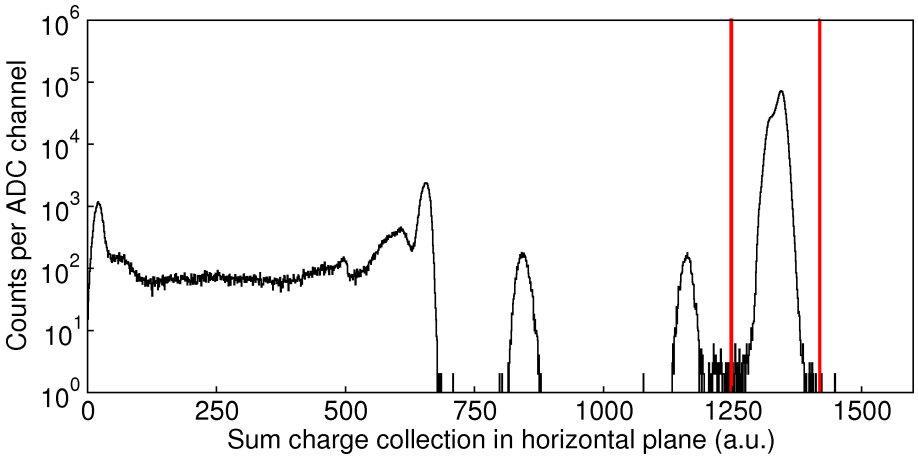

Figure 5.2: Sum charge collection in the horizontal plane of MW41. Data outside of the red lines in removed in the off-line analysis. These checks are also performed in the vertical plane and on MW42.

5.1.2 Charge Collection in Scintillation Detector Sci21

The recordings from scintillation detector Sci21 are checked through comparing the horizontal calibrated position of a particle passing through the detector against the raw charge collection. This is done twice, once each for the two horizontal plane photomultipliers. This is shown in figure 5.3. Similarly to the multiwire, the red lines indicate the data which is used, the rest is removed from the analysis. It can be seen from the plots in the figure that at the mid focus, most of the transmitted nuclei pass through the left side of the beam pipe (near the -100 mm position). Note also that most of the photons emitted during a recording are collected by the photomultiplier

tube which is closest to the location of the interaction. Events which do not show this correlation are poorly resolved in position and so are undesirable, these are the events that have been removed.

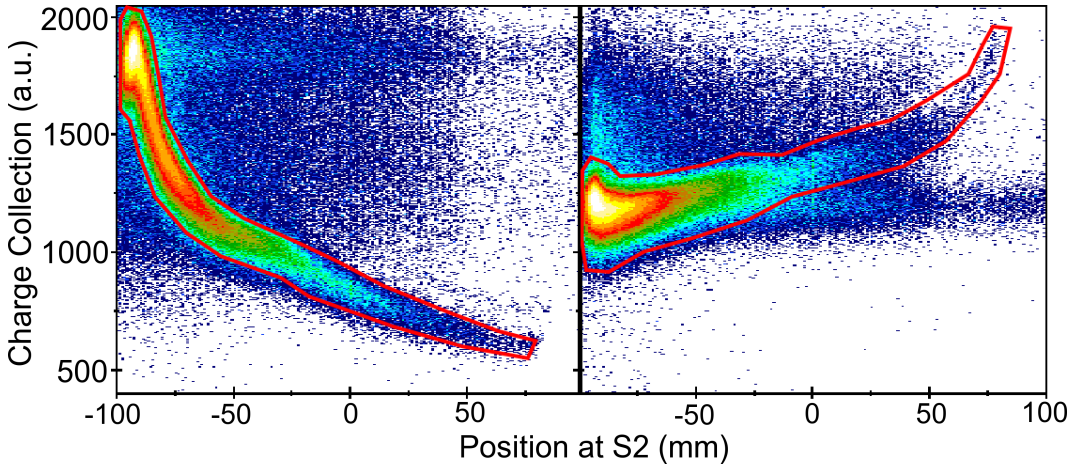

Figure 5.3: The left and right plots respectively show the charge collection from the left and right photomultiplier tubes of scintillation detector Sci21 against the position of particle detection, respectively. Red lines encompass the selected events.

5.1.3 S4 Degrader Reactions

The previous analytical selections have been concerned with ensuring the detectors have operated correctly during an event. This stage of analysis is now complete, the next two steps continue to remove events from the data, but this time for physical rather than technical reasons.

When slowing the nuclei in the S4 degrader so that they may be brought to a halt in the stopper, nuclear reactions (fragmentation continuing to be the dominant mechanism) take place, in this work it has been measured that in total approximately 18 % of nuclei react. This is measured between MUSIC41 and Sci42, (see section 4.2). The S4 degrader is placed at a later stage in the beam line than the particle identification detectors. This means that particles which react in the S4 degrader have been identified as the pre-reacted nucleus, not the final spectroscopically measured nucleus. These reacted nuclei are indistinguishable from unreacted ones when looking at the identifiction plots (see section 5.1.8). By measuring the rate of energy loss of a

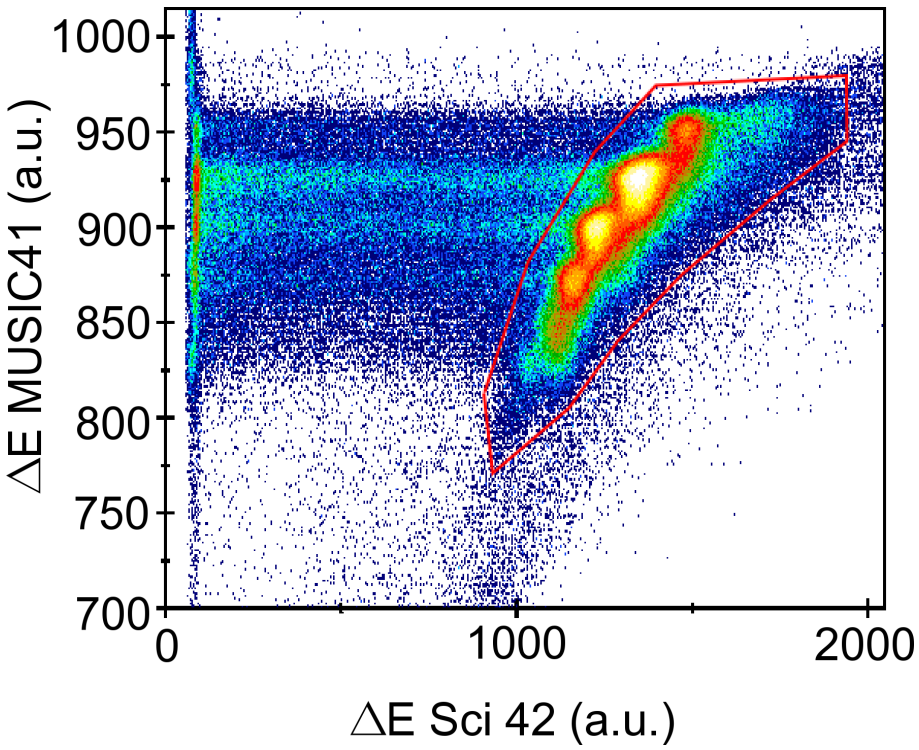

Figure 5.4: Identifying reactions in the S4 degrader by sampling ΔE both before and after the degrader (before: MUSIC41, after: Sci42). The red line surrounds events which did not react, these will continue being used in analysis.

particle both before and after this degrader it is possible to observe whether protons are lost from the nucleus in the S4 degrader. This works due to the Z^2 dependence of electromagnetic scattering interactions [84].

The removal of reactions is demonstrated in figure 5.4. Specifically the figure enables the removal of reactions which take place in all the material after the MUSIC41 detection gas and up to Sci42 (not just losses in the S4 degrader), however the degrader is by far the most important body of material. A similar check can be performed between the two MUSIC detectors, although these reactions are encompassed within the comparison of MUSIC41 and Sci42. The improved accuracy in using two MUSIC chambers removes some bad events that the scintillation detectors cannot, however the improvement is insignificant.

5.1.4 The Veto: Scintillation Detector Sci43

The final stage for removing unwanted events from the data is performed with scintillation detector Sci43. This is the so called "veto" detector. If a fragment does not

stop in the stopper then the veto should observe it, allowing for it to be removed from the analysed data. This also encompasses instances where the incoming nucleus breaks up in the stopper and light fragments from this break up continue to the veto. The veto records "null" signals when particles do not reach it. These events overlap with the calculated total losses due to reactions for any particle implanting in the stopper, as discussed in section 4.3. The implementation of the veto detector on the recorded data is shown in figure 5.5.

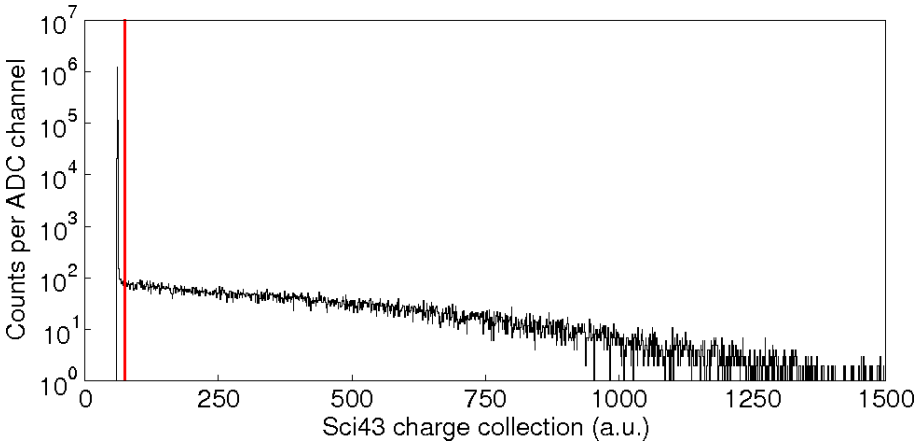

Figure 5.5: Scintillation detector Sci43 acts as a veto, non-zero signals indicate unstopped particles. Left of the red line are events when no particle is observed. Events right of the red line are removed from analysis.

Where possible, all of the unwanted events have now been removed from the analysis. These selections are combined and are collectively referred to as the "cleaning" conditions. All future analysis is performed subject to this cleaning process.

5.1.5 Distribution of Charge States

Final identification of nuclei is performed with A/q measurements, but for this to work, the charge state of each nucleus must first be understood. Nuclei with varying degrees of electronic stripping are transmitted through the FRS. To quantify the charge distribution of the nuclei, the case of ^{204}Pt is now presented as an example, partly because it is near intermediate of the nuclei to be discussed, but primarily because it is the nucleus of most interest in this experiment. The calculated values for other detected nuclides are similar.

From calculation with the GLOBAL code [85] it is known that after fragmenting

on the ^{9}Be target (thickness: 2.526 g/cm^2) and the Nb backing foil (0.221 g/cm^2) the charge states are distributed such that through the first half of the FRS ^{204}Pt is split; 93.7 % fully stripped, 6.2 % H-like (1 electron present) and 0.1 % He-like (2 electrons present). Until the nuclei reach the mid focal plane they do not pass through any more material. Therefore the charge state does not change until the nuclei reach the mid focus, which typically takes $\sim$ 145 ns. Note that a large portion of the beam is removed before S2, skewing the quoted charge distributions for the transmitted beam.

Exiting the mid focus of the FRS the distribution changes to; 76.6 % fully stripped, 21.6 % H-like and 1.8 % He-like (this is independent of the skew due to only part of the beam being transmitted in the first half of the FRS). The change in the distribution is due to the lower beam energy from traversing Sci21 (0.397 g/cm^2), the Al wedge degrader ($\sim$ 4.500 g/cm^2) and a Nb stripper foil (0.108 g/cm^2). The nuclei now travel in vacuum until they exit the FRS, again the charge states do not change during this section of the FRS; this takes $\sim$ 165 ns. Again not all of the beam is transmitted and agian this skews the quoted charge state distributions. Note that these further charge state distribution calculations have also been made with the GLOBAL code [85].

The equilibrium charge state distribution for highly relativistic ^{204}Pt nuclei ($E/A = 400 - 800$ MeV) is reached after traversing $\sim$ 0.470 g/cm^2 of Al (equilibrium depths are calculated using the CHARGE code [85]). The total material traversed at the mid focus is 5.000 g/cm^2, this is 10 times the required material for equilibrium. Because the electrons change charge state such a large number of times, their incoming and outgoing charge states can be considered independent of each other. Given this, it is easy to calculate all permutations for the charge, q, of ^{204}Pt across the entire FRS, up to the Ti exit window. This has been done and the results are presented in table 5.1.

By calculating from the table, the non-charge state changing nuclei ($\Delta q = 0$) are: 98.2 % fully stripped of their electrons, 1.8 % H-like and 0.002 % He-like. Calculating again for Δq = -1 the selection is more pure, 99.5 % of nuclei change at the mid focus from a fully stripped to a H-like state and 0.5 % change from H-like to He-like. Note that these values do not account for deliberate cuts in the beam's transmittence, thus they represent the "worst case" limit. These charge state distributions are important for the next stage of anaylsis, which is a selection on Δq.

Table 5.1: Calculated distribution of ^{204}Pt charge states along the FRS. This assumes no cutting of the secondary beam, see text for details.

Proportion in 1^{st} half of FRS	**Proportion in 2^{nd} half of FRS**
Fully stripped 93.7 %	**Fully stripped** $(93.7 \times 0.766) = 71.8$ % **H-like** $(93.7 \times 0.216) = 20.0$ % **He-like** $(93.7 \times 0.018) = 1.7$ %
H-like 6.2 %	**Fully stripped** $(6.2 \times 0.766) = 4.7$ % **H-like** $(6.2 \times 0.216) = 1.3$ % **He-like** $(6.2 \times 0.018) = 0.1$ %
He-like 0.1 %	**Fully stripped** $(0.1 \times 0.766) = 0.08$ % **H-like** $(0.1 \times 0.216) = 0.02$ % **He-like** $(0.1 \times 0.018) = 0.002$ %

5.1.6 Charge State Identification

One is able to measure the magnetic rigidity, $B\rho$, of each particle across the first and second halves of the FRS. The field strength, B, of all four magnets is recorded. However the radius, ρ, tracked out by each particle is not the same. In the second half of the FRS it is possible to determine the ρ subtended by each particle through using the S2 and S4 measured positions. In the first half of the FRS there is no position measurement at the target and it is assumed that the primary beam is correctly focused on the centre of the beam line. The magnetic rigidities, $B\rho$, in the first half ($B\rho_{1^{st}}$)

and second half ($B\rho_{2^{nd}}$) of the FRS are given by:

$$B\rho_{1^{st}} = 1 - \frac{(S2_x - Mag_{(1-2)} \times 1)}{Dis_{(1-2)}} \ \frac{(B_1 + B_2)}{2} \ \frac{(\rho_1 + \rho_2)}{2}, \tag{5.1}$$

$$B\rho_{2^{nd}} = 1 - \frac{(S4_x - Mag_{(3-4)} \times S2_x)}{Dis_{(3-4)}} \ \frac{(B_3 + B_4)}{2} \ \frac{(\rho_3 + \rho_4)}{2}. \tag{5.2}$$

In equations 5.1 and 5.2 the beam image magnification coefficient and the momentum dispersion coefficient are Mag and Dis, respectively [86]. Their values are constant ($Mag = 1.118$ and $Dis = 7.239$ mm); the ρ_i quoted is the radius of the central path through the dipole magnet; the subscripts 1-4 denote the magnet number index and $S2_x$ and $S4_x$ are the positions of the particle at the beam focal point.

It is appropriate to derive the dependency of A/q and $B\rho$ on each other as this is necessary in understanding the $\Delta B\rho$ parameter. Furthermore it is necessary for the next stage of analysis in understanding how A/q is experimentally measured.

The starting point is to equate the force, F, on a particle due to a magnetic field (equation 5.3) with the force felt by a particle in circular motion (equation 5.4).

$$F = q(v \times B) \tag{5.3}$$

$$F = \frac{\gamma p v}{\rho} \tag{5.4}$$

From these equations the vector notation can be dropped for simplicity; the velocity, v, is next substituted for $v = c\beta$; the momentum is written in terms of mass, m, and velocity; the mass is again re-written in terms of the atomic number, A, and the atomic mass unit (a.m.u.), $u = 931.5\ MeV/c^2$; the charge, q, is the degree of ionisation of the nucleus. By rearranging and making substitutions the final equation is given by;

$$B\rho = \gamma \frac{A}{q} \ \beta \ \frac{931.5 \times 10^6}{c}\,. \tag{5.5}$$

The value of $\Delta B\rho$, is calculated from equations 5.1 and 5.2. All nuclei change their value of $B\rho$ by a considerable amount traversing the S2 degrader (again using ^{204}Pt; the incoming energy is $E/A = 840$ MeV and the outgoing is $E/A = 480$ MeV [46]). The large energy loss affects β (and implicitly to a lesser degree, γ). This change in $B\rho$ is not of direct interest, what matters is the relative change in $B\rho$ between each particle. The S2 degrader is angular as described in section 3.4.6. Depending on the setting its

angle is $\sim$ 5.5 mrad. At the extremes of momentum for a nuclear species the largest difference in depth of material traversed by any two particles is $\sim$ 0.1 mg/cm^2 (this is the maximum realistic difference in the variable "e" from equation 3.3). Calculation is now made from the difference in energy loss, converting it into a $\Delta\beta$ value (as $\Delta\beta \propto \Delta B\rho$, as shown by equation 5.5). The result implies that the *maximum* difference in the change in $B\rho$ between any two ^{204}Pt particles has a ratio 1 : 0.9966 for the path of least material to the path of most material traversed, respectively.

With that ratio in mind, consider again the *difference in* $\Delta B\rho$ for two ^{204}Pt particles. This time both are fully stripped entering the mid focal plane and both pass through the same amount of material, one exits still with zero electrons attached to it and the other is now in a H-like state. Equation 5.5 shows $\Delta B\rho \propto 1/\Delta q$, the ratio of change in $B\rho$ between them is 1 : 0.987, respectively for the H-like to fully stripped nucleus. A comparison of these two ratios highlights that the parameter dominating the relative difference in $\Delta B\rho$ for particles of the same species is not the momentum spread but is a change in the charge state of the particles before and after the mid focal plane. Even at the extremes of momentum difference the charge states are purely separated.

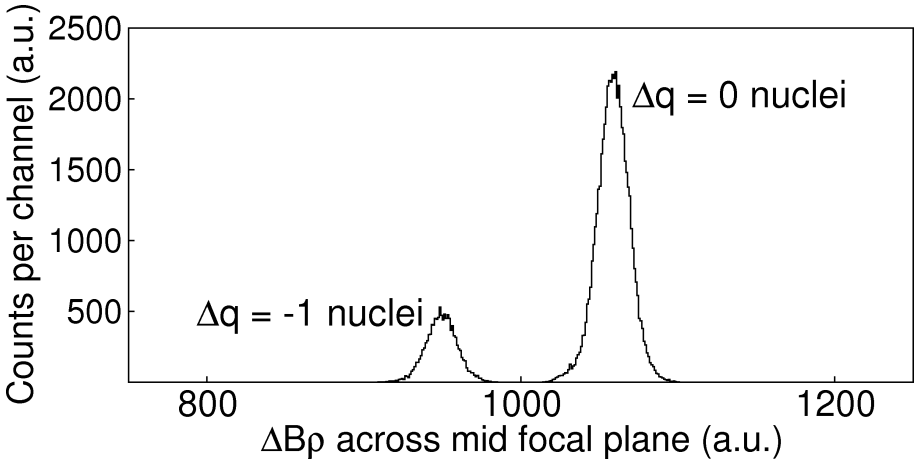

Figure 5.6: Measured charge state separation of ^{204}Pt nuclei from the current work. The width of the peaks relates to $\Delta B\rho$ due to momentum spread while each separate peak refers to different Δq, see text for full details.

Looking at $\Delta B\rho (= B\rho_{1^{st}} - B\rho_{2^{nd}})$ aids the differentiation of charge states. Figure 5.6 shows the charge state separation of ^{204}Pt, which has just been described. It is important to emphasise that the sensitivity of the selection is to *changes* in the

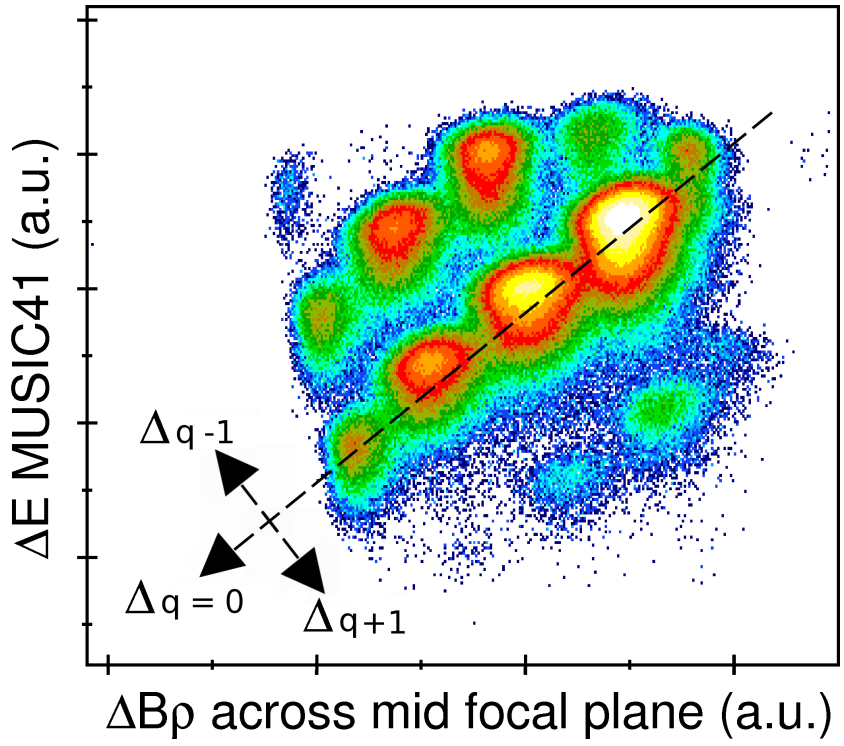

Figure 5.7: Charge state identification. There is a threshold of 2 counts per pixel applied to this plot. This data is taken from the ^{203}Ir setting, see text for detail.

charge state of the measured nucleus, it is not an absolute measurement of the charge state. There is only limited selectivity in this parameter between nuclei which are fully stripped across the entire FRS compared with nuclei which are H-like also across the entire FRS. Both of these cases are $\Delta q = 0$ events, one must rely only on the differences in energy loss due to depths of material traversed at S2, which differ due to their incoming position that has been governed by the different $B\rho_{1^{st}}$ values. With detailed calibration corrections, this can be achieved to a useful degree, however this selection has not been necessary for the current work.

The charge selection of one of the FRS settings is shown in figure 5.7. The $\Delta B\rho$ parameter has now been used in conjunction with ΔE measurements made by a MUSIC chamber. This allows $\Delta q = -1, 0, +1, +2$ events of all elements to be selected simultaneously. Fortunately changes in $\Delta B\rho$ for different isotopes of an element are significantly smaller than the changes due to Δq. This means transmitting numerous isotopes of an element does not interfere with the selection process when using this "all-in-one" selection plot.

Although the absolute charge state of the nuclei is not measured, changes in

charge states are adequate for making a charge state identification. This is true due to the high level of stripping of the beam in the first half of the FRS. As demonstrated in section 5.1.5, of all of the $\Delta q = 0$ nuclei 98.2 % of them are fully stripped and only 1.8 % are H-like (without accounting for artificial cuts on the beam transmission). To first order it can be assumed that for $\Delta q = 0$ nuclei $q = Z$. It will be seen later (see section 5.2) that the H-like and even the He-like contaminations are still a measureable issue, but these can be identified and dealt with.

5.1.7 Separating Elements

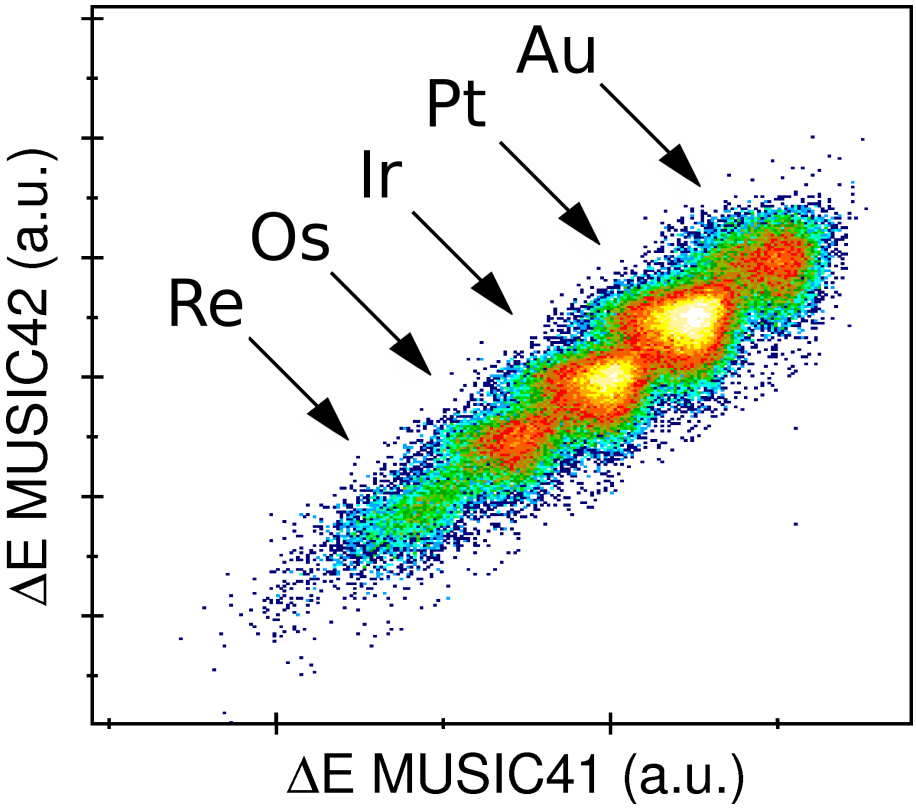

Figure 5.8: Element selection by using MUSIC chambers. This data is taken from the ^{203}Ir setting.

It is interesting to observe the selectivity on Z. The ΔE parameter from the MUSIC chambers has already been used to select charge states, but it is worth discussing in itself. The responses of the two MUSIC chambers have been plotted in figure 5.8. As stated earlier (section 3.4.7) the MUSIC chambers measure the q_{eff} ($\propto Z^2$). The material traversed between the Ti FRS exit window (0.09 m/cm^2) and a selection of other matter (including: glass, air, Mylar and kapton) means the particles have already

travelled through 0.166 g/cm^2 of material before the ΔE measurement. The charge state equilibrium for Ti would be reached after $\sim$ 0.25 g/cm^2 of material. This means that the identified charge states are largely disassociated before MUSIC measurements begin. Hence the measured q_{eff} is near independent of in-flight charge states. Certainly it *is* independent for MUSIC42, which is positioned after MUSIC41 and a Nb stripper (i.e. a lot more material). When both chambers are operating to an equal level the best resolution is achieved by combining their responses. In this experiment this was not the case, the best resolution comes from using MUSIC41 alone.

5.1.8 Nuclide Selection

One is now able to analyse each ionic charge state group independently. For each ionic charge state group a different nuclide identification plot is needed. One such identification plot is shown in figure 5.9 (right). The identification uses the particle A/q ratio. This is extracted by a rearrangement of equation 5.5 and using measured ToF, magnetic rigidity and positions in the second half of the FRS. The A/q ratio is plotted against the position of the particles at the S4$_x$ focal position, this is where the beam reaches its optimum focus. The achromatic nature of the beam following the S2 wedge strongly correlates the postion of particles with Z for any given charge state. This is a result of particle position being determined by $B\rho_{1^{st}}$ and the varying thickness of the S2 degrader across the horizontal plane. Figure 5.9 (left) is the same nuclide identification plot but without charge state selection. Without the charge selection there is an ambiguity over the identification process; compared with the $\Delta q = 0$, many nuclei are $q \neq Z$ throwing doubt over the A of any given A/q and highlighting the need for charge state selection.

A combination of gating on the charge state selection plot and the nuclide selection plot unambiguously identifies particles. Following selection of "clean" events, charge states and individual nuclides, spectroscopic measurements are made.

5.2 Details About the FRS Settings

During the experiment the FRS magnets were tuned to 9 different settings. In each case the S2 degrader achromacity angle and the S4 degrader thicknesses were also

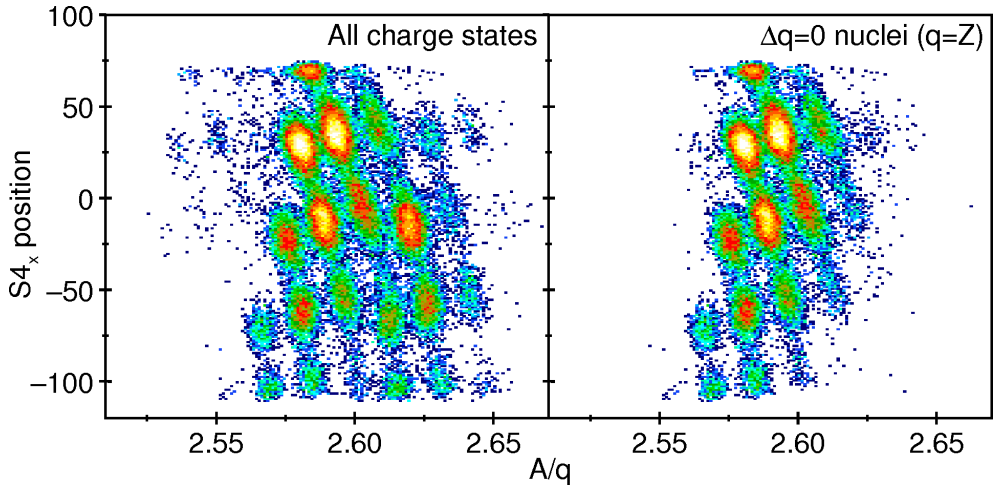

Figure 5.9: Nuclide selection. **Left** : all charge states are plotted. **Right** : only fully stripped ($q = Z$) nuclei are included. There is a two count threshold per pixel applied to both of these plots. This data is taken from the ^{203}Ir setting.

adjusted to optimise selection, identification and particle stopping position. The data presented in this thesis investigates 6 of these settings. They are each named ^{206}Hg, ^{203}Ir, ^{202}Os, ^{199}Os, ^{192}W and ^{185}Lu. In all settings the magnets and degraders were tuned to focus on the (fully stripped) named nuclide, passing it through the centre of the FRS.

For the benefit of those with a more detailed interest in the specifics of the FRS settings, a summary table has been compiled (Table 5.2) including information for all of the six settings. Chronologically the different settings were run in the following order, beginning with the earliest in time: ^{206}Hg, ^{203}Ir, ^{202}Os, ^{192}W, ^{199}Os, ^{185}Lu.

In table 5.2 note that the thickness of the S2 degrader is exclusive of the other material at the S2 location of the FRS. Their are two other objects in the beam line, they are a scintillation detector (Sci21), this is 0.350 g/cm^2 thick for the first five settings and 0.343 mg/cm^2 thick for the ^{185}Lu setting (the original scintillation detector was damaged and replaced for this setting). The second other material at S2 is a Nb stripper, this is 0.108 g/cm^2 thick. The quoted thicknesses of the S2 degrader are the dialled thicknesses, not the actual ones.

Also note that the average spill period is defined as the time between the start of one spill until the start of the next. The spill length is the time span over which the spill particles are transmitted from the SIS-18 to the target. In all cases the stopper was made of perspex.

Table 5.2: Supplementary details for each of the FRS settings.

Information	FRS Setting					
	^{206}Hg	^{203}Ir	^{202}Os	^{199}Os	^{192}W	^{185}Lu
Approx. Time on setting (hrs)	7	22	20	22	40	17
Typical spill intensity (part./spill)	1.6×10^{8}	5.0×10^{8}	7.0×10^{8}	1.0×10^{9}	1.3×10^{9}	1.2×10^{9}
Typical spill length (s)	10	10	2	8	10	5
Typical spill period (s)	18	30	18	23	25	16
Stopper thickness (mm)	7	7	7	9	9	9
Setting fragment A/Z	2.512	2.636	2.658	2.618	2.595	2.606
$B\rho_1$ (T)$_{(\rho=11.2407\ \mathrm{m})}$	12.9100	13.2652	13.1719	13.0617	13.0617	13.1426
$B\rho_2$ (T)$_{(\rho=11.3170\ \mathrm{m})}$	13.0315	13.3880	13.5136	13.2952	13.2115	13.2658
$B\rho_3$ (T)$_{(\rho=11.2908\ \mathrm{m})}$	9.0055	9.5644	9.6773	9.5306	9.5284	9.8015
$B\rho_4$ (T)$_{(\rho=11.2441\ \mathrm{m})}$	9.0076	9.5665	9.6789	9.5327	9.5305	9.8015
S2 degrader thickness[a] (g/cm^2)	4.900	4.900	4.900	4.900	4.900	4.900
S2 degrader angle (mrad)	5.580	5.540	5.520	5.537	5.530	5.506
S4 degrader thickness (g/cm^2)						
→ *Dialled*	2.285	2.985	2.985	2.900	3.185	3.500
→ *Calculated*	2.585	3.073	3.073	3.000	3.300	3.600
S1 Slit acceptance (mm)	$-5 \rightarrow +5$	$-35 \rightarrow +100$	$-100 \rightarrow +100$	$-100 \rightarrow +26$	$-100 \rightarrow +9$	$-100 \rightarrow +16$
S2 Slit acceptance (mm)	$-100 \rightarrow +100$	$-100 \rightarrow +100$	$-100 \rightarrow +100$	$-100 \rightarrow +100$	$-30 \rightarrow +100$	$-68 \rightarrow +100$
S3 Slit acceptance (mm)	$-100 \rightarrow +100$	$-100 \rightarrow +100$	$-100 \rightarrow +100$	$-100 \rightarrow +100$	$-100 \rightarrow +100$	$-100 \rightarrow +100$
S4 Slit acceptance (mm)	$-100 \rightarrow +100$	$-100 \rightarrow +100$	$-100 \rightarrow +100$	$-100 \rightarrow +100$	$-100 \rightarrow +100$	$-100 \rightarrow +100$

[a] *This is exclusive of the other S2 materials, which are a 0.350 g/cm^2 scintillator (or 0.343 g/cm^2 for the ^{185}Lu setting) and a 108 g/cm^2 Nb stripping foil.*

5.3 The Identified Nuclei

Identification plots have been produced for all of these settings in all of the transmitted charge states, they are shown in figures 5.10 to 5.16. Note that in figure 5.10 (top left) that the charge state separation is not as clear as for the other settings. This is a common problem when focusing on nuclei (in this case ^{206}Hg) near the primary beam nucleus (^{208}Pb). One has to set the slits very narrowly in such settings to stop the non-fragmented primary beam particles transmitting, as these have very high intensity. It is plausible due to the narrow slit width that scattering off the slits is interfering with the beam optics.

For the plots in figures 5.11 to 5.16 the labelling assumes: for $\Delta q = 0 \rightarrow q = Z$; for $\Delta q = -1 \rightarrow q = (Z-1)$; for $\Delta q = -2 \rightarrow q = (Z-2)$; for $\Delta q = +1 \rightarrow q = Z$. As stated in section 5.1.5, this assumes that all nuclei are fully stripped in the first half of the FRS, however the assumption is not always true (it is indicatively not true for example of the $\Delta q = +1$ charge states). In other cases where the nucleus is not fully stripped in the first half of the FRS it has been stated. Notice that although only a small fraction of the total beam is not fully stripped (6.3 %), due to the A/q shift for $(Z-1)$ and $(Z-2)$ nuclei, less exotic, higher cross section nuclides are observed in measureable quantities.

There are a handful of instances (all in the ^{206}Hg setting due to the charge selection being imperfect) where nuclides of a given q have been split over two charge-state plots by the charge gating. These instances are: $^{206}\mathrm{Tl}_{(H-He)}$, $^{202-3}\mathrm{Hg}_{(H-H)}$ and $^{205-206}\mathrm{Hg}_{(\Delta q=0)}$. The notations H and He indicate H-like and He-like nuclei, respectively. Their order describes the charge state for the first and second halves of the FRS, respectively. Later F will also be used, indicating that a nucleus is a bare, fully stripped, ion. This notation will become standard for the remainder of this document. These cases of cutting nuclide particle identifications in two sections are confirmed by γ-ray spectroscopy and by their having identical S4$_x$ positions and A/q values on the $\Delta q = 0$ and $\Delta q = -1$ plots. The case of ^{206}Tl was particularly affected, its species is known only because of the observed γ rays, which were used to unambiguously identify decays from ^{206}Tl ions (see section 6.4.1) Once the nuclide was identified by its γ-ray transitions, it was then possible to identify the charge state through atomic number and measured A/q.

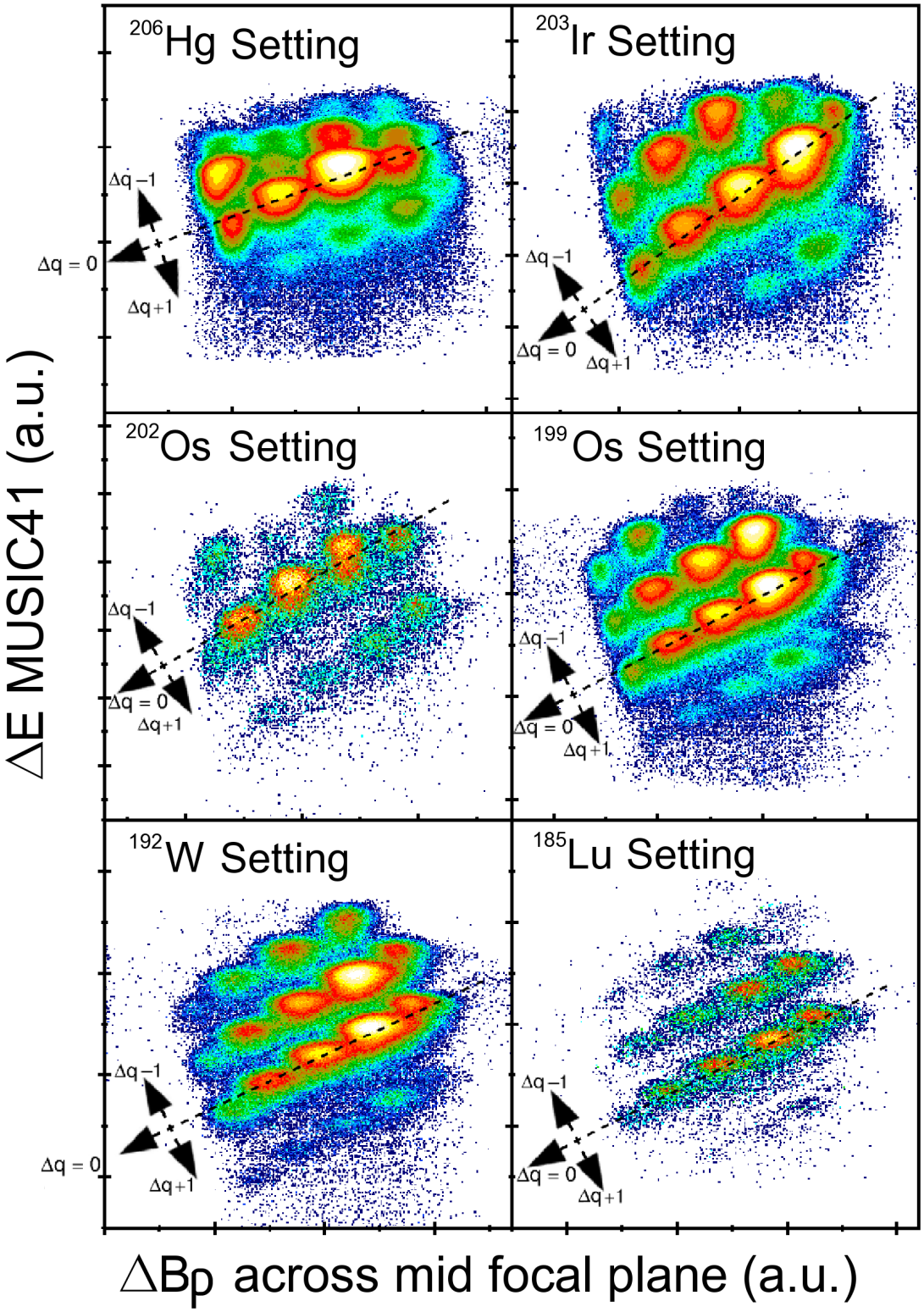

Figure 5.10: Charge state identification plots for the six FRS settings. The settings are named by their fragment of focus, this is written within each plot.

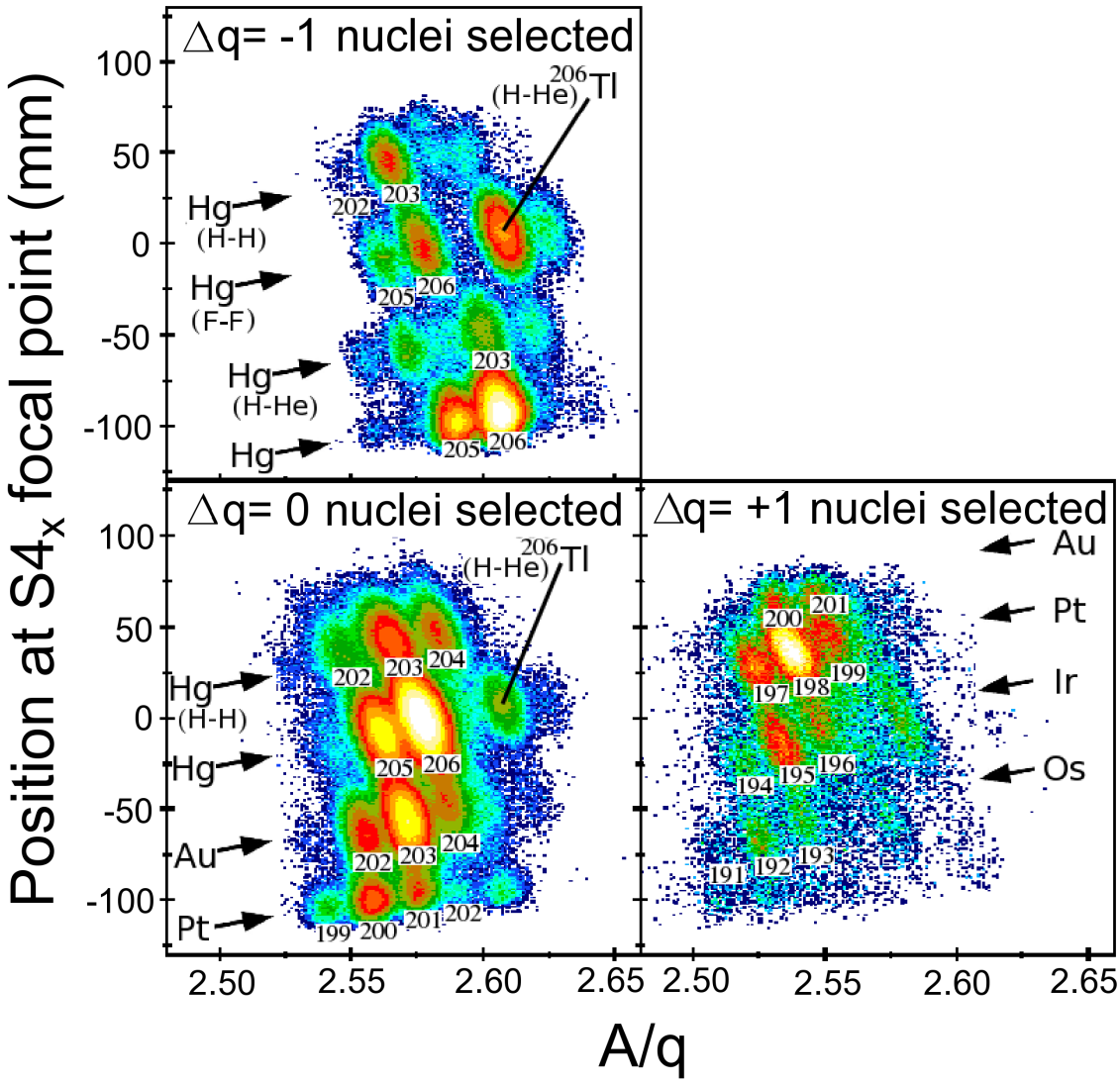

Figure 5.11: Particle identification for the ^{206}Hg setting. Nuclei differing from the assumed charge state of each Δq have their individual charge state noted. Inadequate separation of charge states in figure 5.10 has led to significant bleed through between charge state plots for the $^{206}\mathrm{Tl}_{(H-He)}$, $^{202,203}\mathrm{Hg}_{(H-H)}$ and $^{205,206}\mathrm{Hg}_{(F-F)}$ nuclei.

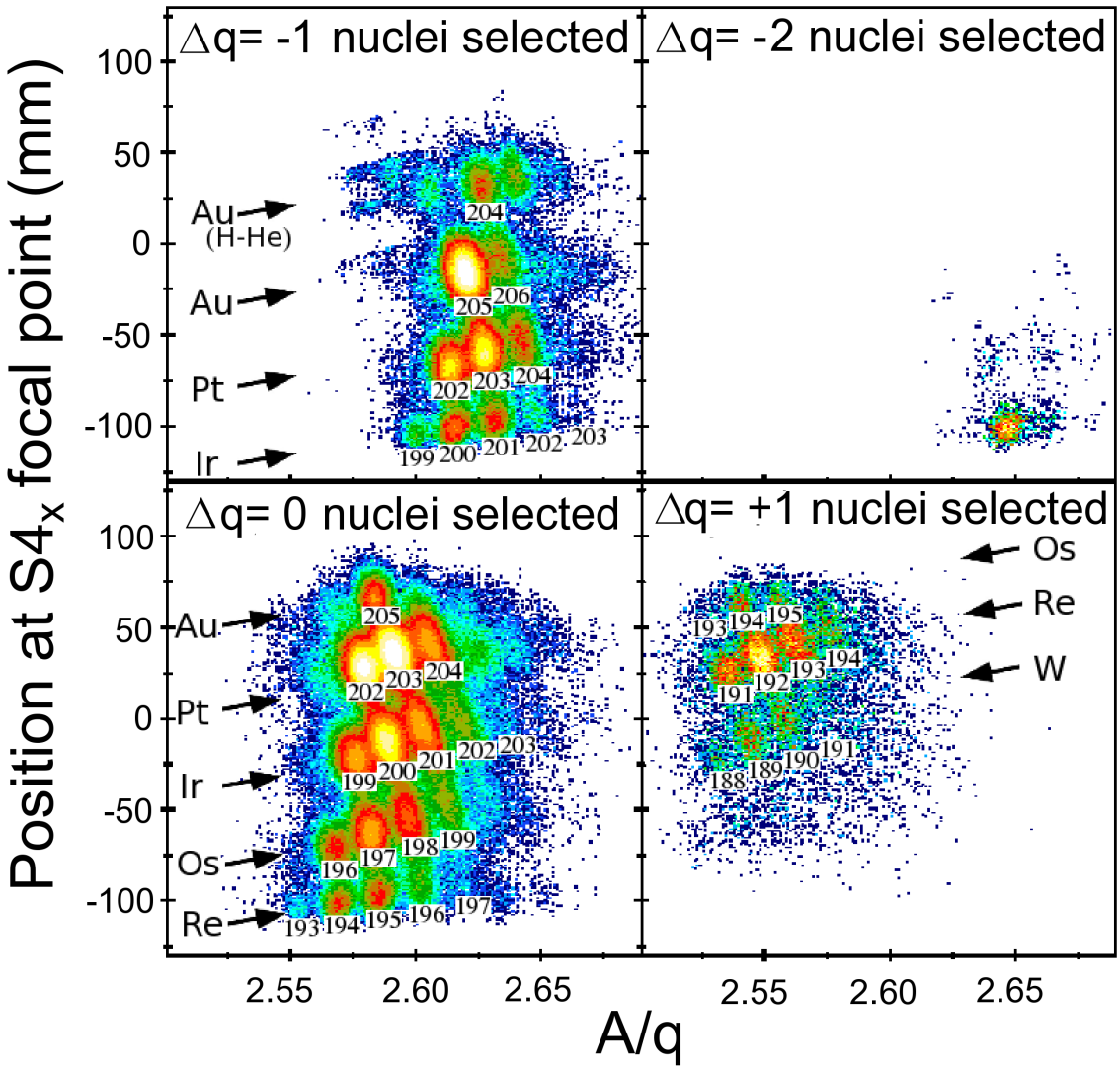

Figure 5.12: Particle identification for the ^{203}Ir setting. Nuclei differing from the assumed charge state of each Δq have their individual charge state noted.

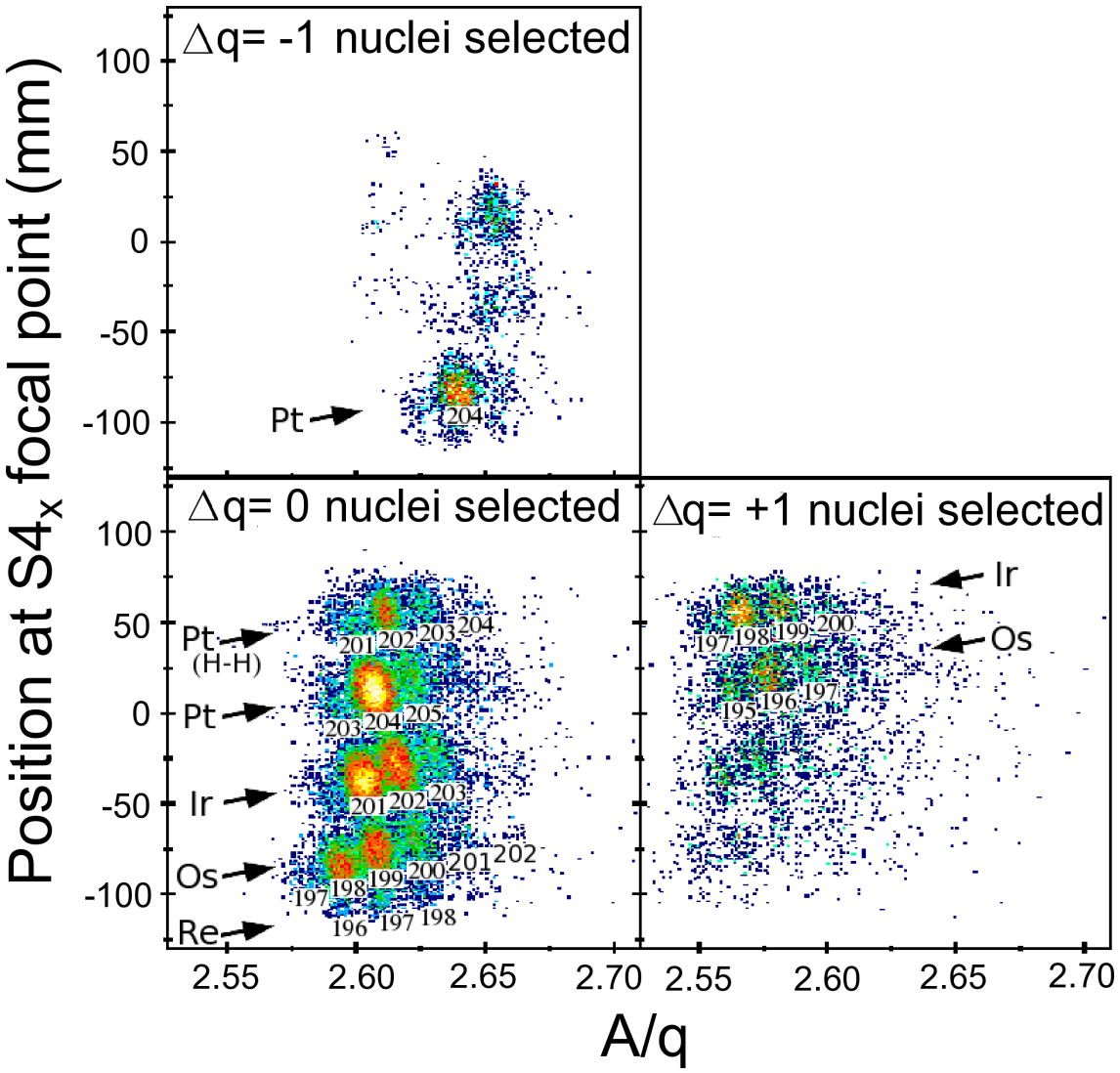

Figure 5.13: Particle identification for the ^{202}Os setting. Nuclei differing from the assumed charge state of each Δq have their individual charge state noted.

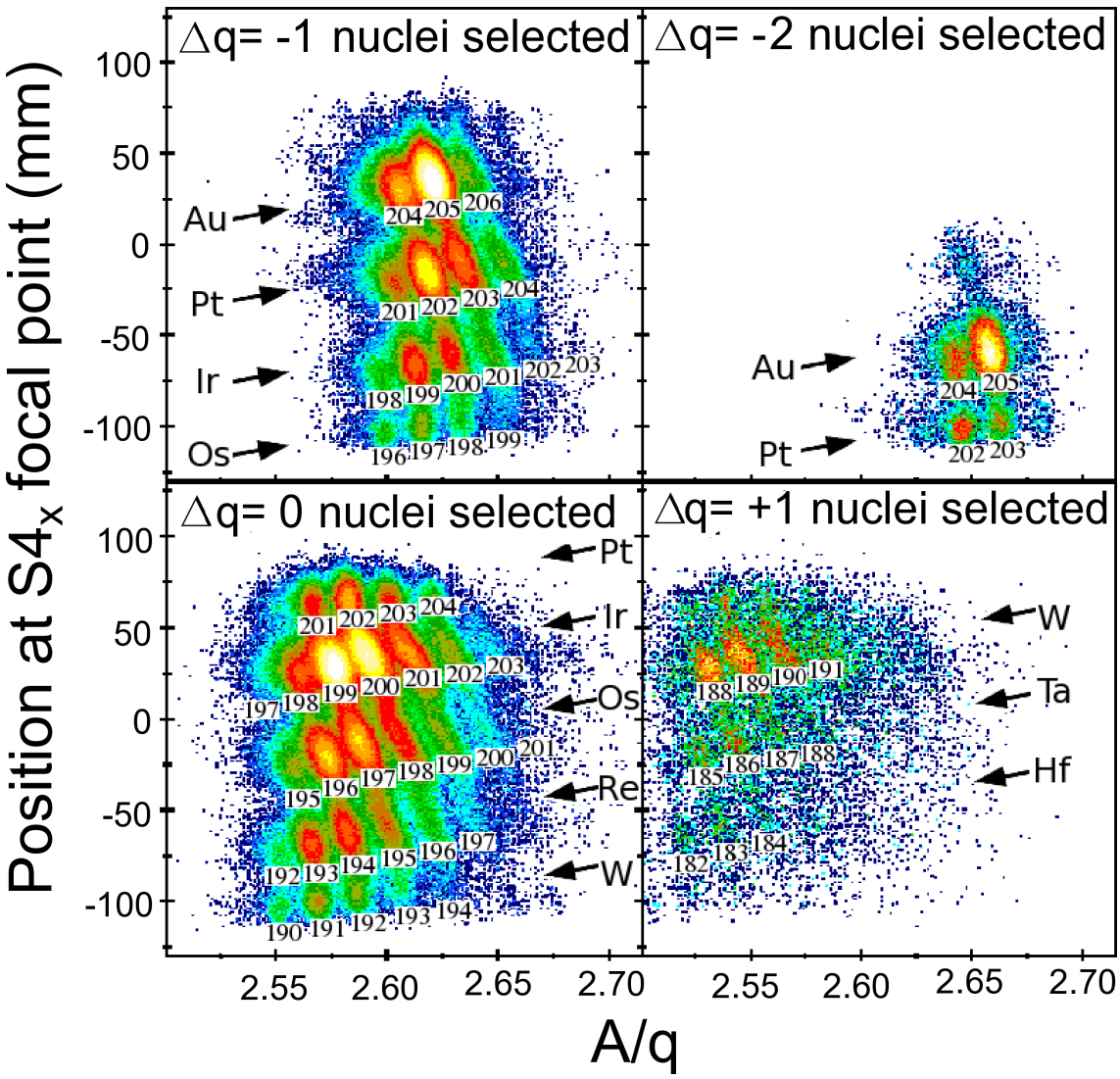

Figure 5.14: Particle identification for the ^{199}Os setting.

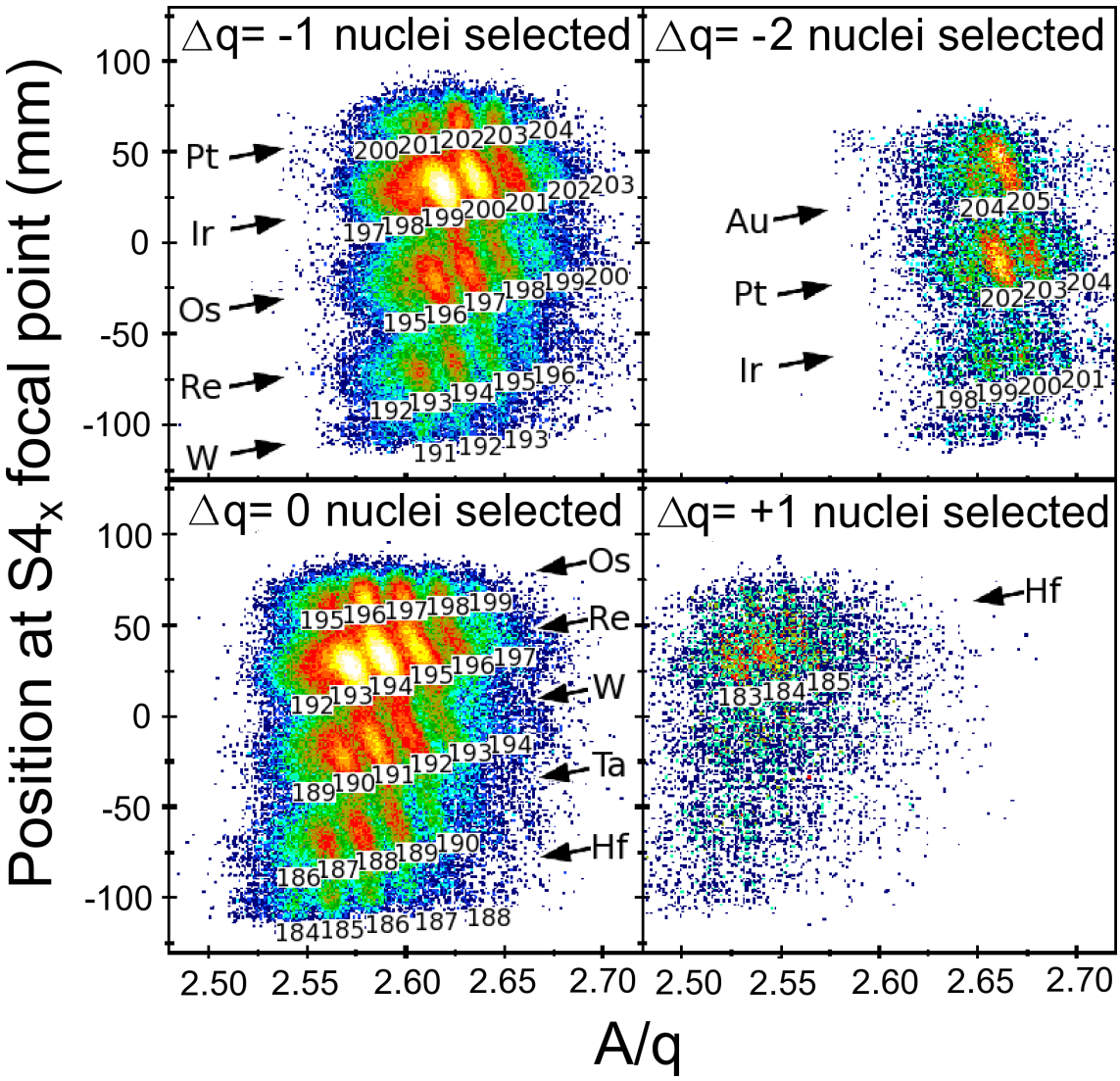

Figure 5.15: Particle identification for the ^{192}W setting.

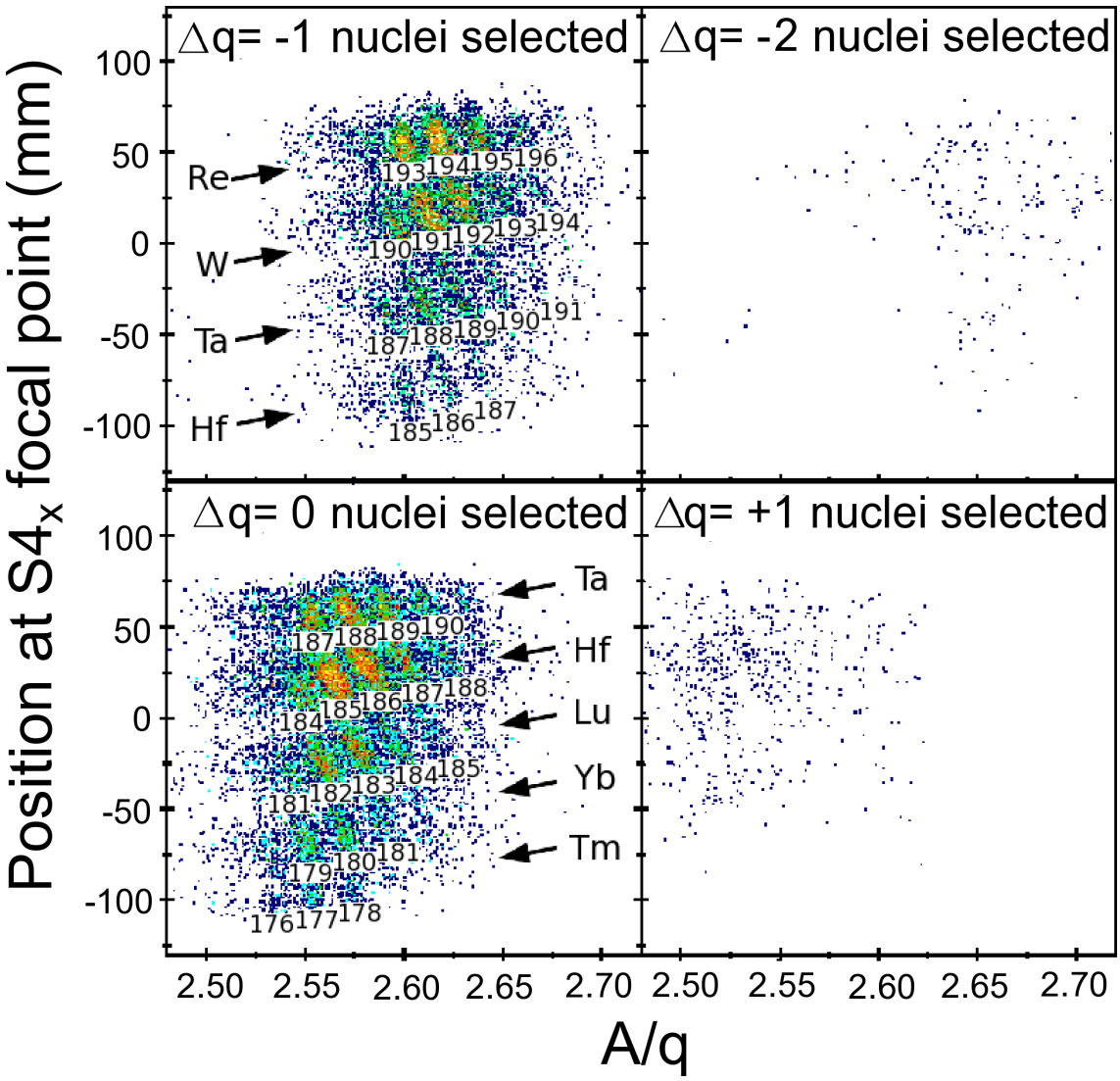

Figure 5.16: Particle identification for the ^{185}Lu setting.

All of the nuclides which have been labelled by atomic mass in the identification plots have had their correlated γ rays examined with the RISING array. In cases where isomeric states have been detected, the nuclide is discussed in the following chapter. The number of nuclei implanted for each nuclide has been counted specifically for isomeric ratio measurements, but also as a gauge to the reader regarding the feasibility of spectroscopic measurements in the present work and lastly it gives a quantitative estimate, if not a formal measurement, of the relative production cross section for the more exotic of the identified nuclei. With regards to the identification plots (figures 5.10 to 5.16) the colour scales are relative within each plot of each figure, no cross-comparison can be made of the intensities. The numbers of nuclei implanted have been counted (see Table 5.3) by their individual charge states (as this is necessary for isomeric ratios) and the total nuclei implanted is also noted. Counting errors were assumed to follow Poisson statistics ($\Delta N = \sqrt{N}$) and are noted in the brackets. Regarding the lower limit of the counting error, the calculated losses upon implantation in the stopper have *not* been included in this table (see section 4.3 for details on these losses).

There is still some doubt over the accuracy of counting. The $\sqrt{N}$ error used may not be a fair assumption as numerous detectors are involved in detecting each individual nucleus. Also, there is a background across the identification plots due to imperfections in the scintillation detector Sci21 "good" charge collection gating. This background tends to be larger at locations where large cross section nuclei are transmitted. For some cases it might be comparable with the total number of nuclei implanted, this has not been quantified.

Table 5.3: Number (in thousands) of implanted nuclei from all six of the experimental settings combined. In each case the charge state of the nucleus in the first half and second half of the FRS is named. The convention runs such that nuclei are F, H or He corresponding to zero electrons, one electron or two electrons attached to the nucleus, respectively.

Nuclide	**Thousands of implanted nuclei (all settings combined)**						
	Total	***F-F***	***F-H***	***F-He***	***H-F***	***H-H***	***H-He***
^{206}**Tl**	85.9(3)	-	-	-	-	-	85.9(3)
^{202}**Hg**	12.2(1)	-	-	-	-	12.2(1)	-
^{203}**Hg**	142.4(4)	-	13.9(1)	-	-	128.2(4)	-
^{204}**Hg**	51.7(2)	-	2.55(5)			40.7(2)	8.35(9)
^{205}**Hg**	417.0(6)	339.5(6)	77.5(3)	-	-	-	-
^{206}**Hg**	1717.7(13)	1393.0(12)	323.9(6)	-	-	-	-
^{200}**Au**	2.14(5)	-	-	-	2.14(5)	-	-
^{201}**Au**	2.70(5)	-	-	-	2.70(5)	-	-
^{202}**Au**	60.5(2)	60.5(2)	-	-	-	-	-
^{203}**Au**	402.0(6)	402.0(6)	-	-	-	-	-
^{204}**Au**	133.3(4)	35.1(2)	61.2(2)	38.9(2)	-	-	-
^{205}**Au**	337.3(6)	6.06(8)	303.8(6)	32.2(2)	-	-	-
^{206}**Au**	19.7(1)	-	19.7(1)	-	-	-	-
^{197}**Pt**	7.4(9)	-	-	-	7.4(9)	-	-
^{198}**Pt**	24.3(2)	-	-	-	24.3(2)	-	-
^{199}**Pt**	8.84(9)	4.0(6)	-	-	4.9(7)	-	-
^{200}**Pt**	64.7(3)	63.0(3)	1.70(4)	-	-	-	-
^{201}**Pt**	68.1(3)	42.8(2)	24.9(2)	1.05(3)	-	0.46(2)	-
^{202}**Pt**	387.5(6)	200.2(4)	148.2(4)	4.16(7)	-	2.03(5)	-
^{203}**Pt**	319.1(6)	216.9(5)	98.6(3)	5.27(7)	-	0.63(3)	-
^{204}**Pt**	92.3(3)	67.0(0.3)	25.2(3)	0.65(3)	-	0.11(0.01)	-
^{205}**Pt**	1.35(4)	1.35(4)	-	-	-	-	-
^{194}**Ir**	1.68(4)	-	-	-	1.68(4)	-	-
^{195}**Ir**	7.96(9)	-	-	-	7.96(9)	-	-

Continued on Next Page...

Table 5.3 – Continued

Nuclide	Thousands of implanted nuclei (all settings combined)						
	Total	*F-F*	*F-H*	*F-He*	*H-F*	*H-H*	*H-He*
^{196}Ir	3.12(6)	-	-	-	3.12(6)	-	-
^{197}Ir	-	-	-	-	-	-	-
^{198}Ir	51.3(2)	28.0(2)	22.0(1)	0.38(2)	1.28(4)	-	-
^{199}Ir	358.3(6)	250.9(5)	106.8(3)	1.09(3)	0.69(3)	-	-
^{200}Ir	353.6(6)	274.1(5)	79.2(3)	1.02(3)	0.22(2)	-	-
^{201}Ir	165.0(4)	135.2(4)	29.8(2)	0.45(2)	-	-	-
^{202}Ir	35.5(2)	30.1(2)	4.62(7)	-	-	-	-
^{203}Ir	8.00(9)	7.10(8)	0.906(3)	-	-	-	-
^{191}Os	0.43(2)	-	-	-	0.43(2)	-	-
^{192}Os	2.26(5)	-	-	-	2.26(5)	-	-
^{193}Os	2.05(5)	-	-	-	2.05(5)	-	-
^{194}Os	1.13(3)	-	-	-	1.13(3)	-	-
^{195}Os	22.3(1)	15.1(1)	5.86(8)	-	1.33(4)	-	-
^{196}Os	121.4(3)	96.9(3)	23.5(2)	-	1.00(3)	-	-
^{197}Os	158.7(4)	134.3(4)	23.9(2)	-	0.56(2)	-	-
^{198}Os	77.8(3)	66.1(3)	11.7(1)	-	-	-	-
^{199}Os	28.6(2)	25.5(2)	3.12(6)	-	-	-	-
^{200}Os	6.28(8)	5.76(8)	0.52(2)	-	-	-	-
^{201}Os	1.39(4)	1.39(4)	-	-	-	-	-
^{202}Os	0.02(1)	0.02(1)	-	-	-	-	-
^{191}Re	2.37(5)	-	-	-	2.37(5)	-	-
^{192}Re	23.0(2)	16.1(1)	1.91(4)	-	5.00(7)	-	-
^{193}Re	90.4(3)	77.9(3)	9.5(1)	-	2.95(5)	-	-
^{194}Re	101.2(3)	92.0(3)	9.2(1)	-	-	-	-
^{195}Re	60.8(2)	55.7(2)	5.11(7)	-	-	-	-
^{196}Re	14.4(1)	12.4(1)	1.94(4)	-	-	-	-
^{197}Re	5.53(7)	5.53(7)	-	-	-	-	-
^{198}Re	0.71(3)	0.71(3)	-	-	-	-	-

Continued on Next Page...

Table 5.3 – Continued

Nuclide	Thousands of implanted nuclei (all settings combined)						
	Total	*F-F*	*F-H*	*F-He*	*H-F*	*H-H*	*H-He*
^{188}W	3.66(6)	-	-	-	3.66(6)	-	-
^{189}W	11.1(1)	5.54(7)	-	-	5.53(7)	-	-
^{190}W	30.4(2)	24.8(2)	0.89(3)	-	4.72(7)	-	-
^{191}W	36.5(2)	31.7(2)	2.65(5)	-	2.08(4)	-	-
^{192}W	20.9(1)	19.0(1)	19.5(4)	-	-	-	-
^{193}W	9.4(1)	0.82(9)	1.20(4)	-	-	-	-
^{194}W	2.87(5)	2.65(5)	0.22(2)	-	-	-	-
^{185}Ta	1.09(3)	-	-	-	1.09(3)	-	-
^{186}Ta	3.57(6)	1.98(5)	-	-	1.59(4)	-	-
^{187}Ta	10.6(1)	9.1(1)	0.32(2)	-	1.27(4)	-	-
^{188}Ta	14.5(1)	13.0(1)	0.71(3)	-	0.78(3)	-	-
^{189}Ta	9.1(1)	8.55(9)	0.56(2)	-	-	-	-
^{190}Ta	3.89(6)	3.61(6)	0.28(2)	-	-	-	-
^{191}Ta	0.26(2)	0.15(1)	0.10(1)	-	-	-	-
^{182}Hf	0.49(2)	-	-	-	0.49(2)	-	-
^{183}Hf	3.01(4)	-	-	-	1.94(4)	-	-
^{184}Hf	5.38(6)	2.12(5)	-	-	1.91(4)	-	-
^{185}Hf	7.14(8)	5.04(7)	0.21(2)	-	0.94(3)	-	-
^{186}Hf	5.16(7)	4.93(7)	0.24(2)	-	-	-	-
^{187}Hf	2.89(5)	2.75(5)	0.14(1)	-	-	-	-
^{188}Hf	1.16(3)	1.16(3)	-	-	-	-	-
^{181}Lu	0.43(2)	0.43(2)	-	-	-	-	-
^{182}Lu	1.32(4)	1.32(4)	-	-	-	-	-
^{183}Lu	1.19(4)	1.19(4)	-	-	-	-	-
^{184}Lu	0.66(3)	0.66(3)	-	-	-	-	-
^{185}Lu	0.29(2)	0.29(2)	-	-	-	-	-
^{179}Yb	0.58(2)	0.58(2)	-	-	-	-	-
^{180}Yb	0.66(3)	0.66(3)	-	-	-	-	-

Continued on Next Page...

Table 5.3 – Continued

Nuclide	Thousands of implanted nuclei (all settings combined)						
	Total	*F-F*	*F-H*	*F-He*	*H-F*	*H-H*	*H-He*
^{181}Yb	0.33(2)	0.33(2)	-	-	-	-	-
^{176}Tm	0.10(1)	0.10(1)	-	-	-	-	-
^{177}Tm	0.17(1)	0.17(1)	-	-	-	-	-
^{178}Tm	0.14(1)	0.14(1)	-	-	-	-	-

Chapter 6

Gamma-ray Spectroscopy and Interpretation

6.1 Confirming the Identification

The nuclei have now been separated, selected and identified preliminarily by their A/q values. Due to the complexity of the calibrations involved in the identification it is important to confirm it with "known" cases. This means implanting and measuring nuclei that exhibit the decay of previously reported isomers with a suitable lifetime.

Chronologically, the first experimental setting focused on ^{206}Hg and this nuclide is one such "known" case [31,87,88]. When selecting the nuclei identified as $^{206}\mathrm{Hg}_{(F-F)}$ γ-rays are observed by the RISING array. In figure 6.1 these are shown as a matrix of energy versus time. The observed 100, 364, 1034, 1068, 1157 and 1257 keV γ rays are consistent with reports on this nuclide from previous experiments [31,87,88]. Figure 6.1 shows two isomers of different lifetimes, which is as expected. Detailed analysis of this nuclide is presented in section 6.4.2, but for now it is sufficient to have established that the particle identification procedure is correct.

Confirming ^{206}Hg does not test all of the calibrations. As it is the nuclide of focus for its setting it travels centrally and at a tangent to the horizontal (and vertical) plane. This means measurements such as extrapolating particle positions at the S4 focal point and the normalisation of the MUSIC chamber responses for particles transmitted at non-central x-positions are not properly tested. With differing degrees of influence, the calibrations of A/q, ΔE and $S4_x$ are affected. In the ^{203}Ir setting $^{202}\mathrm{Pt}_{(F-F)}$ was

not transmitted centrally with respect to the horizontal plane. An isomer has been previously reported in this nuclide [54]. Investigating this isomer in the current data tests the position correction calibrations. The observed γ rays from the selected nuclei are presented in figure 6.2. The result is consistent with previous findings [54].

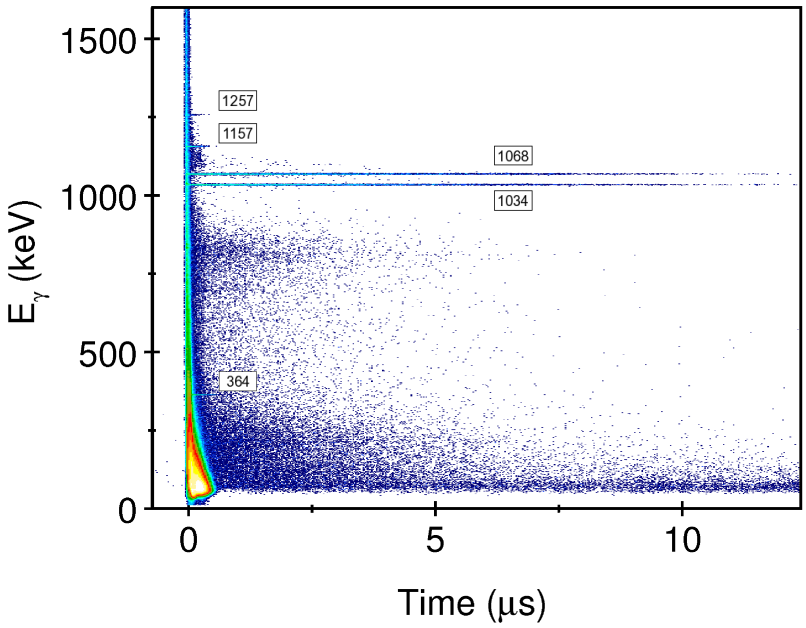

Figure 6.1: A plot of γ-ray energy vs. detection time (DGF) after implantation for nuclei identified as $^{206}\mathrm{Hg}_{(F-F)}$. This plot is subject to a 3 count threshold.

As one continues to make such calibration checks for each setting and each charge state within each setting, the accuracy of the calibrations exhibits significant variation. The variances are not so large that they are a critical issue, however they do make it necessary to confirm all the identification plots individually. This eventuality was anticipated. The reader will find from close examination of figures 5.11 to 5.16 that all settings and charge states either contain a nucleus with a previously reported isomer (see figure 1.1 as a guide); or alternatively the identification plot contains an isomer, which has been unambiguously identified elsewhere in this currently described experiment. These such instances will become apparent following the coming discussions in section 6.5, where isomers identified for the first time in the current work are detailed.

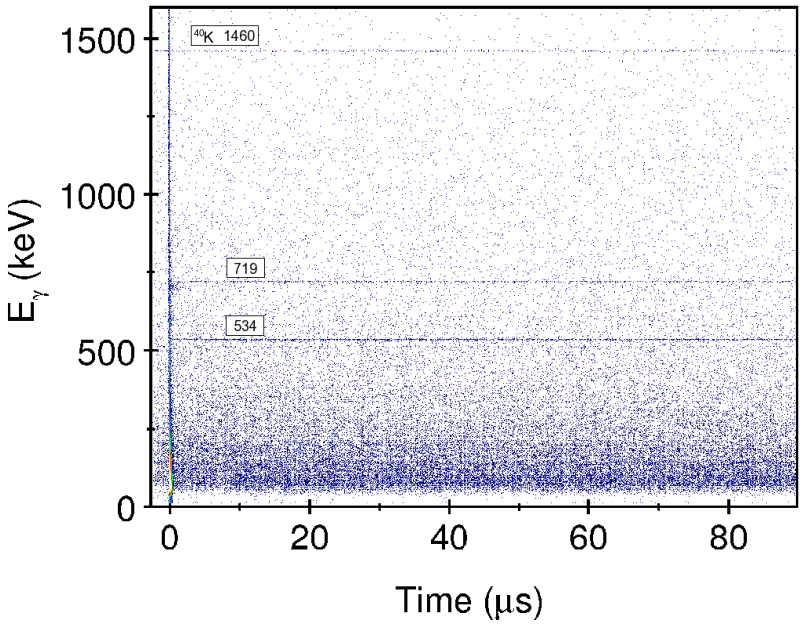

Figure 6.2: A plot of γ-ray energy vs. detection time (DGF) after implantation for nuclei identified as $^{202}\mathrm{Pt}_{(F-F)}$.

6.2 Combining the Data Sets

The identification plots (figures 5.11 to 5.16) overlap with respect to nuclides implanted for measurement. The transmission of varying charge states has amplified this. It is interesting to note that despite the overlap of the 22 different identification plots, ^{197}Ir was beyond the acceptance width of the FRS in all cases. The surrounding Ir isotopes and the neighbouring elements have all been populated and studied in the present work. There are instances where ^{197}Ir is very close to being transmitted, however analysis has shown that the candidate data is actually noise.

When implanted, atoms neutralise with electrons from the stopper. Therefore isomer spectroscopy following implantation is independent of in-flight charge states. All of the γ-ray information for a single nuclide from different settings and all charge states can be, and has been, combined into a single spectrum. This cannot be done when studying the spin population distribution of the fragmentation reaction through isomeric ratios [3, 4]. Differing in-flight charge states affect decay rates of nuclides while traversing the FRS. For isomeric ratio measurements single charge states have been combined from all the FRS settings, but each charge state is examined separately. Strictly speaking the distance travelled and hence time spent by the same nuclide in

the same charge state from two different FRS settings is different, but only by a few nanoseconds; this effect is neglected. In the data there are cases of nuclides that have both been populated initially fully stripped changing to H-like after the mid focus, $(F - H)$, and the reverse case of H-like changing to fully stripped, $(H - F)$. The time-of-flight for the first and second halves of the FRS are similar ($ToF_{1^{st}} \sim 150$ ns *c.f.* $ToF_{2^{nd}} \sim 170$ ns). To reduce the error from counting statistics these two different in-flight charge states have been approximated to be synonymous and so their data has been combined.

From all of the nuclei populated for measurement in this experiment, those which have been observed to decay isomerically are discussed in the following two sections. Discussion will begin with isomers that have been measured previously followed by isomers that have been observed for the first time in this work. In each of these two sections the nuclei will be discussed in order, from the largest Z to the smallest and then by heaviest to lightest isotope. At the start of the discussion for each nuclide a full break down of the settings from which the statistics have been gathered are stated.

6.3 A Problem with the ^{206}Hg and ^{203}Ir Settings

Before beginning the spectroscopy discussion, an electronic problem encountered on the experiment needs to be discussed. The FRS settings focused on ^{206}Hg and ^{203}Ir were the first two to be recorded. At this point in time the Digital Gamma Finder (DGF) modules were set to record γ ray information for their supposed maximum time range, 500 μs, following implantation. Due to a bug in the internal software of the devices they actually operated for a range of only ~ 85 μs. This was realised only after recording data for these two settings. At this stage the modules were corrected for the remainder of the experiment so that they operated for up to 380 μs, which was the maximum actually achievable.

In cases where a nuclide is populated in the ^{206}Hg or ^{203}Ir settings and one or more others this issue limits the analysis to either taking the full statistics for 85 μs or some of the statistics for 380 μs.

6.4 Spectroscopy of Previously Reported Isomers

Most of the nuclei have been analysed in the same fashion, with a few stated exceptions. The first nucleus to be examined, ^{206}Tl, includes an explanation of the analysis method.

6.4.1 Exemplifying the Analysis Method: ^{206}Tl

Setting	Charge state	Number of nuclei implanted
^{206}Hg	H-like → He-like	85,924

This nuclide was transmitted in $(H - He)$ charge states. The proportion of the secondary beam particles with this many electrons is small, but in this case this is balanced by the large production cross section of this less exotic nucleus. On the identification plot (figure 5.11 (top left)) this nuclide deviates from the expected distribution pattern, which is a strong indication that it has different charge properties to the other nuclei on the plot. It has already been discussed that this nucleus has been unavoidably carved into two parts when selecting charge states (see section 5.2), both parts of this data have been combined together now.

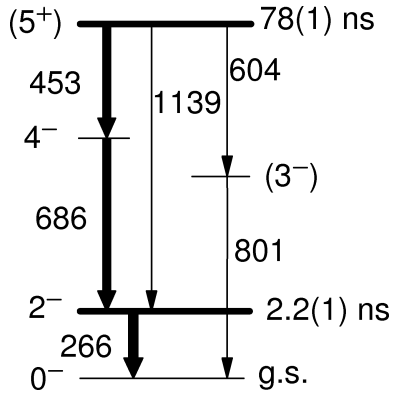

Figure 6.3: Partial level scheme for ^{206}Tl. Relative widths of parallel decay branches indicate the intensity of branches of decay. The decay scheme is taken from reference [89]

Two isomers have previously been reported in ^{206}Tl (see figure 6.3). These are an $I^{\pi} = 2^{-}$ isomer with a measured half-life of 2.2 ns and an $I^{\pi} = 5^{+}$ isomer with a half-life of 78 ns [89]. Notice that although the $I^{\pi} = 2^{-}$ state is isomeric, it is too

short-lived to be observed without the presence of the $I^{\pi} = 5^{+}$ state in the present work. It has been considered to decay immediately following the $I^{\pi} = 5^{+}$ state in the current analysis.

The γ Rays and how they are Selected

When producing a γ ray energy spectrum for any of the nuclei presented in this thesis both the Short Range (SR) and Digital Gamma Finder (DGF) times are considered. They are each plotted against the γ-ray energies (E_{γ}). The DGF modules record γ-ray emissions for up to 380 μs with 25 ns resolution, the SR devices record for up to 850 ns with 0.293 ns resolution (note that the SR efficiency is reduced proportionally with reducing γ-ray energy, see section 4.7 for details). It has been found from the analysis that the isomers with half-lives up to $\sim$ 175 ns are better observed using the SR devices due to their finer temporal resolution, in spite of their reduced efficiency at low energies. At 100 keV with the DGF modules it has been measured in this work that the prompt flash has a $FWHM$ of $\sim$ 300 ns. Transitions from isomers of half-lives similar to or less than 75 ns cannot at all be separated from the prompt flash when using the DGF devices.

Examples of E_{γ} versus time DGF matrices have already been shown in figures 6.1 and 6.2. For completeness a matrix of E_{γ} versus time (SR) is now presented for ^{206}Tl. With the improved temporal resolution of the SR, one is able to greatly reduce the apparent width of the prompt flash. The full width half maxima of the flash with SR devices is $\sim$ 20 ns at energies $>$ 400 keV. Keeping this width as small as possible is critical in observing the shortest-lived of the observed isomers from this experiment.

A region can be selected from the γ-ray energy vs. detection time matrix plots (such as the red line indicates in figure 6.4) which is used to optimise the observation of isomer transitions when projecting the data on the energy or time axes. This region has been determined by eye. Due to the Ge time walk effect, in cases where the isomer is short-lived, such as here for ^{206}Tl, the initial time channel is energy dependent. The asymmetric polygon allows for the removal of the entire prompt flash even at low energies, where the walk effect distorts the time axis. The γ-ray energy spectrum associated with this nuclide (figure 6.6) is a direct projection from the red region.

When making timing measurements, such as the inset plot in figure 6.6, the same red polygon region as for the energy spectrum is used, there is now an additional se-

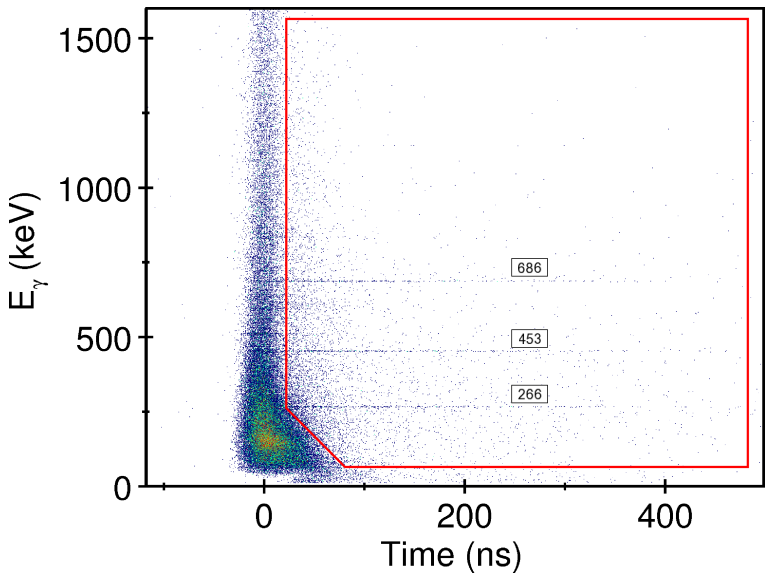

Figure 6.4: A plot of γ-ray energy vs. time (SR) after implantation for $^{206}\mathrm{Tl}_{(H-He)}$. The red line indicates the region of data used for analysis, see text.

lection on the γ-ray transition energies; for time measurements the initial time channel must be the same for all of the γ-rays. A background subtraction is made on this selection. Due to the nature of this experiment, the statistics are few when performing γ-ray analysis (typically $\sim$ hundreds to thousands per spectrum). To ensure a low variance from the background subtraction, regions both directly higher and lower in energy than the transition energy and usually each 5 times wider than the transition energy peak, are selected. This is the background region for each transition. It is normalised and then it is subtracted channel by channel from the time curve of the γ ray peak. Error bars are assumed to be Gaussian in each channel ($\sqrt{N}$) and are combined in quadrature for the peak and background data regions. An example of this technique (taken from the data for ^{206}Tl) is shown in figure 6.5. The resulting time curve is measured by the "least squares" fitting procedure. The shortest-lived of the isomers observed in this work have half-lives comparable in magnitude to the width of the $FWHM$ of the Ge detectors. These isomers have been fitted in an identical way to all of the other isomers measured in this work (i.e. by a pure exponential decay). In section 6.4.9 the previously reported $I^\pi = 7^-$ isomer in ^{200}Pt is used as an example to justify the validity of this approach in place of an exponentially modified Gaussian decay curve.

The Ge walk effect must be considered for the shorter-lived isomers. For γ-rays

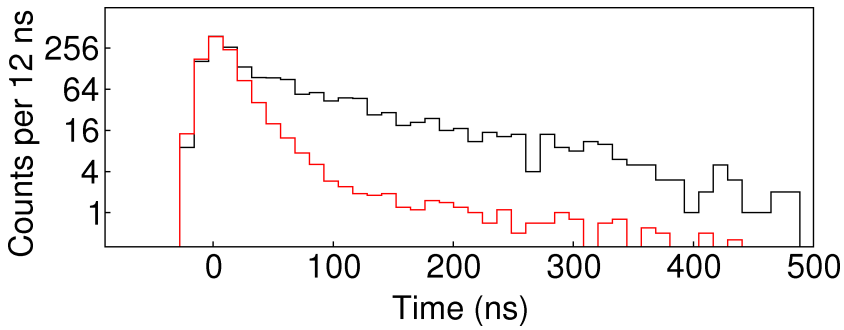

Figure 6.5: Example of the technique for extracting isomer half-lives. The 266, 453 and 686 keV transitions of ^{206}Tl are used here. The black curve is the data for the transitions plus the background; the red curve is the normalised background region.

approximately $\geq$ 250 keV the time data can be combined. For lower energies the time distortion effects from walk require that the time curves each be measured separately. Whenever a time curve is presented in this thesis the γ-rays used to produce it are stated in the figure caption to ensure clarity. For long-lived isomers the time distortion due to the walk is negligible. Better statistical accuracy for time measurements is achieved by combining the data of all transitions in these cases.

The described process for extracting γ-ray energies and associated decay times has been used to produce figure 6.6. The γ-rays associated with ^{206}Tl observed in this work are consistent with previous measurements [89]. Observed are a 266, 453 and 686 keV transition; the previously reported weak competing branches are not. In this experiment the isomer half-life has been measured to be $T_{1/2} = 71(4)$ ns. This is consistent with the accepted value of $T_{1/2} = 78(1)$ ns [89].

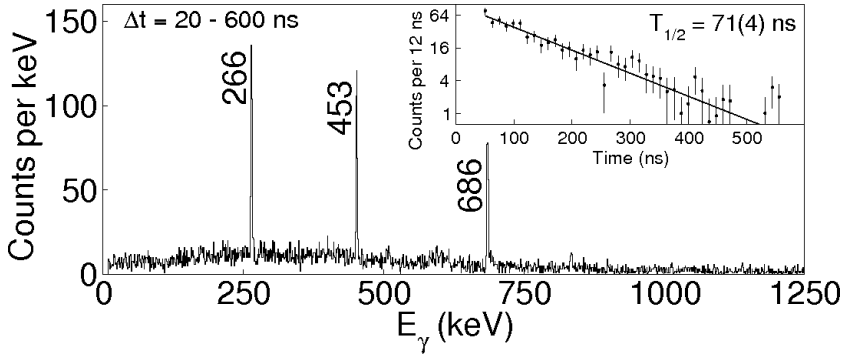

Figure 6.6: Gamma rays associated with ^{206}Tl using the DGF devices. The inset decay curve comes from all three γ-ray peaks.

The Conditions for Measuring an Isomeric Ratio

Where possible, isomeric ratios have been measured. This can be limited when the decay scheme, internal conversion coefficient or transition multipolarity are not known to sufficient detail. The isomeric ratio is measured separately for each of the transmitted charge states. In this ^{206}Tl case, only one charge state was transmitted. When applicable the mean isomeric ratio between charge states is quoted.

With stated exceptions, the half-life of isomers as reported in this work is always used for isomeric ratio measurements. A weighted mean of the intensity of all of the decay transitions that take place during the measuring time is used. This is done by extracting the absolute intensity of each measured γ ray peak, with corrections for branching and internal conversion and then by taking a weighted mean of the values. For cases where the individual γ-ray measuring times begin at different points in time due to the Ge walk effect an average t_i is taken (this is the variable t_i from equation 4.5). The isomeric ratio of the $I^\pi = 5^+$ isomer in ^{206}Tl is given in Table 6.1. The error bars are asymmetric due to the unmeasured losses from reactions taking place upon implantation (see section 4.8 for details). While accounting for internal conversion in-flight, when electrons are present the K_α coefficient for the neutral atom has been used regardless of whether one or two electrons are attached to the nucleus (see section 2.6.3 for details on this).

Table 6.1: Measured isomeric ratio of the $I^\pi = 5^+$ isomer in ^{206}Tl.

Charge state	**Isomeric ratio (%)**
$\boldsymbol{I^\pi = 5^+}$	
H-like → He-like	14.2^{+21}_{-32}

There is also a previously reported higher-lying, yrast $I^\pi = 12^-$ isomer in ^{206}Tl with $T_{1/2} = 3.74(3)$ min [89]. It is plausible that this state will have been populated during the experiment, however the isomer is too long-lived to detect directly. There are other nuclides that are described in this chapter for which two or more isomers have been measured to decay. In all cases the convention for the isomeric ratios written in the tables of this work is such that the isomeric ratio of the lower-lying state is

inclusive of the feeding from the higher-lying isomer. In the relevant text for each table a subtraction for the feeding from the higher isomer is quoted. In this instance as the $I^{\pi} = 12^{-}$ isomer is not measured in the current work, no account is made for it.

6.4.2 ^{206}Hg

Setting	Charge state	Number of nuclei implanted
^{206}Hg	Fully stripped → Fully stripped	1,393,025
^{206}Hg	Fully stripped → H-like	323,972

As has been stated, two isomers have been previously identified in this nuclide [31, 87, 88]. The two isomers have been measured to have half-lives $T_{1/2} = 2.15(21)$ μs for the $I^{\pi} = 5^{-}$ state and $T_{1/2} = 92(8)$ ns for the $I^{\pi} = (10^{+})$. A partial level scheme for ^{206}Hg is given in figure 6.7.

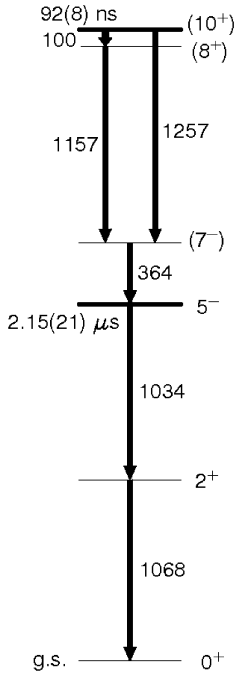

Figure 6.7: A partial decay scheme for ^{206}Hg as proposed in reference [31].

Observed γ Rays

The γ-rays associated with ^{206}Hg nuclei are displayed in figure 6.8. All of the observed γ-ray energies (100, 364, 1034, 1068, 1157 and 1257 keV) are consistent with

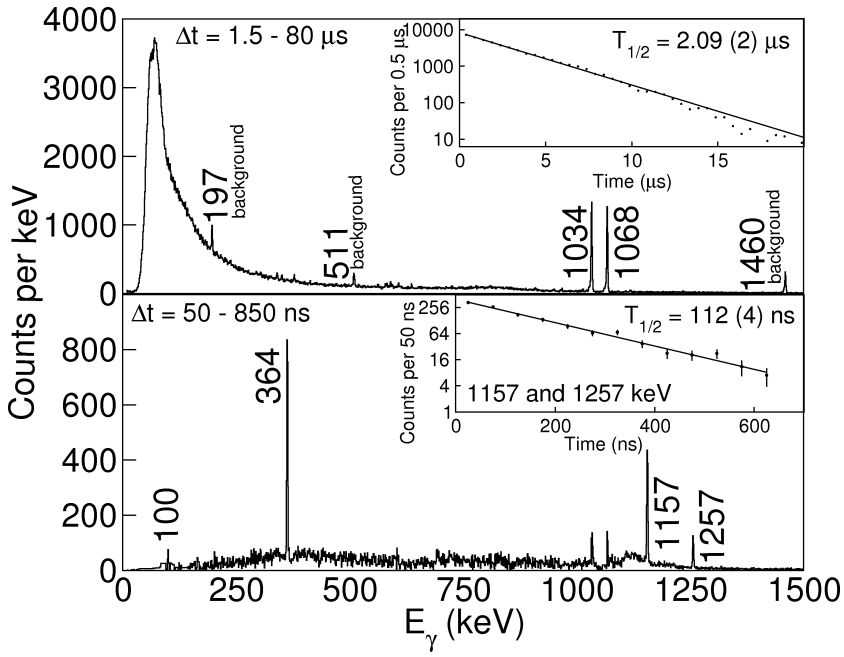

Figure 6.8: Gamma rays associated with ^{206}Hg using the DGF devices. **Top and bottom** : energy spectra for specified time ranges. **Insets** : decay curves of the γ-ray peaks. The top inset is from 1034 and 1068 keV transitions, the bottom is from the 1157 and 1257 keV.

the previously reported work on this nuclide by Fornal *et al.* [31]. This experiment has directly observed the 100 keV transition, this was not possible from the obtained data of the previous observation of this isomer [31]. Note that in figure 6.8 (bottom) a subtraction has been made to the energy spectrum, this is only for visual purposes, all extraction of information from this data is made prior to the background subtraction. The subtraction was made with an energy-time region of identical size to the original, but translated to a point in time many half-lives after implantation. The γ-ray intensity of the new region is normalised to the intensity of the 5^- isomer before subtraction.

The half-lives of the two isomers have been measured in the present work. For the $I^\pi = 5^-$ isomer a half-life of $T_{1/2} = 2.09(2)$ μs is extracted, this is consistent with the previously reported value of $T_{1/2} = 2.15(21)$ μs [31, 87, 88]. The half-life of the $I^\pi = (10^+)$ isomer is determined in the current work to be $T_{1/2} = 112(4)$ ns. In the previous experiment by Fornal *et al.* it was measured to be $T_{1/2} = 92(8)$ ns [31].

Isomeric Ratios

The isomeric ratio of the $I^\pi = 5^-$ isomer (as given in Table 6.2) includes events which first decay through the $I^\pi = (10^+)$ state and then decay through the $I^\pi = 5^-$ state. The isomeric ratio of the $I^\pi = 5^-$ state is measured to be 19.5^{+14}_{-30} % after subtracting for the feeding of the $I^\pi = (10^+)$ isomer, which is measured to have a ratio of 2.2^{+7}_{-8} %.

Table 6.2: Measured isomeric ratios of the $I^\pi = 5^-$ and (10^+) isomers in ^{206}Hg.

Charge state	**Isomeric ratio (%)**
$\boldsymbol{I^\pi = 5^-}$	
Fully stripped → Fully stripped	21.9^{+11}_{-28}
Fully stripped → H-like	21.8^{+13}_{-29}
Mean	21.9^{+12}_{-29}
$\boldsymbol{I^\pi = (10^+)}$	
Fully stripped → Fully stripped	1.9^{+5}_{-6}
Fully stripped → H-like	2.5^{+8}_{-10}
Mean	2.2^{+7}_{-8}

A warning is given regarding the $I^\pi = (10^+)$ isomer isomeric ratio. After accounting for experimental uncertainties, the observed γ-ray intensity of the 364 keV transition is significantly less than the sum of the 1157 and 1257 keV transitions (see Table 6.31 for details on the intensities). They are expected to be the same. Currently the weighted average of all three of the transitions is used for determining the number of observed decays of the isomer. By excluding the 364 keV transition (or vice verse) the $I^\pi = (10^+)$ isomeric ratio is affected. It increases to $(F - F)$ 2.7^{+7}_{-9} and $(F - H)$ 3.5^{+12}_{-15} % or decreases to $(F - H)$ 1.7^{+4}_{-6} and $(F - H)$ 2.1^{+7}_{-9} % when excluding the 364 keV or the 1157 and 1257 keV transtions, respectively. This γ-ray intensity issue has not been definitively explained, but it is possible that the walk effect has reduced the apparent 364 keV intensity.

6.4.3 ^{205}Hg

Setting	Charge state	Number of nuclei implanted
^{206}Hg	Fully stripped → Fully stripped	339,544
^{206}Hg	Fully stripped → H-like	77,494

For ^{205}Hg both a previously reported [90] and an isomer observed for the first time have been detected in this experiment. The newly discovered isomer is discussed in section 6.5.1. In this section only the previously observed $I^{\pi} = 13/2^{+}$ isomer [90–92] is detailed. This isomer has previously been measured to have a half-life of 1.09(4) ms. The decay scheme for the relevant transitions is already confirmed. The relevant part of the previously known scheme for ^{205}Hg is shown in figure 6.9.

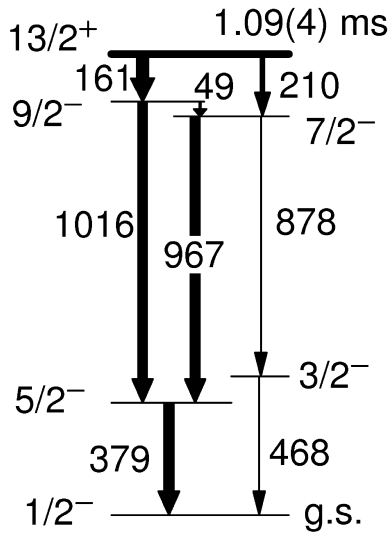

Figure 6.9: A partial decay scheme for ^{205}Hg. Relative widths of decay branches indicate branching ratios. This decay scheme is taken from references [90–92].

Observed γ Rays

The data for ^{205}Hg arises from the ^{206}Hg setting where the maximum timing window is limited to ~ 85 μs (see section 6.3). The long half-life combined with the short timing window forbade accurate measurement of the half-life of this $I^{\pi} = 13/2^{+}$ isomer. The 379, 967 and 1015 keV γ ray transitions, which follow the isomer decay are shown in figure 6.10. This spectrum is contaminated by ^{206}Hg, indicating that

the particle selection gates overlap. Because ^{206}Hg is populated to such a large degree it is not possible to entirely remove it from nuclides that reside next to it on the identification plots in figure 5.11 (top left and bottom right). Indicated in figure 6.10 are the later to be discussed (see section 6.5.1) γ rays of the newly discovered isomer.

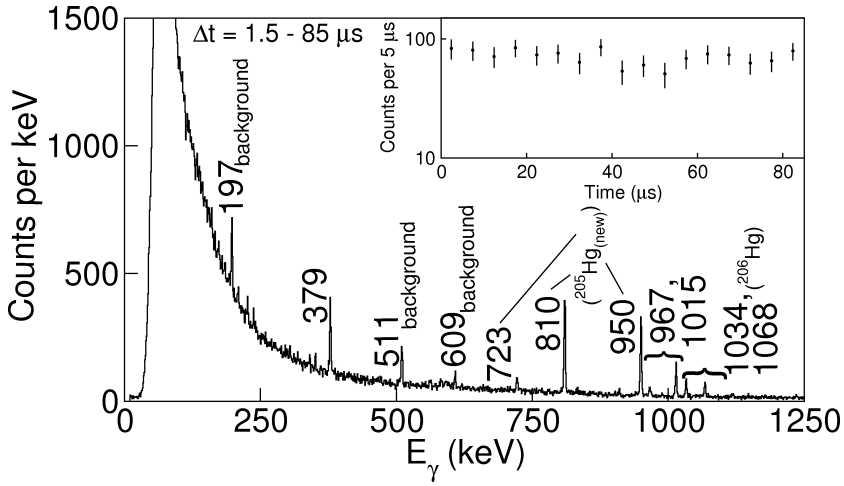

Figure 6.10: Gamma rays associated with ^{205}Hg for 85 μs following implantation using the DGF devices. The inset decay curve comes from the 379, 967 and 1015 keV γ rays.

Note that the weak parallel branches are not intense enough to be identified in the present work. The two transitions that directly depopulate the isomer (161 and 210 keV) are low in energy and highly converted (α=12.0 and 2.7, respectively). For these reasons they have not been detected. The X-rays have not been observed either, this is due to the large background.

Isomeric Ratio

The isomeric ratio for the $I^\pi = 13/2^+$ state in ^{205}Hg is given in Table 6.3. In this case the previously measured half-life of 1.09(4) ms [90–92] has been used for the measurement. After subtracting the effect of feeding from the newly observed isomer (see section 6.5.1) the $I^\pi = 13/2^+$ isomer isomeric ratio becomes 17.2^{+25}_{-40} %.

Table 6.3: Measured isomeric ratio of the $I^\pi = 13/2^+$ isomer in ^{205}Hg.

Charge state	**Isomeric ratio (%)**
$I^\pi = 13/2^+$	
Fully stripped → Fully stripped	19.3^{+19}_{-34}
Fully stripped → H-like	21.6^{+31}_{-47}
Mean	20.5^{+25}_{-40}

6.4.4 ^{204}Hg

Setting	**Charge state**	**Number of nuclei implanted**
^{206}Hg	Fully stripped → H-like	2,550
^{206}Hg	H-like → H-like	40,753

An $I^\pi = 7^-$ isomer has been reported in this nuclide previously [93, 94]. It has a measured half-life of 6.7(5) ns and the decay scheme is established (the relevant part of that scheme is shown in figure 6.11). It decays through a 110 keV $E1$ transition, which has a total internal conversion coefficient of $\alpha = 0.3$. The nuclei excited directly into this isomeric state cannot remain in it long enough to transmit through the FRS, even if the isomeric ratio were 100 %.

Observed γ Rays

The γ-ray energy spectrum in figure 6.12 shows that the $I^\pi = 7^-$ isomer has in fact been detected in the current work. No other isomers are known to exist in this nuclide. This implies the detection of a previously unobserved isomer. This newly seen isomer is discussed in detail in section 6.5.2. Note that the presently measured half-life of the known 437, 692 and 1063 keV transitions is $T_{1/2} = 38(8)$ ns (assuming a pure, single-component exponential decay). This is significantly different from the previous measurements of the half-life of the $I^\pi = 7^-$ isomeric state reported in references [93, 94], further suggesting that a higher-lying isomer has been populated.

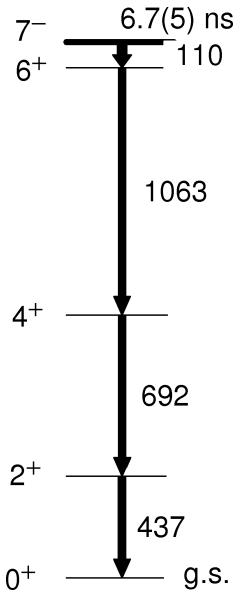

Figure 6.11: A partial decay scheme for ^{204}Hg. Relative widths of decay branches indicate branching ratios.

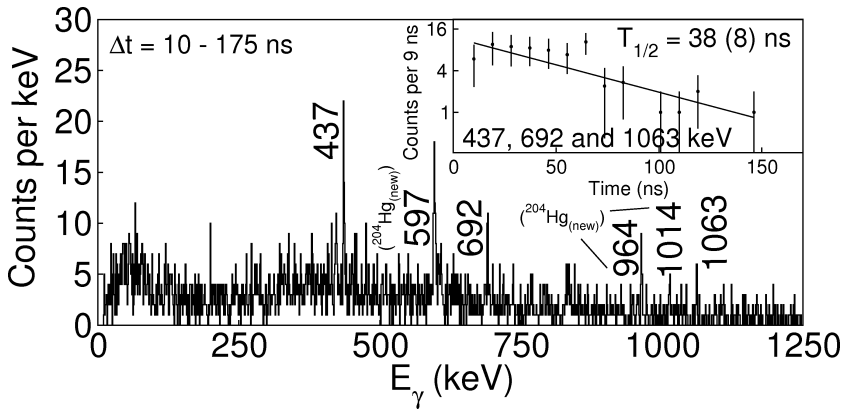

Figure 6.12: Gamma rays associated with ^{204}Hg following implantation using the DGF devices. The inset decay curve comes from the 437, 692 and 1063 keV transitions.

6.4.5 ^{203}Hg

Setting	Charge state	Number of nuclei implanted
^{206}Hg	H-like → H-like	128,294
^{206}Hg	H-like → He-like	13,854

The previously observed $I^\pi = (13/2^+)$ isomer in ^{203}Hg [92,95] has been detected in this experiment. This isomer has similarities to the one seen in ^{205}Hg (see section 6.4.3).

This is understandable in terms of systematics. To first order, the low-lying structure of both nuclides is governed only by the unpaired neutron-hole. A partial decay scheme for ^{203}Hg is shown in figure 6.13.

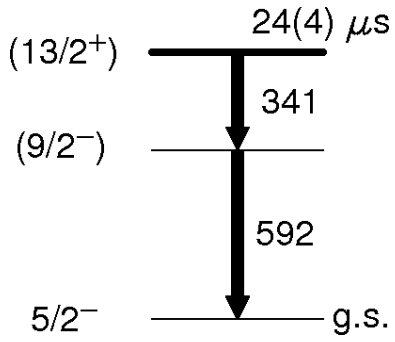

Figure 6.13: A partial decay scheme for ^{203}Hg. This is taken from references [92, 95].

Observed γ Rays

The γ-ray spectrum measured in the current work for ^{203}Hg is presented in figure 6.14. The two γ rays, which decay from the $I^{\pi} = (13/2^{+})$ isomer (341 and 592 keV) are detected, along with X-rays predominantly from the internal conversion branch of the 341 keV $13/2^{+} \rightarrow 9/2^{-} M2$ transition($\alpha = 0.94$). The statistics in this experiment are higher than for the previous investigations. Prior to this experiment the accepted half-life was $T_{1/2} = 24(4)$ μs [92, 95]. The value deduced in the current work is $T_{1/2} = 21.9(10)$ μs.

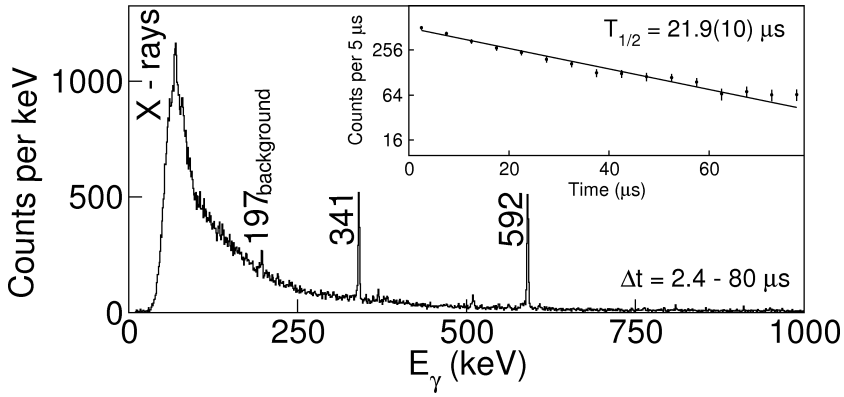

Figure 6.14: Gamma rays associated with ^{203}Hg following implantation using the DGF devices. The inset decay curve comes from both the 341 and 592 keV γ rays.

Isomeric Ratio

The isomeric ratio of the $I^{\pi} = (13/2^{+})$ isomer has been measured. Table 6.4 gives the ratio for the two transmitted charge states. The mean isomeric ratio between the two is 11.8^{+7}_{-15} %.

Table 6.4: Measured isomeric ratio of the $I^{\pi} = (13/2^{+})$ isomer in ^{203}Hg.

Charge state	**Isomeric ratio (%)**
$\boldsymbol{I^{\pi} = (13/2^{+})}$	
H-like → H-like	14.2^{+9}_{-20}
H-like → He-like	9.3^{+12}_{-19}
Mean	11.8^{+11}_{-20}

6.4.6 ^{203}Au

Setting	**Charge state**	**Number of nuclei implanted**
^{206}Hg	Fully stripped → Fully stripped	401,961

A γ-ray transition has previously been observed in this nuclide [54]. The isomer from which it arises has been measured to have a half-life of 40^{+7000}_{-20} μs. Although levels in the decay scheme from earlier work had established a part of the low-lying states [96], the observed transition could not be placed in the scheme.

Observed γ Rays

Spectroscopy of ^{203}Au in the current experiment has observed the previously reported isomer, the γ-ray energy spectrum is presented in figure 6.15 (top). The half-life of the isomer is determined to be $T_{1/2} = 140(44)$ μs in the current work.

It has not been possible to place the observed transition in the decay scheme. In the previous investigation the $11/2^{-}$ state was highlighted as a candidate for being isomeric in nature [54]. Given that this state has an excitation energy of 641 keV [96,97], it is plausible that there are one or more low energy unobserved transitions, which feed

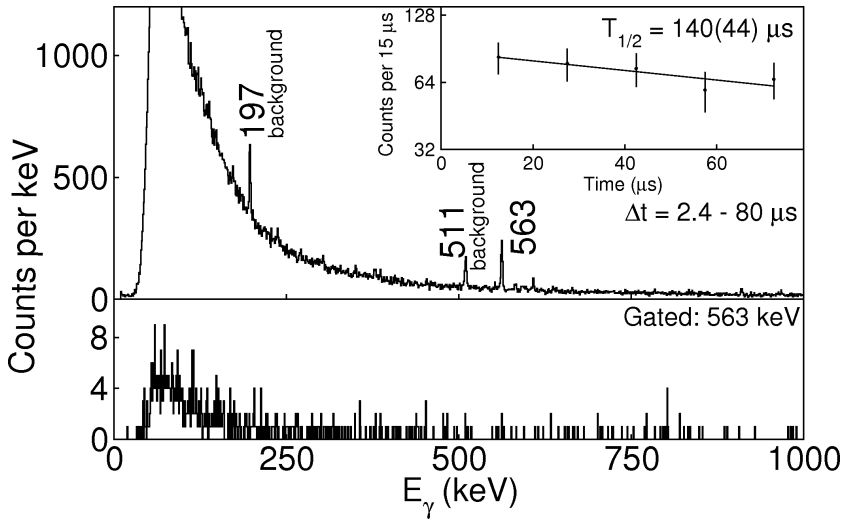

Figure 6.15: Gamma rays associated with ^{203}Au following implantation using the DGF devices. **Top:** gamma-ray singles events. **Bottom:** Gamma rays observed within 1 μs of the 563 keV transition. The inset decay curve comes from the 563 keV γ ray.

or decay from the known 563 keV transition. Figure 6.15 (bottom) is the first instance of γ-γ coincidence analysis in this document. The improved peak-to-total ratio of γ-γ analysis is intended to highlight any low-energy transitions that there might be in the background Compton continuum. By performing γ-γ analysis one improves the peak-to-total ratio of the γ ray peaks, however reduces the overall statistics. Figure 6.15 (bottom) shows all events identified as ^{203}Au where one of the Ge crystals has already observed a 563 keV transition. The spectrum shows the energy signals received by all of the remaining Ge crystals. Despite the improved peak-to-total ratio, no other γ-ray transitions have been observed.

Isomeric Ratio

It is not possible to properly measure an isomeric ratio for an isomer without understanding which transition directly depopulates the isomer and without knowing the internal conversion coefficients for transitions. However for isomers that are much longer-lived than the FRS flight time, and where the transitions are of high energy, internal conversion is a small factor. In Table 6.5 an isomeric ratio has been given assuming the 563 keV has an internal conversion coefficient, $\alpha = 0$. This isomeric ratio also assumes that the branching ratio of the 563 keV transition is 100 %. The isomeric

ratio measured in the presnet work (2.5^{+8}_{-10} %) is consistent with the Caamaño *et al.* measurement [54], which reports value of > 1 %.

Table 6.5: Measured isomeric ratio of the isomer in ^{203}Au, assuming that the 563 keV transition depopulates the isomer and that the branching ratio of the transition is 100 % and $\alpha = 0$.

Charge state	**Isomeric ratio (%)**
$\boldsymbol{I^{\pi}} = \textit{unknown}$	
Fully stripped → Fully stripped	2.5^{+8}_{-10}

6.4.7 ^{202}Pt

Setting	**Charge state**	**Number of nuclei implanted**
^{206}Hg*	Fully stripped → Fully stripped	2,543
^{203}Ir*	Fully stripped → Fully stripped	165,916
^{199}Os	Fully stripped → Fully stripped	31,697
^{203}Ir*	Fully stripped → H-like	30,980
^{199}Os	Fully stripped → H-like	105,229
^{192}W	Fully stripped → H-like	11,963
^{202}Os	H-like → H-like	2,032
^{192}W	H-like → He-like	4,164

**Gamma-ray detection time reduced from 380 to 85 μs for this setting.*

This nuclide has had spectroscopic information measured in one previous experiment only [54]. In that experiment three γ-ray transitions were observed. A tentative decay scheme has been created, however the transitions and spin-parities of the states are not confirmed. This level scheme is shown in figure 6.16.

This nuclide is one that is strongly affected by the software difficulties with the DGF modules (see section 6.3). This means that 56 % of the data recorded γ-ray information for 85 μs, while the remaining 44 % correlated for up to 380 μs. The isomer in ^{202}Pt has previously been measured to have a half-life $T_{1/2} = 280^{+420}_{-190}$ μs.

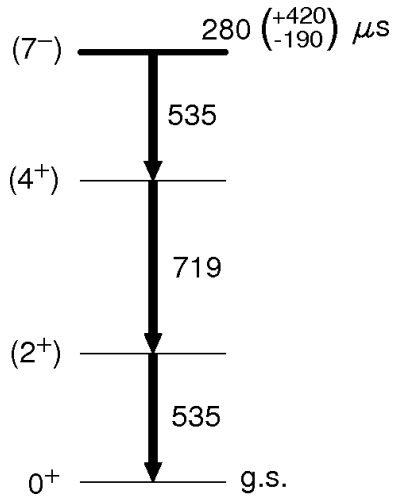

Figure 6.16: The ^{202}Pt decay scheme, taken from reference [54].

In this work the isomer is measured by considering only the 44 % of the data that correlates for 380 μs.

Observed γ Rays

The γ rays associated with ^{202}Pt are shown in figure 6.17 (top). Of the settings and charge states listed at the start of the current section of this document, only those indicated by a * are used for γ-ray spectroscopy. This observation of the excited states in ^{202}Pt in the current work is consistent with the previous measurement by Caamaño *et al.* [54]. The present observation of the isomer has a measured half-life of $T_{1/2} = 141(7)$ μs. For the observation of ^{202}Pt in the current work, γ-γ coincidence analysis has been preformed. These measurements confirm the doublet nature of the 534 keV peak (see figure 6.17 (bottom)).

Isomeric Ratio

The isomeric ratio for the presented $I^\pi = (7^-)$ isomer in ^{202}Pt is shown in Table 6.6. The mean isomeric ratio between the measured charge states is found to be 11.8^{+10}_{-19} %. In the work presented by Caamaño *et al.* there was a large uncertainty on the half-life. This isomeric ratio was found to be > 15 %.

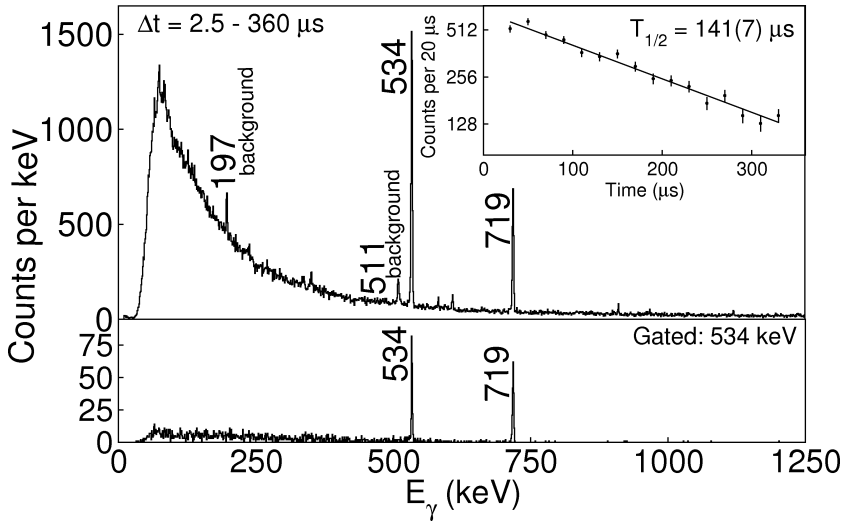

Figure 6.17: Gamma rays associated with ^{202}Pt following implantation using the DGF devices. **Top:** gamma-ray singles events. **Bottom:** gamma rays observed to be emitted within 200 ns of 534 keV γ-rays. The inset decay curve comes from the 534 (doublet) and the 719 keV γ rays.

Table 6.6: Measured isomeric ratio to the assigned $I^{\pi} = (7^{-})$ isomer in ^{202}Pt.

Charge state	**Isomeric ratio (%)**
$\boldsymbol{I^{\pi} = (7^{-})}$	
Fully stripped → Fully stripped	12.0^{+9}_{-17}
Fully stripped → H-like	12.0^{+5}_{-14}
Fully stripped → He-like	11.5^{+17}_{-26}
Mean	11.8^{+10}_{-19}

6.4.8 ^{201}Pt

Setting	**Charge state**	**Number of nuclei implanted**
^{206}Hg	Fully stripped → Fully stripped	27,546
^{199}Os	Fully stripped → Fully stripped	15,206
^{199}Os	Fully stripped → H-like	17,958
^{192}W	Fully stripped → H-like	6,897
^{192}W	Fully stripped → He-like	1,045
^{202}Os	H-like → H-like	463

This nuclide has been previously studied by Caamaño *et al.* [54]. A tentative decay scheme for this nuclide was proposed, this is shown in figure 6.18. The isomer is proposed to decay through an unobserved, $E_\gamma \leq 90$ keV $E2$ transition. The half-life was measured to be $T_{1/2} = 21(3)$ ns.

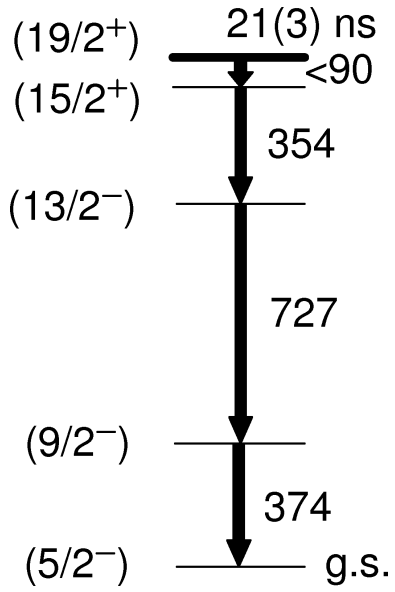

Figure 6.18: The ^{201}Pt decay scheme, taken from reference [54].

Observed γ Rays

The current measurement of ^{201}Pt has less statistics than the study of Caamaño *et al.*, however comparing the two, the current work takes advantage of improved spectroscopic measuring power. Due to this, the level of background radiation is reduced. The γ-ray spectrum for ^{201}Pt for the present work is shown in figure 6.19 (top). The 353, 374 and 727 keV γ rays are observed, but the expected low-energy $E2$ transition is not. The half-life of the isomer is measured to $T_{1/2} = 18.4(13)$ ns, consistent with the value by Caamaño *et al.* $T_{1/2} = 21(3)$ ns [54].

The γ-γ coincidence investigation has not extracted the possible unobserved transition. In figure 6.19 (bottom) all of the three previously reported transitions (353, 374 and 727 keV) are identified and shown to be in coincidence.

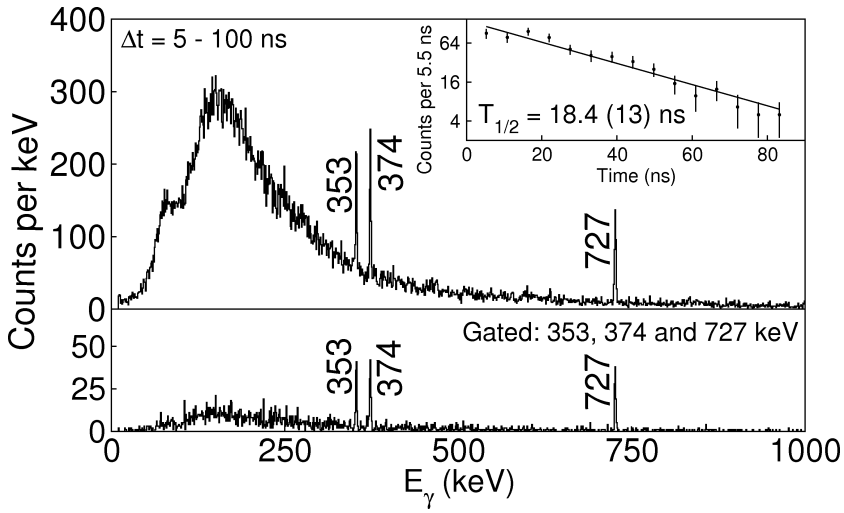

Figure 6.19: Gamma rays associated with ^{201}Pt following implantation using the SR devices. **Top:** gamma ray singles events. The inset decay curve is from the sum of the 353, 374 and 727 keV transitions. **Bottom:** gamma rays observed in the same event as any of the three transitions.

Isomeric Ratio

The level scheme is largely understood for this $I^{\pi} = (19/2^{+})$ isomer, but the internal conversion coefficient for the unobserved transition is not known. A limit is set on the isomeric ratio.

Making the extreme assumption that zero decays take place in-flight, the isomeric ratio would be 3.6^{+15}_{-17} % and 3.8^{+16}_{-19} % for the $(F-F)$ and $(F-H)$ states, respectively. These average to 3.7^{+2}_{-4} %. The zero decay approximation is true in the limit of large α (i.e. dramatically extending the in-flight half-life). If the unobserved $E2$ transition has something similar to $\alpha \geq 500$, then this is the case. H-like nuclei have traversed the second half of the FRS. An internal conversion coefficient of $\alpha = 500$ for an $E2$ transition corresponds to a transition energy of $E_{\gamma} = 37$ keV, which is below the threshold energy for K_{α} conversion. In this limit H-like nuclei would be equally as inhibited as fully stripped nuclei. For transition energies ≤ 37 keV, the isomeric ratio is 3.7^{+15}_{-18} %. The Caamaño *et al.* work finds this isomeric ratio to be > 32 %.

At the opposing extreme, an isomeric ratio of 100 % corresponds to a transition energy of 140(126) keV. It is apparent that energies of ≥ 200 keV would have been directly observed in the presented spectrum. In the previous experiment it was concluded that the transition energy is ≤ 90 keV.

Table 6.7: Lower limit for the isomeric ratio of the $I^{\pi} = (19/2^{+})$ isomer in ^{201}Pt. This assumes $\alpha \geq 500$ for the isomer-depopulating transition.

Charge state	**Isomeric ratio (%)**
$\boldsymbol{I^{\pi} = (19/2^{+})}$	
Fully stripped → Fully stripped	$\geq 3.6^{+15}_{-17}$
Fully stripped → H-like	$\geq 3.8^{+16}_{-19}$
Mean	$\geq 3.7^{+15}_{-18}$

6.4.9 ^{200}Pt

Setting	**Charge state**	**Number of nuclei implanted**
^{206}Hg	Fully stripped → Fully stripped	62,963
^{192}W	Fully stripped → H-like	1,703

Excited states have been measured in this nucleus on three previous occasions [54, 98,99]. These works have observed two isomers in cascade and have confirmed a number of the spin-parities of low-lying yrast excited states. A partial level scheme for ^{200}Pt from these works is presented in figure 6.20. The character of the transition that depopulates the $I^{\pi} = (12^{+})$ isomer is ambiguous; it is suggested that it can be limited to $E1$ or $E2$ character.

Observed γ Rays

Both of the previously reported isomers in this nuclide have been seen in the current work. The previously reported half-lives of the two isomers are comparable in magnitude with the $FWHM$ of the Ge detectors. In the current work the half-lives are measured using a pure exponential decay after the Ge prompt Gaussian rise has reduced in significance. The application of this fitting method in place of an exponentially modified Gaussian decay (EMG) is now justified.

The spectrum in figure 6.21 shows the background subtracted time data recorded for the 463 and 470 keV γ-ray transitions that follow the decay of the $I^{\pi} = (7^{-})$ isomer from the time of implantation until 200 ns later. Note that $t = 0$ corresponds

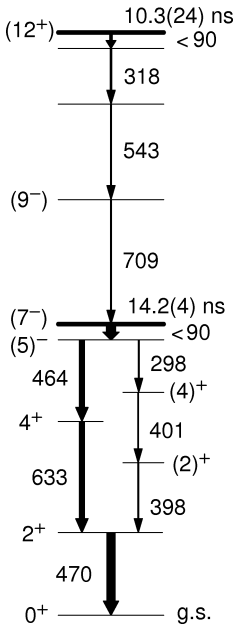

Figure 6.20: A partial ^{200}Pt decay scheme, taken from reference [54].

to the *centroid* arrival time of the prompt flash γ rays. An EMG accounts for both the exponential isomer decay and the uncertainty of arrival time of each recorded γ-ray [100]. The shape of this EMG convolution can be expressed visually with the numerical expression;

$$\begin{aligned} I(t) =& A\ exp\left[0.5\left(\frac{\sigma_G}{\tau}\right)^2\right]\ .\ exp\left[-\frac{(t-t_G)}{\tau}\right] \\ &\times\left[erf\left(\frac{1}{\sqrt{2}}\left(\frac{t_G}{\sigma_G}+\frac{\sigma_G}{\tau}\right)\right)+erf\left(\frac{1}{\sqrt{2}}\left(\frac{t-t_G}{\sigma_G}-\frac{\sigma_G}{\tau}\right)\right)\right] \end{aligned} \tag{6.1}$$

where $I(t)$ is the intensity of observed γ rays at time t; A is a normalising constant; σ_G and t_G are the uncertainty on the width and the centroid of the Gaussian, respectively; τ is the mean lifetime of the isomer; and erf is the mathematical error function [101]. The actual fit of the EMG to the data is performed with a convolution of the exponential and Gaussian functions using the Nanofit program [102]. Equation 6.1 is used for visual purposes only. The EMG fit measures a half-life of $T_{1/2} = 16.6(6)$ ns for the $I^\pi = (7^-)$ isomer (see figure 6.21). When fitting the data for the range $\Delta t = 10 \rightarrow 200$ ns (i.e. when the Gaussian component reduces its significance) with a pure exponential decay curve the half-life is measured to be $T_{1/2} = 17.0(5)$ ns. These two fits are consistent.

The previous reports of the half-life of this isomer are $T_{1/2} = 14.0(6)$ ns [54] and $T_{1/2} = 14.3(6)$ ns [99].

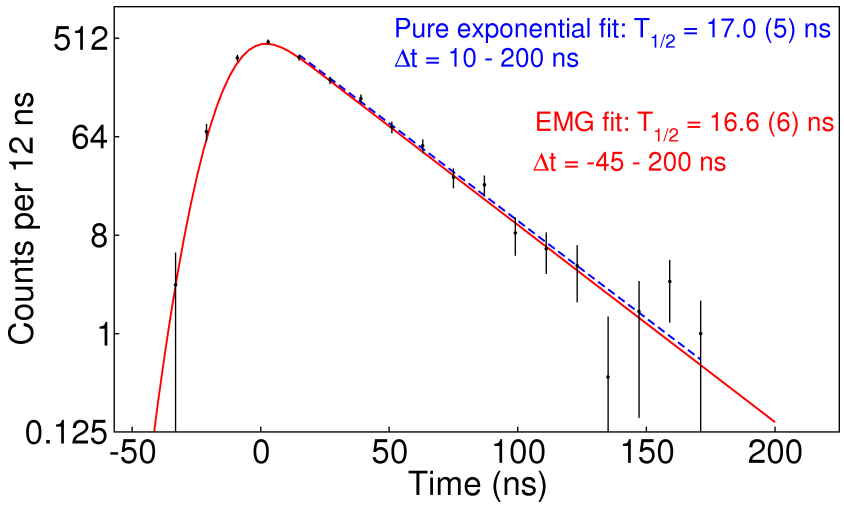

Figure 6.21: Comparison of the EMG and pure exponential fitting routines. The data is background subtracted and taken from the 463 and 470 keV transitions following the decay of the $I^{\pi} = (7^{-})$ isomer in ^{200}Pt. The pure exponential curve (marked in blue) is fitted only over the range $\Delta t = 10 \rightarrow 200$ ns.

Prompt flash radiation dominates the "Gaussian regime" of the decay curve introducing large uncertainties, therefore for less strongly populated isomers observed in the present work with half-lives similar to this case of the $I^{\pi} = (7^{-})$ isomer in ^{200}Pt, poor statistics introduce large uncertainties for the EMG method resulting in there being no unique fit for the half-life. In all cases the pure exponential fit can resolve a unique solution. Even when the EMG fit is applicable, for internal consistency in this work the method of half-life fitting is always with a pure exponential curve after the Ge prompt Gaussian reduces in significance (i.e. at $t \geq 10$ ns).

The $I^{\pi} = (12^{+})$ isomer fitted with a pure exponential decay curve is found in reasonably good agreement with the previous study. In this work the half-life is measured to be $T_{1/2} = 13.9(10)$ ns, compared to the previous value of $T_{1/2} = 10.3(24)$ ns [54]. This is shown in the spectrum in figure 6.22, along with the γ-ray energy data.

Isomeric Ratio

The spectroscopy did not observe the anticipated, but previously unseen, transitions (i.e. those responsible for directly depopulating the isomers). Beginning with

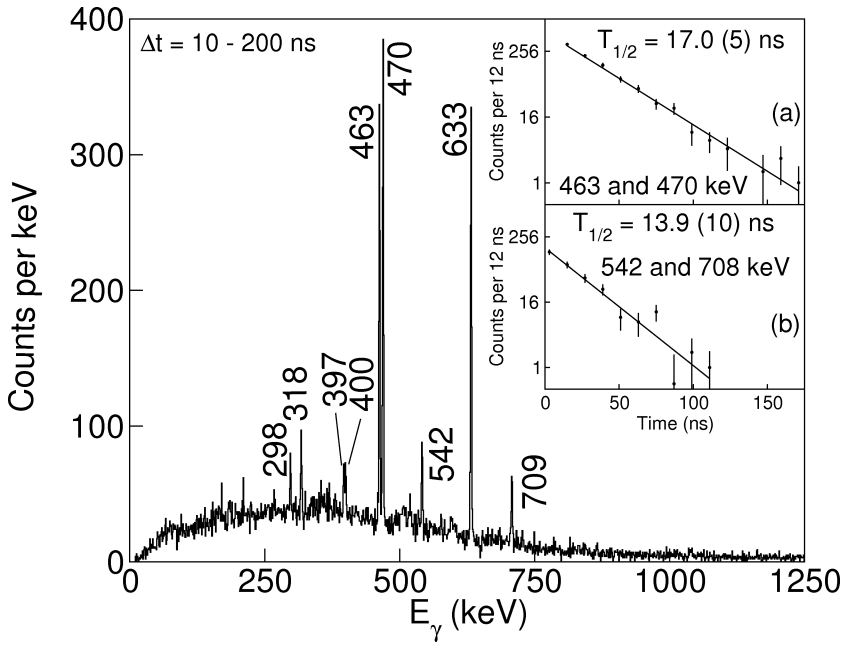

Figure 6.22: Gamma rays associated with ^{200}Pt following implantation using the SR devices. The inset decay curves show the half-lives of the two isomers, The upper inset is the data from the 463 and 470 keV transitions, the lower is from the 542 and 708 keV data.

the higher-lying ($I^\pi = (12^+)$) isomer, a lower limit on the population ratio can be set by assuming zero decays prior to implantation. In this case this would require a total internal conversion coefficient to be approximately ≥ 900, corresponding to an isomeric ratio lower limit of 1.9^{+12}_{-14} %, as tabulated in Table 6.8. The multipolarity is still unconfirmed for this isomer-depopulating transition. Assuming it is of $E2$ character, the limit on the ratio corresponds to a transition energy of < 33 keV. Examining the isomeric ratio upper limit of 100 %, the maximum energy for an $E2$ transition is 121 keV. Assuming the isomer-deopulating transition is of $E1$ character, the transition energy could only be up to a few keV. From investigating γ-ray intensities, the lower-lying, $I^\pi = (7^-)$, isomer is 3.75(1) times more intensely populated than the $I^\pi = (12^+)$ isomer at the time of implantation.

It was previously stated that the energies of the unobserved transitions are ≤ 90 keV [54]. It is presently thought that for the $I^\pi = (12^+)$ isomer this limit is incorrect, in this work it is found to be ≤ 121 keV. Caamaño *et al.* quote limits on the isomeric ratios of > 25 and > 4 % for the $I^\pi = (7^-)$ and (12^+) states, respectively.

Table 6.8: Lower limit for the isomeric ratio of the $I^{\pi} = (12^{+})$ isomer in ^{200}Pt. This assumes 100 % transmission of the isomer in-flight.

Charge state	**Isomeric ratio (%)**
$\boldsymbol{I^{\pi} = (12^{+})}$	
Full Strip → Full Strip	$\geq 1.9^{+12}_{-14}$

6.4.10 ^{198}Pt

Setting	**Charge state**	**Number of nuclei implanted**
^{206}Hg	H-like → Fully stripped	24,269

This β-stable nuclide has been studied in numerous other experiments [7]. This nuclide is the only one in the ^{206}Hg setting, $\Delta q = +1$ charge state identification plot (see figure 5.11 (bottom right)) to have a previously reported isomeric state [93, 103]. There are other isomers observed in that identification plot, which are observed for the first time in this experiment, however none of them are identified elsewhere in the current work. This means that the ^{198}Pt isomer confirms the identification of its setting and charge state.

Observed γ Rays

The γ rays associated with ^{198}Pt in this work are shown in the spectrum in figure 6.23. The observed 382, 407 and 578 keV γ rays have previously been reported to follow the decay of a $(I^{\pi} = 7^{-})$ isomer [93] with a half-life of $T_{1/2} = 3.4(2)$ ns. It is directly depopulated by a 134.9(1) keV transition with a total internal conversion coefficient $\alpha = 1.51$. Even with a high level of electron stripping, direct excitations of this isomer would not be expected to transmit through the FRS. In the present work it is concluded that a second previously reported isomer [104, 105] in ^{198}Pt is also populated in this experiment. Its reported half-life is $T_{1/2} = 36(2)$ ns [105] and it has been suggested that this isomer is of spin $I = (12)$, at an excitation energy of 3017.4(12) keV [106]. Each of the γ-rays that have previously been reported to be emitted following the decay of the $I = (12)$ isomer [105, 106] have been found to be

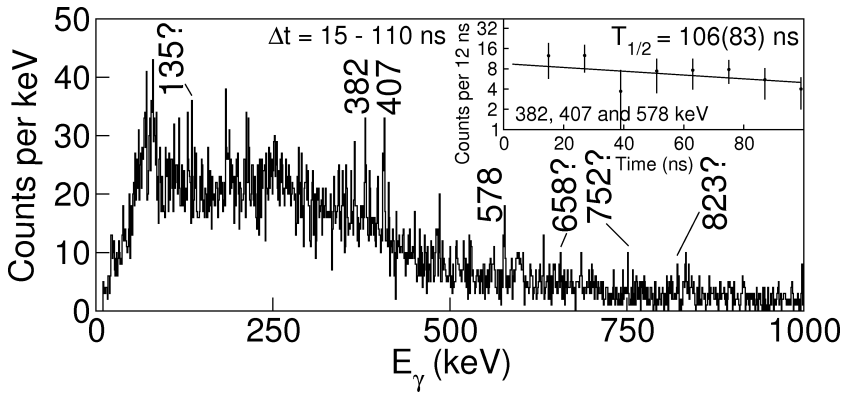

Figure 6.23: Gamma rays associated with ^{198}Pt following implantation using the SR devices, the peaks marked with a ? are uncertain. The inset decay curve is taken from the 382, 407 and 578 keV transitions.

significantly less intense than the 382, 407 and 578 keV transitions. In figure 6.23 of the present work some of these γ-ray transitions (135, 752 and 823 keV) have been tentatively identified. In this work the half-life of the 382, 407 and 578 keV transitions is measured to be $T_{1/2} = 106(83)$ ns assuming a single-component, pure exponential decay. This is consistent with the $I = (12)$ isomer being populated, allowing for the transmission of excited states of ^{198}Pt through the FRS.

6.4.11 ^{199}Ir

Setting	Charge state	Number of nuclei implanted
^{203}Ir	Fully stripped → Fully stripped	54,601
^{199}Os	Fully stripped → Fully stripped	196,253
^{203}Ir	Fully stripped → H-like	8,049
^{199}Os	Fully stripped → H-like	34,905
^{192}W	Fully stripped → H-like	63,814
^{202}Os	H-like → Fully stripped	689
^{192}W	Fully stripped → He-like	1,090

Caamaño *et al.* [54] tentatively identified an isomer in ^{199}Ir. In the current work, higher γ-ray statistics have been recorded for this nuclide. A search has taken place for the previously suggested isomer, but it has not been observed in the currently described experiment. The γ-ray spectrum in figure 6.25 spans an identical time range following

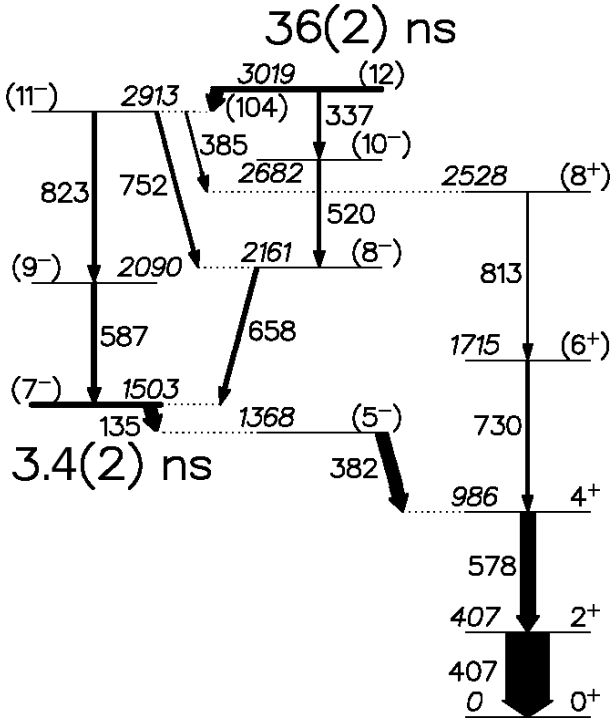

Figure 6.24: A partial ^{198}Pt decay scheme. The relative width of parallel branches are an indication of the decay intensity. This decay scheme is taken from reference [106].

implantation as Caamaño *et al.*. Previously γ rays were speculatively identified at 104, 112, 122 and 162 keV, but there is no evidence for these photopeaks in the present work.

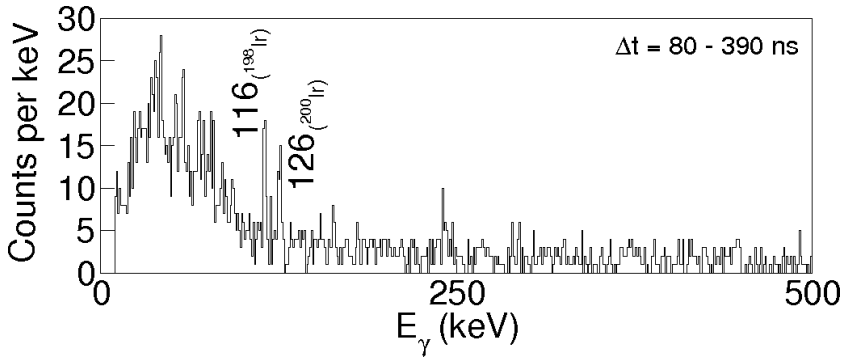

Figure 6.25: Gamma rays associated with ^{199}Ir following implantation using the SR devices. The selected time range is the same as that from the previous study in reference [54].

6.4.12 ^{198}Ir

Setting	Charge state	Number of nuclei implanted
^{199}Os	Fully stripped → Fully stripped	28,028
^{199}Os	Fully stripped → H-like	4,964
^{192}W	Fully stripped → H-like	17,065
^{202}Os	H-like → Fully stripped	1,275
^{192}W	Fully stripped → He-like	376

An isomer has previously been seen in ^{198}Ir by Caamaño *et al.* [54]. Only one transition was observed, it was measured to have a half-life of $T_{1/2} = 77(9)$ ns. Although no level scheme was suggested, it was proposed that the transition was likely to be $E1$ in nature, based on the lack of X-rays and the application of hindrance factors.

Observed γ Rays

The present work has performed a repeat measurement on the half-life of the isomer. The observed transition is shown in figure 6.26. The half-life of the isomer is measured to be $T_{1/2} = 73(11)$ ns, consistent with the previous value of $T_{1/2} = 77(9)$ ns.

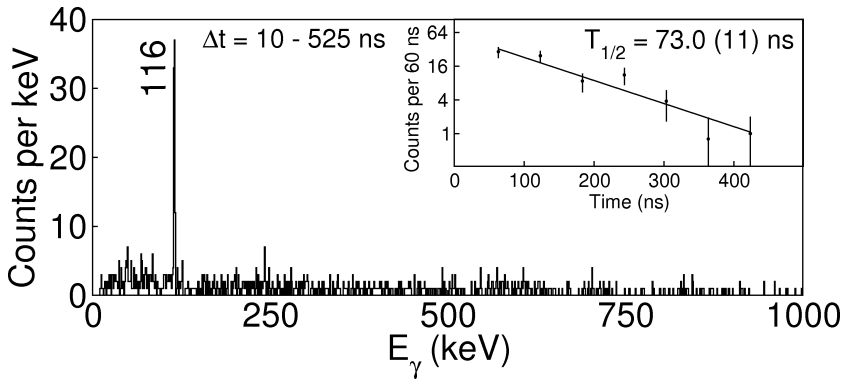

Figure 6.26: Gamma rays associated with ^{198}Ir following implantation using the SR devices. The inset decay curve is fitted using the 116 keV transition.

Isomeric Ratios

The level scheme of this nuclide is not known, but the isomeric ratio is measured under the assumption that, as previously suggested, the γ ray decay is $E1$ in nature.

For this nuclide Caamaño *et al.* measure the isomeric ratio to be 19^{+5}_{-3} %. The present result (see Table 6.9) and that of Caamaño *et al.* are not consistent.

Table 6.9: Measured isomeric ratio of the $I^{\pi} = (7^{-})$ isomer in ^{198}Ir, assuming the isomer is depopulated by an $E1$ decay.

Charge state	**Isomeric ratio (%)**
$\boldsymbol{I^{\pi} = (7^{-})}$	
Fully stripped → Fully stripped	4.3^{+30}_{-33}
Fully stripped → H-like	6.5^{+38}_{-43}
Mean	5.4^{+34}_{-38}

6.4.13 ^{195}Os

Setting	**Charge state**	**Number of nuclei implanted**
^{199}Os	Fully stripped → Fully stripped	10,144
^{192}W	Fully stripped → Fully stripped	4,938
^{192}W	Fully stripped → H-like	5,862
^{203}Ir	H-like → Fully stripped	799
^{202}Os	H-like → Fully stripped	537

This nuclide has been studied previously by Caamaño *et al.* [54]. It has also been observed through deep inelastic collisions on a ^{198}Pt target [104]. The level scheme has not been established. The 439, 493 and 533 keV transitions are in cascade, see γ-γ coincidence results by Valiente-Dobón *et al.* [104]. The 714 keV transition is suggested to have a different intrinsic structure to the other γ rays. This indicates that it is the transition which directly depopulates the isomer, however it has been noted that its high energy implies a small internal conversion coefficient. Since the isomer half-life was measured as $T_{1/2} = 26(4)$ ns, a large degree of internal conversion is required in order to transmit the isomer through the FRS. It is thus likely that there is an unobserved transition. The observation of the isomer from Valiente-Dobón *et al.* [104] using deep-inelastic heavy ion collisions has measured a half-life of $T_{1/2} = 26(9)$ ns.

Observed γ Rays

The current experiment has observed the same four γ ray transitions as the previous studies (438, 493, 533 and 714 keV). This is shown in the spectrum of figure 6.27. Over this time range, there is limited sensitivity to X- or γ- ray transition energies approximately lower than 250 keV. The isomer half-life is currently found to be $T_{1/2} = 34.0(23)$ ns.

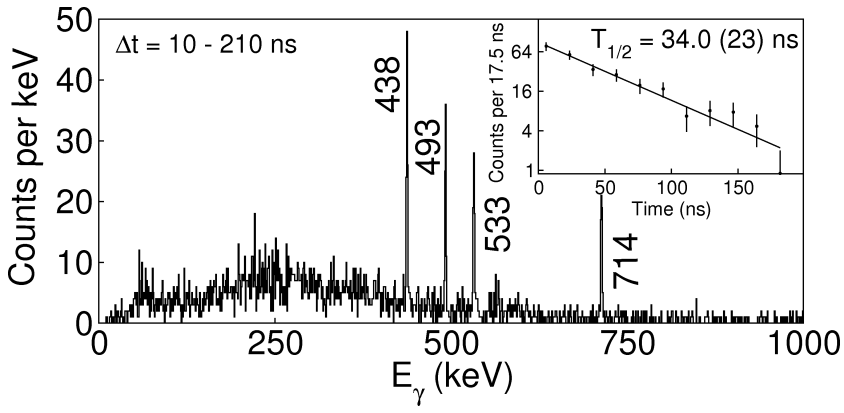

Figure 6.27: Gamma rays associated with ^{195}Os following implantation using the SR devices. The inset decay curve is produced using the 438, 493, 533 and 714 keV transitions.

Isomeric Ratios

As it is currently understood that the isomer-depopulating transition has not been observed, only limits are placed on the isomeric ratio. Assuming that zero decays take place until implantation, the minimum isomeric ratio is 2.4^{+7}_{-8} % for the $(F-F)$ charge state; it is 2.3^{+7}_{-9} % for the combined $(F-H)$ and $(H-F)$ states. This gives a mean minimum of 2.4^{+7}_{-9} % (se Table 6.10). The Caamaño *et al.* work suggests a limit of > 13 %. The current study again disagrees with this. The limit of zero decays in-flight corresponds to a transition with an internal conversion coefficient approximately $\alpha \geq 100$. The assumption is now made that the unobserved, isomer-depopulating transition is of $E1$ character (as explained in the thesis of M. Caamaño [107] using BCS calculations). Given this, it is implied that for transition energies $E_\gamma \leq 50$ keV the isomeric ratio reaches its lower limit of 2.4^{+3}_{-5} %.

Examining the other extreme, for an isomeric ratio of 100 %, the internal con-

Table 6.10: Measured limit on the isomeric ratio of the isomer in ^{195}Os, assuming 100 % transmission of the isomer.

Charge state	**Isomeric ratio (%)**
$\boldsymbol{I^{\pi} = unknown}$	
Fully stripped → Fully stripped	$\geq 2.4^{+7}_{-8}$
Fully stripped → H-like	$\geq 2.3^{+7}_{-9}$
Mean	$\geq 2.4^{+7}_{-9}$

version coefficient is $\alpha \sim 0.1$. For the 714 keV transition to have internal conversion coefficients of this size, but it would require it to be of at least $M3$ or $M4$ character, which is unlikely For an assumed $E1$ transition, an isomeric ratio of 100 % corresponds to an upper limit on the transition energy of 170 keV.

6.4.14 ^{194}Re

Setting	**Charge state**	**Number of nuclei implanted**
^{203}Ir	Fully stripped → Fully stripped	8,762
^{199}Os	Fully stripped → Fully stripped	34,391
^{192}W	Fully stripped → Fully stripped	48,813
^{192}W	Fully stripped → H-like	7,478
^{185}Lu	Fully stripped → H-like	1,753

Caamaño *et al.* [54] also observed this nuclide; but the presence of an isomer was only very tentatively suggested. No time curve was fitted due to poor statistics, possible transitions were identified at 61, 70, 128 and 148 keV.

Observed γ Rays

The current work confirms the existence of the tentatively assumed isomer. There are however differences between the previously suggested transitions and those that are currently identified. In figure 6.28, γ rays associated with ^{194}Re are shown in the range $\Delta t = 2 \rightarrow 50$ μs. Peaks are observed at 61, 69 and 86 keV. The 61 keV transition is

clearly observed; this matches the energy of K_α X-rays of rhenium. The weaker 69 keV peak also matches the K_β X-ray energy. The current work also identifies a peak at 86 keV, which was not reported in the Caamaño *et al.* work. The previously noted candidate transitions at 128 and 148 keV have not been observed presently. The half-life of the 61 keV X-rays and the 86 keV transition is measured to be $T_{1/2} = 45(18)$ μs.

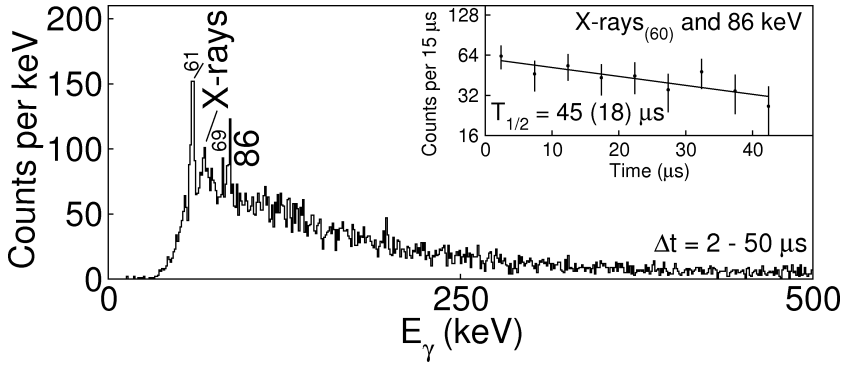

Figure 6.28: Gamma rays associated with ^{194}Re following implantation using the DGF devices. The inset decay curve comes from the 61 keV K_α X-rays and the 86 keV transition.

6.4.15 ^{193}Re

Setting	Charge state	Number of nuclei implanted
^{203}Ir	Fully stripped → Fully stripped	709
^{199}Os	Fully stripped → Fully stripped	23,164
^{192}W	Fully stripped → Fully stripped	54,031
^{192}W	Fully stripped → H-like	8,190
^{185}Lu	Fully stripped → H-like	1,334
^{203}Ir	H-like → Fully stripped	2,952

Excited states in this nuclide have been reported previously by Caamaño *et al.* [54]. The previous measurement identified K_α and K_β X-rays along with a single γ-ray transition at 146 keV. The half-life of the isomer was measured to be $T_{1/2} = 75^{+300}_{-40}$ μs. The upper limit of the half-life was derived by assuming an isomeric ratio of 100 %. No level scheme was suggested.

Observed γ Rays

In this experiment the previously reported [54] X-rays and the γ-ray transition have been observed. Figure 6.29 shows the spectroscopic findings. The half-life of the K_α X-ray combined with the 145 keV γ ray is measured to be $T_{1/2} = 65(9)$ μs, consistent with the previously measured half-life.

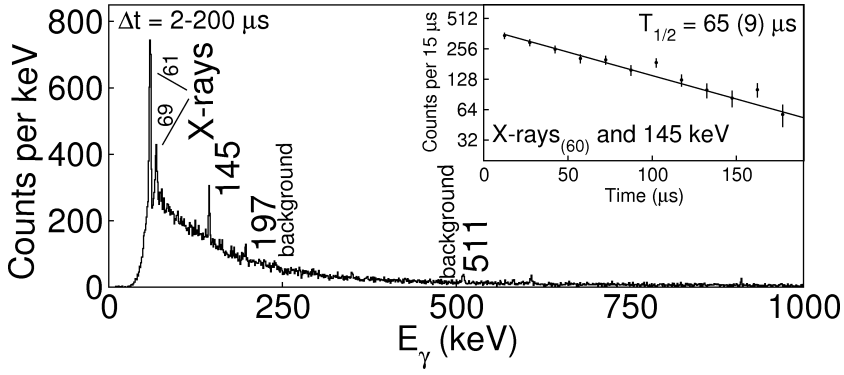

Figure 6.29: Gamma rays associated with ^{193}Re following implantation using the DGF devices. The inset decay curve arises from the 61 keV X-rays and the 145 keV transition.

Isomeric Ratio

This isomer is long-lived compared to the flight time; losses due to decays in-flight are thus not an issue. The multipolarity of the observed γ-ray transition is ambiguous. If it directly depopulates the isomer then lifetime arguments suggest it to be of $M2$ or possibly $E2$ character. It is possible however, that there is a low-energy, unobserved transition. Knowledge of any "unobserved" transition is critical in determining the isomeric ratio. Measurement has been made in this work assuming that the 145 keV transition directly depopulates the isomer first assuming it to be an $M2$ and then to be an $E2$ transition, see Table 6.11. The Caamaño *et al.* suggested a limit of > 19 % for the isomeric ratio, it is not clear to the author if this assumes an $M2$ or $E2$ decay of the isomer through the 145 keV transition or if it assumed that an unobserved transition directly depopulates the isomer.

Table 6.11: Measured isomeric ratio of the isomer in ^{193}Re, assuming the 145 keV transition is of $M2$ or $E2$ character and directly depopulates the isomer with a 100 % branching ratio.

Charge state	**Isomeric ratio (%)**
$\boldsymbol{I^{\pi} = unknown}$ (assuming $M2$ decay)	
Fully stripped → Fully stripped	18.9^{+25}_{-39}
Fully stripped → H-like	12.9^{+50}_{-52}
Mean	15.9^{+40}_{-52}
$\boldsymbol{I^{\pi} = unknown}$ (assuming $E2$ decay)	
Fully stripped → Fully stripped	2.9^{+4}_{-6}
Fully stripped → H-like	2.0^{+8}_{-10}
Mean	2.4^{+6}_{-8}

6.4.16 ^{192}Re

Setting	**Charge state**	**Number of nuclei implanted**
^{199}Os	Fully stripped → Fully stripped	3,868
^{192}W	Fully stripped → Fully stripped	12,214
^{192}W	Fully stripped → H-like	1,908
^{203}Ir	H-like → Fully stripped	4,998

This is another nuclide studied previously, excited states have been reported by Caamaño *et al.* [54]. A single γ ray (160 keV) and also K_{α} and K_{β} X-rays were observed, the isomer half-life was measured to be $T_{1/2} = 120^{+210}_{-50}$ μs. The 160 keV transition was suggested to be of $M1$ character based on intensity balances between the γ ray and the X-rays and by then considering this balance in terms of internal conversion coefficients. $E2$ and $M2$ transitions were also considered plausible. It is also noted that there may be a second transition, which is directly responsible for depopulating the isomer. This would be a low-energy ($\leq$50 keV) $E1$ transition.

Observed γ Rays

Currently the single γ ray at 160 keV and K-shell X rays have been observed consistent with the work in reference [54]. These findings are shown in figure 6.30. The half-life of this isomer is consistent with the previous measurement, in this instance it is found to be $T_{1/2} = 85(10)$ μs.

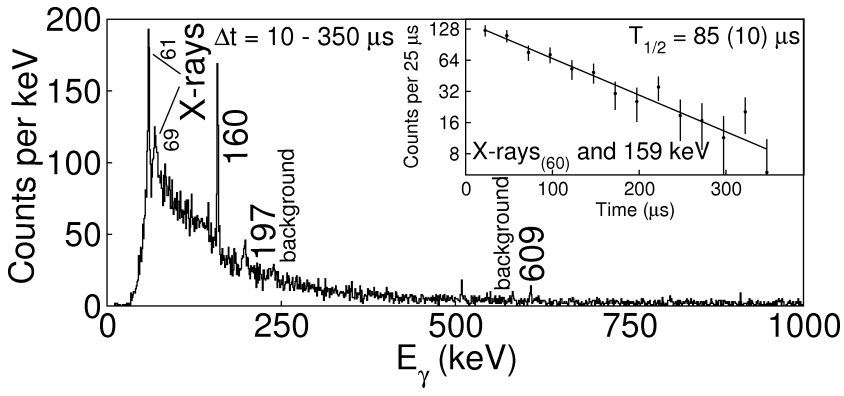

Figure 6.30: Gamma rays associated with ^{192}Re following implantation using DGF devices. The inset decay curve is fitted with the 61 keV X-rays and the 160 keV transition.

Isomeric Ratio

Under the explanation proposed by Caamaño *et al.* [54], the isomer-depopulating γ ray may be of low-energy and unobserved. It is suggested to be an $E1$ transition. The half-life of the isomer is long when compared to the flight time, which negates the influence of in-flight decays on the isomeric ratio. Assuming the unobserved transition is correctly assigned as of $E1$ character, this implies that the observed 160 keV transition is $M1$ (otherwise the observed X-ray intensity is not explained). Given the assumption that a low energy $E1$ transition feeds the $M1$ 160 keV transition, an isomeric ratio can be inferred. This is done in Table 6.12. This gives a mean isomeric ratio of 3.0^{+8}_{-10} %. Caamaño *et al.* measured this ratio to be 21^{+29}_{-7} %.

6.4.17 ^{191}Re

Setting	Charge state	Number of nuclei implanted
^{203}Ir	H-like → Fully stripped	2,372

Table 6.12: Measured isomeric ratio of the isomer in ^{192}Re; assuming that an unobserved low-energy $E1$ transition depopulates the isomer and then feeds the 160 keV transition, which is assumed to be of $M1$ character.

Charge state	**Isomeric ratio (%)**
$\boldsymbol{I^{\pi} = unknown}$	
Fully stripped → Fully stripped	3.5^{+5}_{-7}
Fully stripped → H-like	2.4^{+10}_{-12}
Mean	3.0^{+8}_{-10}

There has been an isomer tentatively identified by Caamaño *et al.* [54] in this nuclide. While no half-life was measured, discrete γ-ray emissions were observed over a 75 μs period. Ten energy peaks were tentatively identified, at energies of 53, 61, 69, 139, 159, 226, 308, 360, 419 and 444 keV.

Observed γ Rays

The current experiment confirms that the isomer exists (see figure 6.31). The previously noted 53, 308 and 360 keV transitions are not observed. In the current work, a single transition has been tentatively identified, at 135 keV, which was not reported previously. The intensity of the 69 keV peak is too great in comparison to the 61 keV peak for it to only arise from the K_{β} X-rays, suggesting that there may be a γ-ray transition with a near identical energy. An attempt has been made to fit a half-life curve to the current data. It is assumed that all of the currently noted transitions arise from a single isomer; statistics from all of them are used when producing the timing data. The half-life is measured to be $T_{1/2} = 77(33)$ μs.

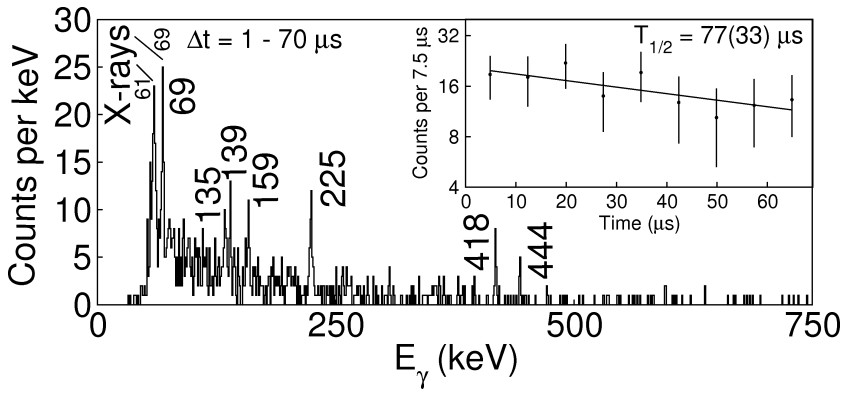

Figure 6.31: Gamma rays associated with ^{191}Re following implantation using the DGF devices. The inset decay curve is fitted with all of the transitions.

6.4.18 ^{190}W

Setting	Charge state	Number of nuclei implanted
^{199}Os	Fully stripped → Fully stripped	2,329
^{192}W	Fully stripped → Fully stripped	22,454
^{185}Lu	Fully stripped → H-like	889
^{203}Ir	H-like → Fully stripped	1,670
^{199}Os	H-like → Fully stripped	3,046

The isomer spectroscopy of this nuclide is not analysed here. It is presently being examined by G.F. Farrelly [108].

6.4.19 ^{188}Ta

Setting	Charge state	Number of nuclei implanted
^{192}W	Fully stripped → Fully stripped	11,395
^{185}Lu	Fully stripped → Fully stripped	1,561
^{185}Lu	Fully stripped → H-like	713
^{199}Os	H-like → Fully stripped	781

Excited states in this nuclide have been studied previously only by Caamaño *et al.* [54]. The study identified one γ-ray transition (at 292 keV) and no X-ray peaks were discernible in that work. Multiple possible explanations of the level scheme were

considered, but no firm conclusion was reached. It is possible that additional unobserved transitions are involved in the decay. If this is not the case, the decay of the isomer is understood to be of $E2$ character based on expected X-ray intensities and decay rates.

Observed γ Rays

The observation of the isomer in ^{188}Ta in the current work is comparable with that of reference [54] in terms of statistics. The measured half-life is found to be $T_{1/2} = 3.5(4)$ μs (see figure 6.32), consistent with the previously measured value of $T_{1/2} = 5(2)$ μs.

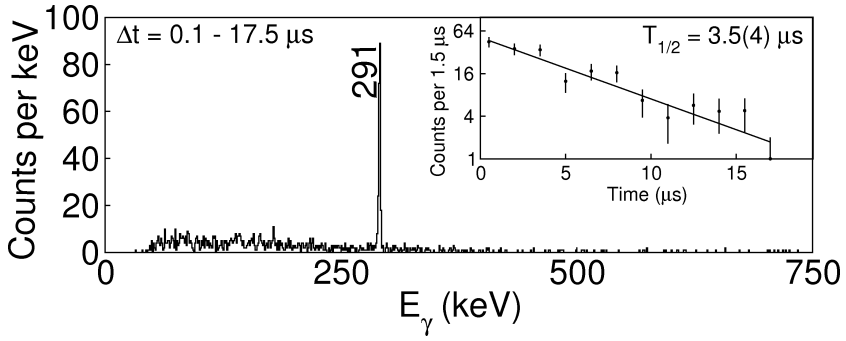

Figure 6.32: Gamma rays associated with ^{188}Ta following implantation using the DGF devices. The inset decay curve comes from the 291 keV transition.

Isomeric Ratio

Under the assumption that the observed 292 keV transition directly depopulates the isomer as an $E2$ decay, an isomeric ratio is extracted. This is done for both of the transmitted charge states, remember that the ^{188}Ta$_{(F-H)}$ and ^{188}Ta$_{(H-F)}$ transmitted charge states are considered synonymous and so combined (see section 6.2). The measured isomeric ratios are quoted in Table 6.13, the mean ratio is found to be 7.9^{+15}_{-21} %, the value obtained in reference [54] was $0.5^{+0.3}_{-0.1}$ %.

Table 6.13: Measured isomeric ratio of the isomer in ^{188}Ta, assuming that the observed transition is an $E2$ decay and that it directly depopulates the isomer.

Charge state	**Isomeric ratio (%)**
I^π = unknown	
Fully stripped → Fully stripped	7.9^{+9}_{-15}
Fully stripped → H-like	7.8^{+21}_{-27}
Mean	7.9^{+15}_{-21}

6.5 Spectroscopy of Previously Unreported Isomers

Shell model calculations have been performed to aid the interpretation of the measured previously unreported isomers nearest to and at $N = 126$. With stated exceptions, these calculations have all been performed by M. Górska [40], using the $s_{1/2}, d_{3/2}, h_{11/2}, d_{5/2}, g_{7/2}$ proton-hole space and $f_{5/2}, p_{1/2}, i_{13/2}, p_{3/2}, f_{7/2}, h_{9/2}$ neutron-hole space around the ^{208}Pb core with the OXBASH code. Single-particle/hole energies were taken from ^{207}Pb, ^{207}Tl and two-body matrix elements from reference [109]. These are based on the Kuo-Herling interaction and include core polarisation, but the decisive elements for the $I^\pi = 2^+$ and 5^- states of ^{206}Hg are adjusted.

6.5.1 ^{205}Hg

Setting	**Charge state**	**Number of nuclei implanted**
^{206}Hg	Fully stripped → Fully stripped	339,544
^{206}Hg	Fully stripped → H-like	77,494

Experimental Information

In addition to the $I^\pi = 13/2^+$ isomer of ^{205}Hg [90], a previously unreported isomer has been detected in the current experiment. The γ rays emitted following the isomer decay are shown in figure 6.33 (top). Four transitions have been identified (227, 723, 810 and 950 keV), which are all in mutual coincidence. No X-rays have been

detected. The measured half-life of the isomer (using the 810 and 950 keV transitions) is $T_{1/2} = 5.89(18)$ μs.

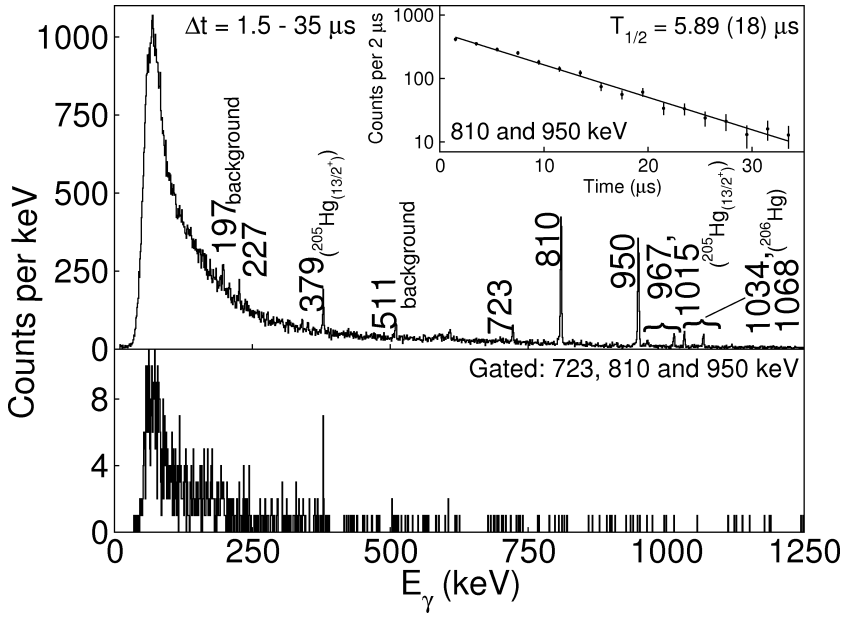

Figure 6.33: **Top:** gamma rays associated with ^{205}Hg following implantation using the DGF devices. The inset decay curve comes from 810 and 950 keV transitions. **Bottom:** gamma rays associated with ^{205}Hg observed at least 250 ns following detection of a 723, 810 or 950 keV γ ray for 80 μs following implantation.

The intensities of the 227 and 723 keV transitions are equal within experimental errors (see Table 6.31). The sum of their transition energies matches the energy of the observed 950 keV transition. The summed intensity of the 227 (or 723) keV transition and the intensity of the 950 keV transition matches the intensity of the 810 keV transition within experimental uncertainty. It can therefore be concluded that the 227 and 723 keV transitions decay in parallel to the 950 keV decay, with a branching ratio of 0.11:0.89(2), respectively (the order of the 227 and 723 keV transitions is not confirmed). These parallel branches feed or are fed by the 810 keV transition, again this ordering cannot be established in the current work.

Through time differentiated γ-γ coincidence analysis, it is proved that these four γ-ray transitions are higher-lying in the ^{205}Hg level scheme than those, which arise due to the $I^{\pi} = 13/2^{+}$ isomer. The proof for this comes from figure 6.33 (bottom), which selects events where the 723, 810 or 950 keV transitions are observed and then shows all of the γ-rays that are observed at least 250 ns later in time for up to 80 μs fol-

lowing implantation. Figure 6.33 (bottom) clearly shows coincidence with the 367 keV transition, which follows the decay of the $I^\pi = 13/2^+$ isomer.

Shell Model Calculation and Interpretation

A shell model calculation is given in figure 6.34 (left) for ^{205}Hg. Only the yrast and near yrast levels below 3.5 MeV and levels predicted to be higher lying than the $I^\pi = 13/2^+$ isomer are shown. The upper cut off derives from the sum energy of the observed γ-rays.

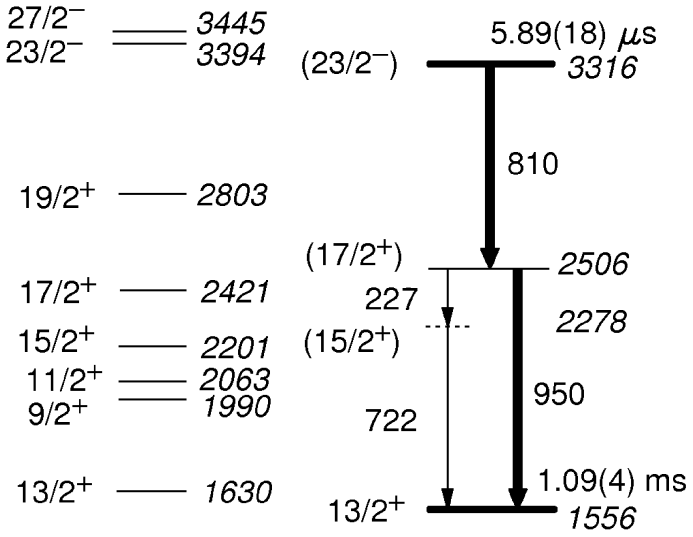

Figure 6.34: **Left:** A ^{205}Hg shell model calculation. Only yrast and near yrast levels that are above the known $I^\pi = 13/2^+$ isomer and below 3.5 MeV are presented. **Right:** The interpreted level scheme. The relative width of parallel γ-ray transitions indicates the intensity of the branch.

Assuming that this nuclides low-lying excitations can be treated as "near" single-particle in nature, there is a unique solution to the level scheme, which is presented in figure 6.34 (right). The isomer decays from the predicted $I^\pi = 27/2^-$ state by an 810 keV $E3$ transition. The measured lifetime corresponds to a reduced transition probability of $B(E3) = 0.35(1)$ W.u.. An $M2$ transition between the $I^\pi = 23/2^-$ and $19/2^+$ states of the same energy would have a reduced transition probability of $B(M2) = 4 \times 10^{-4}$; on this basis, it is discounted. The interpretation suggests that the transition between the $I^\pi = 17/2^+$ level and the $I^\pi = 15/2^+$ is the 227 keV γ ray. It is noted that for the suggested level scheme, the internal conversion coefficients are all <5 % of the total decay intensity, consistent with the lack of observed X-rays.

Isomeric Ratio

For the constructed level scheme, an isomeric ratio has been measured. This has been done for the two different transmitted charge states in Table 6.14. The mean isomeric ratio for this $I^{\pi} = (23/2^{-})$ isomer is 3.3^{+2}_{-4} %.

Table 6.14: Measured isomeric ratio of the $I^{\pi} = (23/2^{-})$ isomer in ^{205}Hg.

Charge state	**Isomeric ratio (%)**
$\boldsymbol{I^{\pi} = (23/2^{-})}$	
Fully stripped → Fully stripped	3.3^{+2}_{-4}
Fully stripped → H-like	3.3^{+3}_{-5}
Mean	3.3^{+2}_{-4}

6.5.2 ^{204}Hg

Setting	**Charge state**	**Number of nuclei implanted**
^{206}Hg	Full strip → H-like	2,550
^{206}Hg	H-like → H-like	40,753

Experimental Information

The energy spectrum of the γ-rays emitted from this nuclide is presented in figure 6.35. The transitions at 597, 965 and 1014 keV are previously unreported. The inset spectrum shows the time curve of these previously unreported transitions. The half-life is measured to be $T_{1/2} = 20(2)$ ns. There are two further candidate transitions at 423 and 609 keV, however due to the low statistics, they are tentative. The low γ-ray statistics attained for this nuclide make intensity balances ambiguous. Due to the short half-life compared to the FRS flight time, the internal conversion branch(es) of the isomer is/are likely to be comparable in intensity to the γ-ray branch(es) and may be the dominant mechanism of decay.

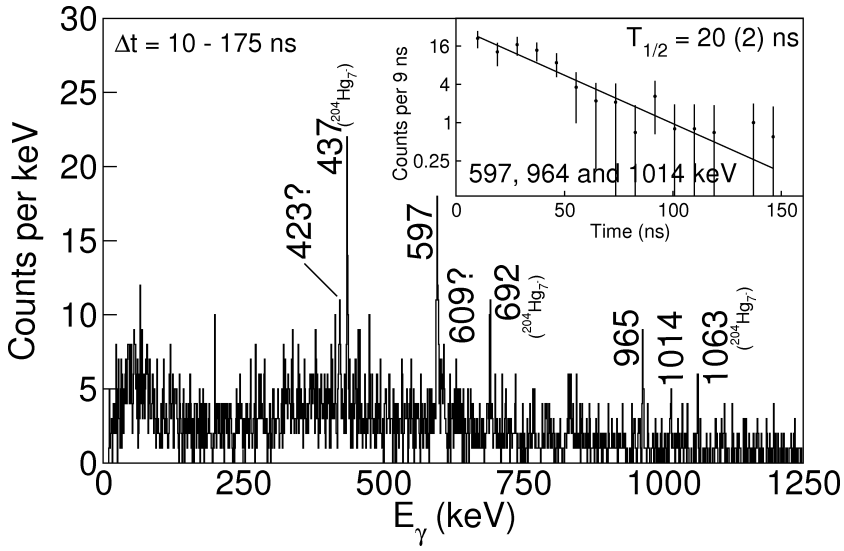

Figure 6.35: Gamma rays associated with ^{204}Hg following implantation using the SR devices. Question marks indicate that a transition is uncertain. The inset decay curve arises from the 597, 964 and the 1014 keV transitions.

Shell Model Calculation and interpretation

Previous work has populated excited states in ^{204}Hg [93]. A 423.7 keV transition was observed to decay into the $I^{\pi} = 7^{-}$ isomer [93,94]. The state emitting the 423.7 keV γ-ray transition was understood to be $I \geq 5$. In the current work this energy matches the tentatively identified transition at 423 keV. This is consistent with the idea that the higher-lying isomer must feed the previously reported lower-lying isomer (or else the $I^{\pi} = 7^{-}$ isomer would not have transmitted through the FRS).

The shell model calculation for ^{204}Hg is presented in figure 6.36 (left). Only states that might be involved following the isomer decay have been shown. The 423 keV transition is understood to arise from the $I^{\pi} = 9^{-}$ state. This is assigned because the calculated excitation energy difference between this state and the $I^{\pi} = 7^{-}$ state (455 keV) is close to the observed transition energy.

It is assumed that the $I^{\pi} = 11^{-}$ state feeds the $I^{\pi} = 9^{-}$ either by the 965 or the 1014 keV transition. For the remainder of the level scheme the confidence over assignments is reduced. The $I^{\pi} = 14^{+}$ state is predicted to be yrast and is a strong candidate for being isomeric. The predicted $I^{\pi} = 12^{+}$ state state would most likely be fed by the decay of such an isomer. If this is the case, based on energetics, some transitions must decay in parallel and there must be transitions unobserved in

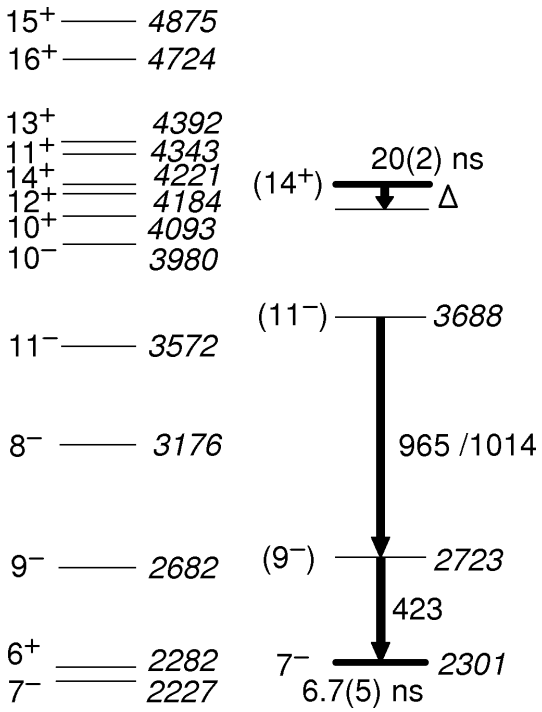

Figure 6.36: **Left:** Results of a shell model calculation for ^{204}Hg. Only near yrast levels that are above the known $I^{\pi} = 7^{-}$ isomer and below 5 MeV are presented. **Right:** The *tentatively* interpreted level scheme. Note that not all of the transitions have not been placed in the current work.

the current work. The possibility of unobserved transitions is consistent with the requirement of a significant internal conversion coefficient in the isomer. The limited experimental evidence forbids further examination, for this isomer it is not possible to establish a robust decay scheme. The limited tentative conclusions are shown in figure 6.36 (right).

6.5.3 ^{205}Au

Setting	Charge state	Number of nuclei implanted
^{203}Ir	Fully stripped → Fully stripped	6,061
^{203}Ir	Fully stripped → H-like	85,506
^{199}Os	Fully stripped → H-like	218,261
^{199}Os	Fully stripped → He-like	27,471
^{192}W	Fully stripped → He-like	4,682

Experimental Information

This is the first experimental information on excited states in ^{205}Au. The ground state has been suggested in a previous work to have $I^{\pi} = (3/2^{+})$ [110]. The transitions observed in this nuclide are presented in figure 6.37.

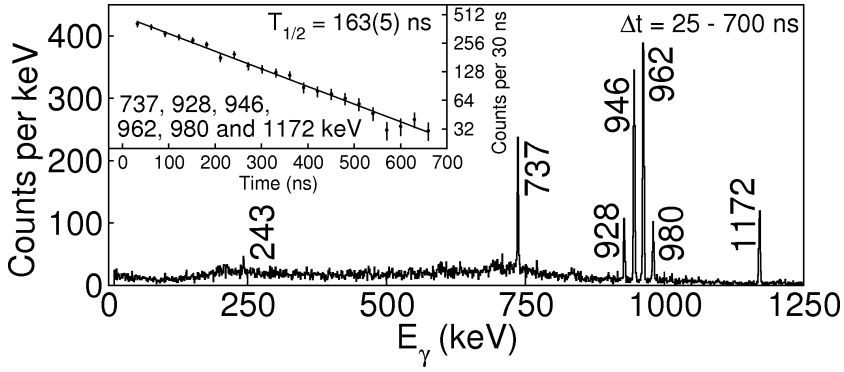

Figure 6.37: Gamma rays associated with ^{205}Au following implantation using the SR devices. The inset decay curve arises from the 737, 928, 946, 962, 980 and 1172 keV transitions.

Seven transitions are observed in the γ-ray spectrum (243, 737, 928, 946, 962, 980 and 1172 keV) for ^{205}Au. They have a measured half-life of $T_{1/2} = 163(5)$ ns. The measured intensities for these transitions (see Table 6.15) are for the absolute number of γ-ray decays; internal conversion branches are not considered.

The energies of the γ rays suggest that there are three parallel decay branches, with an additional cross-branch transition from the 243 keV γ ray. The intensities of the 946 and 962 keV γ rays do not match, indicating that there are more cross-branch transitions, or something more complex.

The statistics gathered allow for γ-γ coincidence analysis. This has been performed in figure 6.38. Selecting each of the transition energies individually, spectra have been produced. These show all of the other γ rays observed to arrive within 100 ns of the selected transition over $\Delta t = 25 \rightarrow 700$ ns.

The γ-γ analysis confirms that there are three decay branches and that the 243 keV transition links two of them. Some ordering of transitions can now be made based on the measured γ-ray intensities, $I(E_{\gamma})$. Since $I(1172) < I(737)$, the 243-928 and the 1172 keV transitions must both feed the 737 keV transition. This also implies that the 980 keV transition is fed by the 928 keV transition. From the γ-γ analy-

Table 6.15: Details of the measurements of ^{205}Au transitions, the statistics are directly extracted from the data presented in figure 6.37

E_γ(keV)	$FWHM$ (keV)	Intensity (a.u.)
243.40	2.2	421 (53)
736.92	2.6	4738 (206)
928.25	2.5	2713 (174)
946.05	2.6	11231 (355)
962.48	2.8	13328 (387)
980.19	3.4	2830 (179)
1171.50	3.0	3859 (204)
$736.92 + 1171.50 = 1908.42$		
$928.25 + 980.19 = 1908.44$		
$946.05 + 962.48 = 1908.53$		
$243.40 + 736.92 + 928.25 = 1908.57$		

sis the 980 keV transition is in coincidence with the 962 keV transition but not the 737 keV. The 962 keV transition must therefore feed the 980 keV. It also feeds the 946 keV transition, as this transition is also observed in coincidence with the 980 keV transition, but with nothing else (these inferences are used to build the level scheme of figure 6.39 (left)).

There are however some unresolved issues with the proposed decay scheme (figure 6.39 (left)). There is no observed coincidence between the 928 and 946 keV transitions. By any ordering of the observed γ rays it is not possible to correctly explain all of the observed γ-γ coincidence spectra of figure 6.38.

One possibility is that the 962 keV transition is a doublet. With this in mind, a possible level scheme is presented in figure 6.39 (right). The transition ordering agrees with all of the measured γ-γ coincidence and the observed γ-ray (and γ-γ coincidence) intensities. There may be a 209 keV transition linking the stronger of the two 962 keV transitions and the 737 keV transition, but this remains experimentally inconclusive from the current data.

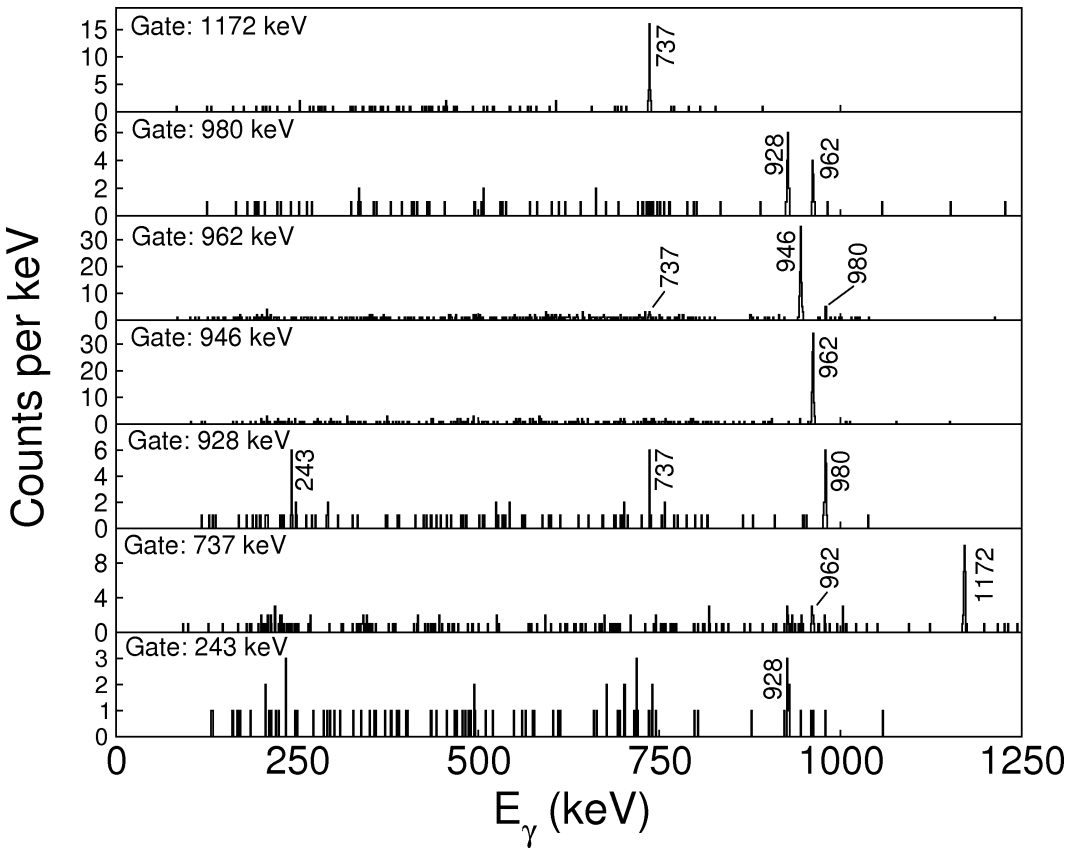

Figure 6.38: Gamma ray coincidences associated with ^{205}Au. The gated transition is noted within each spectrum, the γ-rays in the spectra were observed within 100 ns of the gated one. *All* of the involved γ-rays were observed in the range $\Delta t = 25 \rightarrow 700$ ns.

Shell Model Calculation and Interpretation

A shell model calculation has been performed to interpret the spin-parities of the constructed level scheme. The key levels predicted by the calculation are shown in figure 6.40 (left). Excitation energies up to ~ 3 MeV are shown. The predicted yrast $I^\pi = 11/2^-$ state is expected to be an isomer much longer lived than the sensitivity of the experimental set up (see section 2.7.1). A more recent experiment has confirmed that the isomer exists, it has a half-life seconds long [111]. It is likely, therefore, that the observed isomer is higher-lying than the $I^\pi = 11/2^-$ state.

According to the interpretation presented here, the unobserved 34 keV transition would be of $E2$ character, this would correspond to a $B(E2) = 1.1(2)$ W.u.. The isomer-depopulating 962 keV transition would likely be $E3$ character ($B(E3) = 0.40(9)$ W.u.). The shell model calculation predicts an $I^\pi = 19/2^+$ state to be iso-

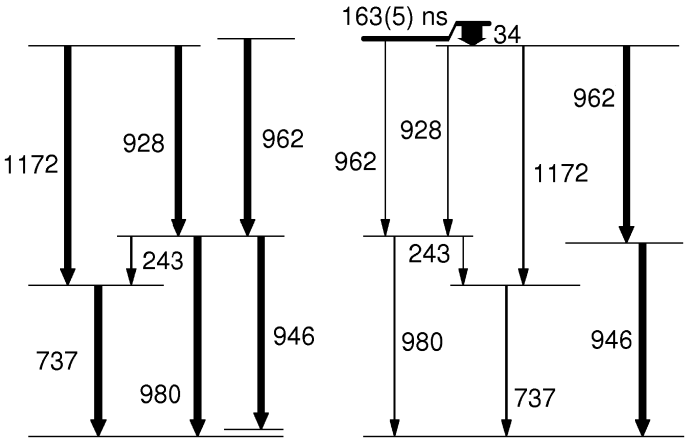

Figure 6.39: Experimental determination of the ^{205}Au level scheme. **Left:** built using only the observed transitions. It fails to match the experimental findings. **Right:** assumes a 962 keV doublet. Note, the proposed 34 keV transition is not observed in the current data. This interpretation agrees with the measured experimental evidence.

meric and to feed the yrast $I^\pi = 15/2^+$ and $13/2^-$ states. This suggests that the theoretically predicted ordering of the $I^\pi = 15/2^+$ and $19/2^+$ levels is the wrong way round. The decay branches from the $I^\pi = 15/2^+$ feed a collection of three states, the $I^\pi = 13/2^-, 15/2^-$ and $11/2^-$. Their ordering is also different to the shell model prediction, however in this case a change of order requires only small perturbations to the level energies. All of these three states then decay into the $I^\pi = 11/2^-$ isomer.

Isomeric Ratio

The isomeric ratio of the proposed $I^\pi = (19/2^+)$ isomer has been measured for all of the three transmitted charge states (see Table 6.16). The He-like state records a distinctly lower ratio than the others. The theoretical internal conversion coefficient of the proposed unobserved 34 keV decay branch is $\alpha = 855$, but the K_α coefficient is zero as the transition is below the electron binding energy. This branch should decay at the same rate for all three charge states. Internal conversion for the proposed $E3$ 962 keV branch would be small and of little effect, meaning that, the rate of decay of the isomer in-flight for the different charge states should be nearly identical. The mean isomeric ratio of the $I^\pi = 19/2^+$ isomer is 6.5^{+10}_{-15} %.

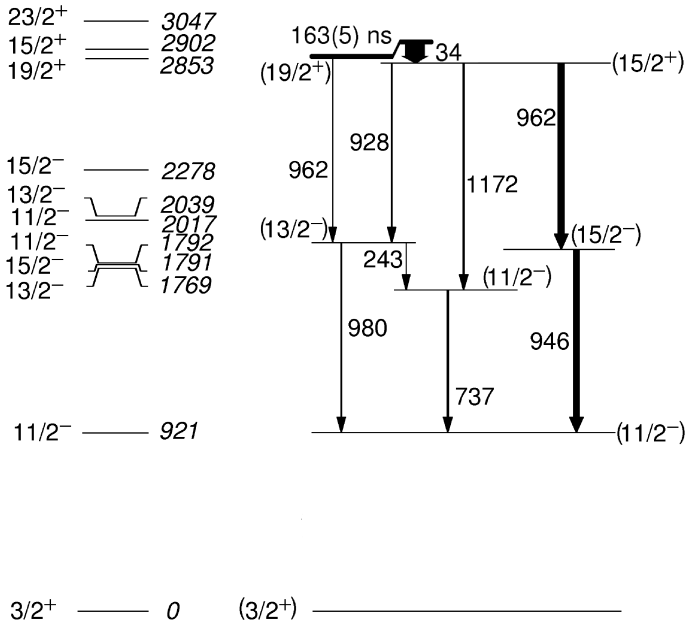

Figure 6.40: **Left:** Results of the shell model calculation for ^{205}Au. Only near yrast levels below $\sim$ 3 MeV and above the $I^{\pi} = 11/2^{-}$ state are presented. **Right:** The interpreted level scheme with speculative spin-parity assignments for ^{205}Au. The relative widths of parallel decay branches are an indication of the branching ratios.

Table 6.16: Measured isomeric ratio of the $I^{\pi} = (19/2^{+})$ isomer in ^{205}Au.

Charge state	**Isomeric ratio (%)**
$\boldsymbol{I^{\pi} = (19/2^{+})}$	
Fully stripped → Fully stripped	7.7^{+17}_{-22}
Fully stripped → H-like	7.6^{+7}_{-12}
Fully stripped → He-like	4.2^{+6}_{-9}
Mean	6.5^{+10}_{-15}

6.5.4 ^{204}Au

Setting	**Charge state**	**Number of nuclei implanted**
^{206}Hg	Fully stripped → Fully stripped	35,051
^{199}Os	Fully stripped → H-like	61,171
^{199}Os	Fully stripped → He-like	37,108
^{192}W	Fully stripped → He-like	1,836

Experimental Information

Only the ($I^\pi = (2^-)$) ground state of this nuclide has been previously reported [112, 113]. The present observation of an isomer is thus the first measurement of excited states in the nuclide. The observed γ-rays are shown in figure 6.41. Both ^{206}Hg and ^{205}Au are situated next to ^{204}Au on the identification plots (see figures 5.11, 5.14 and 5.15). These are two of the most strongly transmitted nuclides in the experiment and so a measurable degree of contamination is present. To a lesser degree, ^{203}Au also contaminates the spectrum.

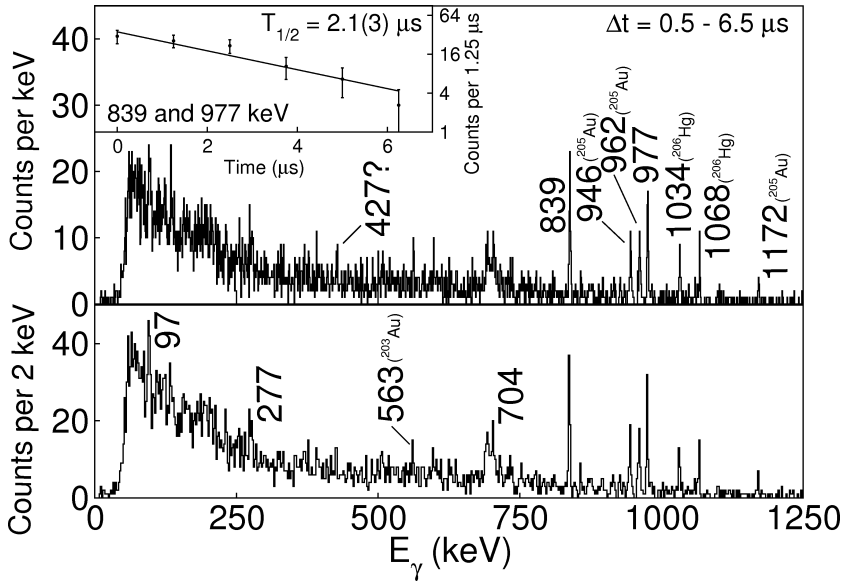

Figure 6.41: Gamma rays associated with ^{204}Au following implantation using the DGF devices. **Top:** One keV per channel binning. The inset decay curve uses the 839 and 977 keV transitions. **Bottom:** Two keV per channel binning with "new" transitions not labelled in the top spectrum indicated.

When binning to 1 keV per channel, two γ-ray transitions have been detected, 839 and 977 keV. Measuring them gives a half-life of $T_{1/2} = 2.1(3)$ μs for the isomer. When the same detected γ rays are binned at 2 keV per channel new candidate transitions are identified, these are 97, 277 427, and 704 keV. Note that the summed energy of the 277 and 427 keV transitions is equal to the 704 keV. There is not enough data available for γ-γ coincidence measurements.

Shell Model Calculation and Interpretation

Results of a shell model calculation for ^{204}Au are presented in figure 6.42. Note that the predicted ground state level of $I^\pi = 0^-$ is in contradiction to the experimental measurement of $I^\pi = (2^-)$ [112, 113]. From the calculation one would expect the $I^\pi = 12^-$ level to be isomeric. The available decay paths would result in an isomer that lives longer than the detection sensitivity. If the $I^\pi = 10^+$ level were below the $I^\pi = 12^-$ in energy, then the isomer half-life would be significantly shortened; the resulting $M2$ decay could have a reasonable reduced transition rate, however this decay would likely be dominated by internal conversion. Assuming 100 % of decays takes place through intenal conversion, experimentally this would result in a total of up to 15 counts of K_α X-rays on top of the background, which is 100 counts. There is no indication that this is the case in figure 6.41. It is not likely that this isomer is the result of decay from the $I^\pi = 12^-$ state. No other candidate state has been identified, from the limited experimental data it is not possible in this instance to construct a level scheme.

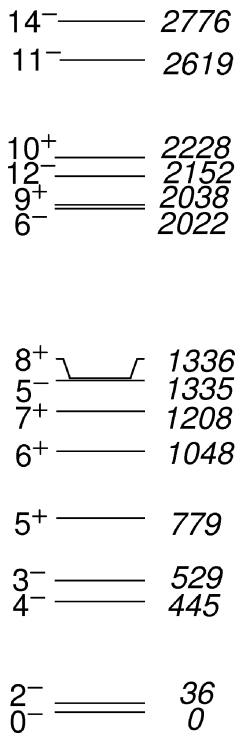

Figure 6.42: **Left:** A ^{204}Au shell model calculation. Only near yrast levels below the predicted first $I^\pi = 14^-$ state are shown here.

6.5.5 ^{202}Au

Setting	Charge state	Number of nuclei implanted
^{206}Hg	Fully stripped → Fully stripped	60,472

Experimental Information

The ground state of this nuclide has previously been observed [114] and is understood to have $I^{\pi} = 1^{-}$. No excited states have been measured previously. The current work has detected γ-ray transitions at 138 and 414 keV (see figure 6.43), with a half-life of the isomer of $T_{1/2}$ =13.1(5) ns (from the 414 keV transition). Gamma-ray γ-γ coincidence measurements have been made, selecting events where the 414 keV transition is detected (see figure 6.43). The 138 keV transition is observed to be in coincidence with the 414 keV transition.

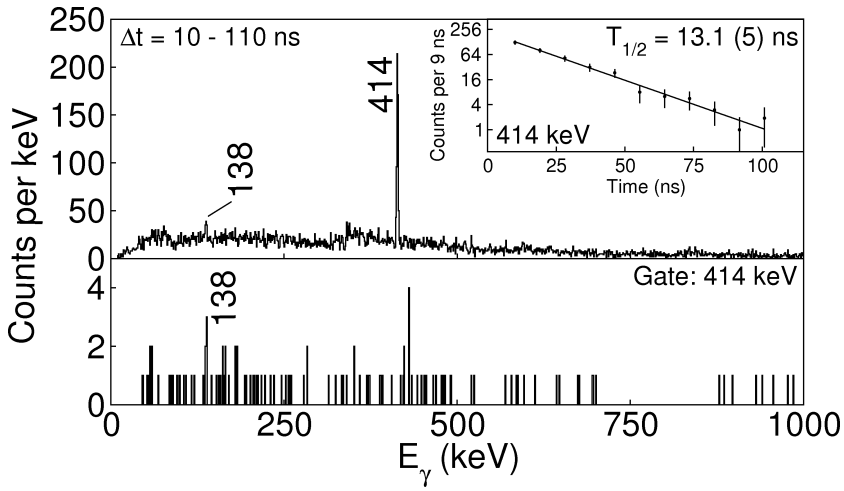

Figure 6.43: Gamma rays associated with ^{202}Au following implantation using the SR devices. **Top:** gamma-ray single events. The inset decay curve arises from the 414 keV transition. **Bottom:** gamma-rays observed when a 414 keV γ-ray is also observed, both in the time range $\Delta t = 10 \rightarrow 110$ ns.

6.5.6 ^{201}Au

Setting	Charge state	Number of nuclei implanted
^{206}Hg	H-like → Fully stripped	2,704

Experimental Information

Excited states have been measured in ^{201}Au, but no γ-ray transitions have previously been reported in this nuclide [96]. The γ rays observed in this experiment are identified in the spectrum shown in figure 6.44. The observed γ-rays do not match with any of the previously measured levels.

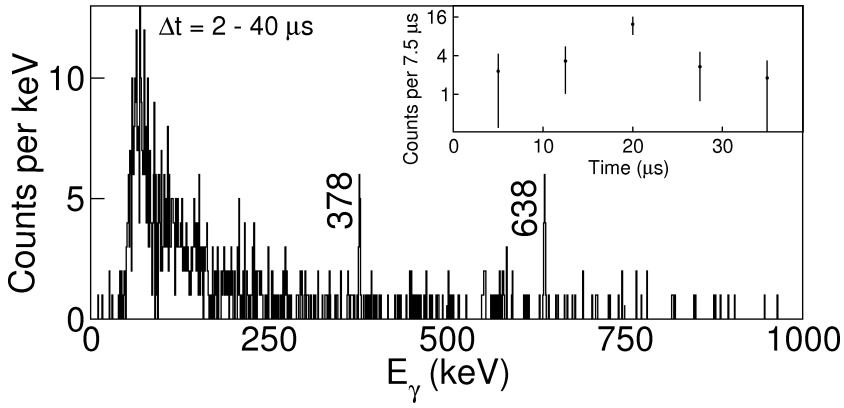

Figure 6.44: Gamma rays associated with ^{201}Au following implantation using the DGF devices. The inset decay curve arises from the 378 and 638 keV transitions.

6.5.7 ^{204}Pt

Setting	Charge state	Number of nuclei implanted
^{203}Ir*	Fully stripped → Fully stripped	54,058
^{199}Os	Fully stripped → Fully stripped	3,951
^{202}Os	Fully stripped → Fully stripped	8,950
^{203}Ir*	Fully stripped → H-like	11,750
^{199}Os	Fully stripped → H-like	11,140
^{202}Os	Fully stripped → H-like	1,567
^{192}W	Fully stripped → H-like	703
^{202}Os	H-like → H-like	109
^{192}W	Fully stripped → He-like	645

**Gamma-ray detection time reduced from 380 to 85 μs for this setting.*

Experimental Information

Previously no measurements had been reported in the literature on ^{204}Pt. The greater portion (71 %) of the statistics for this nuclide in the present work come from the ^{203}Ir FRS setting, where the γ-ray measuring window is only 85 μs long. Two of the isomeric decays here are better observed with the longer correlation time from the other settings. The observed γ rays associated with ^{204}Pt are shown in the spectrum presented in figure 6.45.

In figure 6.45 (a) γ ray peaks are observed at 97, 1061 and 1158 keV for the range $\Delta t = 50 \rightarrow 850$ ns following implantation, platinum X-rays are also observed. The sum of the energy of the 97 and 1061 keV transitions is equal, within experimental errors, to the energy of the 1158 keV transition. It is thus likely that these transitions form two parallel branches. The intensity ratio for the 97-1061 and 1158 keV branches is 0.85:0.15(3). In figure 6.45 (b) and (c), transitions at 872 and 1123 keV are also observed for the longer time ranges of $\Delta t = 1.5 \rightarrow 380$ and 85 μs, respectively. The time curve measured for the 1061 and 1158 keV γ rays gives $T_{1/2} = 146(14)$ ns for this isomer. The 872 and 1123 keV transitions both express the same shaped decay curve, indicating that they are both subject to a 2-component exponential decay. The 146 ns isomer is too short-lived to be the cause of this observed two component decay curve. It is thus concluded that three isomers are observed in the current work, with one associated with an unobserved low-energy transition. The experimental limit on this energy is 78.4 keV, for higher energies either the associated X-rays or the transition itself would be detected. The longer-lived component of the decay of the 872 and 1123 keV γ rays is best fitted using the 29 % of the data which measures for 380 μs following implantation. The shorter component is fitted best using all of the data over the 85 μs range. This is done while using the already extracted half-life for the longer component. Both of these fits are performed using the Bateman equation for two successive exponential decays [17];

$$A(t) = N_{0_1} e^{-\lambda_1 t} + N_{0_2} \frac{\lambda_2 \lambda_1}{\lambda_2 - \lambda_1} (e^{-\lambda_1 t} - e^{-\lambda_2 t}) \tag{6.2}$$

where $A(t)$ is the activity at time t, N_0 is the initial population of the isomeric state, λ is the radioactive decay constant and the labelling 1 and 2 refer to the lower-lying and higher-lying isomers, respectively. The longer component is fitted to be $T_{1/2} = 55(3)$ μs

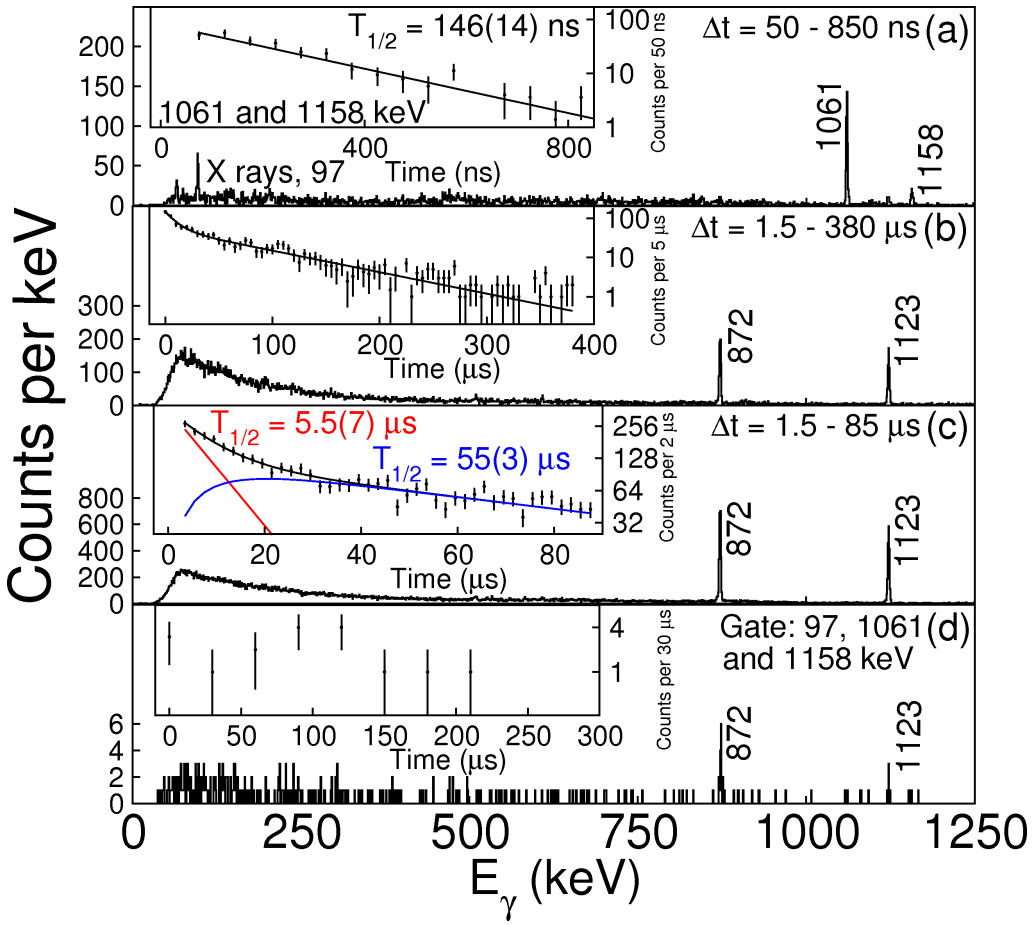

Figure 6.45: Gamma rays associated with ^{204}Pt following implantation using the DGF devices. **(a)** All of the data recorded over the time range $\Delta t = 50 \rightarrow 850$ ns. The inset decay curve arises from the 1061 and 1158 keV transitions. **(b)** the data over the time range $\Delta t = 1.5 \rightarrow 380$ μs. The inset decay curve arises from the 872 and 1123 keV transitions. **(c)** All of the data over the time range $\Delta t = 1.5 \rightarrow 85$ μs, see text for details. The inset decay curve is gated on the 872 and 1123 keV transitions. **(d)** coincident gamma rays measured following observation of a 97, 1061 or 1158 keV transition in the same event. The inset shows the time difference between the arrival of the 97, 1061 or 1158 keV and the 872 or 1123 keV γ rays.

(see the inset plot of figure 6.45 (b)). The shorter of the two isomers was measured to be $T_{1/2} = 7(1)$ μs. Fitting all of the data over 85 μs, the fitted half-life of this shorter isomer was $T_{1/2} = 5.5(7)$, consistent with the value from the longer time gated measurement. The 5.5 μs value is considered to be the final measured value of the isomer.

The decay curve of the 872 and 1123 keV γ rays implies that the 55 μs isomer is

higher lying than the 5.5 μs isomer. In addition, the $T_{1/2} = 55$ μs and 5.5 μs isomers are populated at comparable levels at the time of implantation. For all other combinations of the decay order and the initial population levels, distinctly different decay curves would result. These conclusions are highlighted schematically in figure 6.46.

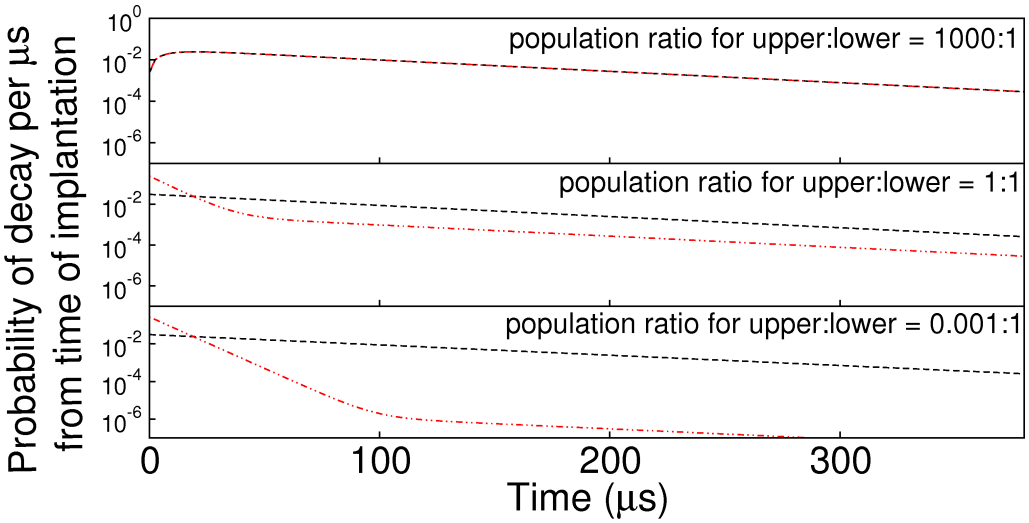

Figure 6.46: Schematic decay curves for transitions following two-component isomer decay. **Black curves:** a 5.5 μs isomer decays followed by a 55 μs isomer. **Red curves:** the order is reversed. Different initial population ratios of the two isomers are used in each case, these ratios are indicated in the spectra.

Coincidence measurements between the 97, 1061 or 1158 keV transitions and any other γ rays emitted later in time but from the same event have been made. These are shown in figure 6.45 (d). The plot shows coincidence with the 872 and 1123 keV transitions. This demonstrates that the $T_{1/2} = 146$ ns isomer is higher lying in the decay scheme than the other two isomers. It also proves that all three isomers are from a single cascade. The implantation rate of ^{204}Pt was 0.4 nuclei/s, thus chance coincidences with selected γ rays emitted from a ^{204}Pt nucleus is negligible. This has similarly been the case for all of the γ-γ measurements in this thesis. The relative population ratio at the time of implantation has been measured for the three isomers; this is consistent with the coincidence measurements. For the 146 ns, 5.5 μs and the 55 μs isomers, the ratio is found to be 1.0:4.5:1.4(6), respectively.

Shell Model Calculation and Interpretation

Figure 6.47 presents two different ^{204}Pt shell model calculations, the interpreted level scheme, part of the experimentally known ^{206}Hg level scheme [31, 87, 88] and two ^{206}Hg shell model calculations. Shell model calculations (b) and (c) are modified from the calculation described in section 6.5. These modifications are detailed at the end of this section. Predictions (a) and (d) use the interaction and matrix elements that were described in 6.5 and these are considered first. For ^{204}Pt this shell model calculation predicts a $I^\pi = 10^+$ state that is likely to be isomeric. The equivalent state in the $N = 126$ isotone ^{206}Hg has been observed previously [31]. The highest-lying of the observed isomers, which emits the 97, 1061 and 1158 keV γ-rays, matches expectations of decay from this $I^\pi = 10^+$ state. Assigning the 1158 keV transition an $E3$ multipolarity, corresponds to a reduced transition probability of 0.19(3) W.u.. This would correspond to the $10^+_1 \rightarrow 7^-_1$ decay. The 97 keV transition then competes, depopulating the $I^\pi = 10^+$ state to the $I^\pi = 8^+$ state. The reduced transition probability for this transition is 0.80(8) W.u.. The 1061 keV is likely emitted promptly following the 97 keV as a result of an $E1$ $8^+ \rightarrow 7^-$ decay.

The assignments relating to the $I^\pi = (10^+)$ isomer are robust. From the coincidence measurements of the present work it is clear that the remaining two isomers follow the decay in the same cascade, i.e. they emit following decay of the proposed $I^\pi = 7^-$ level. Given the initial shell model proposed sequence, (increasing in energy) the predicted order of the $I^\pi = 4^+_1, 7^-_1, 5^-_1$ states is inconsistent with experimental findings. With the predicted order In the shell model predicted order, decay from the $I^\pi = 7^-$ state, which is known to be populated, would be expected to be orders of magnitude longer-lived than the observed value, furthermore only a single isomer be observed, not two. By switching the order of the $I^\pi = 5^-$ and 7^- states one successfully reproduces the prediction of a low-energy unobserved transition, which depopulates the 55 μs isomer. For energies in the range $10 \rightarrow 78$ keV the reduced transition rate of this unobserved γ-ray would be $0.017 \rightarrow 0.0034$ W.u.. In this scenario, the $I^\pi = 4^+$ state would be expected to lie higher than the $I^\pi = 5^-$ state, otherwise the second isomer would be destroyed due to an $E1$ transition between $5^- \rightarrow 4^+$ states. The 5.5 μs isomer can be understood as an $E3$ decay from the yrast $I^\pi = 5^-$ state to the $I^\pi = 2^+$, which then decays to the ground state. This structure is synonymous to that

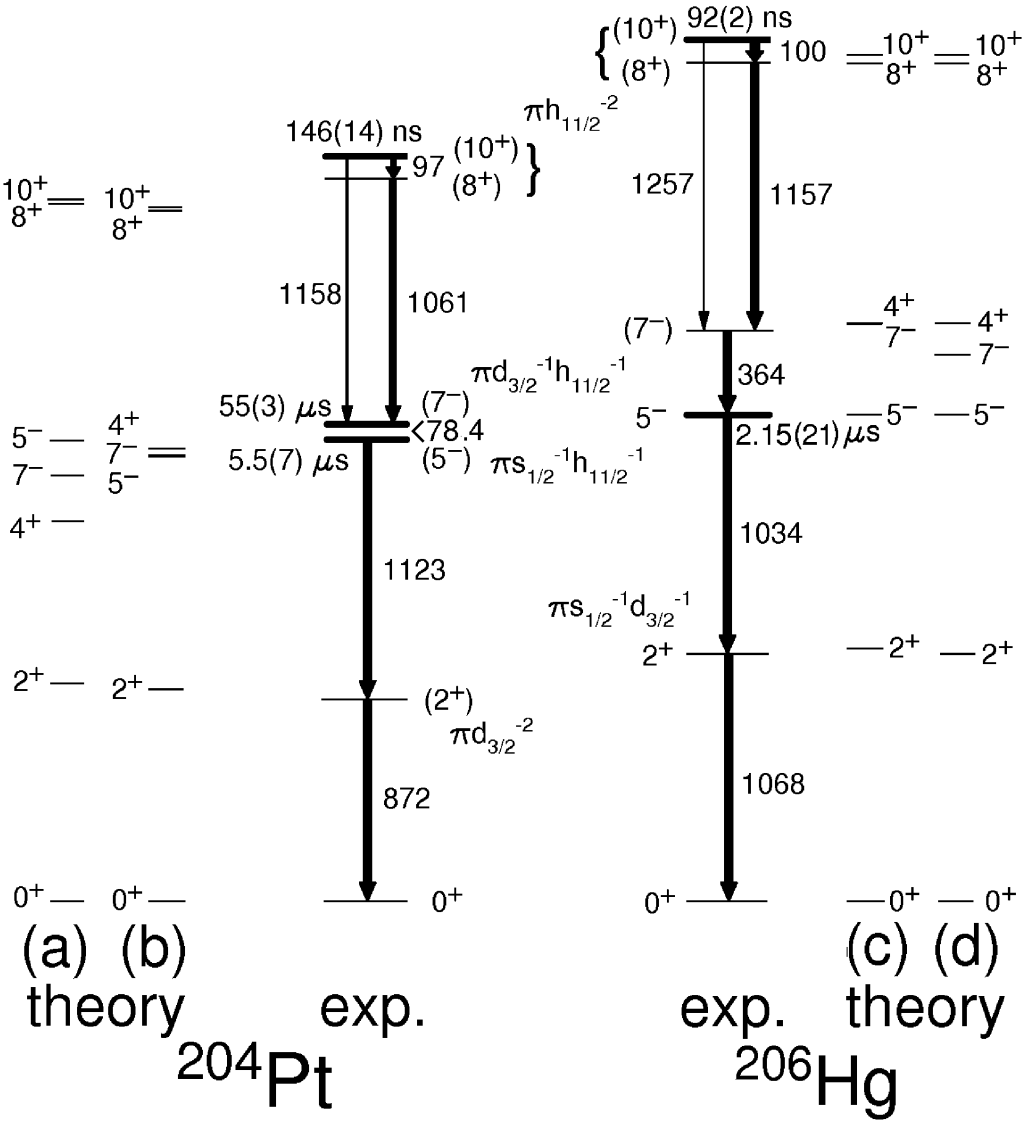

Figure 6.47: **Theory (a) and (d):** A ^{204}Pt and ^{206}Hg shell model calculation, respectively, performed using the interactions and matrix elements described in section 6.5. Only near yrast up to $I^{\pi} = 10^{+}$ state are shown. **Theory (b) and (c):** Modified shell model predictions for the same nuclides, see text for details. **Exp.:** The proposed ^{204}Pt level scheme and a partial level scheme for ^{206}Hg [31]. The dominant orbital configuration for each level is stated and relative γ-ray widths indicate the branching ratios.

of the neighbouring $N = 126$ isotone, ^{206}Hg.

By removing two protons from ^{206}Hg to ^{204}Pt, the shell model calculations predict that the dominant orbital configuration of the $I^{\pi} = 2^{+}$ state changes from being dominated by $(\pi d_{3/2})^{-2}$ to $(\pi d_{3/2})^{-1}(\pi s_{1/2})^{-1}$ [115, 116]. This lowers the excitation energy of the 2^{+} state by about 200 keV when taking into account differences in single

particle $\left((s_{1/2})^{-1}\right.$ vs. $\left.(d_{3/2})^{-1}\right)$ and interaction $\left((d_{3/2})^{-2}\right.$ vs. $\left.(s_{1/2})^{-1}(d_{3/2})^{-1}\right)$ energies. On this basis (i.e. comparison with the shell model calculations) the 872 keV transition is understood to depopulate the $I^{\pi} = 2^{+}$ state. This is compared to a transition of 1068 keV in ^{206}Hg. The 1172 keV transition is thus assigned to depopulate the $I^{\pi} = 5^{-}$ state, with a reduced $B(E3)$ transition rate of 0.039(5) W.u..

Suggested Modifications to the Shell Model Parametrisation

In light of the new $N = 126, Z \leq 82$ proton-hole information (both the present data and that on ^{206}Hg [31]), modifications are suggested to the Rydström interaction [109]. There are three changes suggested by H.G. Maier and H. Grawe [115, 116].

(i) The $(d_{3/2}h_{11/2})_{7^-}$ two-body matrix element has been increased by +135 keV, improving agreement with ^{206}Hg.

(ii) The $(s_{1/2}d_{5/2})$ monopole has been increased by +250 keV. This accounts for the ^{204}Pt 4^{+} level energy and the increased blocking of the $h_{11/2} \otimes 3^{-}$ coupling, lowering the effective $d_{5/2}$ single-hole energy.

(iii) From a systematic search of the influence of non-diagonal two-body matrix elements on the $E2$ strength evolution from ^{206}Hg to ^{204}Pt, the $(s_{1/2}h_{11/2}; d_{3/2}h_{11/2})_{6^-}$ two-body matrix element has been affected by +160 keV.

Using the currently available experimental information it is not possible to fit a unique solution for the modified matrix elements. However with these three simple changes to the Rydström [109], the excited states in both ^{206}Hg and ^{204}Pt are well reproduced. Importantly this includes altering the order of the $5^{-}, 4^{+}$ and 7^{-} states to be consistent with the deduced ordering in ^{204}Pt. These discussed shell model changes for ^{206}Hg and ^{204}Pt are implemented in figure 6.47 (b) and (c). They are *not* applied to any other shell model calculations in this thesis.

The modified shell model calculation $E2$ and $E3$ strengths are in agreement with experiment (see Table 6.17), with the exception of the $5^{-} \rightarrow 2^{+}$ decay in both the ^{206}Hg and ^{204}Pt case. This is most likely due to the $I^{\pi} = 2^{+}$ wave function, which is poorly described in a pure proton model space.

Table 6.17: Transition strengths for experiment, the Rydström [109] shell model (SM) and the new two-body matrix elements (SM_{mod}), in ^{206}Hg and ^{204}Pt. Effective charges for protons of 1.5 and 2.0 e for $E2$ and $E3$, were used, to reproduce the ^{206}Hg $10^+ \rightarrow 8^+$ $E2$ and $10^+ \rightarrow 7^-$ $E3$ transitions [31].

Transition	EL	$B(EL)$ **(W.u.)**		
		exp.	**SM**	$\mathbf{SM_{mod}}$
^{206}Hg				
$10^+ \rightarrow 8^+$	$E2$	0.94(15)	0.87	0.87
$10^+ \rightarrow 7^-$	$E3$	0.25(3)	0.17	0.21
$7^- \rightarrow 5^-$	$E2$	–	2.93	2.89
$5^- \rightarrow 2^+$	$E3$	0.18(2)	1.17	0.91
^{202}Pt				
$10^+ \rightarrow 8^+$	$E2$	0.80(8)	2.64	1.22
$10^+ \rightarrow 7^-$	$E3$	0.19(3)	0.21	0.22
$7^- \rightarrow 5^-$	$E2$	$0.017 \rightarrow 0.0034^a$	1.21	0.0037
$5^- \rightarrow 2^+$	$E3$	0.039(5)	0.713	0.612

[a] *Assuming a transition energy between 10 → 78 keV*

Isomeric Ratios

From the decay scheme established in the current work, the isomeric ratios have been deduced for the three isomers in ^{204}Pt, for both the $(F-F)$ and $(F-H)$ charge states. As the γ-ray (and X-rays) responsible for the depopulation of the $I^\pi = (7^-)$ isomer are not directly observed, 872 and 1123 keV γ rays are used to establish the isomeric ratio of this and the $I^\pi = (5^-)$ isomer. This method propagates significantly the uncertainty of the measurement, despite the large statistics. The results are presented in Table 6.18, the mean isomeric ratios for the $I^\pi = (5^-), (7^-)$ and (10^+) states are 40^{+17}_{-20} %, 26.9^{+72}_{-92} % and 9.2^{+25}_{-32} %, respectively.

The isomeric ratios quoted for the $I^\pi = (5^-)$ and (7^-) states in Table 6.18 each include feeding from the other, higher-lying observed isomers. After subtracting these effects, the mean isomeric ratios become 17.7^{+76}_{-97} % for the $I^\pi = 7^-$ isomer and 22^{+18}_{-22} % for the $I^\pi = 5^-$ isomer.

Table 6.18: Measured isomeric ratios of the $I^{\pi} = (5^-), (7^-)$ and (10^+) isomers in ^{204}Pt.

Charge state	**Isomeric ratio (%)**
$\boldsymbol{I^{\pi} = (5^-)}$	
Fully stripped → Fully stripped	42^{+17}_{-20}
Fully stripped → H-like	39^{+17}_{-20}
Mean	40^{+17}_{-20}
$\boldsymbol{I^{\pi} = (7^-)}$	
Fully stripped → Fully stripped	27.6^{+73}_{-93}
Fully stripped → H-like	26.3^{+71}_{-91}
Mean	26.9^{+72}_{-92}
$\boldsymbol{I^{\pi} = (10^+)}$	
Fully stripped → Fully stripped	8.7^{+22}_{-28}
Fully stripped → H-like	9.7^{+29}_{-36}
Mean	9.2^{+25}_{-32}

6.5.8 ^{203}Pt

Setting	**Charge state**	**Number of nuclei implanted**
^{203}Ir	Fully stripped → Fully stripped	202,945
^{202}Os	Fully stripped → Fully stripped	471
^{199}Os	Fully stripped → Fully stripped	13,487
^{203}Ir	Fully stripped → H-like	41,293
^{199}Os	Fully stripped → H-like	53,230
^{192}W	Fully stripped → H-like	4,065
^{202}Os	H-like → H-like	625
^{199}Os	Fully stripped → He-like	2,937
^{192}W	Fully stripped → He-like	2,335

Experimental Information

In the one previous study on this nuclide, only the tentatively assigned $I^\pi = (1/2^-)$ ground state has been identified [117]. In the current work, an 1104 keV transition has been observed, which is shown in the spectrum in figure 6.48. The half-life of the isomer is measured to be $T_{1/2} = 641(55)$ ns.

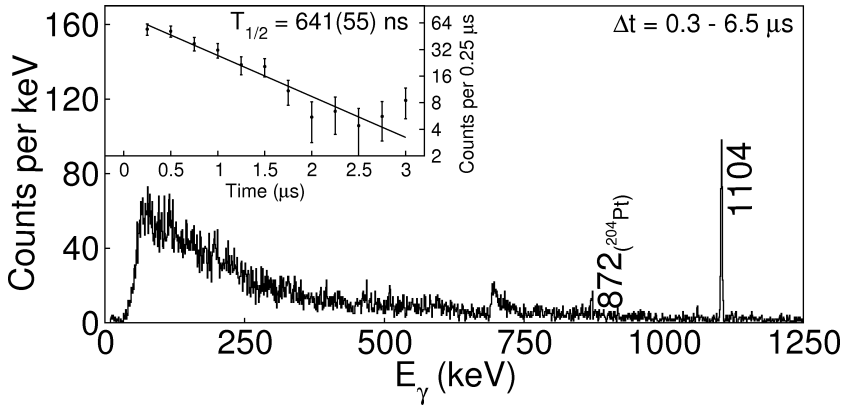

Figure 6.48: Gamma rays associated with ^{203}Pt following implantation using the DGF devices. The inset decay curve arises from the 1104 keV transition.

Shell Model Calculation and Interpretation

In figure 6.49 (left) a shell model calculation for ^{203}Pt is presented. Only the predicted near yrast levels are presented up to ~ 3 MeV. One might expect the predicted $I^\pi = 13/2^+$ level to be isomeric, which is likely longer-lived than the experimental sensitivity. One would also expect to observe a ~ 400 keV transition across the $5/2^- \rightarrow 1/2^-$ states for all decay below the $I^\pi = 13/2^+$ level. It is thus anticipated that the observed isomer is higher-lying than this state, it most probably decays into it.

If the 1104 keV transition depopulates directly the isomer it is likely that the decay is of $E3$ (or possibly $M3$) character based on reduced transition rates. Other explanations for the existence of this isomer depend on introducing unobserved transitions, which are low enough in energy to be beyond detection sensitivity. Noting that the array is sensitive to Platinum K_α X-rays, this places their energies < 78.4 keV.

Examination of the shell model prediction in figure 6.49 does not identify any candidates for decay of the isomer directly by the 1104 keV transition. The addition of an unobserved transition does not explain the structure either.

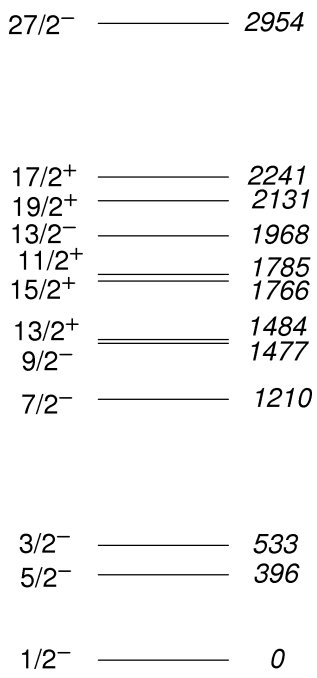

Figure 6.49: A ^{203}Pt shell model calculation. Only yrast and near yrast levels are presented up to ~ 3 MeV.

6.5.9 ^{199}Pt

Setting	Charge state	Number of nuclei implanted
^{206}Hg	Fully stripped → Fully stripped	3,970
^{206}Hg	H-like → Fully stripped	4,869

There have been several previous studies regarding ^{199}Pt [118–124]. Among these studies, an isomer has been observed [118, 119], with spin-parity $I^{\pi} = (13/2^{+})$ and $T_{1/2} = 13.6$ s. The current experiment is not sensitive to such a long-lived isomer

Experimental Information

The observed γ-rays associated with ^{199}Pt are shown in figure 6.50. There are three transitions observed at 319, 419 and 597 keV. The measured half-life of the isomer is $T_{1/2} = 18.6(34)$ ns. Due to the half-life being short compared to the flight time it is assumed that there is a low-energy, highly converted unobserved transition which directly depopulates the isomer.

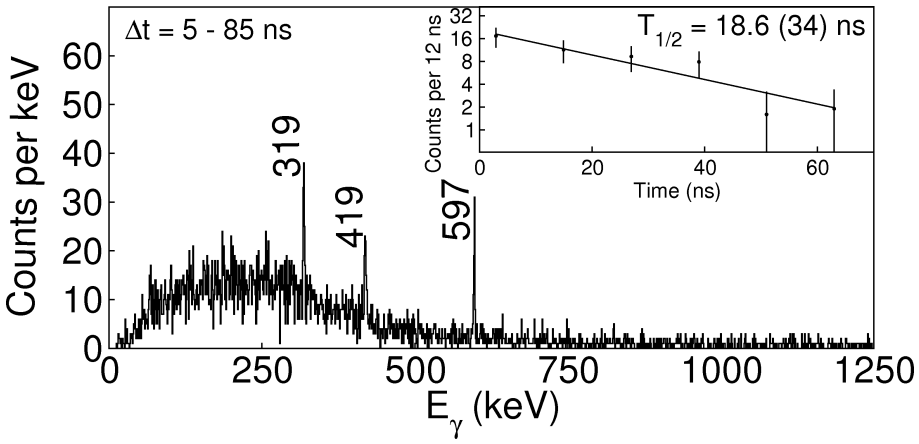

Figure 6.50: Gamma rays associated with ^{199}Pt following implantation using the SR devices. The inset decay curve arises from the 319, 419 and 597 keV transitions.

Isomeric Ratio

In this case the isomer decay scheme has not been deduced, but it is possible to set limits on the isomeric ratio for the $(F - F)$ charge state only. This is achieved by assuming the observed transitions have branching ratios of 100 % and internal conversion coefficients of zero. In the limit of zero decays in-flight the minimum isomeric ratio is found to be 5.4^{+28}_{-32} % (see Table 6.19).

Table 6.19: Minimum limit for the isomeric ratio of the isomer in ^{199}Pt, assuming that all the observed transitions have branching ratios of 100 % and $\alpha = 0$.

Charge state	**Isomeric ratio (%)**
$\boldsymbol{I^{\pi} = unknown}$	
Fully stripped → Fully stripped	$\geq 5.4^{+28}_{-32}$

6.5.10 ^{197}Pt

Setting	**Charge state**	**Number of nuclei implanted**
^{206}Hg	H-like → Fully stripped	7,414

Two isomers have been identified in ^{197}Pt [118,125–130]. The first excited state is an isomer with a half-life of 16.6(2) ns, this decays by a 53 keV $E2$ transition [125–127].

There is also an $I^{\pi} = 13/2^{+}$ isomer, which has a half-life of 95 minutes [118, 127–130]. The currently discussed experiment did not observe either of these.

Experimental Information

The γ rays associated with ^{197}Pt as measured in the current work are shown in the spectra in figure 6.51. Three previously unreported transitions have been observed associated with ^{197}Pt; at 375, 432 and 547 keV. In events where either a 375, 432 or a 547 keV transition is observed in the range $\Delta t = 5 \rightarrow 70$ ns following implantation the remaining two transitions are observed to be coincident over the same time range. The measured half-life of the isomer, using these three transitions is $T_{1/2} = 10.2(12)$ ns.

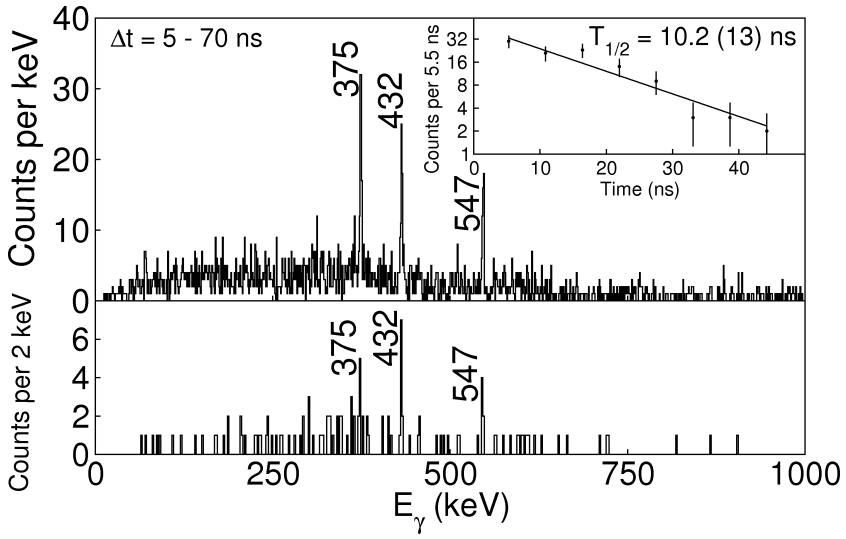

Figure 6.51: Gamma rays associated with ^{197}Pt following implantation using the SR devices. The inset decay curve arises from the 375, 432 and 547 keV transitions.

The short half-life of the observed isomer implies that, for this isomer to transmit through the FRS the direct decay from the isomer must be highly converted. Note that the nuclei were transmitted in $(H - F)$ charge states, internal conversion of K-shell electrons could take place for approximately half of the flight time. It is therefore likely that the isomer-depopulating transition has an energy less than the K-shell binding energy (for a H-like ion) for platinum (i.e. $E_{\gamma} = 91$ keV).

6.5.11 ^{203}Ir

Setting	Charge state	Number of nuclei implanted
^{203}Ir	Fully stripped → Fully stripped	1,296
^{202}Os	Fully stripped → Fully stripped	995
^{199}Os	Fully stripped → Fully stripped	4,807
^{203}Ir	Fully stripped → H-like	153
^{199}Os	Fully stripped → H-like	546
^{192}W	Fully stripped → H-like	207

Experimental Information

No previous studies have been reported in the literature on ^{203}Ir. The current data makes this the lightest $N = 126$ nuclide to have been experimentally measured to date. The γ-rays associated with the implanted nuclei are shown in figure 6.52.

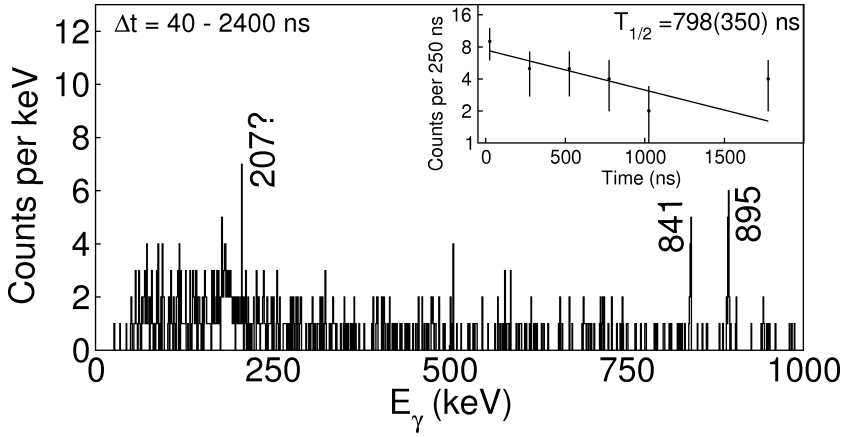

Figure 6.52: Gamma rays associated with ^{203}Ir following implantation using the DGF devices. The decay curve of the left inset is from the 841 and 895 keV transitions, the existence of the 207 keV transition is uncertain.

Two γ-ray peaks have been identified associated with an isomer in ^{203}Ir, at 841 and 895 keV, a third peak is tentatively identified at 207 keV. The half-life associated with the decay of the 841 and 895 keV transitions is $T_{1/2} = 798(350)$ ns.

Shell Model Calculation and Interpretation

A shell model calculation for this $N = 126$, closed shell nuclide is shown in figure 6.53 (left). It has one pair of protons less than $^{205}_{79}$Au, and thus might be expected to exhibit similar low-lying excitations. The shell model predictions for these two nuclides are indeed similar.

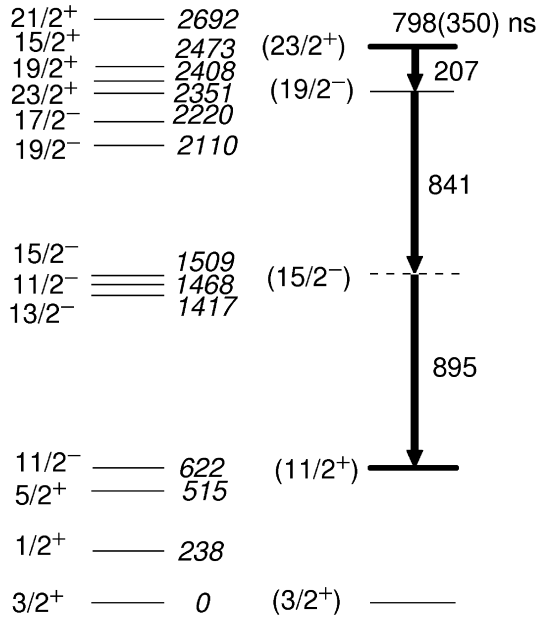

Figure 6.53: **Right:** a ^{203}Ir shell model calculation showing only the predicted near yrast levels up to $I^\pi = 21/2^+$. **Left:** the proposed decay scheme for ^{203}Ir.

As with ^{205}Au, the first $I^\pi = 11/2^-$ state is anticipated to isomeric, with a lifetime greater than the sensitivity of the current experiment. The currently observed isomer most probably decays into this state. Again analogous to ^{205}Au, should any of the group of three states ($I^\pi = 13/2^-, 11/2^-$ and $15/2^-$) be populated, they would most likely decay promptly to the predicted $I^\pi = 11/2^-$ isomer. The predicted energy of such transitions is similar to two of the experimentally observed 841 and 895 KeV transitions.

An important difference between ^{205}Au and ^{203}Ir is that the first $I^\pi = 19/2^-$ state in ^{203}Ir is predicted to lie lower than the $I^\pi = 19/2^+$ state, which in ^{205}Au is proposed to be responsible for the isomerism. An $E1$ decay via $19/2^- \rightarrow 19/2^+$ creates a much quicker decay pathway for this state. In addition, the $I^\pi = 23/2^+$ state is now anticipated to lie lower than the yrast $I^\pi = 19/2^+$ state, but not the $I^\pi = 19/2^-$. With this configuration the $I^\pi = 23/2^+$ state is expected to become isomeric and would likely

decay by an $23/2^+ \rightarrow 19/2^-$ $M2$ transition. The transition could be mediated by the 207 keV candidate γ-ray transition. A 207 keV $M2$ transition would have a reduced transition rate of 0.59 W.u. and an internal conversion coefficient of $\alpha = 3.99$.

Following the proposed $M2$ transition the shell model calculations predict that the $I^\pi = 15/2^-$ state would be populated. Unlike the three parallel routes of ^{205}Au, only one decay branch is anticipated to dominate the decay path. The $15/2^- \rightarrow 11/2^-$ decay is understood to be mediated by either the 895 keV transition or the 841 keV transition, note that the transition assignments are based on their energy when compared to the shell model predictions, the order of the 841 and 895 keV transitions is not measured.

Isomeric Ratio

From the proposed, tentative level scheme for ^{203}Ir, the isomeric ratio has been measured for the $I^\pi = (23/2^-)$ state. The statistics for the $(F - H)$ charge state are too poor for a measurement to be made. Table 6.20 presents the measurement for the $(F - F)$ charge state, this is found to be 4.7^{+31}_{-34} %.

Table 6.20: Measured isomeric ratio of the $I^\pi = 23/2^+$ isomer in ^{203}Ir.

Charge state	**Isomeric ratio (%)**
$\boldsymbol{I^\pi = (23/2^+)}$	
Fully stripped → Fully stripped	4.7^{+31}_{-34}

6.5.12 ^{202}Ir

Setting	**Charge state**	**Number of nuclei implanted**
^{203}Ir	Fully stripped → Fully stripped	11,039
^{202}Ir	Fully stripped → Fully stripped	4,897
^{199}Os	Fully stripped → Fully stripped	14,915
^{203}Ir	Fully stripped → H-like	1,080
^{199}Os	Fully stripped → H-like	1,169
^{192}W	Fully stripped → H-like	2,370

Although the half-life of the ground state of this nuclide has been measured previously [131], the spin-parity is not known. From systematics of similar nuclides the ground state has been predicted to most likely be $I^{\pi} = 1^{-}$ or 2^{-}.

Experimental Information

The γ-rays measured in association with implanted ^{202}Ir nuclei are shown in figure 6.54. Five γ-ray transitions have been detected, these are at 312, 656, 737, 889 and a 968 keV. Iridium K X-rays are also detected. The sum energy of the 312 and 656 keV transitions is equal to the 968 keV transition, suggesting that parallel branch decays take place between a 312-656 route and 968 keV decay path. The half-life of the isomer is measured using the 656, 737 and 889 keV transitions, $T_{1/2} = 3.4(6)$ μs.

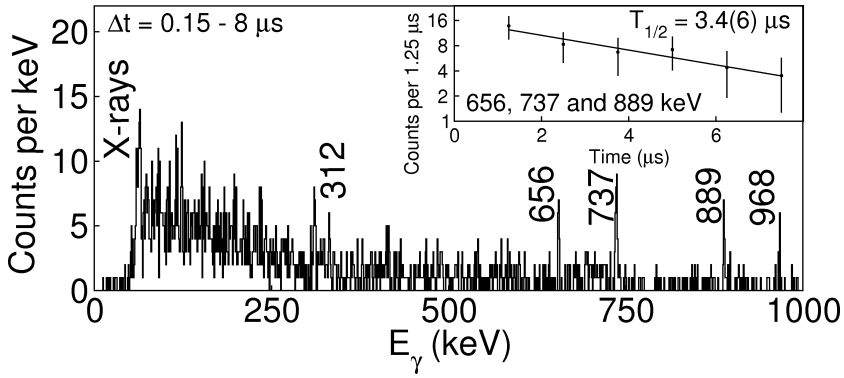

Figure 6.54: Gamma rays associated with ^{202}Ir following implantation using the DGF devices. The inset decay curve is from gates on the 737 and 889 keV transitions.

Comparison with Shell Model Calculations

A shell model calculation for this nuclide is presented in figure 6.55. Notice that an $I^{\pi} = 0^{-}$ state is predicted to be the ground state, counter to the previous systematics prediction [131]. A level scheme cannot be constructed from the available information. It is however probable that the isomer-depopulating transition is of $M2$ character, on the basis that the simplest way in which the isomer can be reproduced is either by decay of $12^{-} \rightarrow 10^{+}$ or $11^{+} \rightarrow 9^{-}$ states. However, both of these decay mechanisms would require considerable adjustment to the predicted excitation energies. All other states would demand even larger changes to the prediction if they are to reproduce the isomer.

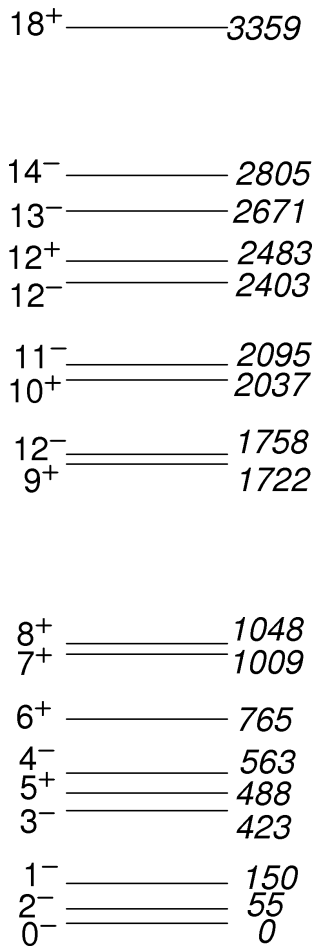

Figure 6.55: Shell model calculation for ^{202}Ir showing predicted near yrast levels up to $I^{\pi} = 18^{+}$.

Given that it is not clear which shell model predicted state corresponds to the observed isomer and also what spin the ground state is, it is not possible to construct a level scheme for this nuclide in the current work. It is concluded here however that the observed X-rays arise due to the internal conversion decay branch of the isomer-depopulating $M2$ transition.

Isomeric Ratio

Although a level scheme has not been established in the current work for ^{202}Ir, it is possible to make a reasonable measurement of the isomeric ratio. Given that the isomer half-life is long when compared to the flight time ($T_{1/2} = 3.4$ μs $\gg ToF \sim$ 300 ns) negligible decays take place in-flight. For the isomeric ratio measurement it is assumed that the most intensely observed γ-ray (737 keV) does not compete with any other

significant decay routes and that this transition has an internal conversion coefficient of $\alpha = 0$. No measurement is made for the $(F - H)$ charge state, due to the limited statistics. The resulting isomeric ratio is found to be $0.7^{+2}_{-3}\%$.

Table 6.21: Measured isomeric ratio of the $I^{\pi} = (11^{-})$ or (12^{+}) isomer in ^{202}Ir, understanding it to decay by an $M2$ transition. The measurement is made using only the 737 keV transition under the assumption that zero decays take place in-flight, that the transition does not compete with other decay paths and that the internal conversion coefficient of the transition is zero.

Charge state	**Isomeric ratio (%)**
$\boldsymbol{I^{\pi} = (11^{-})}$ or $\boldsymbol{(12^{+})}$	
Fully stripped → Fully stripped	0.7^{+2}_{-3}

6.5.13 ^{201}Ir

Setting	**Charge state**	**Number of nuclei implanted**
^{203}Ir	Fully stripped → Fully stripped	65,831
^{202}Os	Fully stripped → Fully stripped	6,950
^{199}Os	Fully stripped → Fully stripped	62,390
^{203}Ir	Fully stripped → H-like	7,764
^{199}Os	Fully stripped → H-like	8,559
^{192}W	Fully stripped → H-like	13,515
^{192}W	Fully stripped → He-like	450

Experimental Information

This nuclide has not been experimentally studied prior to the current work. The γ-rays associated with this nuclide from isomeric decay are presented in figure 6.56. Three characteristic transitions have been observed at energies of 440, 452 and 681 keV. The half-life of the isomer is measured to be $T_{1/2} = 10.5(17)$ ns, suggesting that the decay transition(s) from this isomer is/are significantly converted.

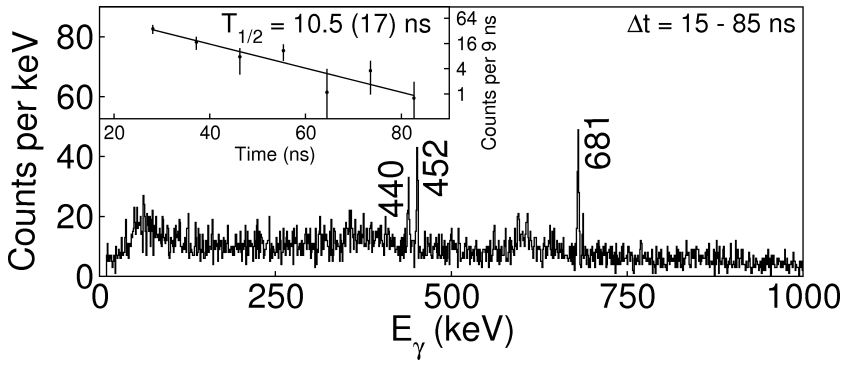

Figure 6.56: Gamma rays associated with ^{201}Ir following implantation using the SR devices. The inset decay curve arises from the 440, 452 and 681 keV transitions.

Isomeric Ratio

In this instance there is considerable uncertainty regarding the branching ratio of transitions. In order to place a limit on the isomeric ratio of the ^{201}Ir isomer measured in this current work it is assumed that the summed intensity of the observed transitions is the total γ ray intensity from the decay of the isomer, that internal conversion coefficients of those transitions are zero, and that there is 100 % transmission of the isomer in-flight. Table 6.22 shows the result for the $(F - F)$ in-flight charge state.

Table 6.22: Minimum limit for the isomeric ratio of the isomer in ^{201}Ir, assuming that the summed intensity of the transitions observed in this work is the total γ ray intensity from the decay of the isomer, that the internal conversion coefficients of those transitions are zero and that there is 100 % transmission of the isomer in-flight.

Charge state	**Isomeric ratio (%)**
$\boldsymbol{I^{\pi} = unknown}$	
Fully stripped → Fully stripped	$\geq 2.7^{+22}_{-24}$

6.5.14 ^{200}Ir

Setting	Charge state	Number of nuclei implanted
^{203}Ir	Fully stripped → Fully stripped	120,099
^{199}Os	Fully stripped → Fully stripped	154,040
^{203}Ir	Fully stripped → H-like	10,811
^{199}Os	Fully stripped → H-like	24,730
^{192}W	Fully stripped → H-like	43,661
^{192}W	Fully stripped → He-like	1,023
^{202}Os	H-like → Fully stripped	224

Experimental Information

No experimental studies have been reported prior to the current study on this nuclide. The γ rays associated with the implantation of ^{200}Ir are shown in the spectrum of figure 6.57 (top). Two transitions are observed, one at 120 and the other at 127 keV. These two transitions are measured to have different half-lives, indicating that they originate from two separate isomers. The half-life associated with the 120 keV transition is $T_{1/2} = 17.1(12)$ ns and the 127 keV is $T_{1/2} = 28.5(15)$ ns.

Note that although the SR timing devices are used for these measurements, the 120 and 127 keV transitions are intense enough to be observed even with the reduced efficiency at low energies. However, as the efficiency continues to drop for decreasing energies, any X-rays that might be associated with them still would not be expected to be detected.

If one of the isomers feeds the other, one of the decay curves would be expected to express a two-component decay shape. Such decay behaviour has not been observed (see figure 6.57 (insets)). Furthermore assuming 100 % feeding of one of the transitions to the other, one expects to observe $\sim$ 16 coincidences between the two transitions in the spectrum in figure 6.57 (bottom). Figure 6.57 (bottom) shows γ-rays observed in the same event as the 120 keV transition gives no such coincidence. It is thus interpreted that that they decay through independent routes.

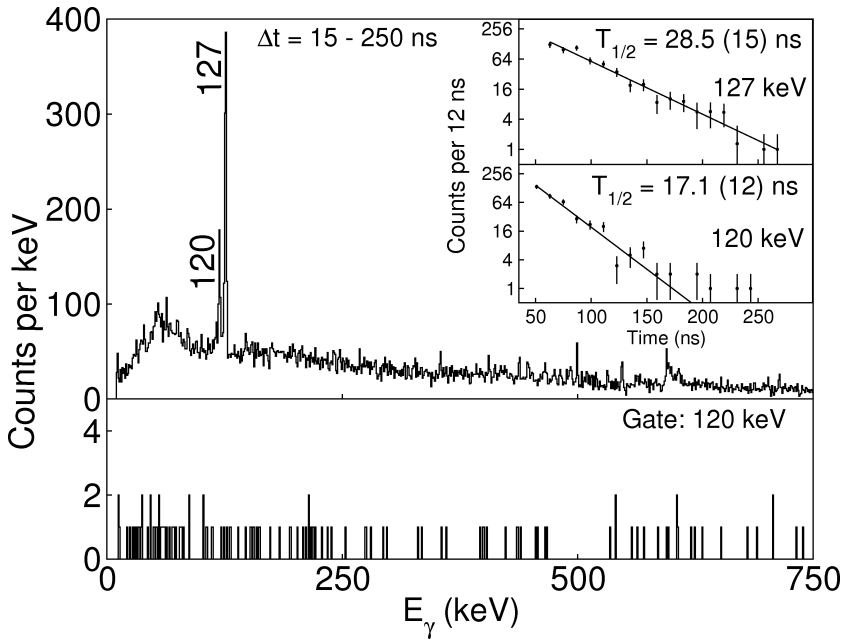

Figure 6.57: Gamma rays associated with ^{200}Ir following implantation using the SR devices. **Top:** gamma-ray single events. The top inset decay curve arises from the 127 keV transition, the lower from the 120 keV transition. **Bottom:** gamma-rays observed in the same event as an observed 120 keV transition over the range $\Delta t = 15 \rightarrow 250$ ns following implantation.

Isomeric Ratios

When assuming 100 % transmission and that the 120 and 127 keV transitions each directly depopulate one of the two ^{200}Ir isomers observed in this work, non-physical results are measured (i.e. the isomeric ratio is found to be greater than 100 %). It has been concluded by the author that this could be due to the significant uncertainty regarding γ-ray detection efficiency with the SR TDC devices at low energies. On this basis, this information is not considered to be a reliable indication of whether or not the isomers are being depopulated by transitions unobserved by the currently described experiment.

Isomeric ratio measurements have been made for the $(F-F)$ charge state for both of the ^{200}Ir isomers observed in this work, assuming that each isomer *is* depopulated by an unobserved transition; 100 % transmission of the isomers through the FRS; that the 120 and 127 keV γ-ray transitions have internal conversion coefficients of zero and are the only branch of decay from the isomers they are associated with. The isomeric ratio values are given in Table 6.23. It is assumed that if there are transitions emitted

following the decay of these isomers, which have not been observed by the present work that the energy of such transitions is less than 250 keV (this is the energy at which the SR efficiency problem becomes pronounced when compared to the DGF efficiency).

Table 6.23: Minimum isomeric ratios of isomers in ^{200}Ir. These assume 100 % transmission of the isomers; the existence of isomer-depopulating transitions unobserved by the present work; zero internal conversion of the 120 and 127 keV transitions and that they are each the only branch of decay from the two isomers.

Charge state	**Isomeric ratio (%)**
$\boldsymbol{I^{\pi} = unknown}$ **(**$\boldsymbol{T_{1/2} = 17.1}$ ns**)**	
Fully stripped → Fully stripped	$\geq 3.5^{+19}_{-22}$
$\boldsymbol{I^{\pi} = unknown}$ **(**$\boldsymbol{T_{1/2} = 28.5}$ ns**)**	
Fully stripped → Fully stripped	$\geq 6.4^{+20}_{-25}$

6.5.15 ^{199}Ir

Setting	**Charge state**	**Number of nuclei implanted**
^{203}Ir	Fully stripped → Fully stripped	54,601
^{199}Os	Fully stripped → Fully stripped	196,253
^{192}W	Fully stripped → Fully stripped	63,814
^{203}Ir	Fully stripped → H-like	8,049
^{199}Os	Fully stripped → H-like	34,905
^{202}Os	H-like → Fully stripped	689
^{192}W	Fully stripped → He-like	1,090

Experimental Information

This nuclide has no previously reported excited states. The tentatively observed isomer from reference [54] has been discounted following the discussion in section 6.4.2. A previously unreported isomer has been observed in the current work, this is shown in figure 6.58.

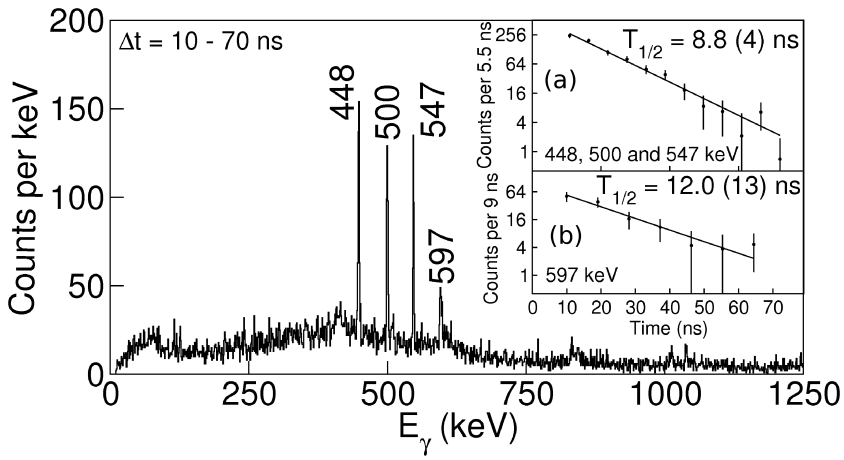

Figure 6.58: Gamma rays associated with ^{199}Ir following implantation using the SR devices. The time curve of inset (a) arises from the 448, 500 and 547 keV γ-rays, the curve of inset (b) comes from the 597 keV.

Figure 6.58 identifies transitions at the energies 448, 500, 547 and 597 keV from isomeric decay in ^{199}Ir. The intensity of the 597 keV transition is distinctly lower than the other transitions. The half-life, measured for the 448, 500 and 547 keV transitions, is found to be $T_{1/2} = 8.8(4)$ ns, while the 597 keV transition gives a value $T_{1/2} = 12.0(13)$ ns. It is thus not clear whether the 597 keV transition is emitted due to the decay of a second isomer.

Coincidence measurements have been performed, see figure 6.59. These indicate that the 500 keV transition is in self-coincidence, suggesting that it is a doublet. Summing the γ rays observed in the range $\Delta t = 10 \rightarrow 70$ ns when a 448, 500 or 547 keV transition is observed in the same range (see figure 6.59 (d)), there is tentative coincidence with the 597 keV transition; this does not eliminate or confirm the possibility that there are two isomers. Given that the time range $10 \rightarrow 70$ ns is near the prompt flash, where the statistics are very sensitive to the data selection, the two sigma agreement of the two half-life measurements has in this work been considered to be from the same isomer. In this work it concluded that only one isomer is observed, but a second is possible. The weighted mean of the half-life measurements is $T_{1/2} = 9.1(4)$ ns.

Caamaño *et al.* [54] have previously measured an isomer in ^{200}Pt to have a half-life of 10.3(24) ns, which was claimed as "the shortest-lived isomer yet observed as a primary product of projectile fragmentation". This isomer in ^{199}Ir in the present work would surpass this limit.

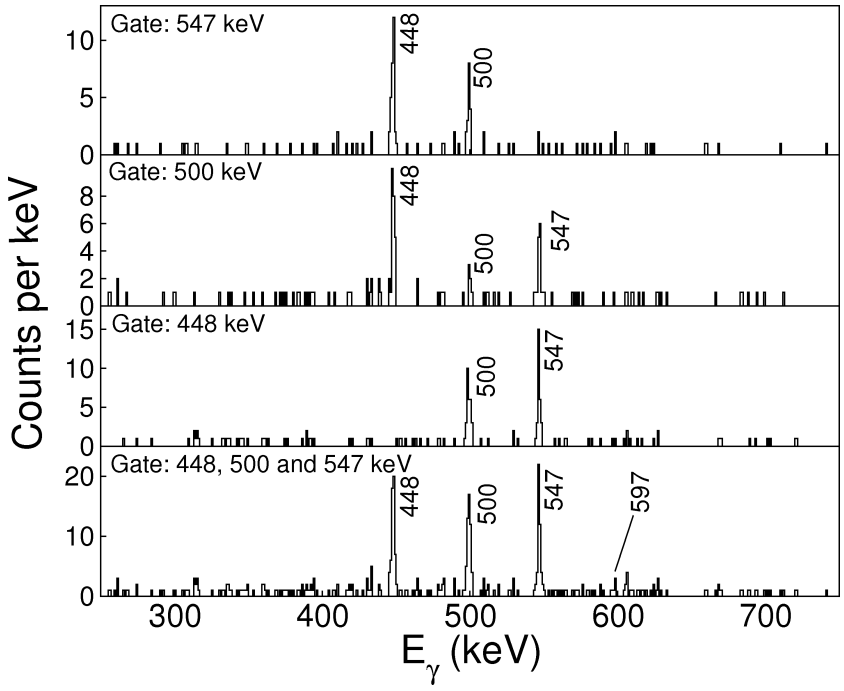

Figure 6.59: Gamma-ray coincidence in ^{199}Ir, the gated transition(s) is/are named within each of the four spectra. The gated and the coincident transitions are all emitted in the time range $\Delta t = 10 \rightarrow 70$ ns following implantation.

Isomeric Ratio

It is likely that the isomer in ^{199}Ir is depopulated by a transition which is unobserved in this work. In the range $\alpha = 0 \rightarrow \infty$ and assuming any one of the observed transitions directly depopulates the isomer it is measured in the current work that the isomeric ratio is non-physical, i.e. it is greater than 100 %.

Assuming that a transition unobserved by the present work depopulates the isomer; 100 % transmission of the isomer; that the 448 keV transtion has an internal convesion coefficient of zero and a branching ratio of 100 % an isomeric ratio is measured for the $(F - F)$ charge state, this is found to be 1.6^{+11}_{-12} %, see Table 6.24. It is determined that the energy of an unobserved tansition is likely to be less than 250 keV, as this is where the efficiency reduction due to using the SR timing devices becomes pronounced.

Table 6.24: The lower limit for the isomeric ratio of the isomer in ^{199}Ir. This assumes that a transition unobserved in the present work depopulates the isomer; 100 % transmission of the isomer; that the 448 keV transition has an internal conversion coefficient of zero and that its branching ratio is 100 %.

Charge state	Isomeric ratio (%)
$I^{\pi} = unknown$	
Fully stripped → Fully stripped	$\geq 1.6^{+11}_{-12}$

6.5.16 ^{195}Ir

Setting	Charge state	Number of nuclei implanted
^{206}Hg	H-like → Fully stripped	7,962

There have been several studies performed previously, which have measured states in ^{195}Ir [132–134]. Importantly the yrast $I^{\pi} = 11/2^{-}$ state has been observed to be isomeric, at an excitation energy of 100 keV with a half-life is $T_{1/2} = 3.8(2)$ hours. It is likely that the currently observed isomer will decay into this isomer, The ground state spin-parity of this nuclide is $I^{\pi} = 3/2^{+}$ [132–134].

Experimental Information

In the γ-ray spectrum shown in figure 6.60, transitions are detected at 268, 405, 477, 538 and 567 keV and the half-life associated with these transitions is $T_{1/2} = 4.4(6)$ μs.

Isomeric Ratio

As the half-life of the isomer is considerably larger than the FRS transmission time ($T_{1/2} = 4.4$ μs *c.f.* $ToF \sim 300$ ns), losses due to in-flight decays can be essentially neglected. Within uncertainties, the intensity of all of the transitions are identical (assuming $\alpha \simeq 0$ for the internal conversion of these transitions), see Table 6.31. The isomeric ratio is measured in Table 6.25, this comes to 1.1^{+2}_{-3} %, assuming that all the transitions have a branching ratio of 100 %.

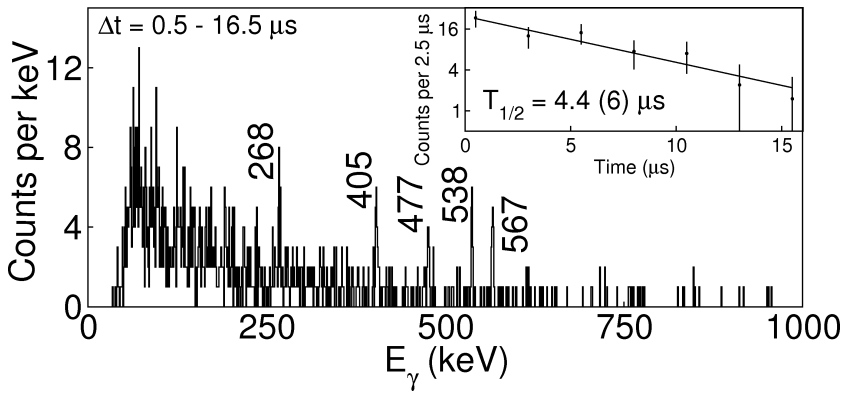

Figure 6.60: Gamma rays associated with ^{195}Ir following implantation using the DGF devices. The inset decay curve is taken from the sum of the 268, 405, 477, 538 and 567 keV transitions.

Table 6.25: Isomeric ratio of the isomer in ^{195}Ir. This assumes that the branching ratios of all the observed transitions is 100 % and that all of their internal conversion coefficients are approximately zero.

Charge state	**Isomeric ratio (%)**
$\boldsymbol{I^{\pi} = unknown}$	
H-like → Fully stripped	1.1^{+2}_{-3}

6.5.17 ^{199}Os

Setting	**Charge state**	**Number of nuclei implanted**
^{203}Ir	Fully stripped → Fully stripped	9,530
^{202}Os	Fully stripped → Fully stripped	3,933
^{199}Os	Fully stripped → Fully stripped	11,491
^{192}W	Fully stripped → Fully stripped	510
^{199}Os	Fully stripped → H-like	719
^{192}W	Fully stripped → H-like	2,405

Experimental Information

The ground state half-life of this nuclide has been measured previously [135], but no excited states have been reported prior to the current work. This study offers the first information on excited states with the observed γ rays presented in the spectrum shown in figure 6.61. Transitions are observed at 379, 402, 425, 736 and 971 keV. The half-life associated with the decay curve of the sum of all of these transitions is $T_{1/2}$ = 25.2(20) ns. As this is another isomer whose half-life is considerably shorter than the FRS transmission time, it is understood that the direct decay conversion electron decay branch(es) is/are large.

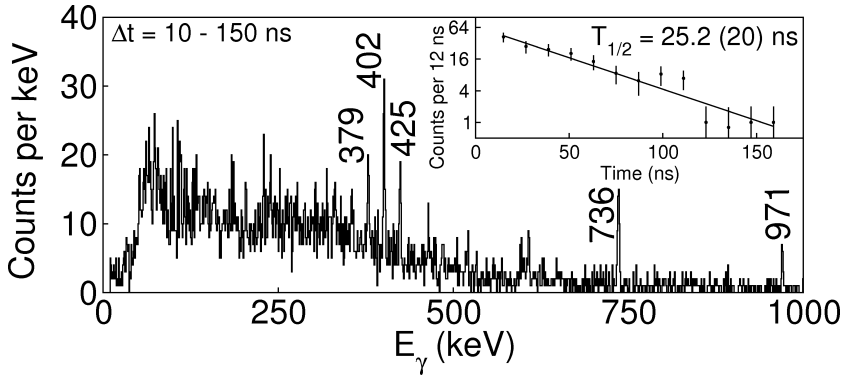

Figure 6.61: Gamma rays associated with ^{199}Os following implantation using the SR devices. The inset decay curve arises from all of the transitions.

Isomeric Ratio

A limit has been placed on the isomeric ratio of the isomer observed in ^{199}Os, this limit assumes 100 % transmission of the isomer in-flight and that the 402 keV transition has a branching ratio of 100 % with an internal conversion coefficent of zero (the 402 keV transition is used as it is the most intensely emitted by ^{199}Os of those observed in this work, see Table 6.31).

Table 6.26: The lower limit for the isomeric ratio of the isomer in ^{199}Os. This assumes that there is 100 % transmission of the isomer in-flight, that the branching ratio of the 402 keV transition is 100 % and that its internal conversion coefficient is zero.

Charge state	Isomeric ratio (%)
$I^{\pi} = unknown$	
Fully stripped → Fully stripped	$\geq 1.4^{+6}_{-7}$

6.5.18 ^{198}Os

Setting	Charge state	Number of nuclei implanted
^{203}Ir	Fully stripped → Fully stripped	28,728
^{202}Os	Fully stripped → Fully stripped	3,081
^{199}Os	Fully stripped → Fully stripped	30,794
^{192}W	Fully stripped → Fully stripped	3,496
^{199}Os	Fully stripped → H-like	2,906
^{192}W	Fully stripped → H-like	8,805

Experimental Information

There have been no previous studies on this nuclide. The γ-ray spectrum in figure 6.62 (top) shows transitions observed at 330, 412, 447, 465, 473, 527, 544, 607, 608 and 886 keV. The 607 and 608 keV transitions are close in energy such that they cannot be independently resolved. By measuring the additional width of the $FWHM$ than for a single peak of similar energy, it has been determined that the two transitions are approximately 1 keV apart, centred about 607.79 keV. The γ-γ coincidence spectrum of figure 6.62 (bottom) proves the existence of the doublet, it also shows that these transitions are not in coincidence with the 412, 473 and 886 keV peaks. The 465 keV coincidence spectrum (shown in figure 6.62 (middle)) shows that this transition is emitted in coincidence with all of the other observed transitions in this nuclide. Other findings regarding the energy of the transitions are that the sum energy of the 412 and 473 keV transitions match the energy of the 886 keV, within

experimental errors. The sum energy of the 607 and 608 keV transitions similarly match that of the 886 (or 412-473) plus the 330 keV transition. These are indications of parallel decay branches and are backed by γ-γ coincidence data.

Decay curves have been fitted for two groups of transitions. The 465, 607 and 608 keV transitions are measured to have a half-life of $T_{1/2} = 16.1(8)$ ns and the 447, 527 and 544 keV transitions are measured to have a half-life of $T_{1/2} = 18.0(28)$ ns. It will be in the next section, where the proposed decay scheme is discussed, that there are most likely two isomers in the present work. The degree of population of the higher-lying isomer (measured by the 447, 527 and 544 keV transitions) is small enough that it has no significant impact on the measurement of the lower, which was fitted as a single pure exponential decay curve.

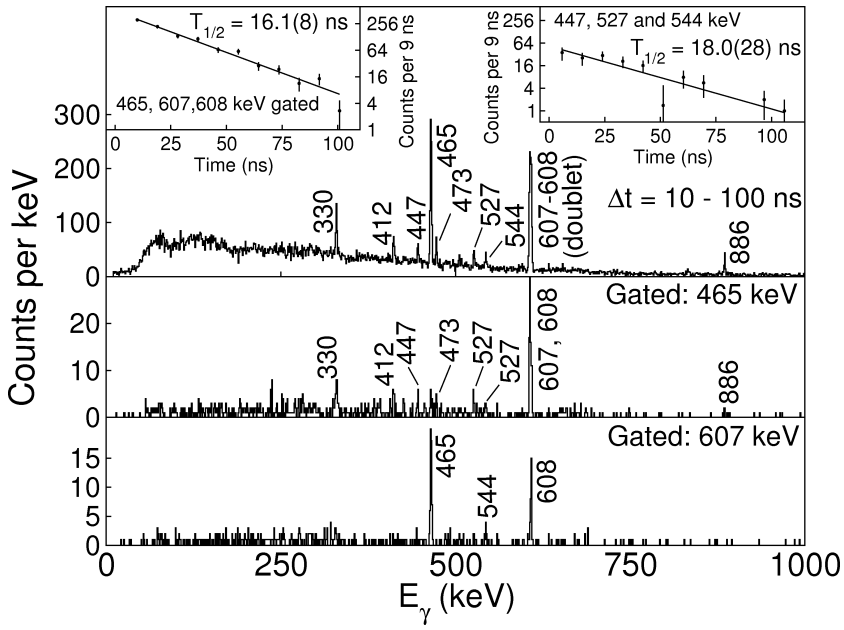

Figure 6.62: Gamma rays associated with ^{198}Os following implantation using the SR devices. **Top:** gamma-ray single events. The left inset decay curve arises from the 465, 607 and 608 keV transitions, the right from the 447, 527 and 544 keV. **Middle:** gamma rays observed in the range $\Delta t = 10 - 100$ ns in events where a 465 keV transition has already been observed in the same time range. **Bottom:** gamma rays observed in the range $\Delta t = 10 - 100$ ns in events where a 607 keV transition has already been observed in the same time range.

Interpretation

For this nuclide, level energy systematics have been used to shed light on the possible decay for the observed transitions. The comparison here is drawn with ^{200}Pt [54], which has 2 protons more than ^{198}Os. The ^{200}Pt level scheme taken from reference [54] and the suggested level scheme for ^{198}Os are both shown in figure 6.63.

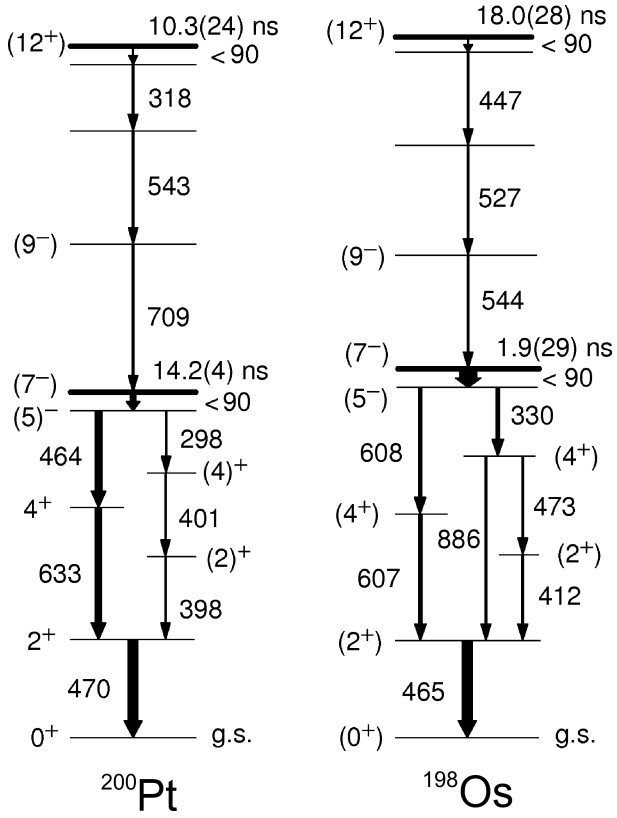

Figure 6.63: The interpreted ^{198}Os decay scheme and comparison with the scheme of ^{200}Pt [54, 98, 99]. The widths of parallel γ-ray transitions are indications of the transition intensities.

Two isomers have been observed in ^{198}Os, one feeding the other. The first excited state in ^{200}Pt, a 470 keV transition, is close in energy to the strong 465 keV transition observed in the current work. The parallel decay branches from the $I^{\pi} = (5^{-})$ state, when summed, are consistent with the intensity of the 465 keV transition and are also observed in coincidence with the decay of the first excited state. This is analogous to the decay cascade from the ^{200}Pt $I^{\pi} = (5)^{-}$ isomer down to the $I^{\pi} = 2^{+}$ state. In the proposed ^{198}Os case however, there is an additional transition as the 886 keV $E2$ transition also competes in decaying from the $I^{\pi} = (4_2^{+})$ state.

In ^{200}Pt a second isomer (at $I^{\pi} = (12^{+})$) is observed. The 447, 527 and 544 keV

transitions in the current work are the possible analogs of this cascade. Their observed intensities are significantly smaller than those of the transitions from the lower-lying isomer. This interpretation requires that an unobserved, low-energy transition depopulates each of the two observed isomers. A precautionary note is made in that the two measured half-lives ($T_{1/2}$ = 16.1(8) ns for $I^{\pi} = (5^{-})$ and $T_{1/2}$ = 18.0(28) ns for $I^{\pi} = (12^{+})$) are equal, within experimental uncertainties.

Isomeric Ratios

Limits have been placed on the isomeric ratios of these two isomers (see Table 6.27). For the 447 and 527 keV transitions of the $I^{\pi} = (12^{+})$ isomer, it is assumed that the conversion coefficients are zero. Only the $(F - F)$ charge state has been considered as K_{α} is unknown, this has an affect on the $(F - H)$ in-flight decay rate.

For the $I^{\pi} = (12^{+})$ isomer the minimum isomeric ratio (i.e. assuming 100 % isomer transmission) is 0.4^{+2}_{-2} %. For the $I^{\pi} = (5^{-})$ isomer this limit is 5.4^{+21}_{-25} %.

At the other extreme, if an isomeric ratio of 100 % is assumed, the minimum internal conversion coefficients would be $\alpha = 1.7$ and 0.95 for the $I^{\pi} = (12^{+})$ and (5^{-}) states, respectively. This corresponds to a maximum decay transition energy of 150 keV for the $I^{\pi} = (5^{-})$ isomer. A maximum of 250 keV is determined for the $I^{\pi} = (12^{+})$ in the present work, it is assumed that higher-energy transitions would have been directly detected during the experiment.

Table 6.27: Minimum isomeric ratio of the $I^{\pi} = (5^{-})$ and (12^{+}) isomers in ^{198}Os. This assumes that the 447 and 527 keV transitions have zero internal conversion.

Charge state	**Isomeric ratio (%)**
$\boldsymbol{I^{\pi} = (12^{+})}$	
Fully stripped → Fully stripped	$\geq 0.4^{+2}_{-2}$
$\boldsymbol{I^{\pi} = (5^{-})}$	
Fully stripped → Fully stripped	$\geq 5.4^{+21}_{-25}$

6.5.19 ^{197}Os

Setting	Charge state	Number of nuclei implanted
^{203}Ir	Fully stripped → Fully stripped	50,568
^{199}Os	Fully stripped → Fully stripped	74,154
^{192}W	Fully stripped → Fully stripped	9,537
^{199}Os	Fully stripped → H-like	5,186
^{192}W	Fully stripped → H-like	18,677
^{202}Os	H-like → Fully stripped	562

Experimental Information

The current work represents the first reported spectroscopic information of states in ^{197}Os. The γ-rays observed in association with the implanted ^{197}Os nuclei are shown in figure 6.64.

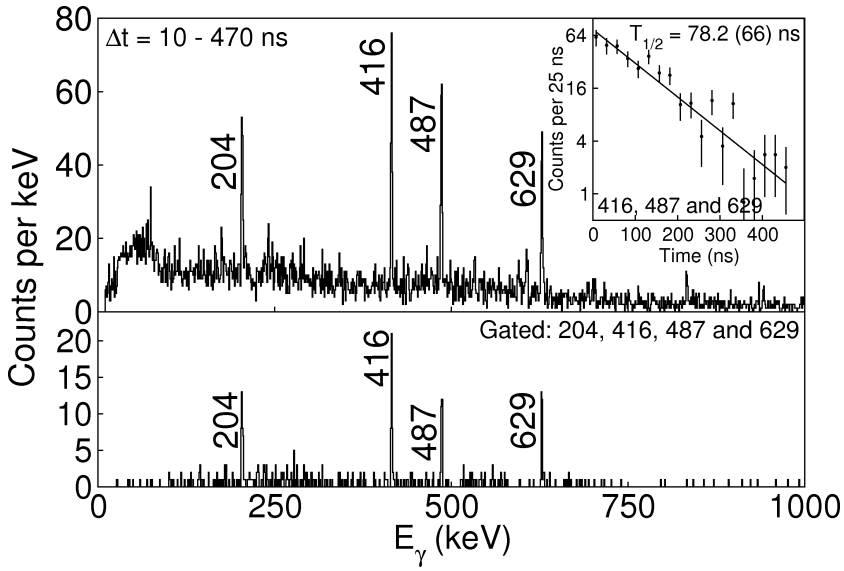

Figure 6.64: Gamma rays associated with ^{197}Os following implantation using the SR devices. **Top:** gamma-ray single events. The inset decay curve arises from the 416, 487 and 629 keV transitions. **Bottom:** gamma-rays observed in the same event as either a 204, 416, 487 or 629 keV transition, where these transitions and those plotted in the spectrum are all observed in the time range $\Delta t = 10 \rightarrow 470$ ns following implantation.

Transitions have been observed at 204, 416, 487 and 629 keV. The isomer half-life has been fitted using the three highest energy transitions, and is measured to be $T_{1/2} = 78.2(66)$ ns. As shown in figure 6.64 (bottom), all of the four transitions are observed to be in mutual coincidence.

Isomeric Ratio

It is assumed that all of the observed transitions from a single cascade, and for the purposes of the isomeric ratio determination, it is also assumed that the internal conversion branch of all of these transitions is zero. It is not clear from the current work whether one of the observed transitions is emitted from the isomer directly, or if there is a low-energy unobserved transition (if the transition exists it likely has an energy $E_\gamma < 250$ keV). When measuring the isomeric ratio assuming zero in-flight decays and that the internal conversion coefficient of the observed decays is zero the isomeric ratio is found to be 0.6^{+2}_{-3} % for the $(F - F)$ charge state, this is shown in Table 6.28

Table 6.28: Range for the isomeric ratio of the isomer in ^{197}Os. This assumes zero internal conversion of the observed transitions and 100 % transmission of the isomer.

Charge state	**Isomeric ratio (%)**
$\boldsymbol{I^\pi = unknown}$	
Fully stripped → Fully stripped	$\geq 0.6^{+2}_{-3}$

6.5.20 ^{193}Os

Setting	**Charge state**	**Number of nuclei implanted**
^{206}Hg	H-like → Fully stripped	1,810
^{203}Ir	H-like → Fully stripped	243

Experimental Information

The isomer observed in the present work has not been reported in previous studies of this nuclide [136, 137]. The current findings are shown in the spectrum shown in

figure 6.65. There is single transition observed at 242 keV, it has a measured half-life of $T_{1/2} = 132(29)$ ns.

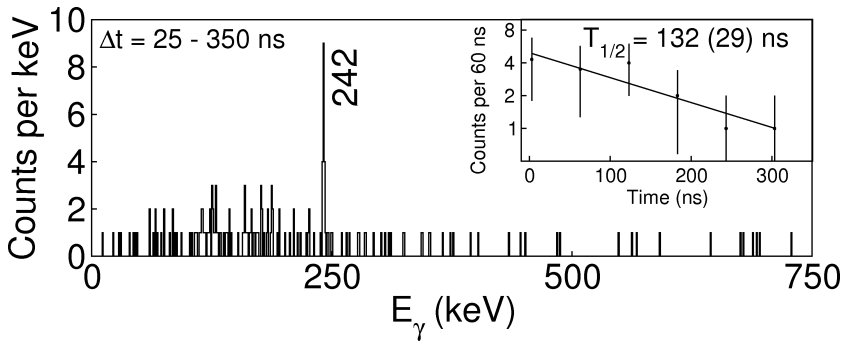

Figure 6.65: Gamma rays associated with ^{193}Os following implantation using the SR devices. The inset decay curve arises from the 242 keV transition.

Isomeric Ratio

A limit has been placed on the isomeric ratio of the isomer in ^{193}Os. This measurement assumes 100 % transmission of the isomer, an internal conversion coefficient of zero for the 242 keV transition and a branching ratio of 100 %.

Table 6.29: Minimum limit on the isomeric ratio of the isomer in ^{193}Os, assuming 100 % transmission of the isomer, an internal conversion coefficient of zero for the 242 keV transition and a branching ratio of 100 %.

Charge state	**Isomeric ratio (%)**
$\boldsymbol{I^{\pi} = unknown}$	
H-like → Fully stripped	$\geq 7.3^{+36}_{-41}$

6.5.21 ^{196}Re

Setting	Charge state	Number of nuclei implanted
^{203}Ir	Fully stripped → Fully stripped	5,049
^{202}Os	Fully stripped → Fully stripped	144
^{192}W	Fully stripped → Fully stripped	7,233
^{192}W	Fully stripped → H-like	1,590
^{185}W	Fully stripped → H-like	354

Experimental Information

Only one previous work has experimentally measured ^{196}Re [135], this observed only the ground state, assigned a spin-parity of $I^{\pi} = 1^{+}$ or 2^{-}. The current work has observed rhenium X-rays associated with this nuclide, indicating the presence of a highly converted transition from a decaying isomer (see figure 6.66).

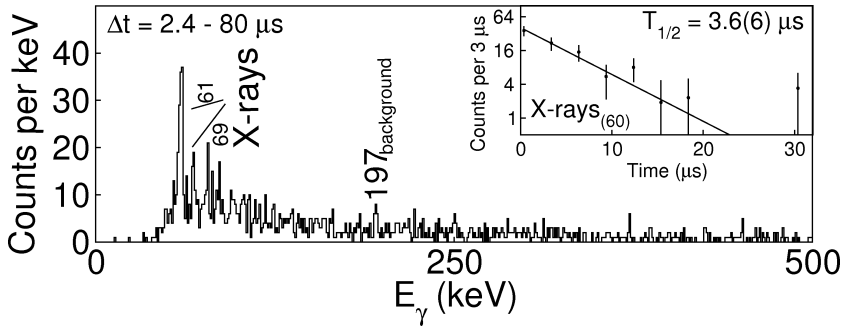

Figure 6.66: Gamma rays associated with ^{196}Re following implantation using the DGF devices. The inset decay curve arises from the 61 keV X-rays.

The half-life associated with the decay of the X-rays is $T_{1/2} = 3.6(6)$ μs. As only X-rays have been observed there has been no attempt to determine an isomeric ratio for the isomer in this work.

6.5.22 ^{191}W

Setting	Charge state	Number of nuclei implanted
^{199}Os	Fully stripped → Fully stripped	25,988
^{192}W	Fully stripped → Fully stripped	5,737
^{192}W	Fully stripped → H-like	913
^{185}Lu	Fully stripped → H-like	1,741
^{203}Ir	H-like → Fully stripped	599
^{199}Os	H-like → Fully stripped	1,484

Experimental Information

The current results are the first reported experimental measurement on excited states in ^{191}W. The γ rays associated with the implanted nuclei are shown in the spectrum in figure 6.67. Transitions are observed at 67 and 168 keV, along with strong K_α and K_β X-rays. The measured half-life of the isomer is $T_{1/2} = 0.36(2)$ μs. It is not possible to balance the intensity of the two observed γ ray transitions when assigning them any combination of multipolarities. It is possible that there are unobserved transitions. Due to this, the branching ratios are unknown. It is not clear by what proportion each transition is responsible for X-ray emission.

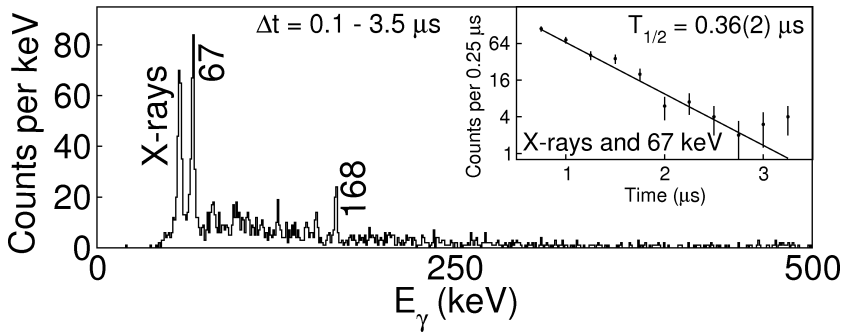

Figure 6.67: Gamma rays associated with ^{191}W following implantation using the DGF devices. The inset decay curve arises from the X-rays and the 67 keV transition.

6.5.23 ^{189}Ta

Setting	Charge state	Number of nuclei implanted
^{192}W	Fully stripped → Fully stripped	7,539
^{185}Lu	Fully stripped → Fully stripped	1,011
^{185}Lu	Fully stripped → H-like	558

Experimental Information

Previously there has been a measurement of the ground state of ^{189}Ta, which was assigned a spin-parity of $I^{\pi} = (7/2^{-})$ [138]. The findings of the current study are presented in figure 6.68 (top). Transitions have been observed at 154, 284, 343, 389 and 482 keV. Fitting the decay curve of the 389 and 482 keV transitions a half-life of $T_{1/2} = 0.58(22)$ μs is deduced for the isomer. Gamma ray γ-γ coincidence measurements have been performed for transitions detected in the time range $\Delta t = 0.2 \rightarrow 6.5$ μs following implantation and arriving within 1 μs of one another. Figure 6.68 (bottom) shows γ rays observed in coincidence with the 154, 284, 343, 389 or 482 keV transitions; each of these transitions is observed to be in tentative coincidence.

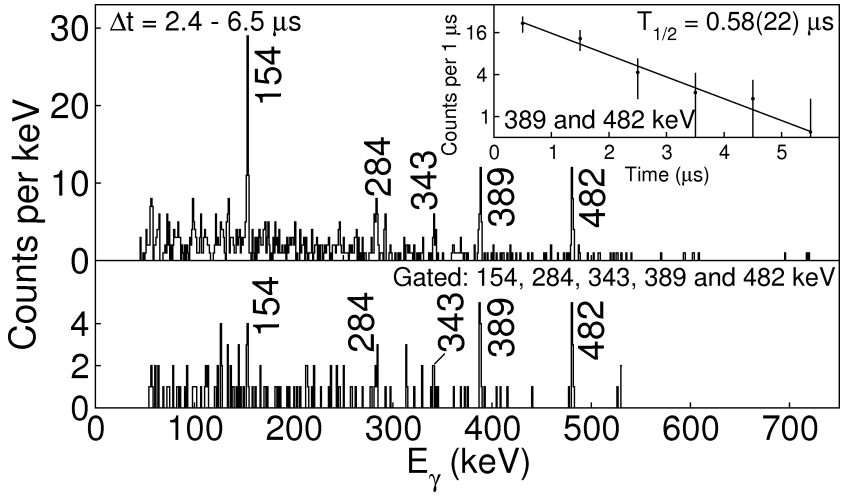

Figure 6.68: Gamma rays associated with ^{189}Ta following implantation using the DGF devices. **Top:** gamma ray singles events, the inset decay is from the 389 and 482 keV transitions. **Bottom:** gamma-gamma coincidence for transitions observed in the range $\Delta t = 0.2 \rightarrow 6.5$ μs and detected within 1 μs of either a 154, 284, 343, 389 or 482 keV transition.

Isomeric Ratio

Assuming 100 % transmission; no intenal conversion in the observed decays and using only the 389 and 482 keV transition to get the yield, a limit on the isomeric ratio has been estimated, this is 2.2^{+7}_{-8} % for the $(F-F)$ charge state (see Table 6.30).

Table 6.30: Isomeric ratio of the isomer in ^{189}Ta. This uses only the 389 and 482 keV transitions and assumes they have branching ratios of 100 % and internal conversion coefficents of zero.

Charge state	**Isomeric ratio (%)**
$\boldsymbol{I^{\pi} = unknown}$	
Full → Full	2.2^{+7}_{-8}

6.6 A Summary of the Observed Isomers

Details of the discussed isomers are given in Table 6.31. An effort has been made to highlight values which are subject to assumptions or specific conditions, in all of these cases a full explanation can be found in the previous discussion of the concerned isomer. The uncertainty on γ-ray energy measurements is considered to be ~ 0.5 keV, this is understood through the accuracy of measurements on calibration data.

Table 6.31: A summary of the γ-spectroscopy investigations.

$\mathbf{E_\gamma}$ **(keV)**[a]	$\boldsymbol{I_\gamma}$[b]	$\boldsymbol{\alpha^c_{TOT}}$	$\boldsymbol{\alpha_K}$[c]	**BR**	$\boldsymbol{T_{1/2}}$[d]	$\boldsymbol{IR}$ **(%)**[e]
^{206}**Tl,** $\boldsymbol{I^{\pi} = (5^+)}$						
265.4	89(6)[f]	0.160	0.086	1[c]	71(4) ns[g]	$_{(H-He)}14.2^{+21}_{-32}$
452.9	90(6)	0.011	0.009	0.93(6)[c]		
685.8	100(7)	0.014	0.011	1[c]		

Continued on Next Page...

Table 6.31 – Continued

E_γ (keV)[a]	I_γ[b]	α^c_{TOT}	α_K[c]	BR	$T_{1/2}$[d]	IR (%)[e]
^{206}Hg, $I^\pi = (10^+)$						
100.9	1(0)[f]	5.660	0.610	0.79(5)	112(4) ns[g]	$_{(F-F)}1.9^{+5}_{-6}$
363.4	21(1)	0.062	0.040	1		$_{(F-H)}2.5^{+8}_{-10}$
1156.3	28(1)	0.002	0.002	1		
1257.2	8(1)	0.008	0.007	0.21(5)		
^{206}Hg, $I^\pi = 5^-$						
1033.7	100(2)	0.013	0.01	1	2.09(2) μs[g]	$_{(F-F)}21.9^{+11}_{-28}$
1068.0	99(2)	0.005	0.040	1		$_{(F-H)}21.8^{+13}_{-29}$
^{205}Hg, $I^\pi = (23/2^-)$						
227.6	8(1)	0.054	0.044	0.12(2)	5.89(18) μs[g]	$_{(F-F)}3.3^{+2}_{-4}$
722.6	11(1)	0.004	0.004	1		$_{(F-H)}3.3^{+3}_{-5}$
810.0	100(3)	0.023	0.016	1		
950.2	87(3)	0.007	0.005	0.88(2)		
^{205}Hg, $I^\pi = 13/2^+$						
49.0[c]	-	0.600	0.000	0.19[c]	1.09(4) ms[c]	$_{(F-F)}19.3^{+19}_{-34}$
161.4[c]	-	12.03	8.580	0.58(6)[c]		$_{(F-H)}21.6^{+31}_{-47}$
210.3[c]	-	2.710	0.407	0.42(5)[c]		
378.9	37(2)	0.055	0.036	1[c]		
467.5[c]	-	0.116	0.095	1[c]		
878.8[c]	-	0.008	0.006	0.06(1)[c]		
967.0	10(2)	0.018	0.015	0.94(2)[c]		
1014.7	33(2)	0.006	0.005	0.81[c]		
^{204}Hg, $I^\pi = (14^+)$[h]						
422.7[i]	35(7)	-	-	-	20(2) ns[g]	-
597.2	100(14)	-	-	-		
608.6[i]	20(6)	-	-	-		
964.8	61(14)	-	-	-		
1013.9	30(10)	-	-	-		

Continued on Next Page...

Table 6.31 – Continued

E_γ (keV)[a]	I_γ[b]	α^c_{TOT}	α_K[c]	BR	$T_{1/2}$[d]	IR (%)[e]
^{204}Hg, $I^\pi = 7^-$						
109.7[c]	-[f]	0.338	0.270	1	6.7(5) ns[c]	-
436.6	59(10)	0.038	0.027	1		
691.8	36(9)	0.038	0.027	1		
1067.7	36(10)	0.013	0.010	1		
^{203}Hg, $I^\pi = (13/2^+)$						
341.0	57(2)	0.937	0.720	1	21.9(10) μs[g]	$_{(H-H)}14.2^{+9}_{-20}$
591.1	100(3)	0.018	0.014	1		$_{(H-He)}9.3^{+12}_{-19}$
^{205}Au, $I^\pi = (19/2^+)$						
34.2	0[f]	855.0	0	0.89(2)	163(5) ns[g]	$_{(F-F)}7.7^{+17}_{-22}$
243.4	4(0)[f]	0.622	0.511	0.19(2)		$_{(F-H)}7.6^{+7}_{-12}$
736.9	42(2)	0.033	0.027	1		$_{(F-He)}4.2^{+6}_{-9}$
928.3	24(2)	0.003	0.002	0.15(1)		
946.1	100(3)	0.006	0.005	1		
962.5	100(5)	0.002	0.002	0.63(1)		
962.5	19(5)	0.015	0.011	0.11(2)		
980.2	25(2)	0.016	0.013	0.81(2)		
1171.5	34(2)	0.002	0.001	0.22(1)		
^{204}Au, $I^\pi = unknown$						
96.9[i]	20(8)	-	-	-	2.1(3) μs[g]	-
276.6[i]	32(10)	-	-	-		
427.0[i]	15(7)	-	-	-		
704.4[i]	34(14)	-	-	-		
839.0	100(15)	-	-	-		
976.6	93(15)	-	-	-		
^{203}Au, $I^\pi = unknown$						
562.8	100(6)	-	-	-	140(44) μs[g]	$_{(F-F)}2.5^{+8}_{-10}$

Continued on Next Page...

Table 6.31 – Continued

E_γ (keV)[a]	I_γ[b]	α^c_{TOT}	α_K[c]	BR	$T_{1/2}$[d]	IR (%)[e]
^{202}Au, I^π = *unknown*						
137.8[f]	21(6)[f]	-	-	-	13.1(5) ns[g]	-
414.2	100(5)	-	-	-		
^{201}Au, I^π = *unknown*						
378.2	58(17)	-	-	-	$\sim 10^2$ μs[g]	-
638.0	100(34)	-	-	-		
^{204}Pt, $I^\pi = (10^+)$						
96.1	1.8(3)[f]	5.670	0.727	0.83(2)	146(14) ns[g]	$_{(F-F)}8.7^{+22}_{-28}$
1060.8	20.7(11)	0.002	0.002	1		$_{(F-H)}9.7^{+29}_{-36}$
1157.5	3.7(5)	0.009	0.007	0.17(2)		
^{204}Pt, $I^\pi = (7^-)$						
< 78.4	0[f]	> 13.6	0	1	55(3) μs[g]	$_{(F-F)}27.6^{+73}_{-93}$
						$_{(F-H)}26.3^{+71}_{-91}$
^{204}Pt, $I^\pi = (5^-)$						
872.4	100(2)	0.007	0.006	1	5.5(7) μs[g]	$_{(F-F)}42^{+17}_{-20}$
1122.7	97(2)	0.010	0.007	1		$_{(F-H)}39^{+17}_{-20}$
^{203}Pt, I^π = *unknown*						
1104.0	100(8)	-	-	-	641(55) ns[g]	-
^{202}Pt, $I^\pi = 7^-$						
534.3	95(2)	0.021	0.016	1	141(7) μs[g]	$_{(F-F)}12.0^{+9}_{-17}$
534.3	95(2)	0.065	0.039	1		$_{(F-H)}12.0^{+5}_{-14}$
718.8	100(3)	0.011	0.009	1		$_{(F-He)}11.5^{+17}_{-26}$
^{201}Pt, $I^\pi = (19/2^+)$						
≤ 140	-	≥ 1.3[j]	-	1	18.4(13) ns[g]	$_{(F-F)} \geq 3.6^{+15}_{-17}$
353.6	76(6)	0.018	0.015	1		$_{(F-H)} \geq 3.8^{+16}_{-19}$
373.9	80(5)	0.053	0.036	1		
726.9	100(6)	0.011	0.084	1		

Continued on Next Page...

Table 6.31 – Continued

E_γ (keV)[a]	I_γ[b]	α^c_{TOT}	α_K[c]	BR	$T_{1/2}$[d]	IR (%)[e]
^{200}Pt, $I^\pi = (12^+)$						
≤ 121	-	$\geq 2.3^j$	-	1	13.9(10) ns[g]	$_{(F-F)} \geq 1.9^{+12}_{-14}$
318.4	16(2)	-	-	1		
542.5	17(2)	-	-	1		
708.6	22(3)	0.011	0.009	1		
^{200}Pt, $I^\pi = (7^-)$						
$\leq 90^c$	-	$\geq 7.8^j$	-	1	17.0(5) ns[g]	$_{(F-F)} \geq 1.9^{+12k}_{-14}$
298.9	8(2)	0.027	0.022	0.22(6)		
397.5	8(2)	0.150	0.124	1		
401.0	8(2)	0.044	0.030	1		
463.6	72(3)	0.010	0.008	0.78(6)		
470.1	87(3)	0.029	0.021	1		
633.0	100(4)	0.014	0.011	1		
^{199}Pt, $I^\pi = unknown$						
318.9	84(19)	-	-	-	18.6(34) ns[g]	$_{(F-H)} \geq 5.4^{+28}_{-32}$
419.6	86(15)	-	-	-		
597.4	100(15)	-	-	-		
^{198}Pt[l], $I^\pi = (12)_{(T_{1/2}=36(2)\ ns^c)}$ and $I^\pi = (7^-)_{(T_{1/2}=3.4(2)\ ns^c)}$						
382.0	54(16)	0.015	0.013	1	See line above	
407.2	100(29)	0.042	0.029	1		
577.8	65(25)	0.018	0.013	1		
^{197}Pt, $I^\pi = unknown$						
374.5	100(12)	-	-	-	10.2(13) ns[g]	-
432.2	72(14)	-	-	-		
546.9	66(12)	-	-	-		

Continued on Next Page...

Table 6.31 – Continued

E_γ (keV)[a]	I_γ[b]	α_{TOT}[c]	α_K[c]	BR	$T_{1/2}$[d]	IR (%)[e]
^{203}Ir, $I^\pi = (23/2^+)$						
207.0[h]	18(8)	3.99	2.98	1	798(350) ns[g]	$_{(F-F)}4.7^{+31}_{-34}$
841.3	73(21)	0.007	0.006	1		
894.7	100(25)	0.007	0.005	1		
^{202}Ir, $I^\pi = (11^-)$ or (12^+)						
311.5	41(13)	-	-	-	3.4(6) μs[g]	$_{(F-F)}0.7^{+2}_{-3}$
655.9	54(17)	-	-	-		
737.2	100(29)	-	-	-		
889.2	51(17)	-	-	-		
967.6	44(15)	-	-	-		
^{201}Ir, $I^\pi =$ *unknown*						
≤ 250	-	-	-	-	10.5(17) ns[g]	$_{(F-F)} \geq 2.7^{+21}_{-24}$
439.6	39(9)	-	-	-		
452.0	51(9)	-	-	-		
680.9	100(13)	-	-	-		
^{200}Ir, $I^\pi =$ *unknown*						
< 250[h,i]	-	-	-	-	17.1(12) ns[g]	$_{(F-F)} \geq 3.5^{+19i}_{-22}$
120.0	30(2)	-	-	1[h]		
^{200}Ir, $I^\pi =$ *unknown*						
< 250[h,i]	-	-	-	-	28.5(15) ns[g]	$_{(F-F)} \geq 6.4^{+20i}_{-25}$
126.6	100(3)	-	-	1[h]		
^{199}Ir, $I^\pi =$ *unknown*						
< 250[h]	-	-	-	-	9.1(4) ns[g]	$_{(F-F)} \geq 1.6^{+11}_{-12}$
448.5	100(7)	-	-	1[h]		
500.2	67(5)	-	-	-		
500.2	14(1)	-	-	-		
547.2	82(7)	-	-	-		
596.6	38(6)	-	-	-		

Continued on Next Page...

Table 6.31 – Continued

E_γ (keV)[a]	I_γ[b]	α^c_{TOT}	α_K[c]	BR	$T_{1/2}$[d]	IR (%)[e]
^{198}Ir, I^π = *unknown*						
116.4	100(17)	0.273	0.220	1	73(11) ns[g]	$_{(F-F)}4.3^{+30}_{-33}$ $_{(F-H)}6.5^{+38}_{-43}$
^{195}Ir, I^π = *unknown*						
268.4	76(19)	-	-	1[h]	4.4(6) μs[g]	$_{(F-F)}1.1^{+2}_{-3}$
404.4	90(30)	-	-	1[h]		
476.7	61(28)	-	-	1[h]		
537.8	96(29)	-	-	1[h]		
566.7	100(30)	-	-	1[h]		
^{199}Os, I^π = *unknown*						
379.3	57(18)	-	-	-	25.2(20) ns[g]	$_{(F-F)} \geq 1.4^{+6}_{-7}$
401.8	100(19)	-	-	-		
424.8	49(13)	-	-	-		
736.5	47(25)	-	-	-		
970.6	48(28)	-	-	-		
^{198}Os, $I^\pi = (12^+)$						
-	-	< 250	-	1	18.0(28) ns[g]	$_{(F-F)} \geq 0.4^{+2}_{-2}$
446.8	11(2)	-	-	1		
526.9	10(2)	-	-	1		
544.0	6(2)	0.019	0.014	1		
^{198}Os, $I^\pi = (7^-)$						
≤ 150	-	< 400	-	1	16.1(8) ns[g]	$_{(F-F)} \geq 5.4^{+21}_{-25}$
329.9	27(3)	0.209	0.174	1		
412.1	16(3)	0.012	0.010	0.14(3)		
465.4	100(4)	0.028	0.020	1		
473.1	13(2)	0.026	0.020	1		
607.3	80(4)	0.015	0.011	1		
608.2	80(4)	0.005	0.004	0.70(3)		
885.6	19(3)	0.015	0.011	0.16(3)		

Continued on Next Page...

Table 6.31 – Continued

E_γ (keV)[a]	I_γ[b]	α^c_{TOT}	α_K[c]	BR	$T_{1/2}$[d]	IR (%)[e]
^{197}Os, I^π = unknown						
< 250[i]	-	-	-	1	78.2(66) ns[g]	$_{(F-F)} \geq 0.6^{+2}_{-3}$
204.4	95(13)	-	-	1		
415.9	92(9)	-	-	1		
486.5	100(10)	-	-	1		
628.8	96(11)	-	-	1		
^{195}Os, I^π = unknown						
< 250	-	≥ 0.1	-	1	34.0(23) ns[g]	$_{(F-F)} \geq 2.4^{+7}_{-8}$
438.6	100(11)	-	-	1		$_{(F-H)} \geq 2.3^{+7}_{-9}$
493.0	73(10)	-	-	1		
533.1	73(10)	-	-	1		
714.0	90(12)	-	-	1		
^{193}Os, I^π = unknown						
242.0	100(26)	-	-	-	132(29) ns[g]	$_{(H-F)} \geq 7.3^{+36}_{-41}$
^{196}Re, I^π = unknown						
-	461(90)[m]	-	-	-	3.6(6) μs[g]	-
^{194}Re, I^π = unknown						
86.3	100(25)	-	-	-	45(18) μs[g]	-
^{193}Re, I^π = unknown						
145.2	100(11)	-	-	-	65(9) μs[g]	$_{(F-F)}18.9^{+40h}_{-52}$
						$_{(F-H)}12.9^{+50h}_{-65}$
^{192}Re, I^π = unknown						
-		-	-	-	85(10) μs[g]	$_{(F-F)}3.5^{+5}_{-7}$
159.3	100(9)	-	-	-		$_{(F-H)}2.4^{+10}_{-12}$

Continued on Next Page...

Table 6.31 – Continued

E_γ (keV)[a]	I_γ[b]	α_{TOT}[c]	α_K[c]	BR	$T_{1/2}$[d]	IR (%)[e]
^{191}Re, I^π = unknown						
134.5	42(11)	-	-	-	77(33) μs[g]	-
139.9	40(11)	-	-	-		-
158.3	57(13)	-	-	-		-
224.6	100(19)	-	-	-		-
418.5	65(18)	-	-	-		-
443.7	42(15)	-	-	-		-
^{191}W, I^π = unknown						
67.5	100(10)	-	-	-	0.36(2) μs [g]	-
167.4	10(5)	-	-	-		-
^{190}W						
See future publications by G. Farrelly of the University of Surrey						
^{189}Ta, I^π = unknown						
153.9	100(19)	-	-	-	0.58(22) μs[g]	$_{(F-F)}2.2^{+7}_{-8}$
283.7	73(17)	-	-	-		-
342.5	47(13)	-	-	-		-
388.7	80(19)	-	-	-		-
481.6	97(21)	-	-	-		-
^{188}Ta, I^π = unknown						
291.9	100(7)	0.090[h]	0.060[h]	1	3.5(4) μs[g]	$_{(F-F)}7.9^{+9}_{-15}$
				1		$_{(F-H)}7.8^{+21}_{-27}$

[a] *Transition energy as measured in the current experiment unless otherwise stated.*
[b] *Efficiency corrected, not α_{TOT} corrected; arbitrarily normalised per* ***nuclide****.*
[c] *Value not currently measured. Either it is calculated or taken from published measurements.*
[d] *These are the half-life values used in the IR measurement.*
[e] *Feeding from higher lying isomers is included in the quoted value.*
[f] *Measured intensity appears reduced due to the Ge walk effect.*
[g] *The half-life of the isomer as it has been currently measured.*
[h] *This value is particularly uncertain.*
[i] *The existence of the transition is questionable.*
[j] *Value inferred by assuming $IR = 100$ %.*
[k] *Assumes zero direct population of the $I^\pi = (7^-)$ isomer.*
[l] *For readability, only the directly observed transitions have been listed.*
[m] *This is the* ***total*** *(not normalised) internal conversion intensity.*

6.7 A Summary of Measured Isomeric Ratios

Nine of the presently measured isomeric ratios have previously been measured by Caamaño *et al.* [54]. Table 6.32 shows a comparison of the isomers that have had their isomeric ratios measured in both works. In all cases, except for the isomer in ^{188}Ta, the presently reported value is less than the values reported by Caamaño *et al.* [54]. The differences between the reported values are significant. At this point in time there are no other experimental reports on the isomeric ratios studied in this thesis.

Table 6.32: Comparison of isomeric ratios for the present and the previous report by Caamaño *et al.* [54].

Nuclide: I^{π}	**Current IR (%)**	**Caamanño *et al.* IR (%)**
^{203}Au: *unknown*	2.5^{+8}_{-10}	≥ 1
^{202}Pt: (7^-)	$\geq 11.8^{+10}_{-19}$	≥ 15
^{201}Pt: $(19/2^+)$	$\geq 3.7^{+15}_{-18}$	≥ 32
^{200}Pt: (12^+)	$\geq 1.9^{+12}_{-14}$	≥ 4
^{198}Ir: *unknown*	5.4^{+34}_{-48}	19^{+5}_{-3}
^{195}Os: *unknown*	$\geq 2.4^{+7}_{-9}$	≥ 13
^{193}Re: *unknown*	15.9^{+40}_{-52} ($E2$) or 2.4^{+6}_{-8} ($M2$)	≥ 19
^{192}Re: *unknown*	3.0^{+8}_{-10}	21^{+29}_{-7}
^{188}Ta: *unknown*	7.9^{+15}_{-21}	0.5^{+3}_{-1}

There is concern over the manner by which Caamaño *et al.* handled the in-flight internal conversion of H-like nuclei. In the opinion of the author the previous work over estimated the influence on isomer decay rates by the presence of a single K-shell electron, this may explain the discrepancy between the two reports on the isomeric ratios. It is also noted that (for the cases where the comparison is applicable) the isomeric ratios obtained by Caamaño *et al.* [54] are suspiciously large when compared to current theoretical predictions [139], however it must further be noted that there are few experimental results by which the predictions have ever been tested.

A comparison of the isomeric ratios measured in this work with current theoretical predictions is not arbitrary. The abrasion-ablation approach published by de Jong *et*

al. [139] and applied by Gladnishki *et al.* [4] in a previous, similar study is not applicable to secondary beam fragments, which are approximately $\Delta A < 10$ from the primary beam. In these cases the assumptions regarding the ablation phase of the reaction break down to an unworkable degree. Alternative approaches consider the individual knockout of nucleons [140] and require computational power demanding shell model calculations along with an understanding of the (often numerous) channels for populating the nucleus through one of more step fragmentation reactions. Theoretical predictions from this approach for up to mass $A \sim 50$ nuclei [141] have been published; the increasing density of excited states for heavier nuclei complicate predictions, presently no direct predictions have been reported in the literature.

Where possible, for the isomers measured in this work, two spectra summarising the measured populating capability of the fragmentation reaction are shown in the spectra in figure 6.69. One spectrum shows the relationship between the isomeric ratio and spin of the isomers and the other shows how the isomeric ratio is related to the number of nucleons removed during the fragmentation reaction.

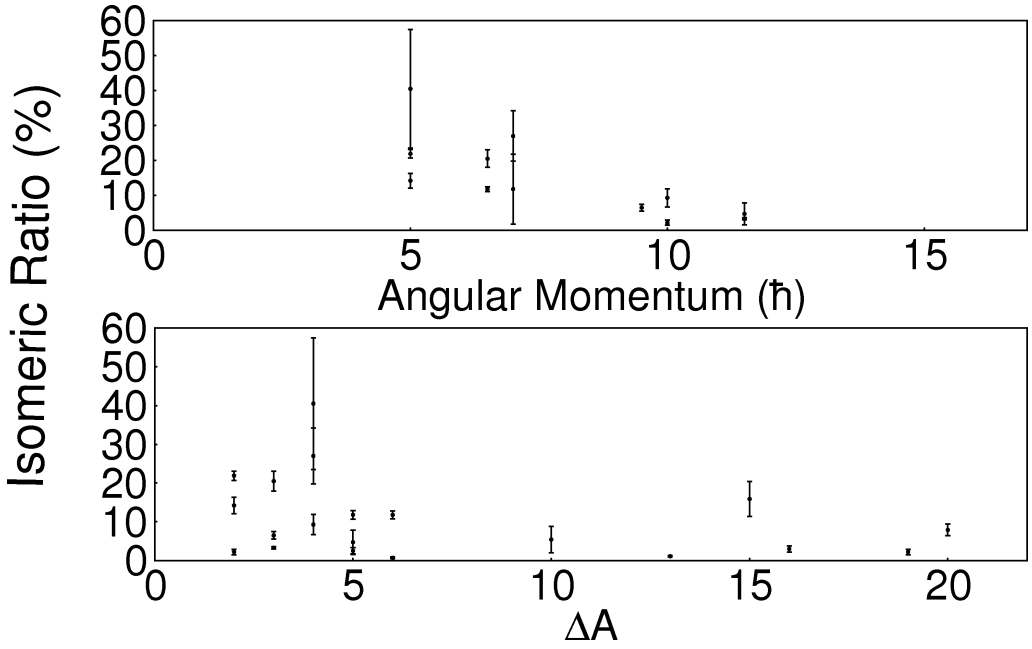

Figure 6.69: Summary of the measured isomeric ratio information. **Top:** the relationship between the isomeric ratio and spin of the isomers measured in this work. **Bottom:** the relationship between the isomeric ratio of isomers and the number of nucleons removed from the nucleus during the fragmentation reaction.

Chapter 7

Concluding Remarks

7.1 Nuclear Structure

The aim of this investigation was threefold. The primary goal was to make experimental measurements of neutron-rich nuclei at $Z < 82$ and $N \leq 126$. This was in order to expand scientific knowledge of nuclear structure. The present study has succeeded in measuring X- and γ-ray emissions from nuclei following the decay of 47 isomers, 27 of which have been discovered in this work; these are distributed among 40 nuclides. Of these nuclides, 16 have had no experimentally measured excited states prior to this work[1] and for 8 more this study has made the first measurement of a particular isomeric decay, the remaining 17 nuclides have had previously reported isomers re-measured, often bringing new structural information to light. Returning to the nuclear chart of figure 1.1, an updated version is now presented in figure 7.1. Now only previously observed isomers, which have been detected in the present experiment and the newly discovered isomers in the current work are displayed.

The key nuclear structure highlight in this investigation is the discovery of isomers at $N = 126$, including the nuclides: ^{205}Au, ^{204}Pt and ^{203}Ir, all of which are lower in Z than any previously reported excited states in an $N = 126$ nucleus. This information on excited states of singly-magic nuclei is invaluable in testing and improving shell model predictions of nuclei. The current state of the shell model calculations have been seen to fail to reproduce the experimentally determined decay scheme for ^{204}Pt. From this some simple modifications have been suggested to improve the model, including adjustments

[1] This includes ^{199}Ir, as the previously observed isomer [54] is now discounted

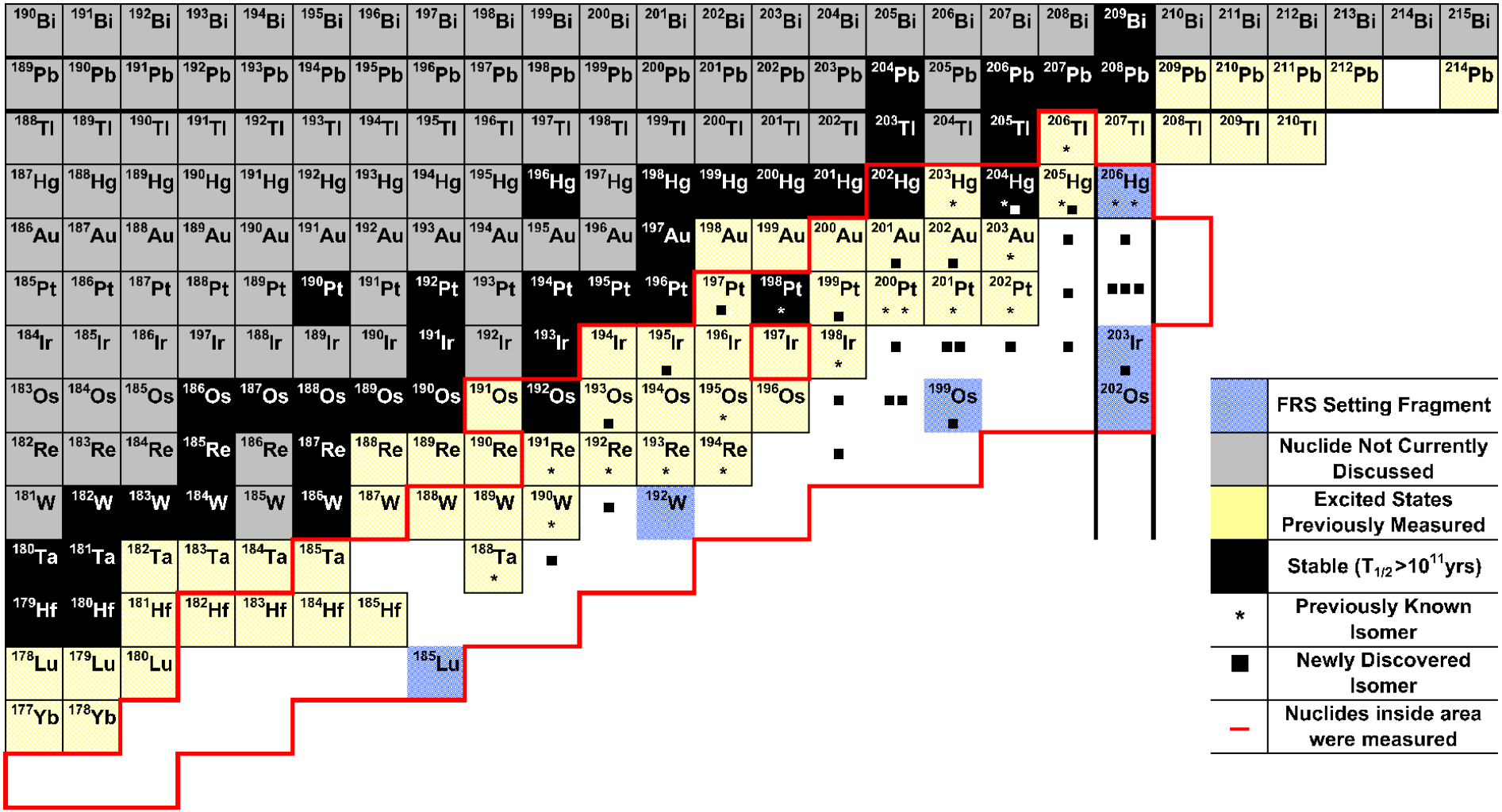

Figure 7.1: A summary of the nuclei populated and measured in the current work; only isomers observed in the current work are indicated.

to the diagonal $(d_{3/2}h_{11/2})_{7^-}$ and the non-diagonal $(s_{1/2}h_{11/2}; d_{3/2}h_{11/2})_{6^-}$ two-body matrix elements and a change to the $s_{1/2}d_{5/2}$ monopole strength. These changes have been shown to improve agreement between the theory and the experimental data for the ^{204}Pt and ^{206}Hg cases.

Further to the interpretation of singly-magic decay schemes, the dozens of isomers observed at $N < 126$ offer diverse benefits. They have importantly tested and in most cases confirmed the results of the previous study by Caamaño *et al.* [54], which was often the only previous investigation of the nuclide. Secondly, nuclear structure has been interpreted through shell model calculations and regional systematics. The measured γ-ray transition energies are critical tags; these will act as the foundations of future studies, which will rely on the presence of at least one characteristic transition to identify the nuclei of interest.

7.2 Reaction Studies

The populating capability of the fragmentation reaction has been tested for 34 of the isomers. Of particular importance is the measurement of the isomeric ratio of the ^{206}Hg isomers. From a theoretical perspective it is possible to model this reaction microscopically, making the experimental result a unique tool for reaction modelling [140]. All of the obtained isomeric ratio information is valuable for determining the spin-energy population capabilities of nuclear fragmentation. It also provides a useful guide for estimating yields of excited states when planning future fragmentation experiments.

7.3 The Broader Motivations

Some progression toward both $N = 126$ shell quenching and the astrophysical r-process is made as a result of this study. As stated regarding the nuclear structure findings, the present study has populated three $Z < 82$, $N = 126$ nuclides, which were previously beyond measure. In addition, $^{202}\mathrm{Os}_{126}$ has been identified in the current work. This leap towards long-term goals of nuclear physics does not yet allow for specific insights regarding shell quenching. This work provides experimental evidence for the persistence of the $N = 126$ neutron shell closure for *at least* five holes in the $Z = 82$ proton shell closure. The improvement to scientific understanding of

the r-process is more tangible. The shell model corrections from the experimental findings on ^{204}Pt will influence the predicted ground state configuration of waiting point nuclei [142], this has a direct influence over β-decay half-lives and hence the abundance of the heaviest stable nuclei. The RISING collaboration aims to continue the study of $N = 126$ nuclei with experimental work focused on observing the structure of low-lying ^{202}Os excitations. In future, when enough additional experimental information is gathered for this region of nuclei, and the shell model two-body matrix elements will be fitted to the data (rather than manually modified as they are currently). Following this, it will be possible to substantially improve upon current network calculations.

7.4 The Future Outlook

It is important to emphasise that for all of the investigations presently made, in no case has the multipolarity of transitions been unambiguously measured. There are a number of instances where the interpretation of decay schemes is robust, but spins and parities of states are not directly measured. In addition only the half-lives of isomeric states have been measured. All the transitions following isomer decay have been grouped as "prompt", their individual half-lives are not known. On a related timing issue, the order of transitions not separated by an isomer is not ever measured or proved.

Readers may have noticed that a common issue with interpreting decay schemes and especially with measuring isomeric ratios are low-energy transitions, which are often the isomer-depopulating transition. It will be important in the future to approach this issue if a full understanding of the nuclear structure is to be reached.

There are several avenues for expanding on the current findings. The use of detectors with higher timing resolution is one solution to refining the nuclear decay schemes. Characteristically detectors with higher timing accuracy forgo energy resolution, such as $LaBr_3$ (Cs); energy resolution is no longer a paramount issue, as transition energies have already been measured. In a similar manner, using detectors that are sensitive to lower energies will be of great use in directly observing the numerous low-energy transitions. In fact, simply solving the efficiency issues encountered with the SR and LR devices would be of great benefit; over half of the findings required the use of the SR timing branch. The reduced efficiency has been a continuing issue during analysis.

For the less exotic nuclei, transfer reactions may now be able to perform studies since γ-ray transitions have been identified.

In this work there are no instances where the isomeric ratio of an isomer has been measured to be different for differring in-flight charge states. Section 2.6.3 detailed previous results on how the internal conversion coefficient may change for highly stripped ions [35, 36], it also detailed the parallel case of electron capture [37, 38]. The results of the work presented in this thesis are not sensitive to perturbations of internal conversion coefficients for highly stripped ions. In principle however the experimental method is capable of detecting these perturbations. It would be interesting in future to measure the isomeric ratio of multiple charge states of highly converted isomers (with half-lives comparable to, or shorter than, the flight time). These states must have isomer-depopulating transitions with energy greater than the K-shell electron binding energy. If the uncertainty on the measurements can be suitably reduced, then the author believes that the isomeric ratio paramater will be a helpful tool for studying variations to internal conversion rates for highly stripped ions, supplementing existing methods [35–38].

Bibliography

[1] J.H. Jensen, *Reviews of Modern Physics*, **29**, 182 (1957).

[2] H. Geissel, G. Müzenberg and K. Rüsager, *Annu. Rev. Nucl. Sci.*, **45**, 163 (1995).

[3] M. Pfützner *et al.*, *Phys. Rev. C*, **65**, 064604 (2002).

[4] K.A. Gladnishki *et al.*, *Phys. Rev. C*, **69**, 024617 (2004).

[5] Zs. Podolyák *et al.*, *Phys. Lett. B*, **632**, 203 (2006).

[6] Y.-Z Qian, *Prog. Part. Nucl. Phys.*, **50**, 153 (2003).

[7] B. Pritychenko, National Nuclear Data Center,
http://www.nndc.bnl.gov/,
(Site Visited: March 2006).

[8] R. F. Casten, *Nuclear Structure from a Simple Perspective*, Oxford University Press, (1999).

[9] A. Bohr and B. R. Mottelson, *Nuclear Structure Volume 1*, W. A. Benjamin Inc., (1969).

[10] P. Ring and P. Schuck, *The Nuclear Many-Body Problem, 3^{rd} edition*, Springer, (2004).

[11] S. Barshay and M. Temmer, *Phys. Rev. Lett.*, **12**, 728 (1964).

[12] G. Breit and E. Wigner, *Phys. Rev.*, **49**, 519 (1936).

[13] W. Pauli, *Z. Phys.*, **31**, 765 (1925).

[14] A. Messiah, *Quantum Mechanics*, Dover Publications, (1999).

[15] W. H. Barkas, *Phys. Rev.*, **55**, 691 (1934).

[16] M. G. Mayer, *Phys. Rev.*, **74**, 235 (1948).

[17] K. S. Krane, *Introductory Nuclear Physics*, John Wiley & Sons, (1988).

[18] R. D. Woods and D. S. Saxon, *Phys. Rev.*, **95**, 577 (1954).

[19] N. Thompson, Private Communication, (2007).

[20] L. J. Jardine, S. G. and J. M. Hollander, *Nucl. Phys. A*, **190**, 261 (1972).

[21] M. Rejmund *et al.*, *Z. Phys.*, **359**, 243 (1997).

[22] A. R. Poletti *et al.*, *Nucl. Phys. A*, **580**, 43 (1994).

[23] C. Ellegard, P. D. Barnes and E. R. Flynn, *Nucl. Phys. A*, **170**, 209 (1971).

[24] M. Pfützner *et al.*, *Phys. Lett. B*, **444**, 32 (1998).

[25] D. Horn *et al.*, *Phys. Rev. Lett.*, **39**, 7 (1977).

[26] W. K. Dawson *et al.*, *Phys. Rev. C*, **22**(2), 928 (1980).

[27] L. G. Sobotka, H. C. Griffin and E. C. Kao, *Phys. Rev. C*, **17**(2), 816 (1980).

[28] J. E. Draper, R. J. McDonald and N. S. P. King, *Phys. Rev. C*, **16**, 1594 (1977).

[29] H. Orihara *et al.*, *Phys. Rev. C*, **9**, 266 (1974).

[30] I. Kumabe *et al.*, *RCNP (Osaka), Ann. Rept.*, page 70 (1980).

[31] B. Fornal *et al.*, *Phys. Rev. Lett.*, **87**, 212501 (2001).

[32] G. A. Jones, Study of Isomers using Reactions with a ^{178}Hf Beam, PhD Thesis: University of Surrey, (2006).

[33] B. Fogelberg, K. Heyde and J. Sau, *Nucl. Phys. A*, **352**, 157 (1981).

[34] J. Kantele, *Handbook of Nuclear Spectroscopy*, Academic Press Limited, London, (1994).

[35] W.R. Phillips *et al.*, *Phys. Rev. Lett.*, **62**, 1025 (1989).

[36] Yu.A. Litvinov *et al.*, *Phys. Lett. B*, **573**, 80 (2003).

[37] T. Ohtsubo *et al.*, *Phys. Rev. Lett.*, **95**, 052501 (2005).

[38] Yu.A. Litvinov *et al.*, *Phys. Rev. Lett.*, **99**, 262501 (2007).

[39] P. M. Walker and G. Dracoulis, *Nature*, **399**, 35 (1999).

[40] M. Górska, Private communication, (March 2008).

[41] F. Rosel *et al.*, *At. Nucl. Data Tables*, **21**, 91 (1978).

[42] J.M. Band and M.B. Trzhaskovskaya, *At. Nucl. Data Tables*, **21**, 1 (1978).

[43] A.K. Kerman, *Annals of Physics*, **12**, 300 (1961).

[44] J.J. Ressler *et al.*, *Phys. Rev. C*, **69**, 034317 (2004).

[45] J.J. Gaimard and K.-H. Schmidt, *Nucl. Phys. A*, **531**, 709 (1991).

[46] D. Bazin *et al.*, *Nucl. Inst. and Meth. A*, **482**, 307 (2002).

[47] GSI Injector Group, UNILAC,
http://www-inj.gsi.de/index.php?section=3&subsection=1,
(Site Visited: November 2007).

[48] P. Spädtke, *Nucl. Inst. and Meth. B*, **139**, 145 (1998).

[49] S. Yaramishev *et al.*, *Proc. International Linear Accelerator Conference*, page 47 (2004).

[50] GSI SIS-18 group, SIS-18,
http://www.gsi.de/beschleuniger/sis18/sis_e.html,
(Site Visited: November 2007).

[51] H. G. *et al.*, ATIMA code,
http://www-linux.gsi.de/∼weick/atima/,
(Site Visited: 2006).

[52] H. Geissel, Private communication, (July 2007).

[53] H. Weick *et al.*, *Nucl. Inst. and Meth. B*, **164 - 165**, 168 (2000).

[54] M. Caamaño *et al.*, *Euro. Phys. J. A: Hadrons and Nuclei*, **23**, 201 (2005).

[55] H. Geissel *et al.*, *Nucl. Inst. and Meth. B*, **70**, 286 (1992).

[56] F. Becker, FRS overview,
http://www-linux.gsi.de/∼fbecker/frs_titlebild.jpg,
(Site Visited: November 2007).

[57] H. Wiedermann, *Particle Accelerator Physics I*, Springer, (1998).

[58] H. Stelzer, *Nucl. Inst. and Meth. A*, **310**, 103 (1991).

[59] H. Weick, MWPCs,
http://www-linux.gsi.de/∼weick/frs/mwpc.html,
(Site Visited: November 2007).

[60] M. V. Ricciardi, High-resolution measurements of light nuclides produced in 1 A GeV ^{238}U-induced reactions in hydrogen and in titanium Thesis: Universidad de Santiago de Compostela, (2005).

[61] Saint-Gobain Ceramics & Plastics inc., Crystals & Detectors Brochure, (2001).

[62] T. Kurtukian Nieto, Production and β decay half-lives of heavy neutron-rich nuclei approaching the stellar nucleosynthesis r-process path around A=195, Thesis: Universidad de Santiago de Compostela, (2007).

[63] R. Anne, D. Bazin and A. C. Mueller, *Nucl. Inst. and Meth. A*, **257**, 215 (1987).

[64] R. Schneider and A. Stolz, Technical manual: ionisation chamber MUSIC80, GSI, (November 2007).

[65] S. Ahlen, *Reviews of Modern Physics*, **52**, 121 (1980).

[66] A. Pullia *et al.*, *IEEE Transactions on Nuclear Science*, **49**(6), 3269 (2002).

[67] H.-J. Wollersheim, Fragment Separator particle selection,
http://www-linux.gsi.de/∼wolle/EB_at_GSI/FRS-WORKING/FRS/GEISSEL/F09.pdf,
(Site Visited: November 2007).

[68] G.F. Knoll, *Radiation Detection and Measurement*, Wiley, (1989).

[69] A.B. Garnsworthy, Private Communication, (2008).

[70] M. Górska *et al.*, *Acta Physica Polonica B*, **38**, 1219 (2007).

[71] The RISING collaboration, Photographs of the detector array, http://www-linux.gsi.de/∼wolle/EB_at_GSI/GE_DETECTOR/index.html, (Site Visited: November 2007).

[72] R.H. Regan *et al.*, *Int. J. of Mod. Phys. E, submitted for review (proceesdings of the 2007 Shanghai workshop on nuclear structure physics)* (2008).

[73] H. Geissel and H. Weick, Mocadi code, http://www-linux.gsi.de/∼weick/mocadi/, (Site Visited: November 2007).

[74] O. Tarasov & D. Bazin, *Nucl. Phys. A*, **746**, 411 (2004).

[75] Zs. Podolyák *et al.*, *Nucl. Phys. A*, **722**, c273 (2003).

[76] S. Pietri *et al.*, *Acta Physica Polonica B*, **38**, 1255 (2007).

[77] J.Eberth *et al.*, *Z. Phys.*, **358**, 139 (1997).

[78] J.Eberth *et al.*, *Prog. Part. Nucl. Phys.*, **28**, 495 (1992).

[79] F. Adams and R. Dams, *Applied Gamma-ray Spectroscopy*, Pergamon Press, (1970).

[80] X-ray Instumentation Associates, User's Manual: Digital Gamma Finder (DGF) XIA, (2004).

[81] S. Pietri, Private communication, (March 2006).

[82] S. Pietri *et al.*, *Nucl. Inst. and Meth. B*, **261**, 1079 (2007).

[83] A. Jungclaus for the RISING Collaboration, NUSTAR presentation: Results from the recent RISING campaign 2006, www-wnt.gsi.de/nustar07/images/contributions/NUSTAR_23-03-07_pdf/NUSTAR07 _2303_02_Jungclaus.pdf, (Site Visited: Novermber 2007).

[84] H. D. Young and R. A. Freedman, *University Physics 11th edition*, Addison-Wesley, (2004).

[85] C. Scheidenberger *et al.*, *Nucl. Inst. and Meth. B*, **142**, 441 (1998).

[86] D.J. Morrissey and B.M. Sherrill, *Phil. Trans. of the Royal Soc. A*, **356**(1744) (1985).

[87] J.A. Becker *et al.*, *Phys. Rev. C*, **26**, 914 (1982).

[88] K.H. Maier *et al.*, *Phys. Rev. C*, **30**, 1702 (1984).

[89] O. Häusser, J.R. Beene, T.K. Alexander, A.B. McDonald and T. Feastermann, *Phys. Lett. B*, **64**, 273 (1976).

[90] A. R. Poletti *et al.*, *Nucl. Phys. A*, **580**, 64 (1994).

[91] K.-H. Maier *et al.*, *Phys. Rev. C*, **32**, 1416 (1985).

[92] P. Zeyen *et al.*, *Z. Phys.*, **325**, 451 (1986).

[93] P. Schuler *et al.*, *Z. Phys.*, **317**, 313 (1984).

[94] A.J.C. Burghardt, The Influence of the Shell Closure on the Microscopic Structure of Even-Even Hg Isotopes. A Study with Electron and Muon Beams, PhD Thesis: University of Amsterdam, (1989).

[95] K. Brandi *et al.*, *Nucl. Phys.*, **59**, 33 (1964).

[96] E.R. Flynn *et al.*, *Phys. Lett. B*, **105**, 125 (1981).

[97] P. Grabmayr *et al.*, *Phys. Rev. C*, **49**, 2971 (1994).

[98] J.A. Cizewski *et al.*, *Phys. Rev. C*, **23**, 1453 (1981).

[99] S.W. Yates *et al.*, *Phys. Rev. C*, **37**, 1889 (1988).

[100] E. Björn, D.C. Baxter and W. French, *J. Anal. At. Spectrom.*, **17**, 1582 (2002).

[101] M.L. Boas, *Mathematical Methods in the Physical Sciences*, John Wiley & Sons, (1983).

[102] C. Wheldon, Nanofit code, Unpublished, (1999).

[103] P.D. Cottle *et al.*, *Bull. Am. Phys. Soc.*, **32**, 1545 (1987).

[104] J.J. Valiente-Dobón *et al.*, *Phys. Rev. C*, **69**, 024316 (2004).

[105] P.H. Regan *et al.*, *Laser Phys. Lett.*, **1**, 317 (2004).

[106] C. Wheldon and J.J. Valiente-Dobön, Private communication, (October 2008).

[107] M. Caamaño, New Isomers in the Neutron-Rich $A \sim 190$ Mass Region, PhD Thesis: University of Surrey, (2002).

[108] G.F. Farrelly, Private communication, (March 2007).

[109] L. Rydström *et al.*, *Nucl. Phys. A*, **512**, 217 (1990).

[110] Ch. Wennemann *et al.*, *Z. Phys.*, **347**, 185 (1994).

[111] Zs. Podolyák *et al.*, *Phys. Lett. B*, *submitted for review* (2008).

[112] A. Pakkanen, T. Komppa and H. Helppi, *Nucl. Phys. A*, **184**, 157 (1972).

[113] D.A. Craig and H.W. Taylor, *J. of Phys. G*, **10**, 1133 (1984).

[114] S. Shi *et al.*, *Z. Phys.*, **342**, 369 (1992).

[115] K.-H. Maier, Private communication, (April 2008).

[116] H. Grawe, Private communication, (April 2008).

[117] T. Kurtukian-Nieto *et al.*, *AIP Conf. Proc.*, **802**, 73 (2005).

[118] I. Uray, *Atomki Kozlem*, **15**, 61 (1982).

[119] M.A. Wahlgren and W.W. Meinke, *Phys. Rev.*, **115**, 191 (1959).

[120] R.F. Casten, D.D. Warner, G.M. Gowdy, N. Rofail and K.P.Lieb, *Phys. Rev. C*, **27**(3), 1310 (1983).

[121] C. Samour *et al.*, *Nucl. Phys. A*, **121**, 65 (1968).

[122] D.G. Burke and G. Kajrys, *Nucl. Phys. A*, **517**, 1 (1990).

[123] P. Mukherjee, *Nucl. Phys.*, **64**, 65 (1965).

[124] C.H. Atwood, *Diss. Abst. Int.*, **40B**, 3162 (1980).

[125] S.G. Malmskog, *Arkiv Fysik*, **34**, 195 (1967).

[126] E. Gerdau, D. Ruter and J. Braunsfurth, *Z. Phys.*, **230**, 72 (1970).

[127] J.C. Soares *et al.*, *Phys. Rev. C*, **25**, 1587 (1982).

[128] A.J. Haverfield, H.T. Easterday and J.M. Hollander, *Nucl. Phys.*, **64**, 379 (1965).

[129] M. Bormann, H.H. Bissem, E. Magiera and R. Warnemünde, *Nucl. Phys. A*, **157**, 481 (1970).

[130] P. Winiwarter, *Nucl. Phys. A*, **158**, 77 (1970).

[131] T. Kurtukian-Nieto *et al.*, *Proc. Int. Symp. on Nuclear Astrophysics*, **008** (2007).

[132] G.G. Colvin *et al.*, *Nucl. Phys. A*, **465**, 240 (1987).

[133] J.F.W. Jansen, A. Faas and W.J.B. Winter, *Z. Phys.*, **261**, 95 (1973).

[134] J.A. Cizewski *et al.*, *Phys. Rev. C*, **27**(3), 1040 (1983).

[135] T. Kurtukian-Nieto *et al.*, *ArXiv pre-preprint*, page 0711.0101v1 (2007).

[136] D. Benson, Jr., P. Kleinheinz, R.K. Sheline, E.B. Shera, *Z. Phys.*, **285**, 405 (1978).

[137] D.D. Warner *et al.*, *Nucl. Phys. A*, **316**, 13 (1979).

[138] Zs. Podolyák *et al.*, *Proc. 2nd Intern. Conf Fission and Properties of Neutron-Rich Nuclei*, page 156 (2000).

[139] M. de Jong, A.V. Ignatyuk and K.-H. Schmidt, *Nucl. Phys. A*, **613**, 435 (1997).

[140] J.A. Tostevin, *Acta Physica Polonica B*, **38**, 1195 (2007).

[141] J.A. Tostevin and B.A. Brown, *Phys. Rev. C*, **74**, 064604 (2006).

[142] S.J. Steer *et al.*, *Phys. Rev. C Rap. Comm.*, *In press* (2008).

Appendix A

Publications and Oral Presentations

Peer-Reviewed Publications

S.J. Steer, Zs. Podolyák, S. Pietri *et al.* [+52 others],
Single Particle Behaviour at $N = 126$; Isomeric Decays in Neutron-Rich ^{204}Pt
Physical Review C, Rapid Communications, **78**, *p.061302* (2008)

S. Pietri, P.H. Regan, Zs. Podolyák, D. Rudolph, S.J. Steer *et al.* [+58 others],
Recent Results in Fragmentation Isomer Spectroscopy With RISING
Nuclear Instruments and Methods B, **261**, *p.1079* (2007)

A. Jungclaus, L.S. Cáceres, M. Górska, ... S.J. Steer *et al.* [+48 authors],
Observation of Isomeric Decays in the r-process Waiting-Point Nucleus ^{130}Cd$_{82}$
Physical Review Letters, **99**, *p.132501* (2007)

A.B. Garnsworthy, P.H. Regan, L.S. Cáceres, S.J. Steer *et al.* [+53 authors],
Neutron-Proton Pairing Competition in $N = Z$ Nuclei: Metastable State Decays in the Proton Dripline Nuclei ^{82}Nb^{41} and ^{86}Tc^{43}
Physics Letters B, **660**, *p.326* (2008)

Zs. Podolyák, G.F. Farrelly, A.B. Garnsworthy, S.J. Steer *et al.* [+37 authors],
Proton-Hole Excitation in the Closed Shell Nucleus ^{205}Au
Submitted to Physics Letters B (2008)

P.H. Regan, A.B. Garnsworthy, S. Pietri, ... S.J. Steer *et al.* [+48 others],
Isomer Spectroscopy Using Relatavistic Projectile Fragmentation at the $N = Z$ Line for $A \sim 80 \rightarrow 90$
Proceedings of NN2006, Rio de Janeiro, Aug 2006
Nuclear Physics A, **787**, *p.491c* (2007)

D. Rudolph, R. Hoischen, M. Hellström, ... S.J. Steer *et al.* [+27 authors],
Isospin Symmetry and Proton Decay: Identification of the 10^+ Isomer in ^{54}Ni
Physical Review C, **78***, p.023101* (2008)

D. Rudolph, R. Hoischen, M. Hellström, ... S.J. Steer *et al.* [+26 authors],
Evidence for an Isomeric $3/2^-$ State in ^{53}Co
European Physical Journal J, **36***, p.131* (2008)

M. Górska, L. S. Cáceres, H. Grawe, ... S.J. Steer *et al.* [+47 authors],
Evolution of the $N = 82$ Shell Gap Below ^{132}Sn Inferred from Core Excited States in ^{131}In
Submitted to Physics Letters B (2008)

A.B. Garnsworthy, P.H. Regan, S. Pietri ... S.J. Steer *et al.* [+52 authors],
Isomeric States in Neutron-Deficient $A \sim 80 - 90$ Nuclei Populated in the Fragmentation of ^{107}Ag
Submitted to Physical Review C (2008)

L. Cáceres, M. Górska, A. Jungclaus, ... S.J. Steer *et al.* [+46 authors],
Spherical Proton-Neutron Structure of Isomeric States in ^{128}Cd
Submitted to Physical Review C Rapid Communications (2008)

Conference Proceedings

S.J. Steer, Zs. Podolyák, S. Pietri *et al.* [+ 53 authors],
Isomeric Decay Studies in Neutron-Rich $N \sim 126$ Nuclei
Proceedings of the 15th Nuclear Physics Workshop "Marie and Pierre Curie", 2008
In Press, International Journal of Modern Physics E, **18** (2008)

S.J. Steer, Zs. Podolyák, S. Pietri *et al.* [+ 48 authors],
Identification of Isomeric States 'South' of ^{208}Pb Via Projectile Fragmentation
Proceedings of the 2006 Zakopane Conference on Nuclear Physics,
Acta Physica Polonica B, **38***, p.1283* (2006)

Zs. Podolyák, S.J. Steer, S. Pietri, *et al.* [+ 59 authors],
Isomeric decay Studies Around ^{204}Pt and ^{148}Tb
The 7th International Conference on Radioactive Nuclear Beams, Cortina dAmpezzo, July 2006
European Physical Journal - Special Topics, **150***, p.165* (2007)

P.H. Regan, A.B. Garnsworthy, S.J. Steer, *et al.* [+50 others],
First Results from the Stopped RISING Campaign at GSI: The Mapping of Isomeric Decays in Highly Exotic Nuclei
Sixth International Conference of the Balkan Physical Union,
Istanbul, August 2006
Conference Proceedings **899**, *p.19* (2007)

S. Pietri, P.H. Regan, Zs. Podolyák, ... S.J. Steer, et al. [+ 57 authors],
First Results from the Stopped Beam Isomer RISING Campaign at GSI
The 41st Zakopane Conference on Nuclear Physics, Zakopane, September 2006
Acta Physica Polonica B, **38**, *p.1255* (2007)

S. Pietri, P.H. Regan, Zs. Podolyák, ... S.J. Steer, *et al.* [+24 authors],
Experimental Details of the Stopped Beam RISING Campaign
The 7th International Conference on Radioactive Nuclear Beams, Cortina dAmpezzo, July 2006
European Physical Journal Special Topics, **150**, *p.319* (2007)

D. Rudolph, S. Pietri, Zs. Podolyák, ... S.J. Steer, *et al.* [+ 58 authors],
Exciting Isomers from the First Stopped-Beam RISING Campaign
The 7th International Conference on Radioactive Nuclear Beams, Cortina dAmpezzo, July 2006
European Physical Journal - Special Topics, **150**, *p.319* (2007)

A.B. Garnsworthy, P.H. Regan, S. Pietri, ... S.J. Steer, *et al.* [+50 authors],
Isomeric States in the Light Tc Isotopes
The 41st Zakopane Conference on Nuclear Physics, Zakopane, September 2006
Acta Physica Polonica B, **38**, *p.1265* (2007)

L.S. Cáceres, M. Górska, A. Jungclaus, ... S.J. Steer, *et al.* [+50 authors],
Identification of Excited States in the $N = Z$ Nucleus ^{82}Nb
The 41st Zakopane Conference on Nuclear Physics, Zakopane, September 2006
Acta Physica Polonica B, **38**, *p.1271* (2007)

S. Myalski, M. Kmiecik, A. Maj, ... S.J. Steer, *et al.* [+49 authors]
Isomeric Ratio for the $I^{\pi} = 8^{+}$ Yrast State in ^{96}Pd Produced in the Relativistic Fragmentation of ^{107}Ag
The 41st Zakopane Conference on Nuclear Physics, Zakopane, September 2006
Acta Phyisica Polonica B, **38**, *p.1277* (2007)

P. Doornenbal, A. Bürger, D. Rudolph, ... S.J. Steer, *et al.* [+71 others],
RISING: Gamma-ray Spectroscopy with Radioactive Beams at GSI
Tours Symposium on Nuclear Physics VI, Tours, September 2006
Conference Proceedings **891**, *p.99* (2007)

P.H. Regan, N.Alkhomashi, N.Al-Dahan, ... S.J. Steer, *et al.* [+38 others],
New Insights into the Structure of Exotic Nuclei Using the RISING Active Stopper
13th International Symposium on Capture Gamma-Ray Spectroscopy and related Topics
Conference Proceedings Submitted, (2008)

N.Al-Dahan, Zs. Podolyák, P.H. Regan, S.J. Steer, *et al.* [+43 others],
Structure of $N \geq 126$ Nuclei Produced in Fragmentation of ^{238}U
13th International Symposium on Capture Gamma-Ray Spectroscopy and related Topics
Conference Proceedings Submitted, (2008)

P.H. Regan, N. Alkhosmashi, N. Al-Dahan, ... S.J. Steer, *et al.* [+38 others],
First Results with the RISING Active Stopper
International Workshop on Nuclear Structure, Shanghai
Conference Proceedings Submitted to Int Jour. Mod. Phys. E, (2008)

Invited Talks

15^{th} Nuclear Physics Workshop "Marie and Pierre Curie"
Decay Spectroscopy of Exotic Nuclei Following Projectile Fragmentation
Kazimierz, Poland, (September 2008)

Workshop on Spectroscopy of Neutron-Rich Nuclei
Decay Spectroscopy of $A \sim 200$ Nuclei on the Neutron-Rich Side of Stability
Chamrousse, France, (March 2008)

Annual NUSTAR meeting
The Stopped Beam RISING Experimental Campaign
GSI, Germany, (January 2008)

Other Contributed Talks

50^{th} Anniversary Symposium on Nuclear Size and Shapes

Isomers in Exotic, Neutron-Rich $A \sim 200$ Nuclei

University of Surrey, UK, (June 2008)

Institute of Physics Annual Conference 2008

Decay Spectroscopy of $A \sim 200$ Nuclei on the Neutron-Rich Side of Stability

University of Liverpool, UK, (April 2008)

Institute of Physics Summer School 2007

Identification of Isomeric States 'South' of ^{208}Pb via Projectile Fragmentation

Newcastle, UK, (September 2007)

Yale Workshop 2007

Isomers in $N = 126$, ^{204}Pt

WNSL, USA, (June 2007)

Institute of Physics Annual Conference 2007

Fragmentation of Heavy, Exotic, Neutron-Rich Nuclei

University of Surrey, UK, (April 2007)

Collaboration Workshop for RISING

RISING: Analysis Techniques

Universidad Autonoma de Madrid, Spain, (November 2006)

Collaboration Workshop for RISING

RISING: Fragmentation of ^{208}Pb Beam

Universidad Autonoma de Madrid, Spain, (November 2006)

41^{st} Conference on Nuclear Physics

Preliminary Findings: Isomeric States 'South' of ^{208}Pb via Projectile Fragmentation

Zakopane, Poland, (September 2006)

Appendix B

First Author Publications

About the Attached Papers

The following pages contain the three papers on which the author is first named, these papers were listed in appendix A. The Physical Review C Rapid Communication and the Acta Physica Polonica B are final published articles. The International Journal of Modern Physics E article has been accepted for publication and is currently in press.

PHYSICAL REVIEW C **78**, 061302(R) (2008)

Single-particle behavior at $N = 126$: Isomeric decays in neutron-rich ^{204}Pt

S. J. Steer,[1,*] Zs. Podolyák,[1] S. Pietri,[1] M. Górska,[2] P. H. Regan,[1] D. Rudolph,[3] E. Werner-Malento,[2] A. B. Garnsworthy,[1,4] R. Hoischen,[3] J. Gerl,[2] H. J. Wollersheim,[2] K. H. Maier,[5,6] H. Grawe,[2] F. Becker,[2] P. Bednarczyk,[2,6] L. Cáceres,[2,7] P. Doornenbal,[2,8] H. Geissel,[2] J. Grębosz,[2,6] A. Kelic,[2] I. Kojouharov,[2] N. Kurz,[2] F. Montes,[2] W. Prokopowicz,[2] T. Saito,[2] H. Schaffner,[2] S. Tashenov,[2] A. Heinz,[4] M. Pfützner,[9] T. Kurtukian-Nieto,[10] G. Benzoni,[11] A. Jungclaus,[7] D. L. Balabanski,[12,13] C. Brandau,[1] B. A. Brown,[1,14] A. M. Bruce,[15] W. N. Catford,[1] I. J. Cullen,[1] Zs. Dombrádi,[16] M. E. Estevez,[17] W. Gelletly,[1] G. Ilie,[8,18] J. Jolie,[8] G. A. Jones,[1] M. Kmiecik,[6] F. G. Kondev,[19] R. Krücken,[20] S. Lalkovski,[15,21] Z. Liu,[1] A. Maj,[6] S. Myalski,[6] S. Schwertel,[20] T. Shizuma,[1,22] P. M. Walker,[1] and O. Wieland[11]

[1]*University of Surrey, Guildford, Surrey GU2 7XH, United Kingdom*
[2]*GSI, Planckstrasse 1, D-64291 Darmstadt, Germany*
[3]*Department of Physics, Lund University, S-22100 Lund, Sweden*
[4]*WNSL, Yale University, 272 Whitney Avenue, New Haven, Connecticut 06520, USA*
[5]*University of West of Scotland, Paisley PA1 2BE, United Kingdom*
[6]*The Institute of Nuclear Physics, PL-31-342 Kraków, Poland*
[7]*Departmento de Fisica Teórica, Universidad Autonoma de Madrid, Madrid, Spain*
[8]*IKP, Universität zu Köln, D-50937 Köln, Germany*
[9]*IEP, Warsaw University, Hoża 69, PL-00-681, Poland*
[10]*Universidad de Santiago de Compostela, Santiago de Campostela, Spain*
[11]*INFN sezione di Milano, I-20133 Milano, Italy*
[12]*INRNE, Bulgarian Academy of Sciences, BG-1784 Sofia, Bulgaria*
[13]*Dipartimento di Fisica, Università di Camerino, I-62032 Camerino, Italy*
[14]*NSCL, Michigan State University, East Lansing, Michigan 48824-1321, USA*
[15]*School of Engineering, University of Brighton, Brighton BN2 4GJ, United Kingdom*
[16]*Institute for Nuclear Research, H-4001 Debrecen, Hungary*
[17]*Instituto de Fisica Corpuscular, Valencia, Spain*
[18]*National Institute of Physics and Nuclear Engineering, Bucharest, Romania*
[19]*Nuclear Engineering Division, Argonne National Laboratory, Argonne, Illinois 60439, USA*
[20]*Physik Department E12, Technische Universität München, Garching, Germany*
[21]*Faculty of Physics, University of Sofia "St. Kliment Ohridski," Sofia, Bulgaria*
[22]*Japan Atomic Energy Research Institute, Kyoto 619-0215, Japan*

(Received 31 March 2008; published 18 December 2008)

The four proton-hole nucleus ^{204}Pt was populated in the fragmentation of an $E/A = 1$ GeV ^{208}Pb beam. The yrast structure of ^{204}Pt has been observed up to angular momentum $I = 10\hbar$ by detecting delayed γ-ray transitions originating from metastable states. These long-lived excited states have been identified to have spin-parities of $I^{\pi} = (10^{+})$, (7^{-}), and (5^{-}) and half-lives of $T_{1/2} = 146(14)$ ns, 55(3) μs, and 5.5(7) μs, respectively. The structure of the magic $N = 126$ ^{204}Pt nucleus is discussed and understood in terms of the spherical shell model. The data suggest a revision of the two-body interaction for $N = 126$, $Z < 82$, which determines the evolution of nuclear structure toward the r-process waiting point nuclei.

DOI: 10.1103/PhysRevC.78.061302 PACS number(s): 23.20.Lv, 21.10.Pc, 27.80.+w, 29.30.Kv

The evolution of the properties of atomic nuclei with respect to neutron and proton numbers is a key question of nuclear physics. The study of unstable, neutron-rich nuclei represents one of the foremost pursuits of modern nuclear physics. Over the coming decade new radioactive ion beam facilities are being built with the main objectives being to probe neutron-rich nuclei. Within recent years surprising phenomena have been observed in neutron-rich nuclei such as neutron skins, halos, and dramatic changes in the ordering and spacing of energy levels [1].

While the stability of the $N = 82$ shell gap is an active topic of research [2,3], an open question is whether or not there is a quenching of the $N = 126$ shell gap as protons are removed from doubly magic ^{208}Pb. The proton dripline has been experimentally reached up to heavy elements [4], our present knowledge of the neutron dripline is limited to light species. The part of the nuclear chart with the least information on neutron-rich nuclei is the $_{76}$Os to $_{82}$Pb region, with experimental knowledge on only a few isotopes. This mass region is, however, an ideal testing ground of nuclear theories. With the removal of just a few protons and neutrons the landscape evolves from spherical to elongated prolate through disk-shaped oblate and triaxial forms [5]. Consequently the information gained on neutron-rich, $N = 126$ nuclei is essential for the understanding of nuclear structure in heavy nuclei. From a longer-term perspective, experiments in this region pave the way toward the proposed

*s.steer@surrey.ac.uk

nuclear-astrophysical r-process waiting point nuclei along the $N = 126$ shell closure [6,7]. Studies of magic nuclei are of fundamental importance in our understanding of nuclear structure because they allow direct tests of the purity of shell model wave functions. Information on the single particle energies and two-body residual interactions can be derived from the experimental observables such as energies of the excited states and transition probabilities.

Experimental information on the neutron-rich, $N = 126$ nuclei is very scarce. Information has been obtained on excited states for only two isotones with $Z < 82$: ^{207}Tl [8] and ^{206}Hg [9–11]. In the case of ^{205}Au only the ground state is known [12]. The lack of information on nuclei "below" ^{208}Pb is due to difficulties in populating these neutron-rich nuclei. Fragmentation has proven to be an efficient tool in producing exotic nuclear species. When projectile fragmentation is combined with high-sensitivity γ-detection arrays, structural information can be gained for otherwise inaccessible nuclei. The highest sensitivity is achieved with both isomeric and β-delayed γ-ray spectroscopy techniques; delayed γ rays are time-correlated with individually identified ions, thereby minimizing the associated background radiation. Information on the excited states populated in this way can be obtained when producing only a few hundred nuclei of interest [13,14].

In this Rapid Communication the first spectroscopic information on the structure of the four proton-hole nucleus ^{204}Pt is presented. Preliminary results were published in conference proceedings [15,16].

The SIS-18 accelerator at GSI provided a ^{208}Pb beam at $E/A = 1$ GeV. The average beam intensity was $\sim 4 \times 10^8$ ion/s and the total operating time was $\sim$105 h. The ^{208}Pb ions impinged on a target of ^{9}Be of thickness 2.5 g/cm^2. The nuclei of interest were selected and identified in flight by the FRagment Separator (FRS) [17]. The FRS was operated in standard achromatic mode using an Al wedge-shaped degrader of thickness 4.9 g/cm^2, positioned at the intermediate focal plane. To maximize the number of fully stripped ($q = Z$) nuclei passing through the FRS, niobium foils of 221 and 108 mg/cm^2 thicknesses were, respectively, placed after both the target and the intermediate focal plane degrader. According to the charge state calculations (using the GLOBAL code [18]), 93.7% of the ^{204}Pt ions were fully stripped exiting the target and 76.6% were stripped after the intermediate focal plane. The identified ions were slowed in an Al degrader and halted in a 7-mm-thick plastic stopper, positioned at the final focal plane of the FRS. Scintillation detectors placed before and after this Al degrader allowed suppression of events where the fragments of interest were destroyed in the slowing down process ($\approx$18%) and in cases where they did not implant in the stopper ($\approx$0.2%). The stopper was surrounded by the RISING array in the "Stopped Beam" configuration [19,20], consisting of 15 former EUROBALL HPGe cluster detectors [21]. The photopeak efficiency of this array was measured to be 15% at 661 keV [22]. These detectors recorded the delayed γ-ray transitions associated with the implanted nuclei.

The identification of the fragments is demonstrated in Fig. 1. The calibration of the particle identification is confirmed by the detection of previously identified γ rays that follow

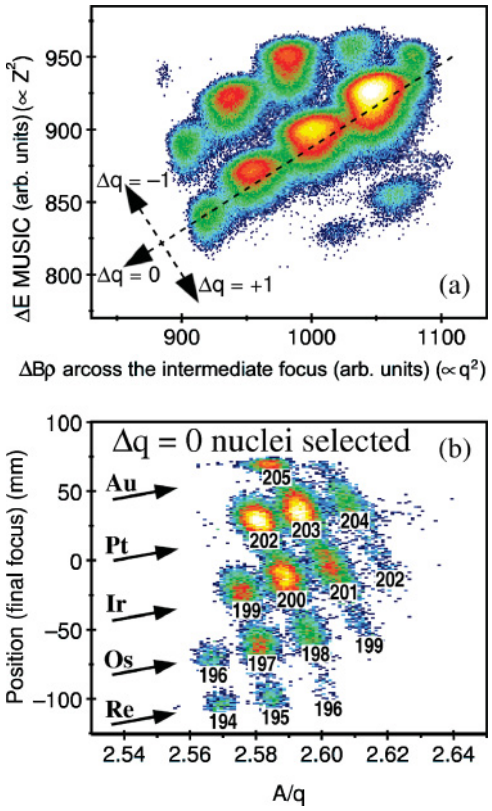

FIG. 1. (Color online) Identification of the fragmentation products in the FRS setting optimized for ^{203}Ir transmission. (**a**) Energy loss at the final focal plane vs change in magnetic rigidity, $\Delta B\rho (\propto q^2)$, at the intermediate focal plane. This distinguishes which nuclei change charge state in the middle of the FRS (approximately all $\Delta q = 0$ correspond to $q = Z$ for the entire FRS flight time). (**b**) Position in the final focal plane versus A/q for fully stripped ($\Delta q = 0$) nuclei.

the deexcitation of the $I^\pi = 7^-$ isomer in ^{202}Pt [23,24]. The identification process is described in more detail in Ref. [25].

The results for ^{204}Pt were obtained from four different magnetic rigidity settings of the FRS. A total of 9.3×10^4 ^{204}Pt ions was implanted in the stopper. Most of the data, $\sim$70% (in 24 h), were recorded in a setting optimized for the transmission of ^{203}Ir. In this setting the delayed γ rays were measured over a range of $0 \rightarrow 80$ μs following implantation. In the other settings, the γ rays were detected over a range of $0 \rightarrow 380$ μs.

Delayed γ rays associated with ^{204}Pt nuclei are shown in Fig. 2. In the sub-microsecond regime three γ-ray transitions with energies of 97, 1061, and 1158 keV, together with characteristic platinum x rays have been identified, all showing similar decay characteristics. The measured half-life is $T_{1/2} =$ 146(14) ns; see inset to Fig. 2 (top). Two additional γ rays with energies 872 and 1123 keV have been observed over a longer time range, see Fig. 2 (middle). However, their decay curve cannot be fitted with a single decay component. Two components must be considered, resulting in one half-life of $T_{1/2} = 5.5(7)$ μs, populated by a higher lying isomer with a longer half-life of $T_{1/2} = 55(3)$ μs.

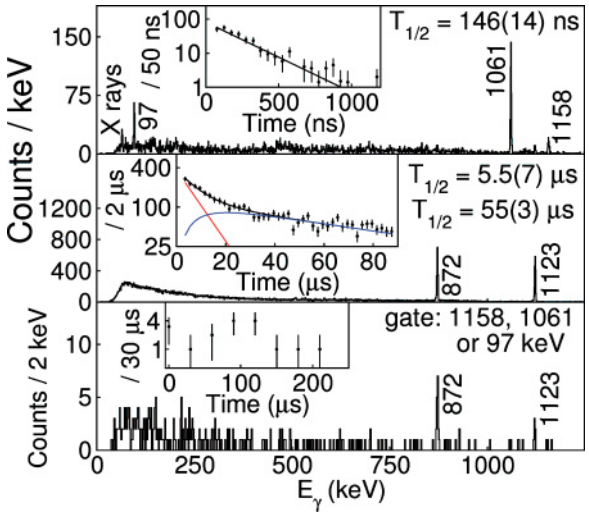

FIG. 2. (Color online) γ-ray spectra associated with ^{204}Pt. (Top) γ rays detected between 50 and 850 ns after implantation. (Inset) Decay curve of 1061 and 1158 keV γ rays. (Middle) γ rays observed between 2.5 and 80 μs after implantation. (Inset) Decay curve of the 872 and 1123 keV γ rays. (Bottom) Time-differentiated $\gamma\gamma$ coincidence. Shown are γ rays detected from 2.5 to 380 μs following implantation, after a $T_{1/2} = 146$ ns associated γ ray (97, 1061, 1158 keV) has been observed over the range 50 to 850 ns. (Inset) Time difference between detection of $T_{1/2} = 146$ ns associated γ rays and the later observed 872 and 1123 keV transitions.

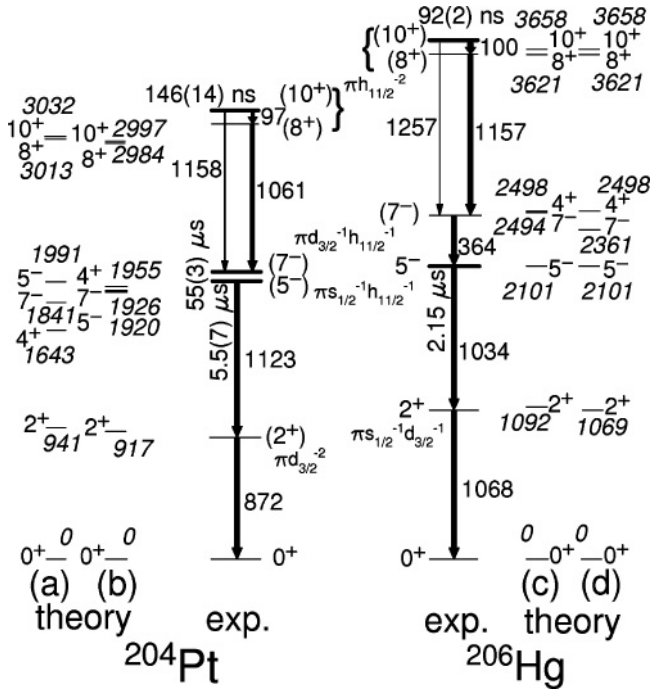

FIG. 3. Experimental and calculated partial level schemes of the $N = 126$ ^{204}Pt and ^{206}Hg [9] nuclei. Arrow widths denote relative intensities of parallel decay branches. The dominant state configurations are indicated. (a) and (d) are calculations using the Rydsrtöm matrix elements, while (b) and (c) are with the modified ones, as described in the text.

The sum energy of the 97 and 1061 keV transitions is equal to that of the third transition (1158 keV). Therefore it is likely that they form a parallel branch. Considering that the 97 and 1061 keV transitions should have identical intensity after allowing for electron conversion of the transition branches, we conclude that the 97 keV transition is of $E2$ or $M1$ character. The 872 and 1123 keV γ-ray peaks have equal intensities within experimental uncertainties. The data allow the extraction of coincidence relationships. The 97 and 1061 keV transitions, as well the 872 and 1123 keV pair, are in mutual coincidence. The spectrum in Fig. 2 (bottom) shows the transitions following the decay out of the short-lived isomer (gating on 97, 1061, and 1158 keV), together with the time difference between the transitions associated with the shorter lived and longer lived isomeric states. This demonstrates that the shorter lived ($T_{1/2} = 146$ ns) isomer decays into both of the longer lived ones. This is in agreement with the extracted relative population at the time of implantation of the isomeric states: 1:4.5:1.4 for $T_{1/2} = 146$ ns, 55 μs, and 5.5 μs, respectively. The implantation rate of ^{204}Pt nuclei is 0.4 nuclei/s; thus the number of chance coincidences in Fig. 2 (bottom) is negligible.

Based on these experimental data the level scheme has been constructed and has been compared with the two proton-hole $N = 126$ isotone ^{206}Hg in Fig. 3. It is established from experiment, except the tentative spin assignments and also the sequence of the 97, 1061 keV and the 872, 1123 keV pairs of transitions, which are respectively taken from comparison with ^{206}Hg and theoretical considerations.

Shell model calculations have been performed in the $s_{1/2}, d_{3/2}, h_{11/2}, d_{5/2}, g_{7/2}$ ^{208}Pb proton-hole space with the OXBASH code using single particle energies from ^{207}Tl and two-body matrix elements (TBME) from Ref. [26]. These are based on the Kuo-Herling interaction including core polarization, but the decisive elements for the then known 2^+ and 5^- states of ^{206}Hg had been adjusted. The resulting states and their main configurations are included in Fig. 3. The 2^+ and 5^- states in ^{206}Hg are trivially well reproduced, but also the 8^+ and 10^+ fit well, while the 7^- is off by 100 keV.

In ^{204}Pt the highest lying 146 ns isomer is without any doubt assigned to the calculated $(h_{11/2})^{-2}10^+$ level and also the 8^+ and 7^- states populated in its decay are certain. The two other lifetimes measured in ^{204}Pt give the proposed spin sequence (moving upward) of 5^-, 7^-, and an unobserved 4^+, while the calculations give 7^- below 5^- and a 4^+ state below both, incompatible with experiment. By this proposal the 7^- to $5^- E2$ transition has the astonishingly large $T_{1/2} = 55$ μs, and the 5.5 μs is ascribed to the 5^- to 2^+ $E3$. If the 4^+ is below the 5^- the possible $E1$ decay would destroy the isomerism and if the 7^- is below the 5^- it could only decay by a much slower low-energy $E3$ to 4^+ or by $E5$ to 2^+. The $B(E2, 10^+ \rightarrow 8^+)$ and $B(E3, 10^+ \rightarrow 7^-)$ agree within errors with those measured in ^{206}Hg [9].

The 872 and 1123 keV γ rays are assigned as the decays from the 5^- isomeric state. It is expected that the 2^+ energy of ^{204}Pt, with a predominantly $(d_{3/2})^{-2}$ orbital configuration, is smaller than that of ^{206}Hg, with a mainly $(d_{3/2})^{-1}(s_{1/2})^{-1}$

TABLE I. Transition strengths for experiment, the Rydström [26] shell model (SM), and the new TBMEs (SM_{mod}) (see text) in ^{204}Pt. Effective charges of 1.5 and 2.0 e for $E2$ and $E3$, respectively, were assumed, which were chosen to reproduce the ^{206}Hg $10^+ \rightarrow 8^+ E2$ and $10^+ \rightarrow 7^- E3$ transitions [9].

Transition	EL	$B(EL)$ (W.u.)		
		Exp.	SM	SM_{mod}
$10^+ \rightarrow 8^+$	$E2$	0.80(8)	2.64	1.22
$10^+ \rightarrow 7^-$	$E3$	0.19(3)	0.21	0.22
$7^- \rightarrow 5^-$	$E2$	0.017 $\rightarrow$ 0.0034[a]	1.21	0.0037
$5^- \rightarrow 2^+$	$E3$	0.039(5)	0.713	0.612

[a]Assuming a transition energy between 10 $\rightarrow$ 78 keV.

configuration. It is lower by about 200 keV, taking into account differences in single particle ($(s_{1/2})^{-1}$ vs $(d_{3/2})^{-1}$) and interaction ($(d_{3/2})^{-2}$ vs $(s_{1/2})^{-1}(d_{3/2})^{-1}$) energies. This suggests that the energy of the first excited state is 872 keV. The $E3$ $5^- \rightarrow 2^+$ transition proceeds mainly from the dominant $(s_{1/2})^{-1}(h_{11/2})^{-1}$ component of the 5^- state to the weak admixture of the $(s_{1/2})^{-1}(d_{5/2})^{-1}$ configuration in the predominantly $(d_{3/2})^{-2}$ state. The experimental $E3$ transition strength is weak (see Table I).

The transition linking the proposed 7^- and 5^- isomeric states was not observed in the present experiment. The lack of K x rays associated with the long-lived decay suggests a transition energy below the binding energy of the K electron (78.4 keV).

In light of the new ^{204}Pt and updated ^{206}Hg data [9] the Rydström interaction [26] was modified in three points: (i) the $(d_{3/2}h_{11/2})_{7^-}$ TBME was increased by +135 keV as requested by ^{206}Hg; (ii) the $(s_{1/2}d_{5/2})$ monopole was increased by +250 keV, which accounts for the 4^+ level energy and the increased blocking of the $h_{11/2} \otimes 3^-$ coupling lowering the effective $d_{5/2}$ single hole energy; (iii) following a systematic search of the influence of nondiagonal TBME on the $E2$ strength evolution from ^{206}Hg to ^{204}Pt the $(s_{1/2}h_{11/2}; d_{3/2}h_{11/2})_{6^-}$ TBME was changed to +160 keV, close to the value for the responding 5^- TBME. With these minor modifications, the observed excited states within both ^{206}Hg and ^{204}Pt are well reproduced, including the ordering of the $5^-, 7^-$, and 4^+ states (see Fig. 3). The calculated $E2$ and $E3$ strengths with the exception of the $5^- \rightarrow 2^+ E3$ agree with experiment (see Table I). The latter discrepancy is common to both ^{206}Hg and ^{204}Pt and most likely due to the 2^+ wave function, which in a pure proton model space is poorly described. Note that $E3$ transitions are mediated by the $h_{11/2} \rightarrow d_{5/2}$ conversion, i.e., the weak $d_{5/2}$ content in the wave functions, and any further components such as, e.g., $N = 126$ cross shell excitations, will reduce this contribution in low-spin states. These revised shell model calculations reproduce the measured magnetic and quadrupole moments of the 5^- isomer in ^{206}Hg: $\mu(5^-)_{\text{the}} = 5.24\ \mu_N$ with $g_s = 0.7 g_{\text{free}}$, $\mu(5^-)_{\text{exp}} = 5.45(5)\ \mu_N$ [11], $Q(5^-)_{\text{the}} = 0.57$ eb, $Q(5^-)_{\text{exp}} = 0.65(13)$ eb [10].

It is thus found that small modifications to the two-body interaction, though not unambiguous, significantly improve the description of levels and γ transition rates in ^{204}Pt. Recently new approaches to infer realistic nucleon-nucleon interactions were made, based on the renormalized G matrix [27,28] and the $V_{\text{low-k}}$ potential [29]. Further investigations, both experimental and theoretical, are needed to understand the nuclear structure evolution of the $N \sim 126$ region toward the anticipated r-process waiting nuclei at $Z \leqslant 72$.

In summary, we have identified excited states in the four proton-hole nucleus ^{204}Pt. The yrast sequence has been established up to spin-parity $I^\pi = (10^+)$, through the observation of decays from three isomers. The character of the excited states can be understood in terms of the shell model, although to get a consistent description of the experimental level scheme the accepted set of matrix elements has been modified to account for the changing intrinsic shell structure affecting the isomer configuration. The persistence of the isomeric structure, the related transition strengths, and their reproduction in a pure proton space strongly support an unquenched $N = 126$ gap. Due to the crucial role of the $\pi h_{11/2}$ orbit in both allowed and first forbidden β decay of $\nu h_{9/2}$ and $\nu i_{13/2}$ neutrons, respectively [7,30], this study paves the way for examining nuclear structure as both the anticipated pathways for the astrophysical r-process and candidate nuclei for shell quenching are approached.

The excellent work of the GSI accelerator staff is acknowledged. This work is supported by the EPSRC (UK) and AWE plc. (UK), the EU Access to Large Scale Facilities Programme (EURONS, EU Contract 506065), The Swedish Research Council, The Polish Ministry of Science and Higher Education, The Bulgarian Science Fund, The US Department of Energy, The Spanish Ministeriode Educacion y Ciencia, The German BMBF, The Hungarian Science Foundation, and the Italian INFN.

[1] A. Klimkiewicz *et al.*, Phys. Rev. C **76**, 051603(R) (2007).
[2] A. Jungclaus *et al.*, Phys. Rev. Lett. **99**, 132501 (2007).
[3] I. Dillmann *et al.*, Phys. Rev. Lett. **91**, 162503 (2003).
[4] P. J. Woods and C. N. Davids, Annu. Rev. Nucl. Part. Sci. **47**, 541 (1997).
[5] P. D. Bond, R. F. Casten, D. D. Warner, and D. Horn, Phys. Lett. **B130**, 167 (1983).
[6] Y.-Z. Qian, Prog. Part. Nucl. Phys. **50**, 153 (2003).
[7] H. Grawe, K. Langanke, and G. Martínez-Pinedo, Rep. Prog. Phys. **70**, 1525 (2007).
[8] D. Eccleshall and M. J. L. Yates, Phys. Lett. **19**, 301 (1965).
[9] B. Fornal *et al.*, Phys. Rev. Lett. **87**, 212501 (2001).
[10] K. H. Maier *et al.*, Phys. Rev. C **30**, 1702 (1984).
[11] J. A. Becker *et al.*, Phys. Rev. C **26**, 914 (1982).
[12] C. Wennemann *et al.*, Z. Phys. A **347**, 185 (1994).
[13] M. Pfützner *et al.*, Phys. Lett. **B444**, 32 (1998).
[14] Z. Podolyák *et al.*, Phys. Lett. **B491**, 225 (2000).
[15] S. J. Steer *et al.*, Acta Phys. Pol. B **38**, 1283 (2007).
[16] Z. Podolyák *et al.*, Eur. Phys. J. Spec. Top. **150**, 165 (2007).
[17] H. Geissel *et al.*, Nucl. Instrum. Methods B **70**, 286 (1992).
[18] C. Scheidenberger *et al.*, Nucl. Instrum. Methods B **142**, 441 (1998).

[19] S. Pietri *et al*., Nucl. Instrum. Methods B **261**, 1079 (2007).
[20] P. H. Regan *et al*., Nucl. Phys. **A787**, 491c (2007).
[21] P. J. Nolan, F. A. Beck, and D. B. Fossan, Annu. Rev. Nucl. Part. Sci. **44**, 561 (1994).
[22] S. Pietri *et al*., Acta Phys. Pol. B **38**, 1255 (2007).
[23] M. Caamaño *et al*., Eur. Phys. J. A **23**, 201 (2005).
[24] Z. Podolyák *et al*., Prog. Theor. Phys. **146**, 467 (2002).
[25] J. Benlliure *et al*., Nucl. Phys. **A660**, 87 (1999).
[26] L. Rydström *et al*., Nucl. Phys. **A512**, 217 (1990).
[27] M. Hjorth-Jensen, T. T. S. Kuo, and E. Osnes, Phys. Rep. **261**, 125 (1995).
[28] B. A. Brown (private communication, 2008).
[29] L. Coraggio, A. Covello, A. Gargano, N. Itaco, and T. T. S. Kuo, Phys. Rev. C **60**, 064306 (1999).
[30] I. M. Borzov, Nucl. Phys. **A777**, 645 (2006).

IDENTIFICATION OF ISOMERIC STATES 'SOUTH' OF ^{208}Pb VIA PROJECTILE FRAGMENTATION*

S.J. Steer[a], Zs. Podolyák[a], S. Pietri[a], P.H. Regan[a]
D. Rudolph[b], E. Werner-Malento[c,d], A.B. Garnsworthy[a,e]
R. Hoischen[b], M. Górska[c], J. Gerl[c], H.J. Wollersheim[c]
F. Becker[c], P. Bednarczyk[c,f], L. Cáceres[c,g], P. Doornenbal[c]
H. Geissel[c], J. Grębosz[c,f], A. Kelic[c], N. Kurz[c]
F. Montes[c], W. Prokopowicz[c,f], T. Saito[c], H. Schaffner[c]
S. Tachenov[c], A. Heinz[e], M. Pfützner[d], T. Kurtukian-Nieto[h]
G. Benzoni[i], A. Jungclaus[g], D.L. Balabanski[j,k], C. Brandau[a,c]
A.M. Bruce[l], W.N. Catford[a], I.J. Cullen[a], Zs. Dombradi[m]
E. Estevez[h], W. Gelletly[a], G. Ilie[o,p], J. Jolie[n], G.A. Jones[a]
M. Kmiecik[f], F.G. Kondev[p], S. Lalkovski[g,l], Z. Liu[a], A. Maj[f]
S. Myalski[f], T. Shizuma[a,s], S. Schwertel[t], P.M. Walker[a]
O. Wieland[i]

[a]Department of Physics, University of Surrey, Guildford, GU2 7XH, UK
[b]Department of Physics, Lund University, S-22100 Lund, Sweden
[c]GSI, Planckstrasse 1, D-64291, Darmstadt, Germany
[d]Institute of Experimental Physics, Warsaw University, Poland
[e]WNSL, Yale University, New Haven, CT, USA
[f]The Institute of Nuclear Physics PAN, Kraków, Poland
[g]Dept. di Fisica Teórica, Universidad Autonoma de Madrid, Madrid, Spain
[h]Universidad de Santiago de Compostela, Santiago de Campostela, Spain
[i]INFN, and Universitá degli Studi di Milano, Italy
[j]INRNE, Bulgarian Academy of Sciences, Sofia, Bulgaria
[k]Dipartimento di Fisica, Universitá di Camerino, Italy
[l]School of Engineering, University of Brighton, Brighton, BN2 4GJ, UK
[m]Institute of Nuclear Research, Debrecen, Hungary
[n]IKP, Universität zu Köln, Germany
[o]National Institute of Physics and Nuclear Engineering, Bucharest, Romania
[p]NED, Argonne National Laboratory, Argonne, USA
[r]Faculty of Physics, University of Sofia, Sofia, Bulgaria
[s]Japan Atomic Energy Agency, Kyoto, Japan
[t]Physik Department E12, Technische Universität München, Garching, Germany

(Received November 3, 2006)

* Presented at the Zakopane Conference on Nuclear Physics, September 4–10, 2006, Zakopane, Poland.

Relativistic fragmentation of ^{208}Pb has been used to produce excited states in neutron-rich nuclei with $N \approx 126$. Spectroscopic information for a range of nuclei has been obtained through observing delayed γ-ray emissions from isomeric states. Preliminary results for ^{203,204}Pt nuclei are presented. For the first time, excited states have been observed in ^{203}Pt and ^{204}Pt. The yrast structure of ^{204}Pt up to spin-parity, $I^{\pi} = (10^{+})$ has been tentatively inferred from the internal decay of two isomeric states.

PACS numbers: 21.10.–k, 23.20.–g, 25.70.Mn, 27.80.+w

1. Introduction

The Rare Isotopes Investigations at GSI (RISING) project has begun the Stopped Beam phase of experiments [1]; reported here are the first results from one of these measurements. Rare, exotic, neutron-rich nuclei in the vicinity of $N = 126$ were produced in the relativistic projectile fragmentation of a ^{208}Pb beam.

A number of $N \approx 126$ nuclei were produced during the fragmentation process. These present an ideal testing ground for the shell model, because of the limited number of valence nucleons involved in forming the low lying, yrast and near yrast excited states in these nuclei. The analysis of such states permits the extraction of information on the single-particle energies and residual shell-model interactions in this region.

2. Experimental details and results

The 1 GeV/nucleon ^{208}Pb beam, provided by the SIS-18 accelerator at GSI, was fragmented on a beryllium target (thickness 2.5 g/cm^2). The FRagment Separator (FRS) [2], operated in standard achromatic mode, was used to separate and identify the desired nuclei (see Fig 1). Once identified, nuclei were brought to a halt in a 7 mm plastic stopper. The delayed γ rays were detected over a 100 μs time range after implantation using the high efficiency RISING array [1], which, in its Stopped Beam configuration, surrounded the implantation target.

Delayed γ-ray spectra associated with ^{202,203,204}Pt are shown in Fig. 2. The observation of the previously identified isomeric state in ^{202}Pt [3] confirms the particle identification. Gamma rays belonging to ^{203}Pt and ^{204}Pt have been seen for the first time in this experiment. The ground state of ^{203}Pt was previously identified in projectile fragmentation at GSI [5], but the isomer in ^{203}Pt represents the first spectroscopic information on this $N = 125$ nucleus. Similarly, this is the first observation of excited states in ^{204}Pt; transitions from two isomeric states have been observed, with three γ rays (96, 1061, 1158 keV) originating from a shorter lived metastable state and two γ rays (872, 1123 keV) originating from a lower-lying, longer-lived isomer.

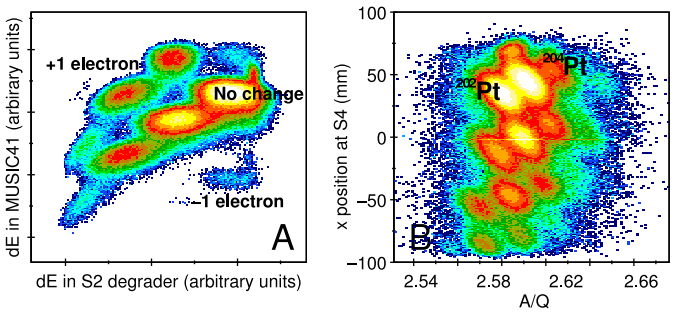

Fig. 1. Fragment identification. (A) Energy loss at the middle focal plane *versus* energy loss at the final focal plane. Charge state changes are distinguished here, allowing selection between nuclei that undergo no change, the loss of or gaining of an electron in the S2 achromatic degrader. (B) A/Q *versus* S4 position tangential to the beam direction. Only $\Delta Q = 0$ nuclei are plotted. Locations of the previously observed ^{202}Pt [3] and the newly identified ^{204}Pt nuclei are highlighted.

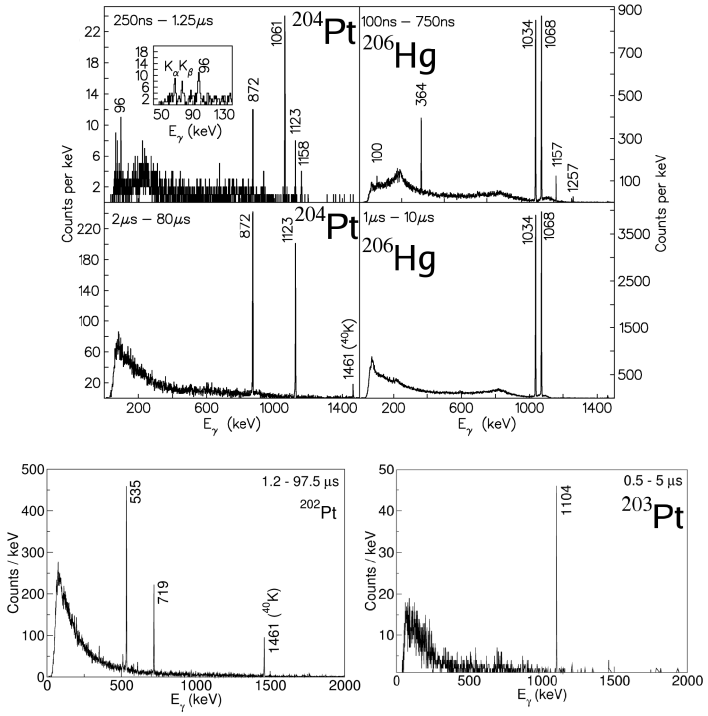

Fig. 2. Delayed γ-ray spectra associated with ^{202,203,204}Pt and ^{206}Hg. Note that the non-physical background suppression of low energy γ rays (up to ∼300 keV) is a result of data analysis techniques. Similar γ-ray spectra are observed for ^{206}Hg and ^{204}Pt, which exhibit 2-proton hole and 4-proton hole structures, respectively.

In producing ^{204}Pt four protons are removed from doubly closed shell ^{208}Pb. Like ^{206}Hg, ^{204}Pt has two isomeric states (see Fig. 2). The higher lying isomer in both cases is expected to be of a $(\pi_{h_{\frac{11}{2}}})^{-2}_{10^+}$ character [4]. This structure is associated with seniority two proton–hole states in the $Z = 82$ shell closure. A more detailed interpretation will be the subject of a future publication.

In conclusion, new spectroscopic information has been obtained on a range of heavy, neutron-rich nuclei, populated in relativistic energy projectile fragmentation. For the first time, excited states in $N = 125$ ^{203}Pt and the $N = 126$ ^{204}Pt have been presented, including the identification of three isomeric states.

This work is sponsored by the EPSRC (UK), the Swedish Research Council, the Polish Ministry of Science and Higher Education (grants 1-P03B-030-30 and 620/E-77/SPB/GSI/P-03/DWM105/2004-2007), the Bulgarian Science Fund VUF06/05, the US Department of Energy (grants DE-FG02-91ER-40609 and W-31-109-ENG-38), the German Federal Ministry of Education and Research under grant 06KY205I and EURONS (European Commision contract number 506065. ABG would like to acknowledge financial support from Nexia Solutions Ltd, FGK acknowledges the support of the US DOE, Office of Nuclear Physics, under Contract No. DE-AC02-06CH11357 and AJ acknowledges the spanish Ministerio de Educacion y Ciencia under project number FPA2005-00696.

REFERENCES

[1] S. Pietri, *et al.*, *Acta Phys. Pol. B* **38**, 1255 (2007) these proceedings.

[2] H. Geissel, *Nucl. Instrum. Methods Phys. Res.* **B70**, 286 (1992).

[3] M. Caamaño, *et al.*, *Eur. Phys. J.* **A23**, 201 (2005); Zs. Podolyák, *et al.*, *Nucl. Phys.* **A722**, 273c (2003).

[4] B. Fornal, *et al.*, *Phys. Rev. Lett.* **87**, 215201 (2001); A.R. Poletti, *et al.*, *Nucl. Phys.* **A580**, 64 (1994).

[5] T. Kurtukian-Nieto, *et al.*, *AIP Conf. Proc.* **802**, 73 (2005).

International Journal of Modern Physics E

ISOMERIC DECAY STUDIES IN NEUTRON-RICH N≈126 NUCLEI

S.J. STEER[1], ZS. PODOLYÁK[1], S. PIETRI[1], M. GÓRSKA[2], G.F. FARRELLY[1], P.H. REGAN[1], D. RUDOLPH[3], A.B. GARNSWORTHY[1,4], R. HOISCHEN[3], J. GERL[2], H.J. WOLLERSHEIM[2], H. GRAWE[2], K.H. MAIER[5,6], F. BECKER[2], P. BEDNARCZYK[2,5], L. CÁCERES[2,7], P. DOORNENBAL[2,8], H. GEISSEL[2], J. GRĘBOSZ[2,5], A. KELIC[2], I. KOJOUHAROV[2], N. KURZ[2], F. MONTES[2], W. PROKOPOWICZ[2], T. SAITO[2], H. SCHAFFNER[2], S. TASHENOV[2], A. HEINZ[4], T. KURTUKIAN-NIETO[9], G. BENZONI[10], M. PFÜTZNER[11], A. JUNGCLAUS[7], D.L. BALABANSKI[12], C. BRANDAU[1], A. BROWN[13,1], A.M. BRUCE[14], W.N. CATFORD[1], I.J. CULLEN[1], ZS. DOMBRÁDI[15], M.E. ESTEVEZ[16], W. GELLETLY[1], G. ILIE[8], J. JOLIE[8], G.A. JONES[1], M. KMIECIK[5], F.G. KONDEV[17], R. KRÜCKEN[18], S. LALKOVSKI[14], Z. LIU[1], A. MAJ[5], S. MYALSKI[5], S. SCHWERTEL[18], T. SHIZUMA[1], P.M. WALKER[1], E. WERNER-MALENTO[2], O. WIELAND[10]

[1] *Department of Physics, University of Surrey, Guildford, GU2 7XH, UK*
[2] *GSI, Planckstrasse 1, D-64291, Darmstadt, Germany*
[3] *Department of Physics, Lund University, S-22100, Lund, Sweden*
[4] *WNSL, Yale University, 272 Whitney Avenue, New Haven, CT, 06520, USA*
[5] *The Institute of Nuclear Physics, PL-31-342, Kraków, Poland*
[6] *Department of Physics, University of the West of Scotland, Paisley, PA1 2BE, Scotland*
[7] *Departmento de Fisica Teórica, Universidad Autonoma de Madrid, Madrid, Spain*
[8] *IKP, Universität zu Köln, D-50937, Köln, Germany*
[9] *Universidad de Santiago de Compostela, Santiago de Campostela, Spain*
[10] *INFN, Università degli Studi di Milano, I-20133, Milano, Italy*
[11] *IEP, Warsaw University, Hoża 69, PL-00-681, Poland*
[12] *INRNE, Bulgarian Academy of Sciences, BG-1784 Sofia, Bulgaria*
[13] *NSCL, Michigan State University, East Lansing, MI 48824-1321, USA*
[14] *School of Environment and Technology, University of Brighton, Brighton, BN2 4GJ, UK*
[15] *Institute for Nuclear Research, H-4001, Debrecen, Hungary*
[16] *Instituto de Fisica Corpuscular, Valencia, Spain*
[17] *Nuclear Engineering Division, Argonne National Laboratory, Argonne, IL-60439, USA*
[18] *Physik Department E12, Technische Universität München, Garching, Germany*

Received October 30, 2008
Revised October 30, 2008

Heavy neutron-rich nuclei were populated via relativistic energy fragmentation of a E/A=1 GeV ^{208}Pb beam. The nuclei of interest were selected and identified by a fragment separator and then implanted in a passive plastic stopper. Delayed γ rays following internal isomeric decays were detected by the RISING array. Experimental information was obtained on a number of nuclei with Z=73-80 (Ta-Hg), providing new information both on the prolate-oblate transitional region as well as on the N=126 closed shell nuclei.

1. Introduction

The evolution of the properties of atomic nuclei with respect to neutron and proton numbers is a key question of nuclear physics. The study of unstable, neutron-rich

Table 1. Approximate number, in thousands, of nuclei implanted in the plastic stopper at the end of the GSI fragment separator. All six settings as well as all charge states are considered.

Nucleus	No. (in 10^3)	Nucleus	No. (in 10^3)	Nucleus	No. (in 10^3)
^{206}Tl	86	^{202}Hg	12	^{203}Hg	142
^{204}Hg	52	^{205}Hg	417	^{206}Hg	1718
^{200}Au	2.1	^{201}Au	2.7	^{202}Au	61
^{203}Au	402	^{204}Au	133	^{205}Au	337
^{206}Au	12	^{197}Pt	7.4	^{198}Pt	24
^{199}Pt	8.8	^{200}Pt	65	^{201}Pt	68
^{202}Pt	388	^{203}Pt	319	^{204}Pt	92
^{205}Pt	1.4	^{194}Ir	1.7	^{195}Ir	8.0
^{196}Ir	3.1	^{198}Ir	51	^{199}Ir	358
^{200}Ir	354	^{201}Ir	165	^{202}Ir	36
^{203}Ir	8.0	^{191}Os	0.43	^{192}Os	2.3
^{193}Os	2.1	^{194}Os	1.1	^{195}Os	22
^{196}Os	121	^{197}Os	159	^{198}Os	78
^{199}Os	29	^{200}Os	6.3	^{201}Os	1.4
^{202}Os	0.02	^{191}Re	2.4	^{192}Re	23
^{193}Re	90	^{194}Re	101	^{195}Re	61
^{196}Re	14	^{197}Re	5.5	^{198}Re	0.71
^{188}W	3.7	^{189}W	11	^{190}W	30
^{191}W	37	^{192}W	21	^{193}W	9.4
^{194}W	2.9	^{185}Ta	1.1	^{186}Ta	3.6
^{187}Ta	11	^{188}Ta	14	^{189}Ta	9.1
^{190}Ta	3.9	^{191}Ta	0.26	^{182}Hf	0.49
^{183}Hf	3.0	^{184}Hf	5.4	^{185}Hf	7.1
^{186}Hf	5.2	^{187}Hf	2.9	^{188}Hf	1.2
^{181}Lu	0.43	^{182}Lu	1.3	^{183}Lu	1.2
^{184}Lu	0.66	^{185}Lu	0.29	^{179}Yb	0.58
^{180}Yb	0.66	^{181}Yb	0.33	^{176}Tm	0.10
^{177}Tm	0.17	^{178}Tm	0.14		

nuclei represents one of the foremost pursuits of modern nuclear physics. Over the coming decade new radioactive ion beam facilities are being constructed with one of the main objectives being to probe the structure of neutron-rich nuclei. The part of the nuclear chart with the least information on neutron-rich nuclei is the $_{76}$Os to $_{82}$Pb region. This mass region is however an ideal testing ground of nuclear theories. With the removal of just a few nucleons the landscape evolves from spherical [1,2,3] to elongated prolate through disk shaped oblate and triaxial forms [4,5,6].

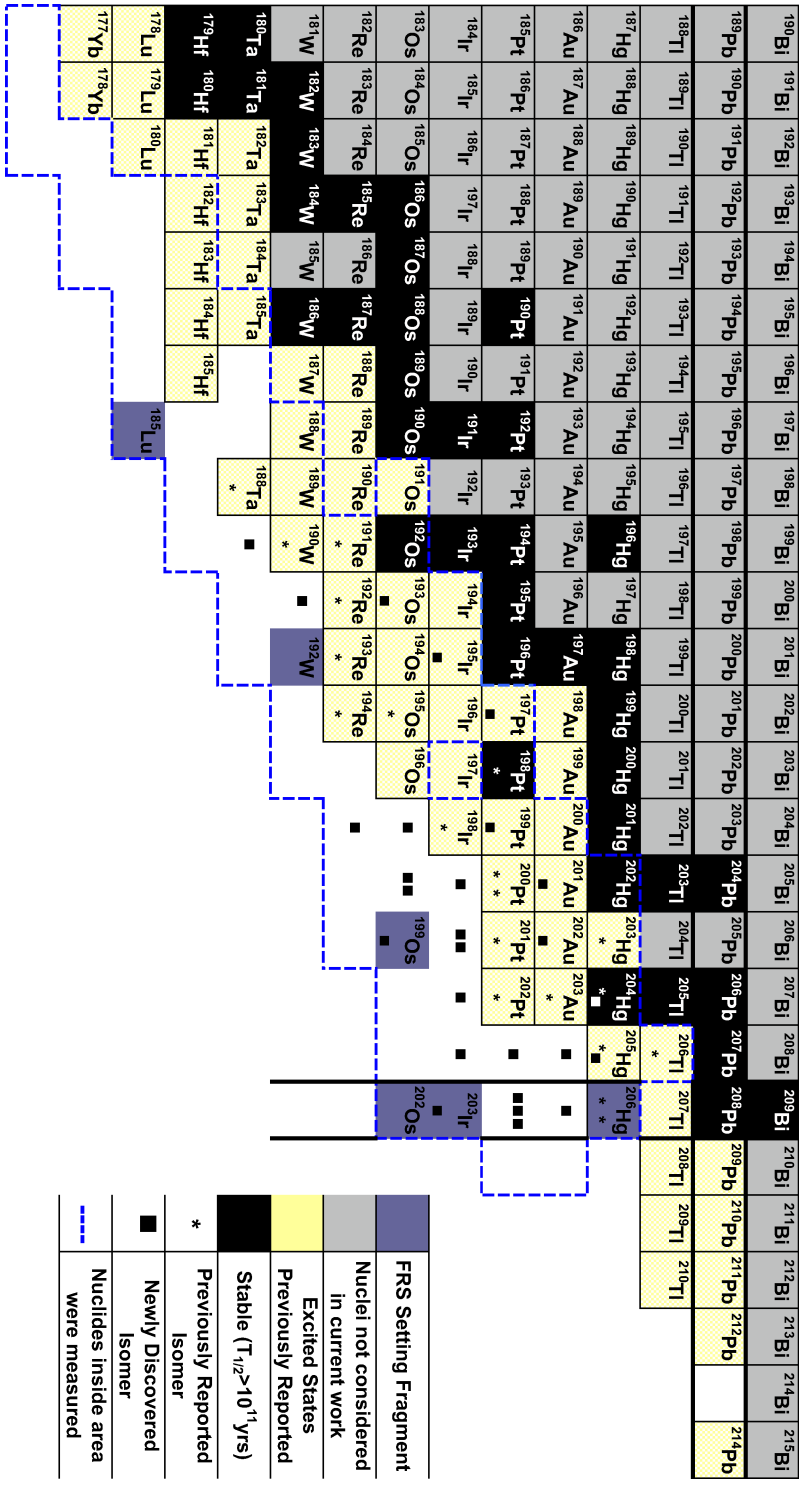

Fig. 1. Section of the nuclear chart indicating the nuclei studied in the present experiment.

2. Experimental details

The SIS-18 accelerator at GSI provided a ^{208}Pb beam at $E/A = 1$ GeV. The ^{208}Pb ions impinged on a target of ^{9}Be of thickness 2.5 g/cm^2. The nuclei of interest were selected and identified in flight by the FRagment Separator (FRS) [7] used in achromatic mode. The identified ions were stopped in a passive stopper, positioned at the final focal plane of the FRS. The stopper was surrounded by the RISING array in the "Stopped Beam" configuration [9,10]. These detectors recorded the delayed γ-ray transitions associated with the implanted nuclei. For details on the experimental setup, identification procedure and analysis see [2,8].

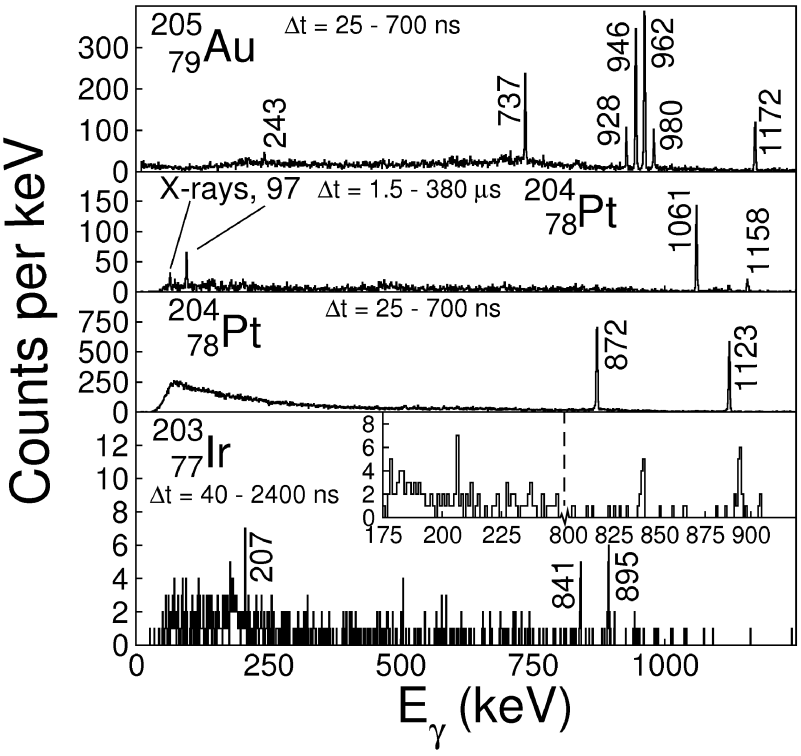

Fig. 2. Delayed γ-ray spectra obtained for the N=126 isotones ^{205}Au, ^{204}Pt [2] and ^{203}Ir.

3. Results

Six different fragment separator settings were used: the magnetic rigidities were set to transmit fully stripped ions of ^{206}Hg, ^{203}Ir, ^{202}Os, ^{199}Os, ^{192}W and ^{185}Lu. An average of 20 hours of beam time was dedicated to each setting, with a primary beam intensity of $\sim 10^9$ ions/22 s spill. The number of the implanted nuclei for individual nuclides are given in table I.

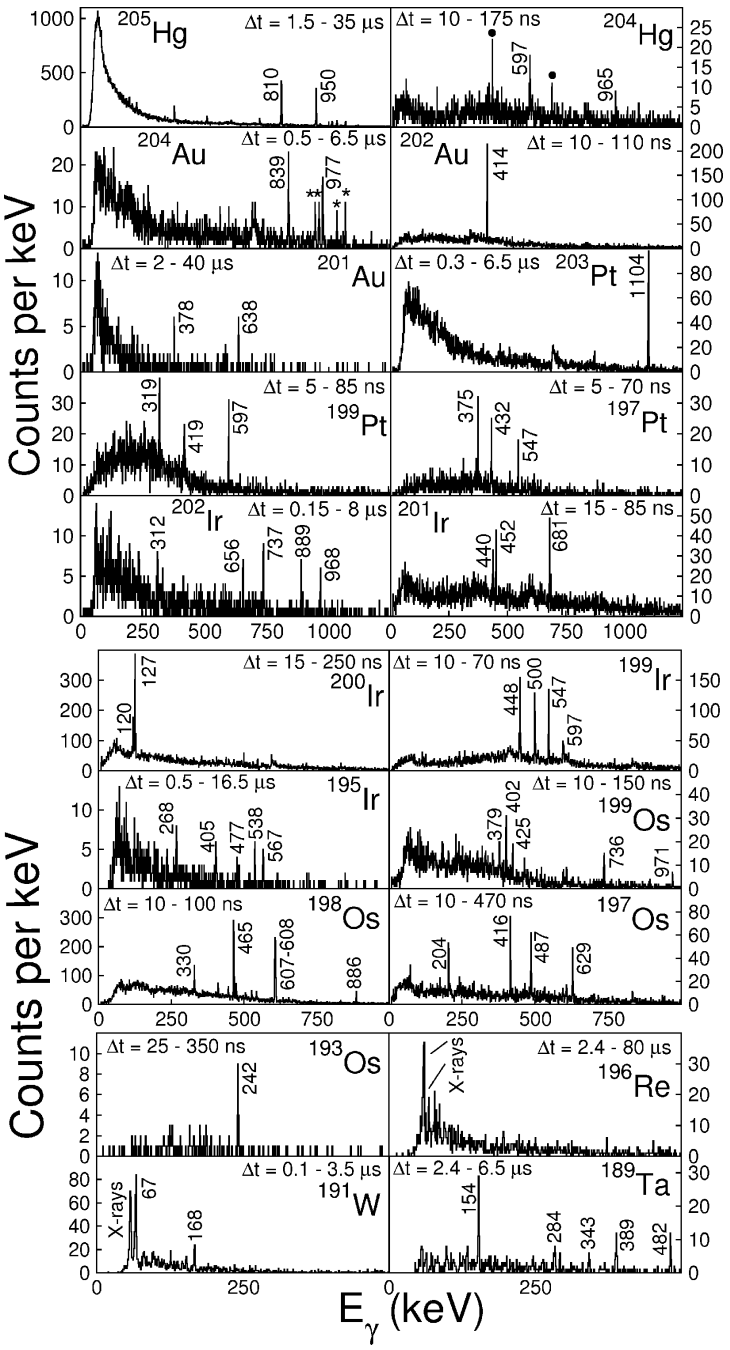

Fig. 3. Examples of delayed γ-ray spectra. The labelled transitions originate from previously unobserved isomeric decays. γ-ray transitions from previously observed isomers are labelled with •, contaminations from other nuclei with *.

The nuclei on which spectroscopic information was obtained in the current experiment are summarised in fig. 1. The experiment had as its main aim the study of neutron-rich N=126 isotones. New experimental information was obtained on three of these, namely ^{205}Au, ^{204}Pt [2] and ^{203}Ir. The delayed gamma-ray spectra are shown in fig. 2. In addition, previously unobserved isomeric decays have been identified for a wide range of nuclei with N<126 (see fig. 3).

4. Conclusions and outlook

Projectile fragmentation when combined with decay spectroscopy is a powerful tool in the study of the structure of exotic nuclei. Experimental results on the heavy neutron-rich nuclei have been presented. The interpretation of the data is in progress.

More recently, further experiments have been performed aimed at the study of neutron-rich N≈126 nuclei. Measurements using the same technique as presented here, but employing an active Si stopper [11], were performed and information on the β decay of several nuclei has been obtained [12,13]. Furthermore, nuclei with N>126 and Z< 82 were populated in the fragmentation of a ^{238}U beam [14]. By combining all the experimental information to be obtained from these studies, a much better understanding of this mass region will be achieved.

Acknowledgements

The excellent work of the GSI accelerator staff is acknowledged. This work is supported by the STFC/EPSRC(UK) and AWE plc.(UK), the EU Access to Large Scale Facilities Programme (EURONS, EU contract 506065), The Swedish Research Council, The Polish Ministry of Science and Higher Education, The Bulgarian Science Fund, The US Dept. of Energy, The Spanish Ministeriode Educacion y Ciencia, The German BMBF, The Hungarian Science Foundation and the Italian INFN.

References

1. K.H. Maier *et al.*, *Phys. Rev. C* **30**, 1702 (1984).
2. S.J. Steer *et al.*, submitted to *Phys. Rev. C*.
3. Zs. Podolyák *et al.*, submitted to *Phys. Lett. B*.
4. P.D. Bond, R.F. Casten, D.D. Warner, D. Horn, *Phys. Lett. B* **130**, 167 (1983).
5. C.Y. Wu *et al.*, *Nucl. Phys. A* **607**, 178 (1996).
6. Zs. Podolyák *et al.*, *Phys. Lett. B***491**, 225 (2000).
7. H. Geissel *et al.*, *Nucl. Inst. and Meth. B* **70**, 286 (1992).
8. Zs. Podolyák *et al.*, *Eur. Phys. J. Spec. Topics* **150**, 165 (2007).
9. S. Pietri *et al.*, *Nucl. Inst. and Meth. B* **261**, 1079 (2007)
10. P.H. Regan *et al.*, *Nucl. Phys. A* **787**, 491c (2007).
11. R. Kumar *et al.*, *Nucl. Inst. and Meth. A*, in press.
12. N. Alkhomashi *et al.*, *Acta Phys. Pol. B*, in press.
13. P.H. Regan *et al.*, *Int. J. of Mod. Phys. E*, in press.
14. N. Al-Dahan *et al.*, *Acta Phys. Pol. B*, in press.